Predictive Turbulence Modeling with Bayesian Inference and Physics-Informed Machine Learning

Jin-Long Wu

Dissertation submitted to the Faculty of the
Virginia Polytechnic Institute and State University
in partial fulfillment of the requirements for the degree of

Doctor of Philosophy
in
Aerospace Engineering

Heng Xiao, Chair
Eric G. Paterson
Christopher J. Roy
K. Todd Lowe

September 6$^{\text{th}}$, 2018
Blacksburg, Virginia

Keywords: Turbulence modeling, RANS, Model-form uncertainty, Data-driven, Uncertainty quantification, Bayesian Inference, Machine learning

Predictive Turbulence Modeling with Bayesian Inference and Physics-Informed Machine Learning

Jin-Long Wu

ABSTRACT

Reynolds-Averaged Navier–Stokes (RANS) simulations are widely used for engineering design and analysis involving turbulent flows. In RANS simulations, the Reynolds stress needs closure models and the existing models have large model-form uncertainties. Therefore, the RANS simulations are known to be unreliable in many flows of engineering relevance, including flows with three-dimensional structures, swirl, pressure gradients, or curvature. This lack of accuracy in complex flows has diminished the utility of RANS simulations as a predictive tool for engineering design, analysis, optimization, and reliability assessments. Recently, data-driven methods have emerged as a promising alternative to develop the model of Reynolds stress for RANS simulations. In this dissertation two physics-informed, data-driven frameworks are presented to improve the accuracy of RANS modeled Reynolds stresses. Specifically, a Bayesian inference approach is presented to calibrate the discrepancies of RANS modeled Reynolds stress by using sparse online measurement data. A machine-learning-assisted approach is also presented to use a large amount of offline high-fidelity simulation data to train a predictive model for the discrepancies of RANS modeled Reynolds stress. The main contribution of this dissertation can be summarized as follows: First, a Bayesian calibration-prediction approach is proposed to quantify and reduce the model-form uncertainty of RANS modeled Reynolds stress. The Bayesian calibration leverages sparse measurement data of mean velocity via an iterative ensemble Kalman method with physical and empirical prior knowledge incorporated, e.g., the realizability of Reynolds stress and the prior uncertainties of modeled Reynolds stress. Second, a physics-informed machine-learning-assisted approach is proposed to utilize high-fidelity simulation data of mean velocity and Reynolds stress via training a functional mapping from some mean flow features to the discrepancies of RANS modeled Reynolds stress. To ensure the important invariance of the trained functional mapping, a systematic approach is presented to extract invariant machine learning inputs and outputs. Finally, two metrics are proposed for an *a priori* assessment of the prediction confidence of machine-learning-assisted Reynolds stress model.

Predictive Turbulence Modeling with Bayesian Inference and Physics-Informed Machine Learning

Jin-Long Wu

GENERAL AUDIENCE ABSTRACT

Reynolds-Averaged Navier–Stokes (RANS) simulations are widely used for engineering design and analysis involving turbulent flows. In RANS simulations, the Reynolds stress needs closure models and the existing models have large model-form uncertainties. Therefore, the RANS simulations are known to be unreliable in many flows of engineering relevance, including flows with three-dimensional structures, swirl, pressure gradients, or curvature. This lack of accuracy in complex flows has diminished the utility of RANS simulations as a predictive tool for engineering design, analysis, optimization, and reliability assessments. Recently, data-driven methods have emerged as a promising alternative to develop the model of Reynolds stress for RANS simulations. In this dissertation I explore two physics-informed, data-driven frameworks to improve RANS modeled Reynolds stresses. First, a Bayesian inference framework is proposed to quantify and reduce the model-form uncertainty of RANS modeled Reynolds stress by leveraging online sparse measurement data with empirical prior knowledge. Second, a machine-learning-assisted framework is proposed to utilize offline high-fidelity simulation databases. Numerical results show that the data-driven RANS models have better prediction of Reynolds stress and other quantities of interest for several canonical flows. Two metrics are also presented for an *a priori* assessment of the prediction confidence for the machine-learning-assisted RANS model. The proposed data-driven methods are also applicable to the computational study of other physical systems whose governing equations have some unresolved physics to be modeled.

To my parents

Acknowledgments

I would like to first thank my advisor, Dr. Heng Xiao, for his passion in both research and teaching and his guidance of my Ph.D. study. Dr. Heng Xiao is knowledgeable in many areas and never hesitates to share his knowledge, and I learned a lot from him. I also would like to thank my committee members, Dr. Eric G. Paterson, Dr. Christopher J. Roy and Dr. K. Todd Lowe, for contributing their time to serve on my doctoral committee and providing valuable feedbacks during my Ph.D. study. In addition, I learned a lot from multiple graduate courses about turbulence and computational fluid dynamics given by Dr. Eric G. Paterson and Dr. Christopher J. Roy.

I am also thankful to all my other collaborators. Specifically, I thank Dr. Jian-Xun Wang for the previous collaboration on the research of data-driven turbulence modeling. I also would like to thank Dr. Rui Sun, Dr. Julia Ling and Dr. Qiqi Wang for the inspiring discussions on our co-authored papers. In addition, I thank Dr. Sylvain Laizet and Dr. Lian Duan for providing high-fidelity simulation databases, which played an important role in my exploration of data-driven methods. I am also thankful to Dr. Roney Thompson, Dr. Luiz Sampaio, Dr. Wouter Edeling and Dr. Gialunca Iaccarino for the helpful discussions during my participation in the summer program at Center for Turbulence Research.

I also would like to thank the summer internship opportunity from Lawrence Berkeley National Laboratory. It was a great research experience for me, and I am thankful to my two mentors, Dr. Karthik Kashinath and Dr. Adrian Albert, and my supervisor Mr Prabhat. I also thank travel awards/grants from Virginia Tech, APS, SIAM, Los Alamos, NCAR and IPAM, which provided me opportunities to share my research progress on various conferences and to exchange ideas with other researchers.

Sincere acknowledgement must also be given to my recent and past colleagues in AOE department at Virginia Tech, especially, Mr. Carlos Michelen-Strofer, Mr. Yang Zeng, Mr. Shunxiang Cao, Mr. Xingsheng Sun and Mr. Yang Song. I also appreciate all the technical support of workstations from Mr. Steve Edwards and all the administrative help from Mrs. Kelsey Wall.

Contents

Chapter 1

Introduction

Reynolds-Averaged Navier–Stokes (RANS) simulations are widely used for engineering design and analysis applications involving turbulent flows. In RANS simulations, the Reynolds stress is the only modeled term. Due to the large model-form uncertainties in existing Reynolds stress models [1, 2], the RANS simulations are known to be unreliable for many flows of engineering relevance, including flows with three-dimensional structures, swirl, pressure gradients, or curvature [3]. This lack of accuracy in complex flows has diminished the utility of RANS as a predictive simulation tool for engineering design, analysis, optimization, and reliability assessments. Recently, the rapid growth of computational power leads to an increase of databases of large eddy simulation (LES) and direct numerical simulation (DNS) for some simple flows. However, it is still infeasible to use LES or DNS in many practical applications, e.g., wall-bounded flows at high Reynolds number. With these existing LES and DNS databases, data-driven methods have emerged as a promising alternative to develop improved models of Reynolds stress for RANS simulations.

The main focus of this work is on developing data-driven methods to reduce the model-form uncertainties in existing RANS models. First, a Bayesian calibration approach is presented to use sparse online data to calibrate the discrepancies of RANS modeled Reynolds stress. Specifically, measurement data of mean velocity are utilized to calibrate the discrepancies of RANS modeled Reynolds stress via an iterative ensemble Kalman method with physical and empirical prior knowledge incorporated, e.g., the realizability of Reynolds stress and the prior uncertainties of modeled Reynolds stress. Second, a machine-learning-assisted approach is presented to use a large amount of offline data to train a predictive model for the discrepancies of RANS modeled Reynolds stress. With machine learning techniques, a functional mapping can be trained from some mean flow features to the discrepancies of RANS modeled Reynolds stress. To ensure the important invariance of the trained functional mapping, a systematic method is presented to extract invariant inputs and outputs for machine learning. Finally, several metrics are proposed for the *a priori* assessment of the prediction confidence of machine-learning-assisted Reynolds stress model.

1.1 Previous work

RANS equations can be written in Eq. 1.1:

$$\frac{\partial U_i}{\partial x_i} = 0 \tag{1.1a}$$

$$\frac{\partial U_i}{\partial t} + \frac{\partial \left(U_i U_j\right)}{\partial x_j} = -\frac{\partial P}{\partial x_i} + \frac{1}{Re}\frac{\partial^2 U_i}{\partial x_j \partial x_j} - \frac{\partial \overline{u_i' u_j'}}{\partial x_j} \tag{1.1b}$$

where U_i denotes the mean velocity, P represents the mean pressure, $Re = \rho U_{\text{ref}} L_{\text{ref}}/\mu$ denotes the Reynolds number, in which U_{ref} and L_{ref} are reference velocity and reference length scale, respectively. It can be seen in Eq. 1.1 that the only unclosed term is the Reynolds stress $\overline{u_i' u_j'}$, which needs to be further modeled. Recently, researcher started to explore data-driven approaches to improve the existing Reynolds stress models. In this dissertation, a literature review is presented for two major types of data-driven approaches, i.e., Bayesian inference and machine learning.

1.1.1 Bayesian inference approaches

The existing Bayesian inference approaches for RANS model-form uncertainties can be summarized as two categories, i.e., parametric approaches and non-parametric approaches.

In parametric approaches, only the parameters in the existing RANS models are calibrated by using Bayesian inference. Cheung et al. [4] applied Bayesian inference to calibrate the coefficients of the Spalart–Allmaras model by using velocity and skin friction data from boundary layer flows. MCMC sampling was used for Bayesian inference, which requires a large number of RANS simulations and is usually computationally infeasible for more complex flows. Kato and Obayashi [5] employed Kalman filtering as an approximate Bayesian inference approach to calibrate the coefficients of the Spalart–Allmaras model from velocity and wall pressure for the zero-pressure gradient boundary layer. They showed that the Kalman filtering method can obtain the correct model coefficients with much less computational cost than MCMC sampling. Kato and Obayashi [6] further extended the Kalman filtering method to more complex flows by calibrating the coefficients of the Spalart–Allmaras model for flows around airfoils. On the other hand, Ray and co-workers [7, 8] used MCMC sampling to infer the model coefficients for a jet-in-cross-flow by building a surrogate model to reduce the computational cost. Several researchers studied different RANS models and found that it is difficult to identify a single best calibrated model in terms of predicting new flows [9, 10]. Consequently, Edeling et al. [10] proposed Bayesian model averaging to construct the best calibrated model based on a class of candidate models. Although the parametric approaches are non-intrusive and thus can be easily implemented for existing CFD software, they neglect uncertainties in the model forms that constrains the quantified uncertainties. Such a constraint can be modeled as an inadequacy term as proposed by Kennedy and O'Hagan [11].

For instance, Cheung et al. [4] used a multiplicative term to characterize the difference between the measured and the RANS simulated velocity profiles. However, Edeling et al. [12] demonstrated that the calibrated inadequacy term varies significantly for different flows.

In non-parametric approaches, the uncertainties are directly calibrated for the modeled term, e.g., the eddy viscosity and the Reynolds stress itself. Dow and Wang [13] injected uncertainties into the eddy viscosity as Gaussian process and solved an optimization problem to determine the optimal eddy viscosity that minimizes the difference between the simulated velocity and the ground truth velocity. Singh and Duraisamy [14] applied a multiplicative term to the source term of ω transport equation and employed maximum a posteriori estimation to determine the optimal multiplicative term. Iaccarino and co-workers [15, 16, 17] pioneered to directly inject uncertainties into Reynolds stress. The realizability of Reynolds stress can be ensured by only perturbing Reynolds stress within Lumley triangle [1] or the equivalent Barycentric triangle [18]. Gorlé et al. [19] proposed a marker function and used it to identify regions where the RANS-predicted Reynolds stress divergence is inaccurate. Edeling [20] proposed a return-to-isotropy model to quantify the model-form uncertainties of Reynolds stress anisotropy. Iaccarino et al. [21] further took into account the uncertainties in the eigenvectors by incorporating two more perturbations. Xiao et al. [22] used the ensemble Kalman method to infer the Reynolds stress model-form uncertainties from sparse velocity data. Wu et al. [23] further demonstrated that the inferred model-form uncertainties can be used to predict unknown flows with proper geometrical transformation. However, such proper transformation is difficult to determine for complex flows, and thus the Bayesian calibration approaches lack the generalization capabilities for predicting flows with vastly different geometries from the calibration flow.

1.1.2 Machine-learning-assisted approaches

To improve the generalization capabilities of the data-driven RANS modeling, researchers explored the use of machine learning techniques to build data-driven turbulence models in the mean flow features space, instead of the physical coordinates space. Such an approach enables the prediction for flows in different geometries yet with similar physics. Tracey et al. [24] demonstrated a proof-of-concept of using kernel regression to predict Reynolds stress anisotropy. Tracey et al. [25] further trained neural networks by using non-dimensional flow variables as the input features and a multiplicative correction term in the Spalart–Allmaras model as the machine learning output. Duraisamy and co-workers [26, 27, 28] performed full field inversion of the multiplicative correction term in the Spalart–Allmaras model from some integral quantities, e.g., wall shear stress, and then trained machine learning models of the multiplicative correction term with regard to some non-dimensional flow variables. Their machine-learning-augmented model demonstrated good generalization capabilities within a class of flows around airfoils [28]. Ling et al. [29] discussed the importance of embedding the tensorial invariance properties in the machine learning process and used this approach to predict the Reynolds stress with a deep neural network. Wang et al. [30] built a machine-

learning model to predict the discrepancies in the RANS modeled Reynolds stresses. Wu et al. [31] pointed out that RANS equations can be ill-conditioned with data-driven Reynolds stress models. To improve the modeling conditioning, Wu et al. [32] proposed a stabilized machine learning scheme by learning linear part and nonlinear part of Reynolds stress separately. A systematic way to construct invariant mean flow features were also presented in [32]. On the other hand, Wu et al. [33] presented an invariant representation of Reynolds stress discrepancies as the outputs of the machine-learning-assisted model. With invariant inputs and outputs, Wu et al. [32] demonstrated that the important invariance (e.g., Galilean invariance) can be preserved in the trained machine-learning-assisted model. A distinctly different approach of machine-learning-assisted modeling is pursued by Weatheritt and Sandsberg [34, 35], who used symbolic regression and gene expression programming to develop algebraic Reynolds stress models. In order to assess the prediction confidence of the machine-learning-assisted models, Wu et al. [36] proposed several metrics to evaluate how well the flow to be predicted is supported by the training flows. Geneva and Zabaras [37] further combined the machine learning prediction and the evaluation of prediction confidence by using Bayesian deep neural networks. The machine learning techniques have also been explored by several researchers to provide data-driven sub-grid scale modeling for large eddy simulations [38, 39, 40, 41, 42], which are not the main focus of this dissertation.

1.2 Contribution

The contribution of this dissertation to the turbulence modeling community can be summarized as follows:

1. A Bayesian inverse modeling framework was developed to calibrate the model-form uncertainties in RANS simulations. This framework incorporates both sparse online measurement data and empirical prior knowledge about the RANS model-form uncertainties. A calibration-prediction approach was also developed to use the calibrated RANS model-form uncertainties for improving the prediction of other closely-related flows where measurement data are not available.

2. A physics-informed machine learning framework was developed to predict the model discrepancies of RANS modeled Reynolds stress. The functional forms of model discrepancies with respect to mean flow features were trained via machine learning algorithms by using existing offline high-fidelity databases. The important invariances (e.g., Galilean invariance) are embedded into the trained functional form by a systematic approach to represent model discrepancies and mean flow features with invariants. In addition, a stabilized machine learning scheme was proposed to avoid the possible ill-conditioning of RANS equations in data-driven RANS modeling.

3. Two metrics are proposed to assess the prediction confidence of machine-learning-trained functional form *a priori*. These metrics are useful to assess the reliability of the

machine learning predicted model discrepancies of Reynolds stress in real applications where the true model discrepancies are unknown.

1.3 Outline

This dissertation is formatted in the "manuscript" format ("multi-paper" format), in which each of the main chapters is in the format of a peer-reviewed journal.

The first chapter introduces the model-form uncertainties in RANS simulations and presents a literature review on previous research of quantification and reduction of RANS model-form uncertainties, with a focus on data-driven approaches. In addition, the contributions of this dissertation are summarized. In Chapter 2, a Bayesian inverse modeling framework was proposed to calibrate the model-form uncertainties in RANS simulations. This Bayesian framework utilizes ensemble Kalman method to quantify and reduce RANS model-form uncertainties by incorporating both sparse online measurement data and empirical prior knowledge. In Chapter 3, a Bayesian calibration-prediction procedure is presented to explore the predictive capability of the calibrated Reynolds stress model-form uncertainties. Specifically, the calibrated model-form uncertainties are re-sampled and transformed geometrically to improve the prediction of other closely-related flows where sparse online measurement data are not available. However, it is usually difficult to determine the proper geometry transformation when the calibration flow and the prediction flow have different geometry configurations. Therefore, the rest chapters of this dissertation focus on building a functional form of Reynolds stress discrepancies with regard to some mean flow features instead of physical coordinates. In Chapter 4, a physics-informed machine learning framework is proposed to build such a functional form via machine learning techniques by training on existing offline high-fidelity simulation databases. Considering that RANS equations can be ill-conditioned for some flows, a stabilized machine learning scheme is proposed to improve the model conditioning. The important invariances (e.g., Galilean invariance) are embedded into the trained functional form by a systematic approach to represent both model discrepancies and mean flow features with invariants. In Chapter 5, a parameterization approach is proposed to represent the discrepancies of Reynolds stress tensor by invariants. This approach is also applicable to extract the invariants from the discrepancies of any second-order tensor and thus has importance in computational mechanics in general. Although the physics-informed machine learning framework have demonstrated predictive capability for closely-related flows, the prediction confidence is usually unknown in real applications where no high-fidelity simulation data are available for comparison. Consequently, several metrics are proposed in Chapter 6 to assess the prediction confidence of the machine-learning-trained functional form *a priori*. These metrics quantify how well the flow to be predicted is supported by the training data within the mean flow features space. Finally, the last chapter concludes the dissertation by highlighting the key contribution and possible directions for the future work.

1.4 Contribution to Co-Authored Papers

Five journal papers were prepared in collaboration with co-authors. The contributions by the author of this dissertation are listed below.

1. Chapter 2.
    - Took part in planning the paper
    - Took part in developing the theory
    - Took part in the numerical implementations
    - Took major part in numerical simulations
    - Took part in writing the paper
2. Chapter 3.
    - Took major part in planning the paper
    - Took major part in developing the theory
    - Made the numerical implementations
    - Made the numerical simulations
    - Wrote major part of the paper
3. Chapter 4.
    - Took major part in planning the paper
    - Took major part in developing the theory
    - Made the numerical implementations
    - Made the numerical simulations
    - Wrote major part of the paper
4. Chapter 5.
    - Took major part in planning the paper
    - Took major part in developing the theory
    - Made the numerical implementations
    - Made the numerical simulations
    - Wrote major part of the paper
5. Chapter 6.
    - Took major part in planning the paper

- Took major part in developing the theory
- Made the numerical implementations
- Made the numerical simulations
- Wrote major part of the paper

Bibliography

[1] S. B. Pope, Turbulent flows, Cambridge university press, 2000.

[2] T. Oliver, R. Moser, Uncertainty quantification for RANS turbulence model predictions, in: APS Division of Fluid Dynamics Meeting Abstracts, 2009.

[3] T. Craft, B. Launder, K. Suga, Development and application of a cubic eddy-viscosity model of turbulence, International Journal of Heat and Fluid Flow 17 (2) (1996) 108–115.

[4] S. H. Cheung, T. A. Oliver, E. E. Prudencio, S. Prudhomme, R. D. Moser, Bayesian uncertainty analysis with applications to turbulence modeling, Reliability Engineering & System Safety 96 (9) (2011) 1137–1149.

[5] H. Kato, S. Obayashi, Approach for uncertainty of turbulence modeling based on data assimilation technique, Computers & Fluids 85 (2013) 2–7.

[6] H. Kato, A. Yoshizawa, G. Ueno, S. Obayashi, A data assimilation methodology for reconstructing turbulent flows around aircraft, Journal of Computational Physics 283 (2015) 559–581.

[7] J. Ray, S. Lefantzi, S. Arunajatesan, L. J. DeChant, Bayesian calibration of a k-ε turbulence model for predictive jet-in-crossflow simulations, in: 44th AIAA Fluid Dynamics Conference, 2014, p. 2085.

[8] J. Ray, S. Lefantzi, S. Arunajatesan, L. Dechant, Bayesian parameter estimation of a k-ε model for accurate jet-in-crossflow simulations, AIAA Journal (2016) 1–17.

[9] T. A. Oliver, R. D. Moser, Bayesian uncertainty quantification applied to RANS turbulence models, in: Journal of Physics: Conference Series, Vol. 318, IOP Publishing, 2011, p. 042032.

[10] W. Edeling, P. Cinnella, R. P. Dwight, Predictive RANS simulations via Bayesian model-scenario averaging, Journal of Computational Physics 275 (2014) 65–91.

[11] M. C. Kennedy, A. O'Hagan, Bayesian calibration of computer models, Journal of the Royal Statistical Society: Series B (Statistical Methodology) 63 (3) (2001) 425–464.

[12] W. Edeling, P. Cinnella, R. P. Dwight, H. Bijl, Bayesian estimates of parameter variability in the k–ε turbulence model, Journal of Computational Physics 258 (2014) 73–94.

[13] E. Dow, Q. Wang, Quantification of structural uncertainties in the k–ω turbulence model, in: 52nd AIAA/ASME/ASCE/AHS/ASC Structures, Structural Dynamics and Materials Conference, AIAA, Denver, Colorado, 2011, pp. 2011–1762.

[14] A. P. Singh, K. Duraisamy, Using field inversion to quantify functional errors in turbulence closures, Physics of Fluids 28 (2016) 045110.

[15] M. Emory, J. Larsson, G. Iaccarino, Modeling of structural uncertainties in Reynolds-averaged Navier-Stokes closures, Physics of Fluids 25 (11) (2013) 110822.

[16] C. Gorlé, G. Iaccarino, A framework for epistemic uncertainty quantification of turbulent scalar flux models for Reynolds-averaged Navier-Stokes simulations, Physics of Fluids 25 (5) (2013) 055105.

[17] M. Emory, G. Iaccarino, G. M. Laskowski, Uncertainty quantification in turbomachinery simulations, in: ASME Turbo Expo 2016: Turbomachinery Technical Conference and Exposition, American Society of Mechanical Engineers, 2016, pp. V02CT39A028–V02CT39A028.

[18] S. Banerjee, R. Krahl, F. Durst, C. Zenger, Presentation of anisotropy properties of turbulence, invariants versus eigenvalue approaches, Journal of Turbulence 8 (32) (2007) 1–27.

[19] C. Gorlé, J. Larsson, M. Emory, G. Iaccarino, The deviation from parallel shear flow as an indicator of linear eddy-viscosity model inaccuracy, Physics of Fluids 26 (5) (2014) 051702.

[20] W. Edeling, G. Iaccarino, P. Cinnella, Data-free and data-driven rans predictions with quantified uncertainty, Flow, Turbulence and Combustion 100 (3) (2018) 593–616.

[21] G. Iaccarino, A. A. Mishra, S. Ghili, Eigenspace perturbations for uncertainty estimation of single-point turbulence closures, Physical Review Fluids 2 (2) (2017) 024605.

[22] H. Xiao, J.-L. Wu, J.-X. Wang, R. Sun, C. Roy, Quantifying and reducing model-form uncertainties in Reynolds-averaged Navier–Stokes simulations: A data-driven, physics-informed bayesian approach, Journal of Computational Physics 324 (2016) 115–136.

[23] J.-L. Wu, J.-X. Wang, H. Xiao, A Bayesian calibration–prediction method for reducing model-form uncertainties with application in RANS simulations, Flow, Turbulence and Combustion (2015) 1–26.

[24] B. Tracey, K. Duraisamy, J. Alonso, Application of supervised learning to quantify uncertainties in turbulence and combustion modeling, in: 51st AIAA Aerospace Sciences Meeting including the New Horizons Forum and Aerospace Exposition, Vol. 259, AIAA, Berlin, Germany, 2013, pp. 1–18.

[25] B. D. Tracey, K. Duraisamy, J. J. Alonso, A machine learning strategy to assist turbulence model development, in: 53rd AIAA Aerospace Sciences Meeting, 2015, p. 1287.

[26] K. Duraisamy, Z. J. Zhang, A. P. Singh, New approaches in turbulence and transition modeling using data-driven techniques, AIAA Paper 1284 (2015) 2015.

[27] E. J. Parish, K. Duraisamy, A paradigm for data-driven predictive modeling using field inversion and machine learning, Journal of Computational Physics 305 (2016) 758–774.

[28] A. P. Singh, S. Medida, K. Duraisamy, Machine-learning-augmented predictive modeling of turbulent separated flows over airfoils, AIAA Journal 55 (7) (2017) 2215–2227.

[29] J. Ling, R. Jones, J. Templeton, Machine learning strategies for systems with invariance properties, Journal of Computational Physics 318 (2016) 22–35.

[30] J.-X. Wang, J.-L. Wu, H. Xiao, Physics-informed machine learning approach for reconstructing Reynolds stress modeling discrepancies based on DNS data, Physical Review Fluids 2 (3) (2017) 034603.

[31] J. Wu, H. Xiao, R. Sun, Q. Wang, Rans equations with reynolds stress closure can be ill-conditioned, arXiv preprint arXiv:1803.05581.

[32] J.-L. Wu, H. Xiao, E. Paterson, Physics-informed machine learning approach for augmenting turbulence models: A comprehensive framework, Physical Review Fluids 3 (7) (2018) 074602.

[33] J. Wu, R. Sun, S. Laizet, H. Xiao, Representation of reynolds stress perturbations with application in machine-learning-assisted turbulence modeling, arXiv preprint arXiv:1709.05683.

[34] J. Weatheritt, R. Sandberg, A novel evolutionary algorithm applied to algebraic modifications of the rans stress–strain relationship, Journal of Computational Physics 325 (2016) 22–37.

[35] J. Weatheritt, R. Sandberg, The development of algebraic stress models using a novel evolutionary algorithm, International Journal of Heat and Fluid Flow.

[36] J.-L. Wu, J.-X. Wang, H. Xiao, J. Ling, A priori assessment of prediction confidence for data-driven turbulence modeling, Flow, Turbulence and Combustion 99 (1) (2017) 25–46.

[37] N. Geneva, N. Zabaras, Quantifying model form uncertainty in reynolds-averaged turbulence models with bayesian deep neural networks, arXiv preprint arXiv:1807.02901.

[38] M. Gamahara, Y. Hattori, Searching for turbulence models by artificial neural network, Physical Review Fluids 2 (5) (2017) 054604.

[39] A. Vollant, G. Balarac, C. Corre, Subgrid-scale scalar flux modelling based on optimal estimation theory and machine-learning procedures, Journal of Turbulence 18 (9) (2017) 854–878.

[40] R. Maulik, O. San, A neural network approach for the blind deconvolution of turbulent flows, Journal of Fluid Mechanics 831 (2017) 151–181.

[41] R. Maulik, O. San, A. Rasheed, P. Vedula, Sub-grid modelling for two-dimensional turbulence using neural networks, arXiv preprint arXiv:1808.02983.

[42] R. N. King, P. E. Hamlington, W. J. Dahm, Autonomic closure for turbulence simulations, Physical Review E 93 (3) (2016) 031301.

Chapter 2

Quantifying and Reducing Model-Form Uncertainties in Reynolds-Averaged Navier–Stokes Simulations

(Published on *Journal of Computational Physics*, 324, 115-136, 2016.)

H. Xiao, J.-L. Wu, J.-X. Wang, R. Sun, C. J. Roy
Department of Aerospace and Ocean Engineering, Virgina Tech, Blacksburg, VA, 24061, USA

Abstract

Despite their well-known limitations, Reynolds-Averaged Navier-Stokes (RANS) models are still the workhorse tools for turbulent flow simulations in today's engineering analysis, design and optimization. While the predictive capability of RANS models depends on many factors, for many practical flows the turbulence models are by far the largest source of uncertainty. As RANS models are used in the design and safety evaluation of many mission-critical systems such as airplanes and nuclear power plants, quantifying their model-form uncertainties has significant implications in enabling risk-informed decision-making. In this work we develop an data-driven, physics-informed Bayesian framework for quantifying model-form uncertainties in RANS simulations. Uncertainties are introduced directly to the Reynolds stresses and are represented with compact parameterization accounting for empirical prior knowledge and physical constraints (e.g., realizability, smoothness, and symmetry). An iterative ensemble Kalman method is used to assimilate the prior knowledge and observation data in a Bayesian framework, and to propagate them to posterior distributions of velocities and other Quantities of Interest (QoIs). We use two representative cases, the flow over periodic

hills and the flow in a square duct, to evaluate the performance of the proposed framework. Both cases are challenging for standard RANS turbulence models. Simulation results suggest that, even with very sparse observations, the obtained posterior mean velocities and other QoIs have significantly better agreement with the benchmark data compared to the baseline results. At most locations the posterior distribution adequately captures the true model error within the developed model form uncertainty bounds. The framework is a major improvement over existing black-box, physics-neutral methods for model-form uncertainty quantification, where prior knowledge and details of the models are not exploited. This approach has potential implications in many fields in which the governing equations are well understood but the model uncertainty comes from unresolved physical processes.

2.1 Introduction

2.1.1 Model-Form Uncertainties in RANS-Based Turbulence Modeling

In Computational Fluid Dynamics (CFD), the Reynolds-Averaged Navier-Stokes (RANS) solvers are still the workhorse tool for turbulent flow simulations in today's engineering analysis, design and optimization, despite their well-known limitations, e.g., poor performance in flows with separation, mean pressure gradient, and mean flow curvature [1]. This is due to the fact that high-fidelity models such as Large Eddy Simulation (LES) and Direct Numerical Simulation (DNS) are still prohibitively expensive for engineering systems of practical interests. Moreover, in engineering design and optimization, many simulations must be performed with short turn-around times, which precludes the use of these high fidelity models.

The RANS equations employ a time- or ensemble-averaging process to eliminate temporal dependency for stationary turbulence. The averaging leads to an unclosed correlation tensor, the Reynolds stress, which needs to be modeled [1, 2]. Turbulence modeling is a primary source of uncertainty in the CFD simulations of turbulent flows. Hundreds of RANS turbulence models have been proposed so far. Each has better performance in certain cases yet none is convincingly superior to others in general. This is due to the fact that the empirical closure models cannot accurately model the regime-dependent, physics-rich phenomena of turbulent flows. Predictions obtained with any of these models have uncertainties that are difficult to quantify. The model-form uncertainties in RANS simulations originating from the turbulence models are the main focus of this work.

2.1.2 Model-Form Uncertainty Quantification: Existing Approaches

A traditional approach for estimating RANS modeling uncertainties involves repeating the simulations by perturbing the coefficients used in the turbulence models, or by using several different turbulence models [3] (e.g., k–ε, k–ω, and eddy-viscosity transport models [1]) and observe the sensitivity of the Quantities of Interests (QoIs). However, different models are often based on similar approximations, and they are likely to share similar biases [4]. Consequently, this *ad hoc* model ensemble approach tends to underestimate of the uncertainty in the model. In turbulence modeling, the Boussinesq assumption states that the Reynolds stress tensor is aligned with and proportional to the local traceless mean strain rate tensor. This assumption is shared by all linear eddy-viscosity models that are commonly used in engineering practice, including the k–ε, k–ω, and eddy-viscosity transport models.

In their seminal work, Kennedy and O'Hagan [5] developed a Bayesian calibration approach that includes a model discrepancy term to account for Model-Form Uncertainty (MFU). In this approach the MFU is quantified by parameterizing the difference between the *outputs* of the computational model and experimental observations as a stationary Gaussian process whose hyperparameters can be inferred from data [5]. This framework has been used in many applications, and a number of sophisticated variants have been developed, e.g., by introducing non-stationary Gaussian processes to model the discrepancy [6], using multiplicative discrepancy term [7], or using high-fidelity models and field measurements to provide observation data [8, 9, 7]. While this approach has had some success, the physics-neutral approach treats the entire numerical model as a black box and does not exploit the prior information that often exists about the nature of the MFU in a given model. Moreover, this framework addresses MFU only in terms of the QoIs, whereas the modeling errors in RANS simulation arise specifically from the modeled Reynolds stress term. Recent work of Brynjarsdottir and O'Hagan [10] emphasized the importance of incorporating prior information, but they also highlighted the difficulties of enforcing prior information in this black-box framework. Even a simple constraint such as zero-gradient boundary condition on the discrepancy is challenging to enforce as shown in [10]. Realistic prior knowledge in engineering practice is generally even more complicated.

Recently, several prominent groups in the CFD community (e.g., Moser and co-workers [11, 12, 13], Iaccarino and co-workers [14, 15, 16, 17, 18], and Dow and Wang [19]) have recognized the limitations of the black-box approach and attempted to open the box by injecting the uncertainties locally into the closure models (i.e., not on the model output directly). Research from these groups is reviewed in detailed below. These approaches have some similarities to earlier work of Berliner et al. [20, 21] in the context of geophysical fluid dynamics, where uncertainties were introduced to the discretized coefficients of the governing geostrophic equations.

Moser and co-workers [11, 12, 13] are the first to explicitly point out and utilize the "composite nature" of the RANS equations. That is, the equations are based on reliable theories describing conservation of mass, momentum, and energy, but contain approximate embedded

models to account for the unresolved or unknown physics, i.e., the Reynolds stress terms. Based on this insight, they introduced a Reynolds stress discrepancy tensor $\boldsymbol{\epsilon}$, which is added to the modeled Reynolds stress ($\tilde{\boldsymbol{\tau}}^{rans}$) in the RANS equations to account for the uncertainty due to the modeling of $\tilde{\boldsymbol{\tau}}^{rans}$. Stochastic differential equations forced by Wiener processes are formulated for the discrepancy $\boldsymbol{\epsilon}$. These equations are structurally similar to but simpler than the Reynolds stress transport equations commonly used in turbulence modeling [e.g., 22, 1]. Applications to plane channel flows (where only the plane shear component of the Reynolds stress tensor is important) at various Reynolds numbers have shown promising results, while extensions to general three-dimensional flows are underway (Moser and Oliver, personal communication).

Iaccarino and co-workers [14, 15, 16, 17, 18] proposed a framework to estimate the model-form uncertainty in RANS modeling by perturbing the Reynolds stress projections towards their limiting states within the physically realizable range. Empirical indicator functions are used to ensure the spatial smoothness (i.e., spatial correlation) of the perturbations in the physical domain, and to inject uncertainties only to the regions where the baseline turbulence model is believed to perform poorly. The novelty of their framework is that both physical realizability and spatial correlations are accounted for, which are two pieces of critical prior information in turbulence modeling. Another advantage of their framework is the moderate computational overhead, since only a few limiting states of the Reynolds stresses are computed. On the other hand, it should be noted that the obtained scattering of the states can only serve as an empirical estimation of the uncertainties, and are not guaranteed to cover the truth. While the true Reynolds stress is a convex linear combination of the Reynolds stresses in the limiting states, the true velocities or other QoIs are not necessarily linear combinations of their respective limiting states.

Dow and Wang [19] quantified model-form uncertainties in the k–ω model by finding the eddy viscosity field that minimizes the misfit in the computed velocity field compared to the DNS data. While their approach has some similarities with that of Iaccarino et al., the most notable difference is that uncertainties are injected to the eddy viscosity and not to the Reynolds stresses directly. Another key difference is that they used DNS data, while Iaccarino et al. did not and instead focused only on forward propagation of uncertainties in the Reynolds stress.

Duraisamy et al. [23, 24, 25], on the other hand, introduced uncertainties as full-field multiplicative discrepancy term β in the production term of the transport equations of turbulent quantities (e.g., $\tilde{\nu}_t$ in the SA model and ω in the k–ω models). Full-field DNS data or sparse data from experimental measurements were used to calibrate and infer uncertainties in this term. It is expected that the inferred discrepancy field can provide valuable insights to the development of turbulence models. They also suggested the possibility of extrapolating the learned discrepancy fields to similar flows via machine learning techniques.

In summary, the CFD community has recognized the advantages of open-box approaches for quantifying model-form uncertainties in RANS simulations, and promising results have been

obtained. However, much work is still needed.

2.1.3 Objective and Novelty of the Present Work

In this work, we focus on a scenario where a limited amount of data (usually from measurements at a few locations) is available. This is often the case when CFD is used in practical applications in conjunction with experimental data to provide predictions. Examples include prediction of flows in a wind farm and atmospheric pollutant dispersion in a city [14]. Built on existing insights and experiences in the literature, the objective of this work is to develop a rigorous, open-box, physics-informed framework for quantifying model-form uncertainties in RANS simulations. Compared to the pioneering framework of Iaccarino et al. [14, 15, 16, 17, 18] where the model-form uncertainty in RANS simulations was estimated by perturbing the Reynolds stresses towards their three limiting states, the novelty of our approach is that an ensemble-based Bayesian inference method is used to incorporate all sources of available information, including empirical prior knowledge, physical constraints (e.g., realizability, smoothness, and symmetric), and available observation data.

This work aims to quantify and reduce the model form uncertainty by utilizing both state-of-the-art statistical inference techniques and domain knowledge in turbulence modeling. As a first step, we focus on an idealized scenario where model-form uncertainty is the dominant source of uncertainty, and the coupling with other uncertainties, e.g., model input uncertainty and numerical uncertainty, is not considered.

The proposed framework has been evaluated on two canonical flows, the flow over periodic hills and the flow in a square duct, in the present work. Further application to a more complicated, three dimensional flow of critical relevance to aerospace engineering, i.e., the flow over a wing–body junction, has also been explored and presented in a separate work [26]. While the authors believe that the present contribution is novel and represents an advancement over the state of the art, we expect significant challenges that need to be addressed before the proposed approach can be extended to industrial flows, e.g., the flows past an aircraft or in a gas turbine.

The rest of the paper is organized as follows. The model-form uncertainty quantification framework is introduced in Section 2.2, and numerical implementation details are given in Section 2.3. Numerical results for two application cases, the flow over periodic hills and the flow in a square duct, are presented in Section 2.4 to assess the merits and limitations of the developed framework. The success, limitations, practical significance, and possible extensions of the proposed method are further discussed in Section 2.5. Finally, Section 2.6 concludes the paper.

2.2 Proposed Framework

2.2.1 Prior Knowledge in RANS Modeling

An important feature of the proposed framework is the explicit, straightforward representation of prior knowledge in a Bayesian inference framework. As such, we summarize the prior knowledge in RANS-based turbulent flow simulations below, some of which has been reviewed in Section 2.1:

1. *Composite model:* The uncertainties in the modeled Reynolds stresses are the main source uncertainties in the RANS model predictions [11].
2. *Physical realizability:* The true Reynolds stress at any point in the domain resides in a subspace of a six-dimensional space [27, 17].
3. *Spatial smoothness:* The Reynolds stress field usually has smooth spatial distributions except across certain discontinuous features (e.g., shocks and abrupt changes of geometry).
4. *Problem-specific prior knowledge:* There are some well-known scenarios where eddy viscosity models are expected to perform poorly as enumerated above, e.g., flow separation, mean flow curvature. Taking the flow over periodic hills as shown in Fig. 2.1 for example, the flood contour indicates typical prior knowledge of the relative magnitude of the Reynolds stress discrepancies in each region, i.e., the regions with recirculation, non-parallel free-shear flow, and the strong mean flow curvature have larger discrepancies.

2.2.2 Representations of Prior Knowledge in the Modeling Framework

In light of the prior knowledge presented above and based on the existing methods in the literature [11, 17, 19], we make the following modeling choices to represent the prior knowledge.

Composite Model

The true Reynolds stress $\boldsymbol{\tau}$ is modeled as a random field of symmetric tensors with $\tilde{\boldsymbol{\tau}}^{rans}$ as its deterministic mean field, where $\tilde{\boldsymbol{\tau}}^{rans}$ is the Reynolds stress field given in the baseline RANS simulation whose model-form uncertainty is to be quantified.[1]

[1] We use $\tilde{}$ to emphasize the fact that $\tilde{\boldsymbol{\tau}}^{rans}$ is a deterministic field, which is in contrast to the random field $\boldsymbol{\tau}$.

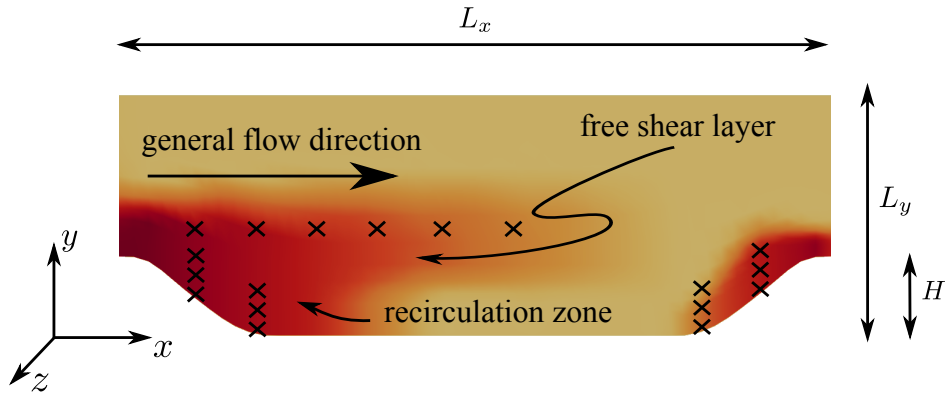

Figure 2.1: Domain shape for the flow over periodic hills. The x-, y- and z-coordinates are aligned with streamwise, wall-normal and spanwise directions, respectively. All dimensions are normalized with H with $L_x/H = 9$, $L_y/H = 3.036$. The contour shows the variance field $\sigma(x)$, where darker color represents the larger variance. The locations where velocities are observed are indicated as crosses ($\times$).

Physical Realizability of Reynolds Stresses

To ensure physical realizability of its realizations, the value of the Reynolds stress field $\boldsymbol{\tau}$ at any given location x is projected onto a space with six physically meaningful dimensions via the following eigen-decomposition [17, 14]:

$$\boldsymbol{\tau} = 2k\left(\frac{1}{3}\mathbf{I} + \mathbf{a}\right) = 2k\left(\frac{1}{3}\mathbf{I} + \mathbf{V}\Lambda\mathbf{V}^T\right) \tag{2.1}$$

where k is the turbulent kinetic energy, $\mathbf{I}$ is the second order unit tensor, $\mathbf{a}$ is the anisotropy tensor, $\mathbf{V} = [\mathbf{v}_1, \mathbf{v}_2, \mathbf{v}_3]$, and $\Lambda = \mathrm{diag}[\lambda_1, \lambda_2, \lambda_3]$ are its orthonormal eigenvectors and eigenvalues, respectively, with $\lambda_1 + \lambda_2 + \lambda_3 = 0$. This decomposition transforms the Reynolds stress to a space represented by six variables with clear physical interpretations: magnitude (represented by the turbulent kinetic energy k, which must be non-negative), shape (represented by two scalars λ_1, λ_2), and orientation (represented by three mutually orthonormal vectors[2] $\mathbf{v}_1$, $\mathbf{v}_2$, and $\mathbf{v}_3$) of the Reynolds stress tensor [28, 14]. Further, λ_1, λ_2, and λ_3 are transformed to the Barycentric coordinates (C_1, C_2, C_3), with $C_1 + C_2 + C_3 = 1$, and subsequently to the natural coordinates (ξ, η). With the mapping from Barycentric coordinates to natural coordinates (see Fig. 2.2), the physically realizable turbulent stresses enclosed in the Barycentric triangle (panel a) are transformed to a square (panel b), i.e., $\{(\xi, \eta) \,|\, \xi \in [-1, 1], \eta \in [-1, 1]\}$, which is more convenient for parameterization. Details of the mapping are presented in 2.6. In summary, we transform the Reynolds stress tensor to six physical dimensions denoted as $(k, \xi, \eta, \mathbf{v}_1, \mathbf{v}_2, \mathbf{v}_3)$. All mappings involved are linear and invertible except for a trivial singular point in $(C_1, C_2, C_3) \mapsto (\xi, \eta)$.

[2]They can be considered as the three orthogonal axes of an ellipsoid, and thus the three vectors have three degrees of freedom in total, i.e., its orientation in three-dimensional space.

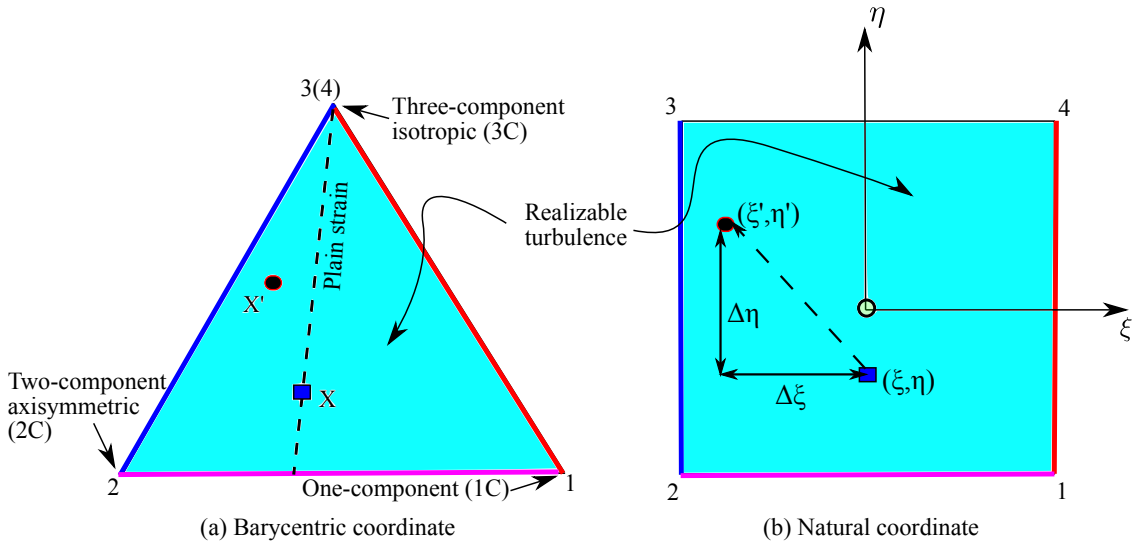

Figure 2.2: Mapping between Barycentric coordinates and natural coordinates, transforming the Barycentric triangle that encloses all physically realizable states [28, 16] to a square via standard finite element shape functions (detailed in 2.6). Corresponding edges in the two coordinates are indicated with matching colors. The singular point 3(4) in the Barycentric coordinate, which maps to the edge 3–4 in the natural coordinate, does not pose any practical difficulties.

After the mapping of Reynolds stress $\tilde{\boldsymbol{\tau}}^{rans}$ to the physically meaningful dimensions, i.e., k, ξ, η, uncertainties are injected to the projected space on these variables. This is achieved by modeling the corresponding truths $k(x)$, $\xi(x)$, and $\eta(x)$ as random fields with $\tilde{k}^{rans}(x)$, $\tilde{\xi}^{rans}(x)$, and $\tilde{\eta}^{rans}(x)$ as priors. Specifically,

$$\log k(x) = \log \tilde{k}^{rans}(x) + \delta^k(x) \tag{2.2a}$$

$$\xi(x) = \tilde{\xi}^{rans}(x) + \delta^\xi(x) \tag{2.2b}$$

$$\eta(x) = \tilde{\eta}^{rans}(x) + \delta^\eta(x) \tag{2.2c}$$

where the spatial coordinate x is the index of the random fields. Note that the logarithmic discrepancy of the turbulent kinetic energy k is modeled in Eq. (2.2a) to ensure the non-negativity of k.

The realizability in this framework is ensured by bounding the perturbed anisotropy (η, ξ) within the square $[-1, 1] \times [-1, 1]$ in the ξ–η plane as shown in Fig. 2.2b. Any perturbed state outside this range will be bounded to the edge of the square, which is admittedly an ad hoc modeling choice. As a result, the prior may become non-Gaussian and the perturbation sample may deviate from zero-mean if a large number of perturbations are bounded. However, note that for a Gaussian prior the percentage of out-of-bound points can be estimated, and thus the variance of the perturbation can be controlled straightforwardly given an allowable ratio of out-of-bound points. This is one of the advantages of mapping the Barycentric

triangle to the square before introducing perturbation as opposed to directly perturbing the baseline within the Barycentric triangle.

The bounding scheme for ensuring realizability can distort the distribution of the sampled Reynolds stresses from the specified prior. Specifically, when the baseline Reynolds stresses are located near the realizability boundaries, e.g., the top vertex of the Barycentric triangle for points near walls, the bounding can cause the sample distribution to become truncated Gaussian. However, note that the tail truncation and the associated probability mass concentration near the boundaries are caused by the bounding procedure to ensure realizability, regardless of whether Barycentric coordinates or natural coordinates are used. This issue is further investigated in two follow-on studies [29, 30], where we proposed a random matrix approach which directly samples a maximum entropy distribution defined on the set of positive semidefinite matrices, and the artificial probability mass concentration described above is avoided. However, note that the approximate Bayesian inference method (i.e., the ensemble Kalman method) used in this work is not sensitive to the prior. From a practical point of view, the prior can be alternatively interpreted as an "initial guess" used in optimization [e.g., 24].

Perturbing the orientations of the modeled Reynolds stress tensor can potentially cause instability in the RANS momentum equation. Consistent with the work of Iaccarino et al., we focus on the magnitude (k) and the shape (λ_1 and λ_2, or equivalently the natural coordinates ξ and η) of the Reynolds stress tensor $\boldsymbol{\tau}$, and do not introduce uncertainties into the orientations $(\mathbf{v}_1, \mathbf{v}_2, \mathbf{v}_3)$. Consequently, the assumed uncertainty space of Reynolds stresses may not contain the truth because the true Reynolds stresses are likely to have different orientations from those of the RANS predictions. The implications of this fact will be further discussed in Section 2.4.1.

Spatial Smoothness of Reynolds Stress Distribution

To ensure spatial smoothness and to reduce the dimension of the uncertainty space, the random fields to be inferred, i.e., δ^k, δ^ξ, and δ^η, are projected to a deterministic functional basis set $\{\phi_i(x)\}$. That is,

$$\delta^k(x, \theta^k) = \sum_{i=1}^{\infty} \omega_i^k|_{\theta^k} \ \phi_i(x) \tag{2.3a}$$

$$\delta^\xi(x, \theta^\xi) = \sum_{i=1}^{\infty} \omega_i^\xi|_{\theta^\xi} \ \phi_i(x) \tag{2.3b}$$

$$\delta^\eta(x, \theta^\eta) = \sum_{i=1}^{\infty} \omega_i^\eta|_{\theta^\eta} \ \phi_i(x) \tag{2.3c}$$

where the coefficients of the i^{th} mode ω_i^k, ω_i^ξ, and ω_i^η are random variables[3] depending on the realized outcome of θ^k, θ^ξ, and θ^η, respectively, and $\phi_i(x)$ are deterministic spatial basis functions. An orthogonal basis set is chosen in this work as will be detailed below, but the orthogonality is not mandatory.

Remarks: The mapping in Section 2.2.2 involves linear transformation of the Reynolds stress at a given point to physical variables, which ensures the physical realizability of the Reynolds stresses in the prior. The orthogonal projection in Section 2.2.2 aims to represent the spatial distribution function on a basis set in a compact manner, which ensures spatial smoothness and reduces the uncertainty dimensions of $\boldsymbol{\tau}(x)$.

Representation of Problem-Specific Prior Knowledge

Finally, problem-specific knowledge is encoded in the choice of basis set $\{\phi_i\}$. Here we will use the flow over periodic hills as example to illustrate the representation of the problem-specific prior knowledge.

We model the prior of the discrepancies δ^k, δ^ξ and δ^η as zero-mean Gaussian random fields (also known as Gaussian processes) $\mathcal{GP}(0, K)$, where

$$K(x, x') = \sigma(x)\sigma(x') \exp\left(-\frac{|x - x'|^2}{l^2}\right) \tag{2.4}$$

is the kernel indicating the covariance at two locations x and x'. The variance $\sigma(x)$ is a spatially varying field specified (see the flood contour in Fig. 2.1) to reflect the prior knowledge that large discrepancies in modeled Reynolds stress are expected in certain regions. The correlation length scale l can be specified based on the local turbulence length scale, but is taken as constant in this work for simplicity.

The orthogonal basis functions $\phi_i(x)$ in Eq. (2.3) take the form $\phi_i(x) = \sqrt{\hat{\lambda}_i}\hat{\phi}_i(x)$, where $\hat{\lambda}_i$ and $\hat{\phi}_i(x)$ are eigenvalues and eigenfunctions, respectively, of the kernel K in Eq. (2.4) computed from the Fredholm integral equation [31]:

$$\int K(x, x')\hat{\phi}(x')\, dx' = \hat{\lambda}\hat{\phi}(x)\,. \tag{2.5}$$

With this choice of basis set the expansions in Eq. (2.3) for the fields δ^k, δ^ξ and δ^η become Karhunen–Loeve (KL) expansions [31], such that ω_i^k, ω_i^ξ, and ω_i^η are uncorrelated random variables with zero means and unit variances.

[3]Throughout the manuscript, subscripts denote indices, and superscripts indicate explanation of the variable. For example, ω_i^k is the coefficient for the i^{th} mode in the expansion of the discrepancy field δ^k for the turbulent kinetic energy k. Tensors are denotes in bold (e.g., $\boldsymbol{\tau}$) and not with index notation.

Remarks The Gaussian process and KL expansions are intentionally presented in this Section to emphasize the fact that they are our specific choices for this problem and prior knowledge only. The optimal choice of basis set depends on the specific characteristics (e.g., smoothness, compactness of support) of the prior. Other functional basis sets, including wavelets [32] or radial basis functions [33], will be explored in future work.

2.2.3 Inverse Modeling Based on an Iterative Ensemble Kalman Method

After the transformations above, the Reynolds stress random field $\boldsymbol{\tau}(x)$ is parameterized by the coefficients ω_i^k, ω_i^ξ, and ω_i^η in Eq. (2.3), which are truncated to m modes and written in a stacked vector form as follows[4]:

$$\boldsymbol{\omega} \equiv [\omega_1^k,\, \omega_1^\xi,\, \omega_1^\eta,\, \omega_2^k,\, \omega_2^\xi,\, \omega_2^\eta,\, \cdots,\, \omega_m^k,\, \omega_m^\xi,\, \omega_m^\eta] \tag{2.6}$$

We employ an *iterative, ensemble-based* Bayesian inference method [34] to combine the prior knowledge as represented above and the available data to infer the distribution of $\boldsymbol{\omega}$. This method is closely related to ensemble filtering methods (e.g., ensemble Kalman filtering), which are a class of standard data assimilation techniques commonly used in numerical weather forecasting [35]. An overview of the ensemble Kalman method based inverse modeling procedure is presented in Fig. 2.3. In the iterative ensemble method, the state of the system $\mathbf{x}$ is defined to include both the physical variables (i.e., velocity field $\mathbf{u}$) and the unknown coefficients $\boldsymbol{\omega}$, i.e., $\mathbf{x} \equiv [\mathbf{u}, \boldsymbol{\omega}]^T$. This is called "state augmentation" [34]. One starts with an ensemble of states $\{\mathbf{x}_j\}_{j=1}^N$ drawn from their prior distributions. During each iteration, all samples in the ensemble are updated to incorporate the observations through the following procedure:

1. reconstruction of Reynolds stresses from the coefficients $\boldsymbol{\omega}$,
2. computation of velocity fields from the given Reynolds stress fields by solving the RANS equations (implemented as forward model tauFoam, detailed in Section 2.3), and
3. a Kalman filtering procedure to assimilate the velocity observation data to the computed states, leading to an updated ensemble.

The updating procedure is repeated until the ensemble is statistically converged. The convergence is achieved when the two-norm of the misfit between the predictions and the observations falls below the noises level of the observations [34]. The converged ensemble is

[4] It is trivial for each variable to have a different number of modes, but this possibility is omitted here to simplify notation.

considered a sample-based representation of the posterior distribution of the system state, from which the mean, variance, and higher moments can be computed. The algorithm of the inversion scheme is presented in 2.6, and further details can be found in [34].

The noises added to the observations represent a combination of measurement errors and process errors [36]. The former is likely to be negligible for DNS data. However, the latter can be significant and is used to account for the fact that the observed system and the system described in the numerical model can have different dynamics. From a Bayesian perspective, adding the process noise allows the likelihood and the prior distribution to have overlap in their supports and thus be able to reconcile with each other in the inference procedure. As long as the chosen noise level σ_{obs} is larger than a threshold (1% of truth in this work), the inferred posterior means are not sensitive to this parameter. See further discussion in [e.g., 34].

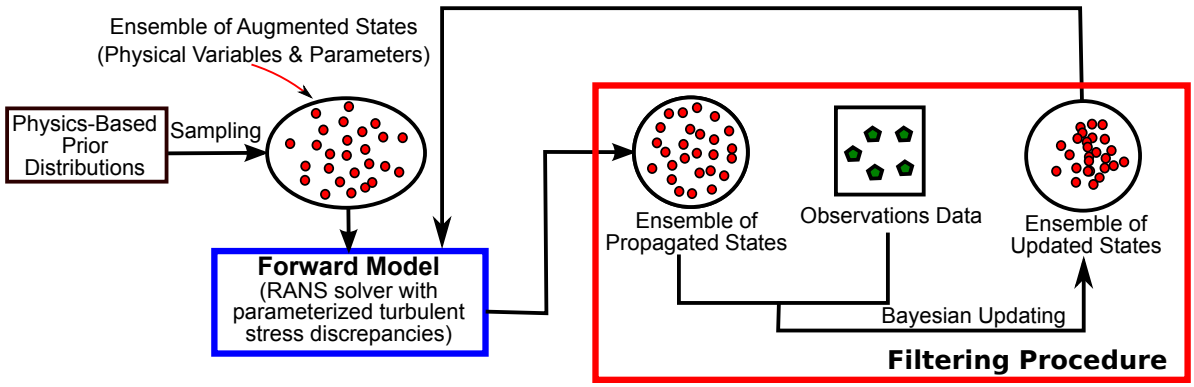

Figure 2.3: Inference of coefficients in the parameterized model discrepancies (e.g., discrepancies in RANS modeled Reynolds stresses) using an iterative ensemble Kalman inversion method. This approach combines prior knowledge of a given problem and available data to quantify and reduce model-form uncertainty.

An important property of the iterative ensemble Kalman method is that the posterior ensembles and its mean all lie in the linear space $\mathcal{A}$ spanned by the prior ensemble $\{\mathbf{x}_j\}_{j=1}^N$. In essence, this scheme attempts to search the space $\mathcal{A}$ to find the optimal solution that minimizes the misfit between the posterior mean and the observations, accounting for the uncertainties in both [34]. As with many inverse problems, this problem is intrinsically ill-posed. Specifically, because of the sparseness of the observation (the scenario of concern in our work), the amount of data is usually not sufficient to constrain the uncertainties in the states, which include the model discrepancies as components. The forward model essentially provides the regularization of the ill-posedness with its physical representation of the system dynamics.

The ensemble Kalman-based uncertainty quantification scheme used here is an approximate Bayesian method, and is computationally cheaper than the exact Bayesian scheme based on Markov Chain Monte Carlo sampling. It is not expected to give posterior distributions with

comparable accuracy to those obtained from exact Bayesian schemes [37]. This limitation will be further discussed in Section 2.5.

2.2.4 Summary of the Algorithm in the Proposed Framework

In summary, the overall algorithm of the proposed framework for quantifying and reducing uncertainties in a RANS simulation is presented as follows.

1. Perform the baseline RANS simulation to obtain the velocity $\tilde{\boldsymbol{u}}^{rans}(x)$ and Reynolds stress $\tilde{\boldsymbol{\tau}}^{rans}(x)$.
2. Perform the transformation $\tilde{\boldsymbol{\tau}}^{rans} \mapsto (\tilde{k}^{rans}, \tilde{\xi}^{rans}, \tilde{\eta}^{rans})$.
3. Compute KL expansion to obtain basis set $\{\phi_i(x)\}_{i=1}^m$, where m is the number of modes retained.
4. Generate initial prior ensemble of coefficient vectors $\{\boldsymbol{\omega}_j\}_{j=1}^N$, where N is the ensemble size.
5. Use iterative scheme shown in Fig. 2.3 to obtain the posterior ensemble of the state distribution. Specifically, in each iteration do the following:
   (a) Recover the discrepancy fields δ^k, δ^ξ, and δ^η from the coefficient $\{\boldsymbol{\omega}_j\}_{j=1}^N$ in the current state and the basis functions via Eq. (2.3), and obtain realizations of k, ξ, and η from Eq. (2.2) for each sample in the ensemble.
   (b) Obtain Reynolds stress ensembles $\{\boldsymbol{\tau}_j\}_{j=1}^N$ via mapping $(k, \xi, \eta) \mapsto \boldsymbol{\tau}$.
   (c) For each sample in the ensemble $\{\boldsymbol{\tau}_j\}_{j=1}^N$, solve the RANS equations for velocity field $\boldsymbol{u}_j$ with given Reynolds stress field $\boldsymbol{\tau}_j$.
   (d) Compare the ensemble mean with velocity observations, and use the Kalman filtering procedure to correct the augmented system state ensemble $\{\mathbf{x}_j\}_{j=1}^N$, where $\mathbf{x}_j = [\mathbf{u}_j, \boldsymbol{\omega}_j]^T$. The updated coefficient vector ensemble $\boldsymbol{\omega}_j$ is thus obtained as part of the system state ensemble.
   (e) Stop if statistical convergence of the ensemble as defined in Section 2.2.3 is achieved.

2.3 Implementation and Numerical Methods

The uncertainty quantification framework including the mapping of Reynolds stresses and the iterative ensemble Kalman method is implemented in Python, which interfaces with RANS models and the KL expansion procedures to form the complete framework. The package

UQTk developed by Sandia National Laboratories is used to perform the KL expansions [38]. Two types of RANS solvers are used in this framework, a conventional baseline RANS solver `simpleFoam` and a forward RANS solver `tauFoam` which computes velocity field with a given Reynolds stress field. Both solvers are described as below.

The baseline simulation uses a built-in RANS solver `simpleFoam` in OpenFOAM for incompressible, steady-state turbulent flow simulations. OpenFOAM (for "Open source Field Operation And Manipulation") is an open-source, general-purpose CFD platform based on finite-volume discretization. The platform consists of a wide range of solvers and post-processing utilities. The SIMPLE (Semi-Implicit Method for Pressure Linked Equations) algorithm [39] is used to solve the coupled momentum and pressure equations. Collocated grids are used, and the Rhie and Chow interpolation is used to prevent the pressure–velocity decoupling [40]. Second-order spatial discretization schemes are used to solve the equations on an unstructured, body-fitting mesh. Given the specification of the flow including initial conditions (to start the iteration), boundary conditions, geometry, and the choice of turbulence model, the `simpleFoam` solver computes the velocity field along with Reynolds stresses by solving the RANS equations as well as the equations for the turbulence quantities (e.g., turbulent kinetic energy k and the rate of dissipation ε for k–ε models). We choose the Launder–Sharma low Reynolds number k–ε model [41] in the baseline simulations. Accordingly, the meshes are refined wall-normal direction near the wall to resolve the boundary layer. This is to avoid the complexity of using wall-functions, which is in consistent with the work of Emory et al. [17]. As can be seen in the overall algorithm presented in Section 2.2.4, for each uncertainty quantification case the baseline simulation is performed only once.

The forward RANS model `tauFoam` is invoked repeatedly in the Bayesian inference procedure. This solver is adopted from and similar to `simpleFoam` except that it computes the velocity directly with a *given Reynolds stress field*. There is no need to specify a turbulence model and or to solve the equations for turbulence quantities, since the Reynolds stress is given. Moreover, as the forward RANS simulations are initialized with the converged baseline solutions, the number of iterations needed to achieve convergence is much smaller than that in the baseline simulation. As a result, the computational cost for each call of the forward RANS model `tauFoam` is much lower than that of the conventional RANS solver `simpleFoam`. In the simulations presented below, the forward RANS simulations need only 10% of the computational cost as that of the baseline simulation to achieve the same residual.

2.4 Numerical Simulations

Two canonical flows, the flow in a channel with periodic constrictions (periodic hills) and the fully developed turbulent flow in a square duct, are chosen to evaluate the performance of the proposed framework. The periodic hill flow features a recirculation zone formed by a forced separation, a strong mean flow curvature due to the domain geometry, and a shear layer that is not aligned with the overall flow direction. All these features are known to pose

challenges for turbulence modeling. The square duct flow is characterized by a secondary flow pattern in the plane perpendicular to the main flow. The in-plane secondary flow is driven by the imbalance in the normal components of the Reynolds stress tensor, which cannot be captured by models with isotropic eddy viscosity turbulent models including most of the widely used models such as k–ε, k–ω, and eddy viscosity transport models. The two challenging cases are chosen to demonstrate the capability of the proposed framework in quantifying and reducing uncertainties in the RANS model predictions by incorporating sparse observations.

2.4.1 Flow over Periodic Hills

Case Setup

The periodic hill flow is widely used in the CFD community to evaluate the performance of turbulence models due to the availability of experimental and numerical benchmark data [42]. The geometry of the computational domain and the coordinate system are shown in Fig. 2.1. The Reynolds number based on the crest height H and the bulk flow velocity U_b at the crest is $Re_b = 2800$. Periodic boundary conditions are applied in the streamwise (x) direction, and non-slip boundary conditions are applied at the walls. The mean flow is two-dimensional, and thus the spanwise (z) direction is not considered for the RANS simulations.

The mesh and computational parameters used in the uncertainty quantification procedure are presented in Table 2.1. Despite the coarse meshes, the walls are adequately resolved in both cases as required by the Lauder–Sharma turbulence model [41]. The distance between the center of the first cell and the wall is smaller than 1 in most regions for periodic hill case and 0.7 for the square duct case. Parameters of the meshes for both cases are shown in Table 2.1.

The uncertainties in ξ, η, k are all considered, and thus δ^ξ, δ^η and δ^k are all random fields. This choice is based on our prior knowledge that both the Reynolds stress anisotropy (indicated by the shape $\boldsymbol{\tau}$, or equivalently, ξ and η) and turbulent kinetic energy k predicted by the RANS model are biased, and both are important for the accurate prediction of the flow behavior. The length scale parameter l is chosen according to the approximate length scale of the flow, which can be obtained either from our physical understanding of the flow or, if that is not available, from the baseline RANS simulation. Velocity observations are generated by adding Gaussian random noises with standard deviation σ_{obs} to the truth from DNS data. Specifically, the observations used in each iteration are independent realizations from a Gaussian distribution whose mean is the truth and standard deviation σ_{obs} is 10% of the true mean value. The noises at different locations are uncorrelated. The observation points are arranged so that they are closer in regions where the spatial changes of the flow are more rapid (the recirculation zone leeward of the hill and the reattached flow region windward of the hill), and are further apart in the free shear region downstream of the hill

crest. This arrangement of observations is expected in actual experiments. The ensemble usually converges in approximately 10 iterations. For all cases presented in this work, 60 samples are used in the ensemble. We have performed detailed sensitivity studies on the ensemble size, and it was found that the inferred velocities and QoIs do not vary if more than 30 samples are used. This finding is consistent with earlier studies when EnKF was used in data assimilations in applications such as weather forecasting [43]. The computational cost of the proposed procedure is further discussed in Section 2.5.1.

The non-stationary Gaussian process models for δ^ξ, δ^η and δ^k share the same variance field $\sigma(x)$, which are shown as flood contour in Fig. 2.1. Design of the variance field is strictly based on physical prior knowledge as described in Section 2.2.2, and does not take the DNS data into account, since the complete field of the true Reynolds stresses are rarely known in practical applications. Specifically, the variance fields of the priors as shown in Figs. 2.1 and 2.10 are constructed by superimposing a constant background value σ_0 and a spatially varying field $\sigma_{local}(x)$, i.e., $\sigma(x) = \sigma_0 + \sigma_{local}(x)$. For the periodic hill case, the background σ_0 is set to be 0.2. To obtain the field $\sigma_{local}(x)$, we specify that $\sigma_{local} = 0.5$ at the following locations, where RANS predictions are considered less reliable: (1) the hill crest, (2) the center of the recirculation region, (3) the windward side of the hill, and (4) the free-shear layer downstream the crest. Interpolations based on radial basis functions with exponential kernels are used to obtain $\sigma_{local}(x)$ at other locations. As such, its value decays to zero far away from the locations specified above. The length scale of the basis functions is estimated based on the characteristic length of the mean flows, which is chosen as the hill height H.

The first sixteen modes obtained from the KL expansion are used to reconstruct the discrepancy field. The number of modes retained is chosen such that the reconstructed field has at least 80% of the total variance of the original random field. A rule of thumb is that a coverage ratio of 80% is adequate for a faithful representation. Increasing the number of modes increases the difficulty of the inference and may lead to deteriorated results for a given amount of observation data.

Parameter sensitivity analysis has been conducted to ensure that reasonable variations of the computational parameters above do not lead to significantly different results or conclusions. In particular, we have shown in a follow-on study [44] that even in the complete absence of prior knowledge (i.e., a constant variance field $\sigma(x)$), the inferred velocities are still significantly improved, albeit slightly less so than that with an informative prior. Specifically, in the region near the upper wall, much more uncertainties are presented in the posterior ensemble when a non-informative, constant variance field is used.

Results

The first six modes of the KL expansion are presented in Fig. 2.4 along with two typical realizations. This is to illustrate the uncertainty space of the Reynolds stress discrepancy field (or more precisely its projections δ^ξ, δ^η and δ^k) . All the modes have been shifted and

Table 2.1: Mesh and computational parameters used in the flow over periodic hills and the flow in a square duct.

cases	**periodic hill**	**square duct**
mesh ($n_x \times n_y$)	50×30	30×30
domain size ($L_x \times L_y \times L_z$)	$9H \times 3.306H \times 0.1H$	$0.4D \times 0.5D \times 0.5D$
$\Delta x \times \Delta y \times \Delta z$ in y^+	$35 \times [2, 65] \times 850$	$24 \times [1.4, 30] \times [1.4, 30]$
first grid point in y^+	~ 1, below $2y^+$ in most region	0.7
number of samples N	60	
fields with uncertainty	ξ, η, k	ξ, η
number of modes m per field	16	8
length scale[(a)]	H	0.1D
number of observation	18	25[(b)]
std. dev. observation noise (σ_{obs})	10% of truth	

(a) Normalized by hill crest height H and domain size h for the periodic hill case and square duct case, respectively.
(b) Only 13 points of velocity data are supplied effectively due to the diagonal symmetry.

normalized to the range $[0, 1]$. It can be seen that in all the models and the realizations the variations mostly concentrate in the three pre-specified regions (recirculation zone, free shear region, and the reattached flow windward of the hill), and the upper part of the channel has rather small variations. This is consistent with our physical prior knowledge specified through the variance field design.

Accurate predictions of the recirculation and the reattachment of the flow are of the most interest in the flow over periodic hills. Therefore, we identify three quantifies of interest for this case: (1) the velocity field, in particular the velocities in the recirculation zone and reattached flow region windward of the hill, (2) the distribution of shear stresses τ_w on the bottom wall, and (3) the reattachment point x_{attach}. Other quantities that are important in engineering design and analysis (e.g., friction drag, form drag, size of separation bubble) are closely related to the three QoIs above.

The prior and posterior ensembles of the velocities are presented in Fig. 2.5 with comparison to the DNS benchmark results. The geometry of the domain is also shown to facilitate visualization. From Fig. 2.5a it can be seen that the prior mean velocity profiles are very close to those from the baseline RANS simulation, with only minor differences at a few locations (e.g., near the bottom wall at $x/H = 4$, 5, and 6). This is not surprising, since the Reynolds stresses prior ensemble use the RANS modeled Reynolds stress $\tilde{\boldsymbol{\tau}}^{rans}$ as the mean. In other words, the ensemble is obtained by introducing perturbations to the $\tilde{\boldsymbol{\tau}}^{rans}$. Therefore, the similarity between the velocity profiles in the baseline simulation and those of the prior ensemble indicates that the mapping from Reynolds stress to velocity is approximately linear with respect to the perturbations introduced to the prior Reynolds stresses ensemble. Clearly,

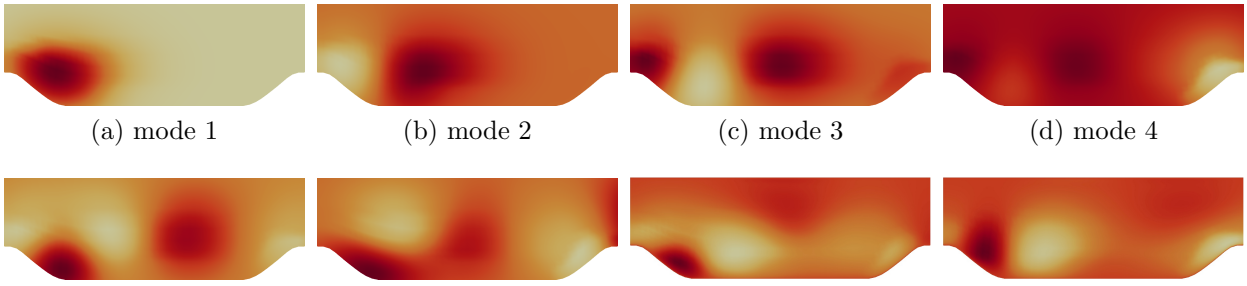

(a) mode 1 (b) mode 2 (c) mode 3 (d) mode 4

(e) mode 5 (f) mode 6 (g) realization 1 (h) realization 2

Figure 2.4: Illutstration of KL expansion modes of the periodic hill case. All the modes have been shifted and scaled into the range between 0 (lightest) and 1 (darkest) to facilitate presentation, and the legend is thus omitted. Panels (a) to (f) represent modes 1 to 6, respectively. Lower modes are more important. Panels (g) and (h) show the turbulent kinetic energy associated with two typical realizations of the Reynolds stress discrepancy fields.

both the baseline velocities and the prior mean velocities deviate significantly from the benchmark results, particularly in the recirculation region (leeward of the hill). From Fig. 2.5 it can be seen that the posterior ensemble mean of the velocities along all the lines are significantly improved compared to the baseline results.

The remaining differences between the obtained posterior mean and the benchmark data can be attributed to two sources: (1) the sparseness of the observation data, and (2) the inadequacy of the proposed inference model, specifically, the posterior mean Reynolds stress does not reside in the space $\mathcal{A}$ spanned by the prior ensemble. However, note that obtaining the correct Reynolds stresses is a sufficient but not necessary condition to infer the correct velocities. For example, if the divergence of the true Reynolds stresses resides in the space spanned by the prior ensemble, the true mean velocity can still be obtained. This is not surprising since it is the divergence of the Reynolds stress tensor field that appears as source term in the RANS momentum equation. To illustrate this point, it is particularly interesting to investigate the scenario when large amounts of data are available, since any remaining discrepancies should then be explained solely by the inadequacy of the inference processes. We performed an experiment where all the benchmark velocities along ten sampled lines at $x/H = 0, 0.5, 1, 2, \cdots, 8$ were used as observations. In this scenario the posterior mean velocities agree with the benchmark data very well, even in the regions between the sample lines, where no data are available. However, significant discrepancies still remain between the inferred posterior mean of the Reynolds stresses and the benchmark. We argue that the inability to obtain the correct Reynolds stress field is *not an intrinsic limitation* of the proposed method. Rather, it can be explained by the non-unique mapping between Reynolds stress and velocities as described by the RANS equations. That is, two distinctly different Reynolds stress fields can lead to identical or very similar velocity fields, because the divergence of the Reynolds stress appears in the RANS equation as pointed out above. The

non-unique mapping is further discussed in Section 2.5.3. However, when we assume that some sparse measurements of Reynolds stresses are available, which admittedly are difficult to obtain in practical experiments, the inferred Reynolds stresses did improve significantly. The results are omitted here for brevity.

In order to obtain the true Reynolds stresses, the posterior mean Reynolds stress must reside in the space $\mathcal{A}$ spanned by the prior ensemble, but in practical inferences there is no guarantee this will be the case. There are two reasons for this. First, uncertainties are only introduced to the magnitude (k) and shape (ξ and η) of the baseline Reynolds stresses, and not to the orientations ($\mathbf{v}_1$, $\mathbf{v}_2$, and $\mathbf{v}_3$). Second, a limited number of modes are retained in the KL expansion, which correspond to very smooth fields of Reynolds stress discrepancies. Therefore, if we think of the true Reynolds stress as residing in a high-dimensional space, in the current framework we assume that the truth is reasonably close to the baseline prediction $\tilde{\boldsymbol{\tau}}^{rans}$, and thus we only search the vicinity of $\tilde{\boldsymbol{\tau}}^{rans}$ for realizable candidates. This is justified by the confidence that the chosen baseline RANS model is rather capable, usually backed by previous experiences accumulated by the community on the model of concern.

Finally, we emphasize that if the true Reynolds stresses do reside in the space spanned by the prior ensemble, the posterior mean velocity and the Reynolds stresses would indeed coincide with the truths. This scenario could occur if the baseline Reynolds stress $\tilde{\boldsymbol{\tau}}^{rans}$ only differs from the true Reynolds stress in magnitude k and shape ξ and η, and the discrepancy is smooth enough to be represented by the chosen number of modes. However, both scenarios are rather unlikely in any nontrivial cases. For verification purposes we have designed a case of flow over periodic hills with synthetic data (as opposed to DNS data) that satisfies the requirements above, and have confirmed that the obtained posterior mean velocity indeed exactly agrees with the truth in this case, and that the true Reynolds stress can also be obtained. The results are detailed in a separate work [44].

This claim that the prior has small influence to the prior is apparently contradictory to the Bayesian inference theory, which states that the posterior is proportional to the product of the prior and the likelihood informed by the observation data. However, in the ensemble Kalman method used in this work, the observation data are imposed on the prior iteratively (albeit with different noises in each iteration). As a result, the influence of the prior on the posterior diminishes as the posterior proceeds to statistical convergence. From a practical perspective, the iterative ensemble Kalman method can also be interpreted as an optimization procedure (e.g., that used by Parish et al. [24]), with the prior corresponding to the initial guess. This interpretation, as an alternative to the Bayesian interpretation, has been advocated in the literature [34, 45].

Figure 2.6 shows the 95% credible intervals estimated from the data in the prior and posterior velocity ensembles. That is, at each point, 95% of the samples fall within the shaded region (light/pink shaded for the prior and dark/blue shaded for the posterior). Note that the credible intervals shown here are point estimations and do not contain information on the spatial correlations of the velocity profiles. It can be seen from Fig. 2.6 that the 95%

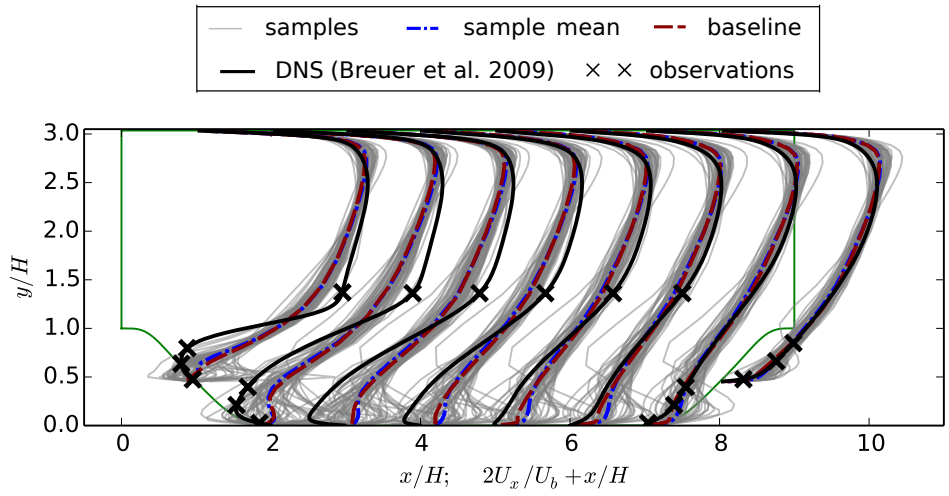

(a) Prior velocities ensemble

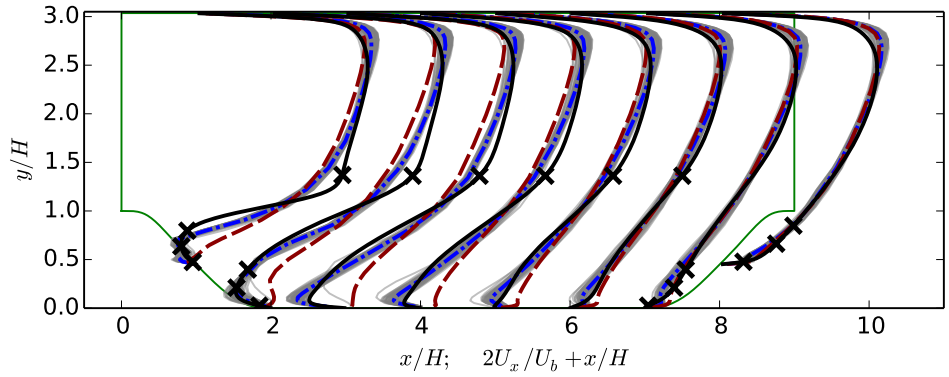

(b) Posterior velocities ensemble

Figure 2.5: The prior and posterior ensembles of velocity profile for the flow over periodic hill at eight locations $x/H = 1, \cdots, 8$ compared with benchmark data and baseline results. The locations where velocities are observed are indicated with crosses ($\times$).

credible interval in the posterior is significantly narrowed compared to that in the prior, which suggests that the model form uncertainty is reduced by incorporating the velocity observation data. Such a reduction of uncertainty is more visible in the recirculation zone, where more observation data are available. In contrast, the prior uncertainty near the upper wall largely remains, which is due to the lack of observation data in this region.

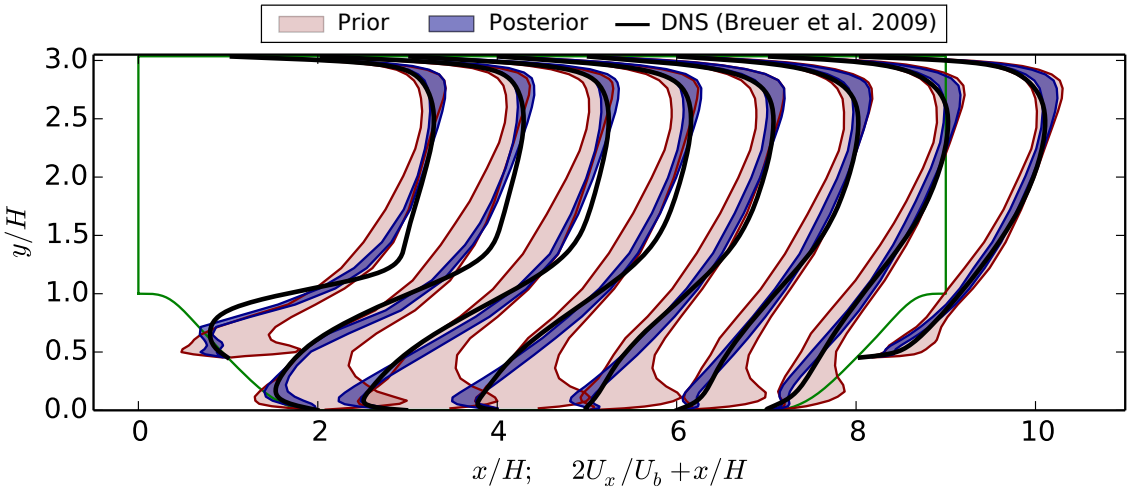

Figure 2.6: The 95% credible intervals of the prior (light/pink shaded region) and posterior (dark/blue shaded region) ensembles of velocity profiles for the flow over periodic hills.

The other two QoIs, bottom wall shear stress τ_w and the reattachment point x_{attach}, are shown in Fig. 2.7. Similar to the velocity profiles in Fig. 2.5, both prior and posterior ensembles are presented and compared with benchmark data and baseline results. It can be seen from Fig. 2.7a that the prior ensemble means of both τ_w and x_{attach} deviate from the benchmark DNS data significantly. In particular, the baseline RANS simulation predicts a much smaller recirculation zone than the truth. Figure 2.7b shows that in most of the region (between $x/H = 1$ and $x/H = 8$) the posterior ensemble mean has better agreement with the DNS data than the baseline results. In fact, in this region, all samples in the posterior ensemble have better agreement with the benchmark than the baseline results in terms of both wall shear stress and reattachment point. This improvement demonstrates the merits of the current framework. Incorporating observation data and physical prior knowledge indeed leads to improved predictions of both QoIs.

It is noted that in the immediate vicinity of the hill crest, i.e., near $x/H = 0.5$ and $x/H = 8.5$, the posterior ensemble is similar to or even slightly deteriorated compared to the baseline in terms of agreement with DNS data. The reason is that in this region the flow has rapid spatial variations. Specifically, there is a separation between $0 < x/H < 1$, and a large mean flow curvature with strong pressure gradient between $8 < x/H < 9$. Consequently, the length scales of the coherent structures in this region are small, and thus the correlations between this part of the flow and other regions are weak. On the other hand, no velocity observations are available in this region. Here we point out an important fact that the Bayesian

inference based on ensemble Kalman method primarily relies on the *correlation* between the predicted system state variables at different locations to make corrections. Specifically, the observations only bring information to the states at the locations correlated to the observed states. Hence, poor prediction is expected for a region that has neither observations within it nor statistically significant correlations with the regions that have observations. The role of correlation in the current framework is further discussed in Section 2.5.2.

The prior and posterior distributions of the reattachment point represented by samples are shown in Fig. 2.7 (bottom panels). It can be seen that the bias in the prior distribution as compared to the DNS data is large, while in the posterior distribution the bias is significantly corrected. Moreover, the prior sample scattering is wide, indicating large uncertainties. In contrast, the posterior distribution is significantly narrowed, which indicates increased confidence in the prediction by incorporating velocity observations into the Bayesian inference.

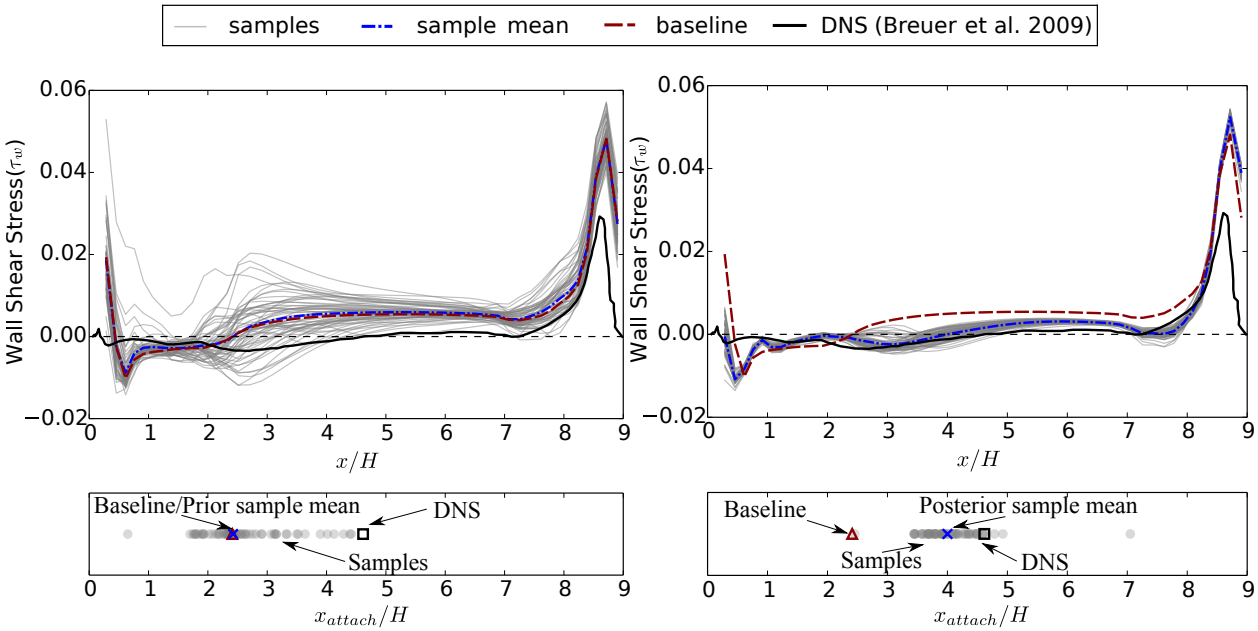

(a) Prior ensemble (b) Posterior ensemble

Figure 2.7: (a) Prior ensemble and (b) posterior ensemble of the bottom wall shear stress τ_w (*top panels*) and reattachment point x_{attach} (*bottom panels*) for the flow over periodic hills. The region with negative shear stress τ_w indicates the extent of recirculation zone on the bottom wall. The reattachment point is the downstream end of the recirculation zone, which can be determined by the location at which the wall shear stress changes from negative to positive. Note that certain samples in the ensemble have two recirculation zones that are very close to each other. In these cases the reattachment point of the downstream one is taken.

The comparison of 95% credible interval obtained from the prior and posterior ensemble of wall shear stresses are presented in Figure 2.8. Similar reduction of model-form uncertainty

as shown in Fig. 2.6 is observed here. Compared to that in the prior, the 95% credible interval in the posterior has a much smaller uncertainty and a better coverage of the benchmark data in the region between $x/H = 1$ and 5. This is because there are more observations available in the vicinity. Admittedly, in some regions, e.g., between $0 < x/H < 1$ and $8 < x/H < 9$, the posterior credible interval does not improve or even deteriorate compared to the prior, which is due to the lack of observation data and the relatively small length scale in these regions as discussed above. It is noted that in some regions the 95% credit intervals, e.g., in Figs. 2.6 and 2.8, failed to cover the truth, which indicates that the current method should still be used with caution when making high-consequence decisions. The iterative ensemble Kalman method tends to underestimate uncertainties in the posterior distributions, a difficulty shared by many other maximum likelihood estimators as well [46].

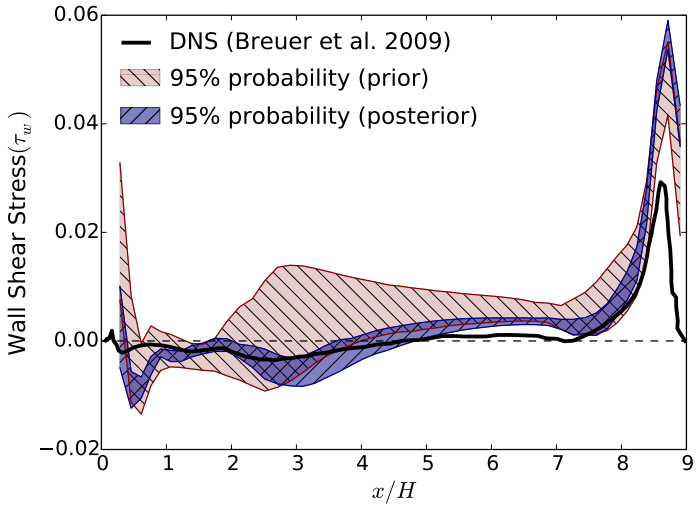

Figure 2.8: The 95% credible intervals of the prior (light/pink shaded region) and posterior (dark/blue shaded region) ensembles of bottom wall shear stress for the flow over periodic hills.

Figure 2.9 shows that the bias in the turbulent kinetic energy (TKE) from baseline RANS prediction has been partly corrected, especially for the upstream region. It is possible that the production of TKE due to the instability in the free-shear region after the separation is the driving factor. Consequently, the improved prediction of TKE in this region leads to the corrections for the velocities and other QoIs in the entire field. However, note that the posterior mean of TKE is not necessarily better than the baseline results at all locations. The TKE levels immediately downstream of the hill crest have been increased, but at the downstream locations the posterior mean are not significantly better than the baseline. In the process of minimizing misfit with the observations, some compromises are inevitably made, with some regions such as the upstream experiencing more corrections than other regions such as the downstream region. A possible explanation is that the TKE in the free-shear region has stronger correlations with the velocities at the observed locations. However, it is also possible that the TKE does not necessarily need to be improved to provide better

velocity field due to the non-unique mapping from Reynolds stress field to velocity field, as has been discussed above. More detailed discussion can be found in Section 2.5.3.

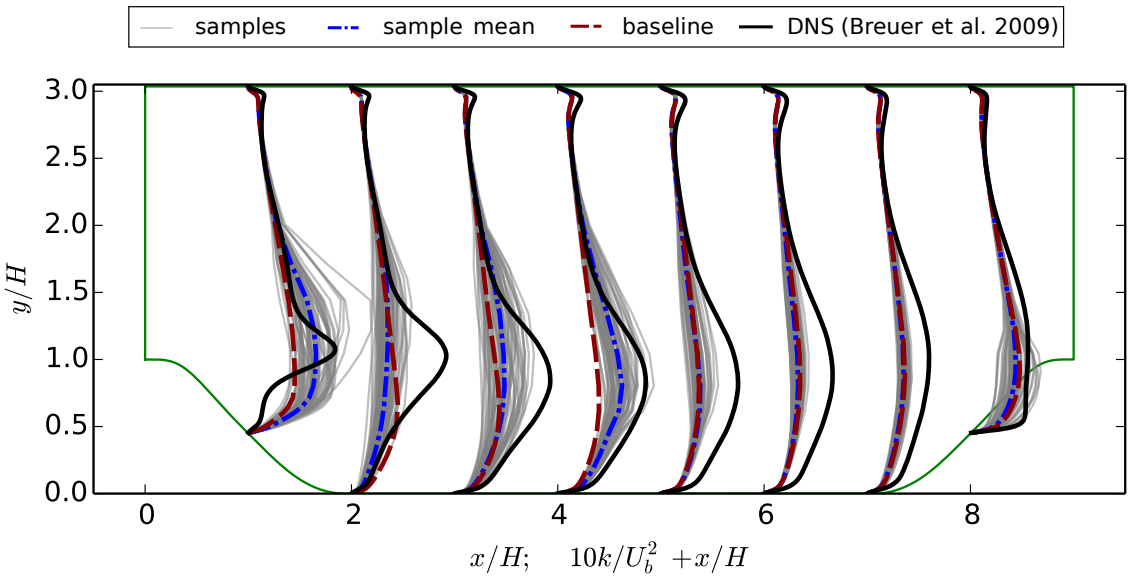

Figure 2.9: Posterior ensemble of the turbulent kinetic energy k with its mean compared to the baseline results and the benchmark DNS data. The prior ensemble is omitted for k, since its mean is the same as the baseline prediction.

2.4.2 Fully Developed Turbulent Flow in a Square Duct

Case Setup

The fully developed turbulent flow in a square duct is a widely known case for which many turbulence models fail to predict the secondary flow induced by the Reynolds stresses. The geometry of the case is shown in Fig. 2.10. The Reynolds number based on the edge length D of the square and the bulk velocity U_b is $Re_b = 10320$. All lengths presented below are normalized by the height h of the computational domain, which is half of D. Extensive benchmark data from DNS are available in the literature [47, 48].

Standard computational setup as used in the literature is adopted in this work. Only one quadrant of the physical domain is simulated considering the symmetry of the flow with respect to the centerlines along y- and z-axes as indicated in Fig. 2.10. We emphasize here that our study is concerned with the mean flow, since the objective is to quantify the uncertainties in RANS simulations. The instantaneous flows are beyond the scope of our discussions, and they do not have the symmetries mentioned here. Non-slip boundary conditions are imposed at the walls and symmetry boundary conditions (zero in-plane velocities) are applied on the symmetry planes. Theoretically, one can further reduce the computational domain size to

1/8 of the physical domain by utilizing the symmetry with respect to the square diagonal. However, this symmetry is not exploited, as it would be difficult to impose proper boundary conditions on the diagonal. The symmetry in the baseline RANS simulation results is implied by the diagonal symmetry of the geometry and boundary conditions. When conducting forward RANS simulations with given Reynolds stress fields, caution must be exercised to ensure that the perturbations introduced to $\tilde{\boldsymbol{\tau}}^{rans}$ have diagonal symmetry, which will be discussed later. Otherwise, the posterior velocities may be asymmetric with respective to the diagonal.

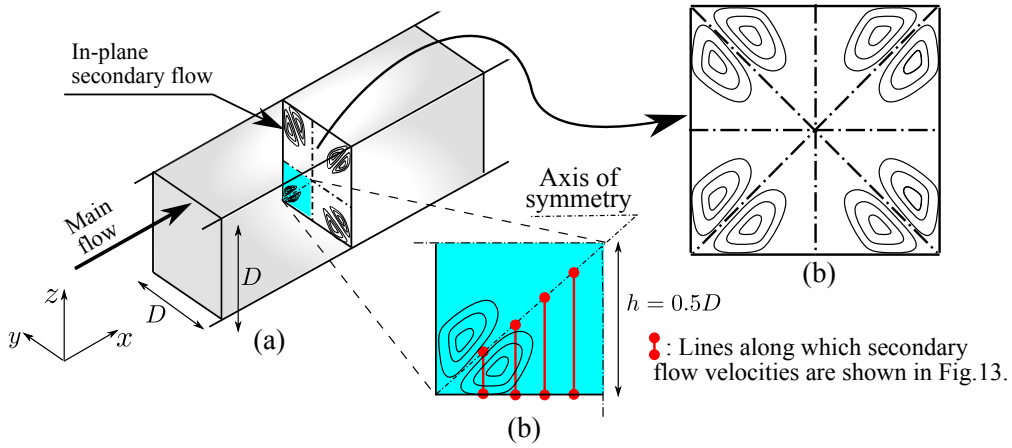

Figure 2.10: (a) Schematic for the fully developed turbulent flow in a square duct. The x axis is aligned with the streamwise direction. Secondary flows exist in the y–z plane, which are schematically represented with contours. (b) Symmetry of the (mean) flow with respect to the centerlines in y- and z-directions and along the diagonals. (c) The computational domain covers only a quarter of the physical domain due to the centerline symmetry. The cross-sections along which QoIs (e.g., velocities and Reynolds stress imbalance) are compared to benchmark data are also indicated.

The mesh and computational parameters for this case are shown in Table 2.1. Choice of parameters can be motivated similarly as in the periodic hill case. A notable difference is that only uncertainties in the shape of the Reynolds stress (i.e., ξ and η) are considered in the square duct flow case. The QoI for this flow is the in-plane flow velocities, which are primarily driven by the normal stress imbalance $\tau_{yy} - \tau_{zz}$, a quantity that is associated with the shape of $\boldsymbol{\tau}$. The design of the variance field σ is based on the same principle as in the periodic hill flow. Specifically, we chose $\sigma_0 = 0.2$ throughout the field and $\sigma_{local} = 0.5$ at the lower left corner. The length scale of the radial basis kernel is chosen as 0.1D based on the estimation of length scale of secondary flow (see Table 2.1). It is known that RANS models have more difficulties in predicting the flow near the corner, which justifies the large value of $\sigma(x)$ near the corner and the gradual decrease away from the corner as well as towards the diagonal. Moreover, the variance field is chosen to be symmetric along the diagonal of the y–z plane in consideration of the flow symmetry.

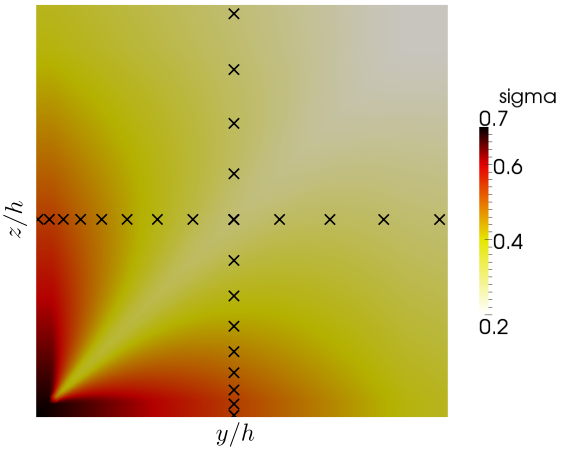

Figure 2.11: Contour of the variance field $\sigma(x)$ and locations of the observations for the square duct flow case. Larger variances are allowed near the corner due to the difficulties RANS models have in predicting the secondary flow in this region. The variance field is chosen to be symmetric along the diagonal of the y–z plane in consideration of the flow symmetry.

Results

The first six modes of KL expansion are shown in Fig. 2.12 along with two typical realizations. All the modes have been shifted and normalized into the range $[0, 1]$. Only the diagonally symmetric modes are retained to guarantee the symmetry of the Reynolds stress along the diagonal, which leads to the symmetry of the posterior velocities. The observations are obtained from the DNS data [47] by adding Gaussian random noises as in the periodic hill flow. Velocities are observed at 25 points as shown in Fig 2.10, half of which are distributed along the line $y/h = 0.5$ and the other half along $z/h = 0.5$. Note that half of the information from the observations is redundant due to the diagonal symmetry of the flow.

The ability of a numerical model to predict the secondary flow in y–z plane is of most interest for the flow in square duct. Therefore, the in-plane velocity field is identified as the QoI for this case. The in-plane flow velocity (U_y) on the four cross-sections as indicated in Fig. 2.10 are presented to facilitate quantitative comparison with the baseline and benchmark results. The velocity profiles U_z in the z direction have similar characteristics as U_y (but are not identical) and are thus omitted. The prior and posterior ensembles of the velocity profiles for U_y are shown in Fig. 2.13. Only the velocity profiles in the region below the diagonal are presented due to the diagonal symmetry. It can be seen from Fig. 2.13 that the baseline RANS simulation predicts uniformly zero in-plane velocities as expected. Around the baseline prediction, the prior ensembles are scattered due to the perturbation of δ_ξ and δ_η. The large range of scattering indicates that the secondary flow is sensitive to the anisotropy

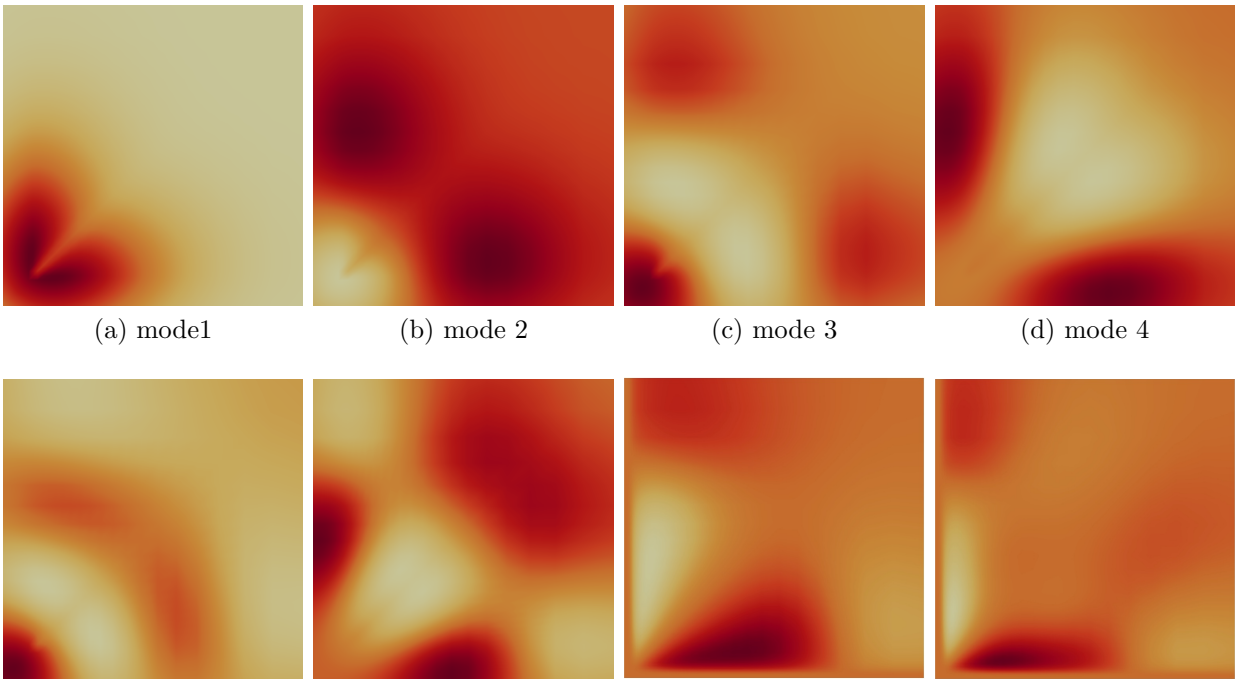

(a) mode1 (b) mode 2 (c) mode 3 (d) mode 4

(e) mode 5 (f) mode 6 (g) realization 1 (h) realization 2

Figure 2.12: Illustration of KL expansion modes for the square duct flow case. All presented modes have been shifted and scaled into a range of 0 (lightest) to 1 (darkest) to facilitate presentation, and the legend is thus omitted. Panels (a) to (f) denote modes 1 to 6, respectively, with lower modes being more important. Only the modes with diagonal symmetry are retained to guarantee the symmetry of perturbed Reynolds stresses field. Panels (g) and (h) show the magnitude of Reynolds stress imbalance $|\tau_{yy} - \tau_{zz}|$ associated with two typical realizations of the discrepancy fields.

of Reynolds stresses tensor, which has been reported in previous studies [18, 47]. Compared to the prior ensemble mean and the baseline RANS prediction, the posterior ensemble mean of the velocities are significantly improved along all four cross sections, as shown by good agreements with the benchmark data. The scattering has been significantly reduced as well, while still covering the truth adequately in most regions. The remaining differences and the regions where the ensemble fails to cover the truth can be explained similarly as in the periodic hill case. Similar to that in the periodic hill case,

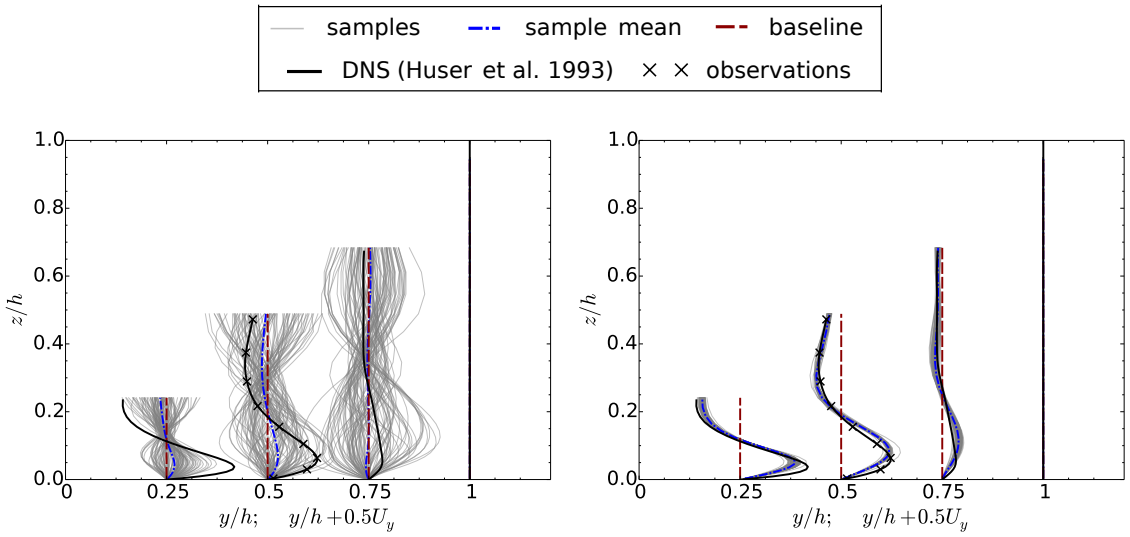

(a) Prior ensemble (b) Posterior ensemble

Figure 2.13: (a) Prior velocity ensemble and (b) posterior velocity ensemble at four spanwise locations $y/h = 0.25, 0.5, 0.75$ and 1 with comparison to baseline and benchmark results. The velocity U_z in the z direction have similar characteristics and are thus omitted. The velocity profiles in the prior ensemble are scaled by a factor of 0.3 for clarity.

Figure 2.14 shows a comparison of the posterior ensemble mean field of the in-plane flow velocity and the benchmark data. They are presented as vector plots to show the overall features of secondary flow and particularly the vortex structure. The length and direction of an arrow indicate the magnitude and direction, respectively, of the in-plane flow velocity at that location. The plots are arranged such that a perfect agreement between the two would show as exact symmetry of the two panels along the center line. The vector plot of the velocity field from the baseline RANS prediction is omitted since it is uniformly zero. It can be seen that the posterior ensemble mean demonstrates a very good agreement with the benchmark data in most aspects, i.e., the direction and the intensity of secondary flow at most locations as well as the center of vortex structure. Only minor differences between the two can be identified. For example, the posterior mean velocity has a slightly smaller gradient of velocity magnitude compared to the benchmark results near the symmetry line. The agreement clearly demonstrates the merits of the current framework, particularly considering the fact that most of the commonly used turbulence models are not capable of

predicting the in-plane flow. Specifically, all isotropic eddy viscosity models completely miss the secondary flow, which is explained by the negligible $\partial U_y/\partial y$ and $\partial U_z/\partial z$ terms and the Boussinesq assumption that Reynolds stress is proportional to local strain rate of the mean flow. Even advanced models (e.g., Reynolds stress transport models) tend to underestimate the flow intensity [49]. Admittedly, velocity observations at some locations are used in this method, but the amount of data used in the inference is rather small compared to the total degrees of freedom of the Reynolds stress field.

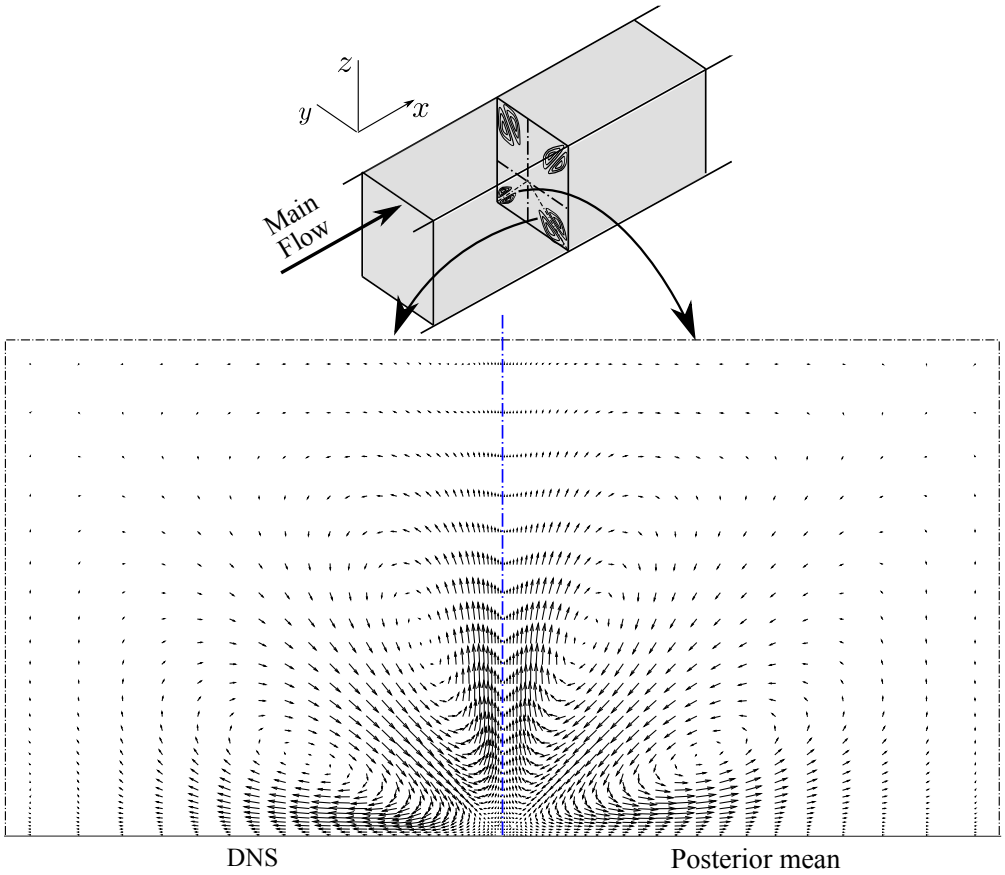

Figure 2.14: Comparison of the velocity field in a square duct between the posterior mean and benchmark DNS data.The length and direction of an arrow indicate the magnitude and direction, respectively, of the in-plane flow velocity. The plots are arranged such that a perfect agreement between the two would show as exact symmetry of the two panels along the vertical center line. The vector field from the baseline RANS prediction is omitted since it is uniformly zero.

As mentioned above, the normal stress imbalance $\tau_{yy} - \tau_{zz}$ is the main driving force of the secondary flow. Therefore, the prior and posterior ensembles of the imbalance at five locations, $y/h = 0.25, 0.5, 0.6, 0.75$, and 1, are presented in Fig. 2.15. It can be seen that the baseline RANS prediction of $\tau_{yy} - \tau_{zz}$ is zero. Compared to the baseline RANS prediction, the posterior normal stress imbalance shows a significant improvement in regions close to

the observations ($y/h = 0.5$), although differences still exist, especially in the regions far away from the observations (e.g., at $y/h = 1$). It is consistent with the argument made in Section 2.2.2 that the correlation decreases with distance, and that the quality of correction heavily depends on correlations. Note that the inferred stress imbalances at $y/h = 0.75$ agree with the benchmark much better than do those at $y/h = 0.25$, although they have approximately the same distances from the observations, which are distributed along $y/h = 0.5$. This can be explained by the fact that the length scale of the flow decreases towards the corner (e.g., near $y/h = 0.25$) due to the constriction of the duct walls, and thus the correlation decreases much faster in this region than near the symmetry line.

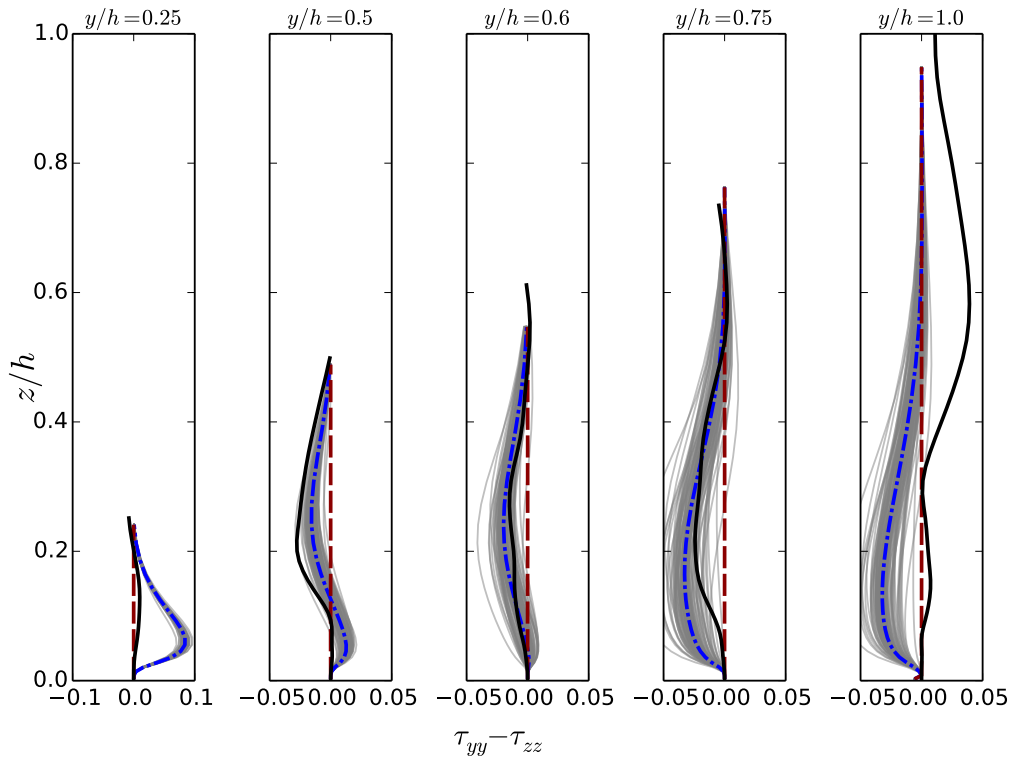

Figure 2.15: Comparison of the normal stresses imbalance at five locations $y/h = 0.25, 0.5, 0.6, 0.75$ and 1.0. A larger horizontal axis range is used in the panel for $y/h = 0.25$ due the large range of values $\tau_{yy} - \tau_{zz}$ at this location.

2.5 Discussion

2.5.1 Computational Cost of the Model-Form Uncertainty Quantification

As mentioned in Sections 2.3. The ensemble Kalman method uses 60 samples (see Table 2.1) and needs approximately 10 iterations to achieve statistical convergence. Therefore, each uncertainty quantification case involves 600 evaluations of the forward RANS model `tauFoam`. Since each forward RANS evaluation is only 10% as expensive as a baseline RANS simulation (see Section 2.3), the total computational cost of the uncertainty quantification procedure is 60 times as that of the baseline simulation. However, note that the propagation of samples can be done in parallel, i.e., in each iteration the 60 forward RANS simulations were run simultaneously on 60 CPU cores. As a result, the wall time of the uncertainty quantification procedure is approximately the same as that of the baseline simulation, assuming the latter is run on a single core. Finally, the computational costs associated with the projection of Reynolds stresses, the KL expansion, and the Kalman filtering are all neglected in the analysis above. This is justified because the computational cost of the uncertainty quantification is indeed dominated by the forward model evaluations.

2.5.2 The Role of Correlation in Current Framework

It has been pointed out that the relatively poor inference performance is expected in the vicinity of the crest, which is due to the lack of observations in the region and statistically significant correlations with the regions that have observations. The concept of correlation plays an important role in the current inference framework and warrants further discussions.

In three-dimensional complex flows more measurement data may be needed to obtain results of similar quality as presented here. In particular, when the flow consists of a number of distinct regions that are weakly correlated, a design of experiment study is needed to ensure all regions of interest have measurements data if possible. However, note that the correlation within the flow field can be studied a priori solely based on an ensemble of RANS simulations before any measurements are performed. Based on the study of correlations, the measurements can subsequently be optimized. Therefore, such simulation-informed experimental design is feasible in practice. We have performed such a correlation study in a more complex flow, the flow over a wing-body junction, and the detailed results are presented in ref. [26].

It is essential to choose proper correlation length scales based on that of the mean flow, which is part of the physics-based prior knowledge. While an overly small length scale would fail to make corrections to the regions without observation, an overly large length scale would lead to spurious corrections. The correlation structure (e.g., of the velocities) in a flow field is very complex and difficult to visualize due to the high dimensionality of the state. However, we

can illustrate the idea by considering the streamlines of the mean flow. Intuitively, velocities at two points on the same streamline should have a relatively high correlation. Consequently, observing the velocity at one point can inform us about velocities at other points on the same streamline. Two points in different coherent structures or regions as mentioned above, e.g., one point in the recirculation zone and another in the shear zone, are likely to be on different streamlines. This explains why points within the same region have higher correlations than the correlations among different regions. That also justifies the arrangement of observation points shown in Fig. 2.1 with observations scattered in all three regions of interest. This explanation of correlation structure is of course a highly simplified picture. In reality, fluid flows are highly complex, coupled dynamic systems. Velocities at different points can be correlated due to continuity requirements and pressure. It is well known that the pressure is described by an elliptic equation (for incompressible flows), which has whole-domain coupling characteristics.

2.5.3 Success and Limitation of the Current Framework

The overall idea of the proposed method is to improve flow field and QoI predictions and to quantify the uncertainties therein by combining all sources of available information, including observation data, physical prior knowledge, and RANS model predictions. A Bayesian framework based on an iterative ensemble Kalman method is used for the uncertainty quantification. Numerical simulation results have demonstrated the feasibility of the framework. In particular, even with velocity observations at very few locations, the posterior velocities are significantly improved compared to the baseline results.

One may also expect that the uncertainties in the modeled Reynolds stresses can be quantified and reduced. Indeed, the posterior ensemble obtained from the Bayesian inference process also has information on the Reynolds stresses. However, our experience suggests that the posterior mean of an arbitrarily chosen component or projection of the Reynolds stresses is not significantly more accurate than those of the baseline prediction.

This apparent contradiction can be explained from two perspectives: the high dimensionality of the Reynolds stress field and the mapping $\boldsymbol{\tau} \mapsto \mathbf{u}$ from Reynolds stresses to mean velocities. The most straightforward reason as mentioned in Section 2.2.3 is that the Reynolds stress discrepancy is a tensor field in a high-dimensional uncertainty space, and thus the amount of velocity data is not sufficient to constrain its uncertainties, even when other prior information is considered. Moreover, the RANS equations describe a many-to-one mapping from Reynolds stresses to mean velocities, and thus the mapping $\boldsymbol{\tau} \mapsto \mathbf{u}$ is not invertible (i.e., a given velocity field may correspond to many possible Reynolds stress fields). This is evident from the fact that the divergence of the Reynolds stress tensor, rather than the Reynolds stress itself, appears in the RANS equation. Although difficult to prove rigorously, we postulate that even Reynolds stress fields that have different divergences can map to very similar velocity fields. One can loosely think of the velocity field as being driven by a

projection of the Reynolds stress on a *low-dimensional manifold*. The specific form of the projection depends on the physics of individual flow. Taking the flow in a square duct for example, it has been demonstrated by analytical derivations [50, 47, 18] that the secondary flow is primarily generated by the normal stress imbalance field $\tau_{yy} - \tau_{zz}$, or more precisely, its cross spatial derivative $\frac{\partial^2}{\partial y \partial z}(\tau_{yy} - \tau_{zz})$. The imbalance scalar can be obtained from the Reynolds stress tensor through linear mapping described by a rank deficient matrix. Since only velocity observation data are used in the Bayesian inference in this work, one can only reasonably expect to infer the projection (i.e., the imbalance), but not the full Reynolds stress field. This can be partly explained by the fact that the projection has a lower dimension, but more importantly, the projection is an observable variable from a control-theoretic perspective. This has been demonstrated in Fig. 2.15. The mapping between Reynolds stresses and velocity as describe by the RANS equations are extremely complex due to the their nonlinearity. This complexity and its implications to the current framework will be further investigated.

Another limitation of the current framework lies in the iterative ensemble method used for the uncertainty quantification, which is a computationally affordable method for approximate Bayesian inference. The posterior distribution obtained with this method may deviate from the true distribution. This compromise is made in this work in consideration of the high computational costs of RANS models (e.g., hours to days for realistic flow simulations), which makes more accurate sampling methods such as those based on the Markov Chain Monte-Carlo method prohibitively expensive. The accuracy of the ensemble-based method will be assessed in future work by comparing current results with those obtained with MCMC, possibly by utilizing recently developed dimension-reduction methods (e.g., active subspace methods [51], likelihood informed dimension-reduction [52]) and sampling techniques (e.g., delayed rejection adaptive metropolis [53]), or by building surrogate models to facilitate the MCMC sampling.

2.5.4 What If There Are No Observation Data Available?

In light of the limitations of the framework as described above, two legitimate follow-up questions can be raised. That is, given that the full Reynolds stress discrepancy field cannot be inferred accurately from the velocity observations, (1) what would the value of the framework be in engineering practice and (2) how can this framework can be used in scenarios with no observation data.

Regarding the first question, sparse observation data are often available for engineering systems that are in operation. For example, real-time monitoring sensors are often installed in wind farms, nuclear power plants, and many other important facilities and devices. For these cases, the current framework can provide a powerful method for combining information from the numerical models (often greatly simplified due to stringent positive lead-time requirement in predictions), observation data, and physical prior knowledge.

In scenarios where there are no observation data available as posed in the second question, the current framework can be used in two ways. First, with the absence of observation data the inference procedure essentially degenerates to forward uncertainty propagation, i.e., propagating the uncertainties in the form of physical prior knowledge on Reynolds stresses to uncertainties in QoIs (e.g., velocity, wall shear stresses, and reattachment point). This is somewhat similar to but more comprehensive than the framework of Iaccarino and coworkers [14, 15, 16, 17, 18], since the prior in our work covers an uncertainty space rather than only a few limit states. Second, when observation data are available in a geometrically similar case but perhaps at a lower Reynolds number (e.g., the downscaled model in a laboratory experiment), the model uncertainties can first be quantified and reduced with the data available on the scaled model. After the calibration, the posterior Reynolds stress uncertainty distribution is extrapolated to the case of concern (e.g., the flow in a geometrically similar prototype at a higher Reynolds number) to make predictions. Dow and Wang [19] used a similar calibration–prediction procedure to predict flows in channels of different geometries by using Gaussian processes describing the eddy viscosity discrepancy. Similar ideas have been suggested and advocated by Duraisamy et al. [23, 24]. In all cases the calibration–prediction procedure relies upon a crucial assumption that the calibration case and the prediction case share physically similar characteristics, despite the differences in specific flow conditions (e.g., Reynolds number or geometry). The feasibility of the calibration–prediction method based on the current framework has been preliminarily explored by Wu et al. [54], which showed promising results when the calibrated Reynolds stress discrepancies are used to predict flows in the same geometry but at a Reynolds number one order of magnitude higher. Prediction of flows in a different geometry, on the other hand, has achieved less successes. However, extreme caution must be exercised and expert opinions must be consulted when using such an extrapolation method as presented in [54], since even a slight change of Reynolds number can lead to significant changes of flow characteristics. Ultimately, the use of this assumption has to be the judgment of the user, which is clearly undesirable. An improved, more intelligent framework should be sought for. It seems that modern machine learning methods have the potential of alleviating users of such burdens, which is a topic of current research [23].

2.6 Conclusion

In this work we propose an open-box, physics-informed, Bayesian framework for quantifying and reducing model-form uncertainties in RANS simulations. Uncertainties are introduced directly to the Reynolds stresses and are represented with compact parameterization accounting for empirical prior knowledge and physical constraints (e.g., realizability, smoothness, and symmetry). An iterative ensemble Kalman method is used to incorporate the prior knowledge with available observation data in a Bayesian framework and propagate the uncertainties to posterior distributions of the Reynolds stresses and other QoIs. Two test cases, the flow over periodic hills and the flow in a square duct, have been used to demonstrate the feasibility and to evaluate the performance of the proposed framework. Simulation results

suggest that even with sparse observations, the obtained posterior mean velocities have significantly better agreement with the benchmark data compared to the baseline results. The methodology provides a general framework for combining information from physical prior knowledge, observation data, and low-fidelity numerical models (including RANS models and beyond) that are frequently used in engineering practice.

A notable limitation is that the full Reynolds stress field inferred from this method is not accurate. This is attributed to the high dimension of the Reynolds stress uncertainty space, the sparseness of the velocity observation data, and the nonlinear, possibly even non-unique, mapping between the Reynolds stresses and velocities as described by the RANS equations. However, we argue that the inferred Reynolds stresses are still valuable despite this limitation, and that they can be extrapolated to cases with similar physical characteristics. Another limitation of the current framework lies in the iterative ensemble method used for the uncertainty quantification, which is computationally less intensive but less accurate than exact Bayesian inference based on Markov Chain Monte-Carlo sampling. The impact of the approximate Bayesian inference method will be investigated in future studies.

Acknowledgment

We thank the anonymous reviewers for their comments, which helped in improving the quality and clarity of the manuscript. We gratefully acknowledge partial funding of graduate research assistantships for JLW, JXW, and RS from the Institute for Critical Technology and Applied Science (ICTAS, Grant number 175258).

Bibliography

[1] D. C. Wilcox, Turbulence modeling for CFD, 3rd Edition, DCW Industries, 2006.

[2] S. B. Pope, Turbulent Flows, Cambridge University Press, Cambridge, 2000.

[3] C. J. Roy, W. L. Oberkampf, A comprehensive framework for verification, validation, and uncertainty quantification in scientific computing, Computer Methods in Applied Mechanics and Engineering 200 (25) (2011) 2131–2144.

[4] A. Saltelli, P. Stano, P. B. Stark, W. Becker, Climate models as economic guides: Scientific challenge or quixotic quest?, Issues in Science and Technology 31 (3).

[5] M. C. Kennedy, A. O'Hagan, Bayesian calibration of computer models, Journal of the Royal Statistical Society: Series B (Statistical Methodology) 63 (3) (2001) 425–464.

[6] Y. Xiong, W. Chen, D. Apley, X. Ding, A non-stationary covariance-based kriging method for metamodelling in engineering design, International Journal for Numerical Methods in Engineering 71 (6) (2007) 733–756.

[7] D. Huang, T. Allen, W. Notz, R. Miller, Sequential kriging optimization using multiple-fidelity evaluations, Structural and Multidisciplinary Optimization 32 (5) (2006) 369–382.

[8] S. Conti, J. P. Gosling, J. E. Oakley, A. O'Hagan, Gaussian process emulation of dynamic computer codes, Biometrika 96 (3) (2009) 663–676.

[9] D. Higdon, M. Kennedy, J. C. Cavendish, J. A. Cafeo, R. D. Ryne, Combining field data and computer simulations for calibration and prediction, SIAM Journal on Scientific Computing 26 (2) (2004) 448–466.

[10] J. Brynjarsdóttir, A. O'Hagan, Learning about physical parameters: The importance of model discrepancy., Inverse Problems 30 (2014) 114007.

[11] T. Oliver, R. Moser, Uncertainty quantification for RANS turbulence model predictions, in: APS Division of Fluid Dynamics Meeting Abstracts, Vol. 1, 2009.

[12] T. A. Oliver, R. D. Moser, Bayesian uncertainty quantification applied to RANS turbulence models, in: Journal of Physics: Conference Series, Vol. 318, IOP Publishing, 2011, p. 042032.

[13] S. H. Cheung, T. A. Oliver, E. E. Prudencio, S. Prudhomme, R. D. Moser, Bayesian uncertainty analysis with applications to turbulence modeling, Reliability Engineering & System Safety 96 (9) (2011) 1137–1149.

[14] C. Gorlé, G. Iaccarino, A framework for epistemic uncertainty quantification of turbulent scalar flux models for Reynolds-averaged Navier-Stokes simulations, Physics of Fluids 25 (5) (2013) 055105.

[15] C. Gorlé, J. Larsson, M. Emory, G. Iaccarino, The deviation from parallel shear flow as an indicator of linear eddy-viscosity model inaccuracy, Physics of Fluids 26 (5) (2014) 051702.

[16] M. Emory, J. Larsson, G. Iaccarino, Modeling of structural uncertainties in Reynolds-averaged Navier-Stokes closures, Physics of Fluids 25 (11) (2013) 110822.

[17] M. Emory, R. Pecnik, G. Iaccarino, Modeling structural uncertainties in Reynolds-averaged computations of shock/boundary layer interactions, AIAA paper 479 (2011) 1–16.

[18] M. A. Emory, Estimating model-form uncertainty in Reynolds-averaged Navier–Stokes closures, Ph.D. thesis, Stanford University (2014).

[19] E. Dow, Q. Wang, Quantification of structural uncertainties in the k–ω turbulence model, in: 52nd AIAA/ASME/ASCE/AHS/ASC Structures, Structural Dynamics and Materials Conference, AIAA, Denver, Colorado, 2011, AIAA Paper, 2011-1762.

[20] C. K. Wikle, R. F. Milliff, D. Nychka, L. M. Berliner, Spatiotemporal hierarchical bayesian modeling tropical ocean surface winds, Journal of the American Statistical Association 96 (454) (2001) 382–397.

[21] L. M. Berliner, Physical-statistical modeling in geophysics, Journal of Geophysical Research: Atmospheres 108 (D24).

[22] B. Launder, G. Reece, W. Rodi, Progress in development of a Reynolds-stress turbulence closure, Journal of Fluid Mechanics 68 (1975) 537–566.

[23] B. Tracey, K. Duraisamy, J. J. Alonso, A machine learning strategy to assist turbulence model development, AIAA Paper 1287 (2015) 2015.

[24] E. J. Parish, K. Duraisamy, A paradigm for data-driven predictive modeling using field inversion and machine learning, Journal of Computational Physics 305 (2016) 758–774.

[25] A. P. Singh, K. Duraisamy, Using field inversion to quantify functional errors in turbulence closures, Physics of Fluids 28 (2016) 045110.

[26] J.-L. Wu, J.-X. Wang, H. Xiao, Quantifying model form uncertainty in rans simulation of wing–body junction flow, available at: arXiv:1605.05962 (2016).

[27] H. Tennekes, J. L. Lumley, A first course in turbulence, MIT press, 1972.

[28] S. Banerjee, R. Krahl, F. Durst, C. Zenger, Presentation of anisotropy properties of turbulence, invariants versus eigenvalue approaches, Journal of Turbulence 8 (32) (2007) 1–27.

[29] H. Xiao, J.-X. Wang, R. G. Ghanem, A random matrix approach for quantifying model-form uncertainties in turbulence modeling, submitted. Available at http://arxiv.org/abs/1603.09656 (2016).

[30] J.-X. Wang, R. Sun, H. Xiao, Quantification of uncertainties in turbulence modeling: A comparison of physics-based and random matrix theoretic approaches, submitted. Available at http://arxiv.org/abs/1603.05549 (2016).

[31] O. P. Le Maître, O. M. Knio, Spectral methods for uncertainty quantification: with applications to computational fluid dynamics, Springer, 2010.

[32] I. Daubechies, Orthonormal bases of compactly supported wavelets, Communications on pure and applied mathematics 41 (7) (1988) 909–996.

[33] M. D. Buhmann, Radial basis functions: theory and implementations, Cambridge university press, 2003.

[34] M. A. Iglesias, K. J. Law, A. M. Stuart, Ensemble Kalman methods for inverse problems, Inverse Problems 29 (4) (2013) 045001.

[35] G. Evensen, Data assimilation: the ensemble Kalman filter, Springer, 2009.

[36] B. Dennis, J. M. Ponciano, S. R. Lele, M. L. Taper, D. F. Staples, Estimating density dependence, process noise, and observation error, Ecological Monographs 76 (3) (2006) 323–341.

[37] K. Law, A. Stuart, Evaluating data assimilation algorithms, Monthly Weather Review 140 (2012) 3757–3782.

[38] B. Debusschere, K. Sargsyan, C. Safta, UQTk User Manual, Sandia National Laboratories, Albuquerque, NM 87185 and Livermore, CA 94550, version 2.1 Edition (June 2014).

[39] S. V. Patankar, D. B. Spalding, A calculation procedure for heat, mass and momentum transfer in three-dimensional parabolic flows, International Journal of Heat and Mass Transfer 15 (10) (1972) 1787–1806.

[40] C. M. Rhie, W. L. Chow, A numerical study of the turbulent flow past an isolated airfoil with trailing edge separation, AIAA 21 (11) (1983) 1525–1532.

[41] B. E. Launder, B. I. Sharma, Application of the energy dissipation model of turbulence to the calculation of flow near a spinning disc, Letter of Heat Mass Transfer, 1 (1974) 131–138.

[42] M. Breuer, N. Peller, C. Rapp, M. Manhart, Flow over periodic hills–numerical and experimental study in a wide range of Reynolds numbers, Computers & Fluids 38 (2) (2009) 433–457.

[43] P. Houtekamer, H. L. Mitchell, X. Deng, Model error representation in an operational ensemble Kalman filter, Monthly Weather Review 137 (7) (2009) 2126–2143.

[44] J.-X. Wang, J.-L. Wu, H. Xiao, Incorporating prior knowledge for quantifying and reducing model-form uncertainty in RANS simulations, submitted. Available at http://arxiv.org/abs/1512.01750 (2015).

[45] C. Schillings, A. M. Stuart, Analysis of the ensemble Kalman filter for inverse problems, submitted. Available at http://arxiv.org/abs/1602.02020 (2016).

[46] S. P. Neuman, Maximum likelihood Bayesian averaging of uncertain model predictions, Stochastic Environmental Research and Risk Assessment 17 (5) (2003) 291–305.

[47] A. Huser, S. Biringen, Direct numerical simulation of turbulent flow in a square duct, Journal of Fluid Mechanics 257 (1993) 65–95.

[48] AGARD, A selection of test cases for the validation of large-eddy simulations of turbulent flows, Tech. Rep. 345, AGARD Advisory Report (1998).

[49] A. Demuren, W. Rodi, Calculation of turbulence-driven secondary motion in non-circular ducts, Journal of Fluid Mechanics 140 (1984) 189–222.

[50] H. Perkins, The formation of streamwise vorticity in turbulent flow, Journal of Fluid Mechanics 44 (04) (1970) 721–740.

[51] P. G. Constantine, E. Dow, Q. Wang, Active subspace methods in theory and practice: Applications to kriging surfaces, SIAM Journal on Scientific Computing 36 (4) (2014) A1500–A1524.

[52] T. Cui, J. Martin, Y. M. Marzouk, A. Solonen, A. Spantini, Likelihood-informed dimension reduction for nonlinear inverse problems, Inverse Problems 30 (11) (2014) 114015.

[53] H. Haario, M. Laine, A. Mira, E. Saksman, DRAM: efficient adaptive MCMC, Statistics and Computing 16 (4) (2006) 339–354.

[54] J.-L. Wu, J.-X. Wang, H. Xiao, A Bayesian calibration-prediction method for reducing model-form uncertainties with application in RANS simulations, Flow, Turbulence and Combustion.

[55] C. Hua, An inverse transformation for quadrilateral isoparametric elements: analysis and application, Finite elements in analysis and design 7 (2) (1990) 159–166.

Appendix

Appendix.A Mapping from Barycentric Coordinates to Natural Coordinates

Following the work of Iaccarino et al., we introduce uncertainties (also referred to as perturbations) to the Reynolds stresses by perturbing its magnitude (the turbulent kinetic energy k) and the shape (the eigenvalues λ_1 and λ_2 of the anisotropy tensor) as shown in Eq. (2.1). The eigenvalues can be linearly transformed to the Barycentric coordinate (C_1, C_2, C_3) as

follows [28, 17]:

$$C_1 = \lambda_1 - \lambda_2 \tag{2.7a}$$
$$C_2 = 2(\lambda_2 - \lambda_3) \tag{2.7b}$$
$$C_3 = 3\lambda_3 + 1 \tag{2.7c}$$

where C_1, C_2, and C_3 indicate the portion of areas of the three sub-triangles in the Barycentric triangle, and thus they sum to 1. Placing the triangle in a Cartesian coordinate $\mathbf{x}^b \equiv (y^b, y^b)$, the location of any point within the triangle is a convex combination of those of the three vertices, i.e.,

$$\mathbf{x}^b = \mathbf{x}^b_{1c} C_1 + \mathbf{x}^b_{2c} C_2 + \mathbf{x}^b_{3c} C_3 \tag{2.8}$$

where $\mathbf{x}^b_{1c}$, $\mathbf{x}^b_{2c}$, and $\mathbf{x}^b_{3c}$ are the coordinates of the three vertices of the triangle (see Fig. 2.2). The superscript b is used to distinguish it from the coordinate system for the fluid flow problems.

While Emory[17] perturbed the Reynolds stress towards the three limiting states (the vertices of the triangle), we need to parameterize and explore the entire triangle. To facilitate parameterization with minimum artificial capping of Reynolds stresses falling outside the realizable range, we further transform the Cartesian coordinate (x^b, y^b) to the natural coordinate (ξ, η) by using the standard finite element shape functions:

$$x^b = x(\xi, \eta) = \sum_{i=1}^{4} N_i(\xi, \eta) x^b_i \tag{2.9a}$$
$$y^b = y(\xi, \eta) = \sum_{i=1}^{4} N_i(\xi, \eta) y^b_i \tag{2.9b}$$

where (x^b_i, y^b_i) are the coordinates of four vertices, and N_1, N_2, N_3, and N_4 are shape functions defined as

$$N_1(\xi, \eta) = \frac{(1-\xi)(1-\eta)}{4}$$
$$N_2(\xi, \eta) = \frac{(1+\xi)(1-\eta)}{4}$$
$$N_3(\xi, \eta) = \frac{(1+\xi)(1+\eta)}{4}$$
$$N_4(\xi, \eta) = \frac{(1-\xi)(1+\eta)}{4}.$$

The mapping from the natural coordinate (ξ, η) to the physical coordinate (x^b, y^b) as shown in Eq. (2.9) is routinely used in finite element methods. However, the inverse mapping, i.e., computing the natural coordinate (ξ, η) for a given physical coordinate (x^b, y^b), is nontrivial and uncommon due to the difficulty of solving the bilinear equation system Eq. (2.9). In this work we use the analytical results from [55] to obtain this mapping.

In summary, the Reynolds stresses field $\tilde{\boldsymbol{\tau}}^{rans}$ computed from the baseline RANS simulation are mapped to the physical interpretable variables $\tilde{k}^{rans}, \tilde{\xi}^{rans}, \tilde{\eta}^{rans}$ via the following sequence:

$$\tilde{\boldsymbol{\tau}} \xrightarrow{(2.1)} (\tilde{k}, \tilde{\lambda}_1, \tilde{\lambda}_2) \xrightarrow{(2.7)} (\tilde{k}, \tilde{C}_1, \tilde{C}_2) \xrightarrow{(2.8)} (\tilde{k}, \tilde{x}^b, \tilde{y}^b) \xrightarrow{\text{inv. of (2.9)}} (\tilde{k}, \tilde{\xi}, \tilde{\eta})$$

where unperturbed quantities $\mathbf{v}_1^{rans}$, $\mathbf{v}_2^{rans}$, and $\mathbf{v}_3^{rans}$, dependent variables λ_3 and C_3, and superscript *rans* are omitted for simplicity of notation. Equations describing the mappings are indicated above the corresponding arrow. Equation (2.1) indicates eigen-decomposition and reconstruction. After the sequence of mapping, uncertainties are introduced into these transformed quantities by modeling the truth of k, ξ, η as random fields with their respective baseline results as priors (see Eq. (2.2)). They are subsequently used to obtain Reynolds stresses via the inverse of mapping sequence as above:

$$(k, \xi, \eta) \xrightarrow{(2.9)} (k, x^b, y^b) \xrightarrow{\text{inv. of (2.8)}} (k, C_1, C_2) \xrightarrow{\text{inv. of (2.7)}} (k, \lambda_1, \lambda_2) \xrightarrow{(2.1)} \boldsymbol{\tau}$$

Appendix.B: Iterative Ensemble Kalman Method for Inverse Modeling

The algorithm of the iterative ensemble Kalman method for inverse modeling is summarized below. See [34] for details.

Given velocity prediction from the baseline RANS simulation $\mathbf{u}^{rans}$ and observations with error covariance matrix R, the following steps are performed:

1. **(Sampling step)** Generate initial ensemble $\{\mathbf{x}_j\}_{j=1}^N$ of size N, where the augmented system state is:
$$\mathbf{x}_j = [\mathbf{u}^{rans}, \boldsymbol{\omega}]_j$$
2. **(Prediction step)**
   (a) Propagate the state from current state n to the next iteration level $n+1$ with the forward model `tauFoam`, indicated as $\mathcal{F}$,
   $$\hat{\mathbf{x}}_j^{(n+1)} = \mathcal{F}[\mathbf{x}_j^{(n)}]$$
   This step involves reconstructing Reynolds stress fields for each sample and computing the velocities from the RANS equations.

(b) Estimate the mean $\bar{\mathbf{x}}$ and covariance $P^{(n+1)}$ of the ensemble as:

$$\bar{\mathbf{x}}^{(n+1)} = \frac{1}{N}\sum_{j=1}^{N}\hat{\mathbf{x}}_j^{(n+1)}$$

$$P^{(n+1)} = \frac{1}{N-1}\sum_{j=1}^{N}\left(\hat{\mathbf{x}}_j\hat{\mathbf{x}}_j^T - \bar{\mathbf{x}}\bar{\mathbf{x}}^T\right)^{(n+1)}$$

3. **(Analysis step)**

   (a) Compute the Kalman gain matrix as:

   $$K^{(n+1)} = P^{(n+1)}H^T(HP^{(n+1)}H^T + R)^{-1}$$

   (b) Update each sample in the predicted ensemble as follows:

   $$\mathbf{x}_j^{(n+1)} = \hat{\mathbf{x}}_j^{(n+1)} + K(\mathbf{y} - H\hat{\mathbf{x}}_j^{(n+1)})$$

   The vector $\mathbf{y}$ represents observation and H is the observation matrix, which maps state space to the observation space.

4. Repeat the prediction and analysis steps until the ensemble is statistically converged.

Chapter 3

A Bayesian Calibration–Prediction Method for Reducing Model-Form Uncertainties with Application in RANS Simulations

(Published on *Flow, Turbulence and Combustion*, 97 (3): 761-786, 2016.)

J.-L. Wu, J.-X. Wang, H. Xiao
Department of Aerospace and Ocean Engineering, Virgina Tech, Blacksburg, VA, 24061, USA

Abstract

Model-form uncertainties in complex mechanics systems are a major obstacle for predictive simulations. Reducing these uncertainties is critical for stake-holders to make risk-informed decisions based on numerical simulations. For example, Reynolds-Averaged Navier-Stokes (RANS) simulations are increasingly used in the design, analysis, and safety assessment of mission-critical systems involving turbulent flows. However, for many practical flows the RANS predictions have large model-form uncertainties originating from the uncertainty in the modeled Reynolds stresses. Recently, a physics-informed Bayesian framework has been proposed to quantify and reduce model-form uncertainties in RANS simulations for flows by utilizing sparse observation data. However, in the design stage of engineering systems, when the system or device has not been built yet, measurement data are usually not available. In the present work we extend the original framework to scenarios where there are no available data on the flow to be predicted. In the proposed method, we first calibrate the model discrepancy on a related flow with available data, leading to a statistical model for the uncertainty distribution of the Reynolds stress discrepancy. The obtained distribution is

then sampled to correct the RANS-modeled Reynolds stresses for the flow to be predicted. The extended framework is a Bayesian calibration–prediction method for reducing model-form uncertainties. The merits of the proposed method are demonstrated on two flows that are challenging to standard RANS models. By not requiring observation data on the flow to be predicted, the present calibration–prediction method will gain wider acceptance in practical engineering design and analysis compared to the original framework. While RANS modeling is chosen to demonstrate the merits of the proposed framework, the methodology is generally applicable to other complex mechanics models involving solids, fluids flows, or the coupling between the two (e.g., mechanics models for the cardiovascular systems), where model-form uncertainties are present in the constitutive relations.

3.1 Introduction

Model-form uncertainties in complex mechanics systems are a major obstacle for predictive simulations. Reducing these uncertainties is critical for stake-holders to make risk-informed decisions based on numerical simulations. For example, the Reynolds-Averaged Navier–Stokes (RANS) simulations have been increasingly used in the design and analysis of mission-critical systems involving turbulent flows, thanks to the sustained growth of computational resources in the past decades. Examples include gas turbines, hydraulic turbines, aircrafts, and more recently the thermohydraulic system of nuclear power plants [1, 2]. Although RANS solvers are more accurate than the state-of-the-art empirical methods and low-fidelity models [e.g., 3], their predictions still have significant uncertainties. For many practical flows in engineering, the uncertainty in the turbulence closure model embedded in the RANS equations is the dominant source for the uncertainties in the predicted Quantities of Interest (QoIs). This is referred to as model-form uncertainty, which is arguably the most challenging uncertainty to quantify in RANS models and in other complex mechanics models.

Several approaches that are generally applicable to different applications have been used to quantify the model-form uncertainties in RANS simulations. A widely adopted method in the engineering communities is the parametric perturbation or model ensemble approach, in which the baseline simulations are repeated by perturbing the coefficients in the turbulence model or by using several turbulence models. The scattering in the obtained ensemble is used as an empirical indication of the prediction uncertainty. However, this ad hoc approach tends to underestimate the true uncertainties, since different models usually share similar assumptions (e.g., the Boussinesq assumption) and thus have similar biases. The Bayesian calibration method of Kennedy and O'Hagan [4] is a widely used approach for quantifying model-form uncertainties. In their framework the discrepancy in the predicted QoI is modeled as a Gaussian process, whose hyperparameters are calibrated with data. However, this physics-neutral framework treats the numerical model as a black-box, which leads to inefficient use of calibration data and makes it difficult for the users to specify prior knowledge based on their insights of the model and the problem. In the past few years, some

researchers have proposed open-box approaches to quantify the model-form uncertainties in RANS simulations, which are in contrast to the general-purpose, physics-neutral approaches described above. Dow and Wang [5] modeled the true eddy viscosity field as a Gaussian process, and used Direct Numerical Simulation (DNS) data to infer its hyperparameters and to find the optimal mean field that minimizes the misfit. Iaccarino and co-workers [6, 7, 8] introduced smooth perturbations on the Reynolds stress towards several limiting states in the physically realizable range [9, 10]. Oliver et al. [11] introduced discrepancy to the Reynolds stress tensor, and modeled the discrepancy term with a stochastic differential equation. The essential differences among the three open-box approaches lie in the treatment of physical prior knowledge and calibration data. Dow and Wang [5] used DNS data to reduce uncertainties, resulting in a calibration–prediction procedure. In contrast, Iaccarino et al. [6, 7, 8] and Oliver et al. [11] focused on uncertainty quantification and propagation by exploiting the physical insight on the Reynolds stresses, and they did not directly use data to reduce uncertainties.

More recently, Xiao et al. [12] proposed an open-box, physics-informed, Bayesian framework for quantifying and reducing model-form uncertainties in RANS simulations. Uncertainties are introduced to the Reynolds stresses and are parameterized compactly with physical realizability and spatial smoothness guaranteed [11, 6]. A Bayesian inference procedure based on an iterative ensemble Kalman method [13] is used to quantify and reduce the uncertainties by incorporating observation data. This method combines all sources of available information in a Bayesian framework including physical constraints, empirical knowledge, and observation data. In scenarios where observation data (e.g., sparse velocity measurements) are available, this framework provides a powerful method of predicting the whole-field velocity and other QoIs with quantified uncertainties.

However, in the design stage of engineering systems or devices, the target configuration (e.g., the new design of an aircraft or a gas turbine) has not been built yet, and thus measurement data are not available [14, 15]. The framework of Xiao et al. [12] is not directly applicable to these scenarios. Without observation data the framework would degenerate to an uncertainty estimation procedure, and the potential of the Bayesian framework cannot be fully exploited. Therefore, in the present work we extend the original framework to predict flows with no observation data by utilizing data from a different yet related flow. Specifically, we first build a statistical model for the Reynolds stress discrepancy on a related flow by incorporating available data (i.e., infer its uncertainty distribution), and then we sample the inferred uncertainty distribution to predict the flow of interest. The extended framework is essentially a Bayesian calibration–prediction procedure. We consider two typical scenarios where observation data could be available on a related flow. (1) When mission-critical systems are developed, laboratory experiments are often performed on a down-scaled, geometrically similar model. Unfortunately, the experiments often have to be performed at a reduced Reynolds number than in the prototype, possibly due to limitations of the facilities or to avoid violating other similitudes (e.g., Mach number similarity). Although the Reynolds number similitude is not achieved, the experimental data obtained in the laboratory

scale model can be valuable for quantifying uncertainties in the RANS-predicted Reynolds stresses. (2) Industrial product developments often consist of small incremental modifications of existing, well tested products, e.g., when a new gas turbine model is added to a family of existing products. In this case it is possible that measurement data, obtained from either experiments or field operations, are available on flows in a slightly different geometry from the flow to be predicted.

In the calibration–prediction framework outlined above, a pivotal assumption is that the Reynolds stress discrepancies in the two flows, the one used for calibration and the one to be predicted, can be described by the same statistical model. This assumption allows the extrapolation of Reynolds stress discrepancies from the calibration case to the prediction case, where "extrapolation" should be interpreted in a *statistical sense*. The extrapolation of the Reynolds stress discrepancy is justified if the two cases share overall physical characteristics despite the differences in their specific flow conditions (e.g., Reynolds number and geometry). The same assumption is the basis of many wind tunnel experiments in which it is infeasible to achieve the prototype Reynolds number with the laboratory setup.

Although the broad concept of using Reynolds stress from other simulations to improve the RANS simulation has been recognized in some engineering applications, e.g, the gas turbine design, this work provides a novel approach to calibrate the discrepancy of Reynolds stress anisotropy for a given flow by Bayesian inference, and to use the calibrated discrepancy to improve the RANS simulation of a closely related flow. It should be noted that it is the anisotropy of the Reynolds stress that we extrapolate from the calibration case to the prediction case, which is physically reasonable if the mean flow feature and the geometry constraints of the two flows are closely related.

The objective of the present work is to explore the feasibility of such a calibration–prediction procedure. The performance of the proposed extension is evaluated on two canonical flows, the flow over periodic hills and the flow in a square duct, at several Reynolds numbers. In both cases the Reynolds stress discrepancies are calibrated in a lower Reynolds number flow with sparse observation of velocities and then are used to predict flows at higher Reynolds numbers. Moreover, we also explore the feasibility of extrapolating the Reynolds stress discrepancy calibrated in a square duct flow to the flow in a rectangular duct. The remaining of the paper is organized as follows. Section 3.2 outlines the model-form uncertainty quantification framework proposed in Xiao et al. [12] and presents the extension proposed in the current work. Section 3.3 presents and discusses numerical simulation results for two canonical flows that are challenging for standard RANS models. Section 3.4 discusses the valid scenario and the limitation of the proposed calibration-prediction method. Finally, Section 3.5 concludes the paper.

3.2 Methodology of the Bayesian Calibration–Prediction Framework

Consider two flows that are closely related, e.g., flows in the same geometry but at a different Reynolds number, or flows in slightly different geometries. One flow (to be used for calibration) has some velocity observation data available, while the other flow (to be predicted) has no observation data. The overall idea of the proposed calibration–prediction framework can be summarized as follows. Baseline RANS simulations are first performed for both the calibration flow and the flow to be predicted, both having discrepancies in the RANS-predicted Reynolds stresses that are *a priori* unknown. In the present framework, we assume that the discrepancies in both cases have the same statistical distributions and model them as a random field. We first utilized prior knowledge and observation data to build a statistical model of the discrepancy. Subsequently, the obtained uncertainty distribution of the discrepancy is sampled and used to correct the baseline Reynolds stress in the prediction case, which is then propagated to uncertainties in velocities and in other QoIs by solving the RANS equations with the corrected Reynolds stresses.

Admittedly, since flows at different Reynolds numbers can have significantly different Reynolds stress magnitudes, direct extrapolation of the Reynolds stress discrepancy tensor field from one flow to another is likely to be problematic. Therefore, when extrapolating the Reynolds stress discrepancies to the flow to be predicted, we extrapolate the projections (magnitude, shape, orientation) of the discrepancies and not the componentwise discrepancies. Specifically, the log-discrepancy of the magnitude and discrepancies of the shapes parameters of the Reynolds stress tensors are extrapolated. These projections can be considered normalized quantities independent of the magnitude of the Reynolds stresses, and thus they can be extrapolated from one flow to another. Note that in the calibration of Reynolds stress discrepancies, the uncertainty space is also parameterized on the physical projections to guarantee the physical realizability (i.e., Reynolds stress tensor must correspond to a physically possible state [10]).

In Fig. 3.1 we summarize the probabilistic calibration–prediction framework for RANS modeling with uncertainty quantifications . The two components of the framework, calibration and prediction, are introduced in Sections 3.2.1 and 3.2.2, respectively.

3.2.1 Calibration by Building a Statistical Model of the Reynolds Stress Discrepancy

The calibration procedure uses the method of Xiao et al. [12] for quantifying and reducing model-form uncertainties. The procedure is briefly summarized here for completeness. In the framework, the true Reynolds stress $\boldsymbol{\tau}(x)$ is modeled as a random tensorial field with the spatial coordinate x as index and the RANS-predicted Reynolds stress $\tilde{\boldsymbol{\tau}}^{rans}(x)$ as prior

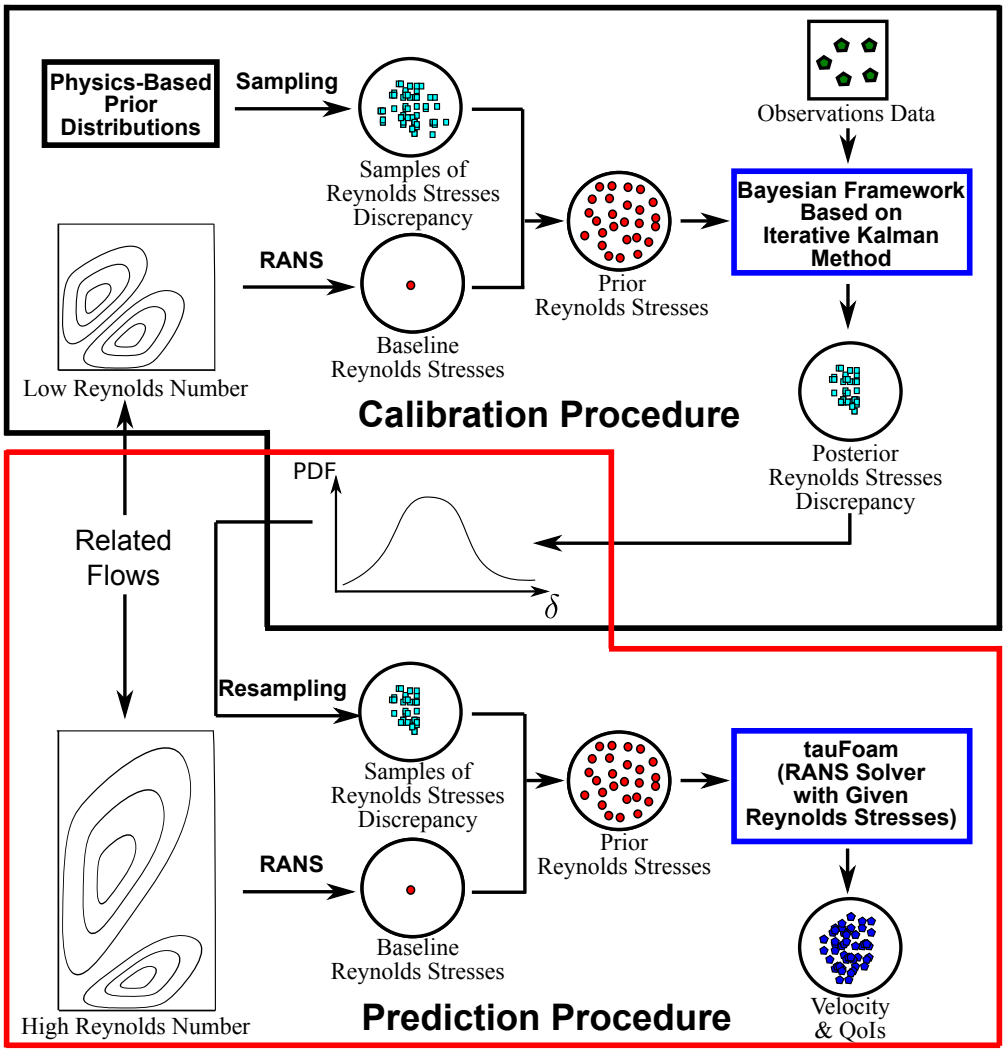

Figure 3.1: Schematic overview of the calibration–prediction procedure for the quantification, reduction, and propagation of uncertainties in RANS models. An example is used to illustrate the overall algorithm. In this example the uncertainty distribution of the Reynolds stress discrepancy is calibrated in a square duct flow at a low Reynolds number, and then the calibrated distribution is used to predict the flow in a rectangular duct at a higher Reynolds number where no data are available.

mean. To ensure physical realizability, uncertainties are injected to the physically meaningful projections of the Reynolds stress tensor, which is transformed as follows [6]:

$$\boldsymbol{\tau} = 2k\left(\frac{1}{3}\mathbf{I} + \mathbf{a}\right) = 2k\left(\frac{1}{3}\mathbf{I} + \mathbf{V}\Lambda\mathbf{V}^T\right) \tag{3.1}$$

where k is the turbulent kinetic energy which indicate the magnitude of $\boldsymbol{\tau}$; $\mathbf{I}$ is the second order identity tensor; $\mathbf{a}$ is the anisotropy tensor; $\mathbf{V} = [\mathbf{v}_1, \mathbf{v}_2, \mathbf{v}_3]$, and $\Lambda = \mathrm{diag}[\lambda_1, \lambda_2, \lambda_3]$ with $\lambda_1 + \lambda_2 + \lambda_3 = 0$ are the orthonormal eigenvectors and eigenvalues of $\mathbf{a}$, respectively, indicating the shape and orientation of $\boldsymbol{\tau}$. After the decomposition, the eigenvalues λ_1, λ_2, and λ_3 are mapped to a Barycentric coordinates (C_1, C_2, C_3) with $C_1 + C_2 + C_3 = 1$. Consequently, all physically realizable states are enclosed in the Barycentric triangle shown in Fig. 3.2a. To facilitate parameterization, the Barycentric coordinates are further transformed to the natural coordinates (ξ, η) with the triangle mapped to the square as shown in Fig. 3.2b. After the mapping, uncertainties are introduced to the mapped quantities k, ξ, and η by adding discrepancy terms to the corresponding RANS predictions, i.e.,

$$\log k(x) = \log \tilde{k}^{rans}(x) + \delta^k(x) \tag{3.2a}$$

$$\xi(x) = \tilde{\xi}^{rans}(x) + \delta^{\xi}(x) \tag{3.2b}$$

$$\eta(x) = \tilde{\eta}^{rans}(x) + \delta^{\eta}(x) \tag{3.2c}$$

where $\delta^k(x)$ is the log-discrepancy of the turbulent kinetic energy; $\delta^{\xi}(x)$ and $\delta^{\eta}(x)$ are discrepancies of the Reynolds stress shape parameters ξ and η, respectively. It should be noted that the perturbation of $\mathbf{v}_1, \mathbf{v}_2$ and $\mathbf{v}_3$ may lead to a reconstructed Reynolds stresses field that has the momentum flux from the low momentum cell to the high momentum one, which has the similar effect as a reverse diffusion term. Although this scenario can be physical in some turbulence structures, it may also lead to unphysical solutions. Therefore, the perturbation is not injected into the orientations of Reynolds stress due to the lack of understanding about the negative effect of enabling such perturbation.

In this work, the discrepancy is built as a function of the spatial coordinate, which is consistent with the framework proposed by Xiao et al. [12]. However, it should be mentioned that there are other possible candidates to build the discrepancy such as the wall distance or the strain rate tensor. These indicators show advantages for some particular scenarios. For instance, the wall distance can indicate the near wall region which is of interest in many engineering applications. On the other hand, the strain rate can indicate the misalignment of the principal axis compared to the Reynolds stress tensor, which also explains the possible failure of eddy-viscosity-based models. Therefore, properly incorporating these indicators into the building of discrepancy may further improve the performance of this work.

Another piece of prior information is the smooth spatial distribution of the Reynolds stresses. The smoothness is guaranteed by representing the Reynolds stress discrepancy fields δ^k, δ^{ξ}, and δ^{η} (generically denoted as δ below) with smooth basis functions. Specifically, the prior distributions of the discrepancies are chosen as nonstationary zero-mean Gaussian

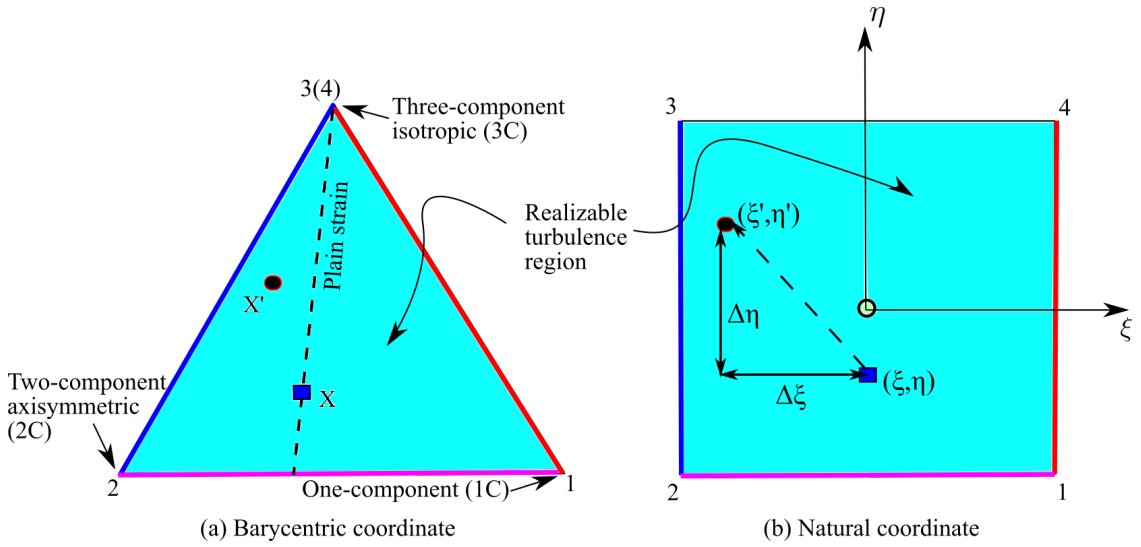

Figure 3.2: Mapping between the Barycentric coordinate to the natural coordinate, transforming the Barycentric triangle enclosing all physically realizable states [9, 7] to a square through standard finite element shape functions. Details of the mapping can be found in the appendix of ref. [12]. Corresponding edges in the two coordinates are indicated with matching colors.

random fields $\mathcal{GP}(0, K)$ (also know as Gaussian processes), and the basis set is chosen as the eigenfunctions of the kernel K [16]. This choice of basis function leads to the Karhunen–Loeve (KL) expansions of the random field. That is, the discrepancies can be represented as follows:

$$\delta(x, \theta) = \sum_{i=1}^{\infty} \omega_i|_{\theta_i} \, \phi_i(x), \tag{3.3}$$

where θ is the realized outcome, and the coefficients ω_i (denoting ω_i^k, ω_i^ξ, and ω_i^η for discrepancy fields δ^k, δ^ξ, and δ^η, respectively) are independent standard Gaussian random variables. In practice the infinite series is truncated to m terms with m depending on the smoothness of the kernel K.

With the projections above, the discrepancies are parameterized by the coefficients ω_i^k, ω_i^ξ, ω_i^η with $i = 1, 2, \cdots, m$. The uncertainty distributions of the coefficients are then inferred by using an iterative ensemble Kalman method [13, 17]. In this method the prior distribution of Reynolds stresses (as parameterized by the coefficients) is first represented with samples drawn from the distribution. The collection of the samples, referred to as prior ensemble, is propagated to velocities by using a forward RANS solver. The Kalman filtering procedure is used to incorporate velocity observation data to the prediction, yielding a corrected ensemble. The procedure is repeated until statistical convergence is achieved. The converged posterior ensemble is a sample based representation of the uncertainty distributions of the Reynolds stresses and other QoIs.

The forward RANS solver `tauFoam` used in the Bayesian inference above basically computes velocities from a *given Reynolds stress field*. It is developed based on a conventional steady-state RANS solver in OpenFOAM [18] by replacing the turbulence modeling component (i.e., solution of the transport equations for turbulent quantities) with a supplied Reynolds stress field.

3.2.2 Prediction for Flows without Observation Data with Corrected Reynolds Stresses

The calibration procedure outlined in Section 3.2.1 builds a statistical model by inferring the uncertainty distribution of the Reynolds stress discrepancy, which is represented by the posterior ensemble obtained from the iterative Kalman method. Next, we use the obtained statistical model of the Reynolds stresses discrepancy to make predictions on flows with no observation data. To this end, we extrapolate the Reynolds stress discrepancy from the calibration case to the prediction case, and then we use the forward RANS solver to propagate the samples of corrected Reynolds stresses to the corresponding velocities and other QoIs.

Extrapolation to flow at a different Reynolds number

After calibrating the uncertainty distribution of the Reynolds stress discrepancy, it is straightforward to extrapolate to a flow with geometric similarity but not dynamic similarity (i.e., at a different Reynolds number). Here we merely emphasize two potential pitfalls as mentioned above. First, the analyst must ensure that the two flows indeed have the same overall characteristics. If the calibration case is a flow over an airfoil without separation while the flow to be predicted has a massive separation, the extrapolation can lead to incorrect results even though the two cases have the same geometry. Second, it is the discrepancies of the physical projections of the Reynolds stress that are extrapolated. Since these are also the discrepancies inferred in the calibration procedure, it does not pose any practical difficulties.

Extrapolation to flow in a different geometry

When the calibration case and the prediction case differ not only in Reynolds number but also in geometry, extrapolation of the Reynolds stress discrepancies poses additional challenges. That is, how to map a field from one geometry (e.g., a square) to another (e.g., a rectangle). The mapping scheme depends on the physical characteristics of the two flows. The choice is inevitably case-specific and relies on the judgment of the analyst.

In Fig. 3.3 we use an example to illustrate the mapping scheme, where the Reynolds stress discrepancy calibrated on the flow in a square duct is used to predict the flow in a rectangular

duct. Results for this case will be presented in Section 3.3.2. In the calibration (Fig. 3.3a), the two contours symmetric along the diagonal indicate spatial distribution of Reynolds stress discrepancy due to particular features of the flow, e.g., vortices. The shaded region in Fig. 3.3b indicates that the Reynolds stress discrepancy in the prediction case, the flow in the rectangular geometry, is unknown before the knowledge from the square duct case is incorporated. There are at least three possbile schemes of extrapolating discrepancies calibrated in the square geometry to the rectangle:

1. *Direct mapping.* As shown in Fig. 3.3c, the obtained discrepancy field in the square is directly mapped to the lower half of the rectangle, while the Reynolds stress discrepancies in the upper half are still unknown. Prior knowledge can still be specified on the discrepancy in the unmapped region, but the uncertainty distribution in this region does not reflect information from the calibration case.

   The mapping between the two geometries can be better understood by comparing the vertex numbering (A, B, C, D) in the square domain in Fig. 3.3a and the rectangle domains in Fig. 3.3c.

2. *Stretching the entire domain.* As shown in Fig. 3.3d, the calibrated field is mapped linearly to the entire domain of the rectangle, i.e., both contours are stretched in the mapped domain.

3. *Direct mapping of lower right domain and stretching of upper left domain.* As shown in Fig. 3.3e, the lower left half of the calibrated discrepancy field (A-B-C) below the diagonal is directly mapped to the same triangle in the rectangular domain, and the upper triangle (A-C-D) is mapped to the quadrilateral (A-C-C'-D) in the rectangular domain.

The analyst must rely on the physical understanding of the flow to be predicted (i.e., the flow in the rectangular geometry in Fig. 3.3b) to decide which mapping schemes described above are reasonable. Even though no data is directly available from the flow to be predicted, we still utilizes the two ingredients of a Bayesian framework, prior knowledge and data, to make predictions. The prior knowledge is formulated based on the relations between the flows in the calibration and prediction cases, while the data come from the calibration case. Therefore, as with the original framework of Xiao et al. [12], the extended calibration–prediction procedure is a Bayesian framework.

Resampling the posterior ensemble

Once we identify a scheme for mapping the discrepancies, we can sample the posterior distribution of the discrepancy obtained in the calibration and use them to make predictions. Sampling from a statistical model of a random field can be achieved with established methods [e.g., 19]. However, the actual implementation is not straightforward and it thus worthes

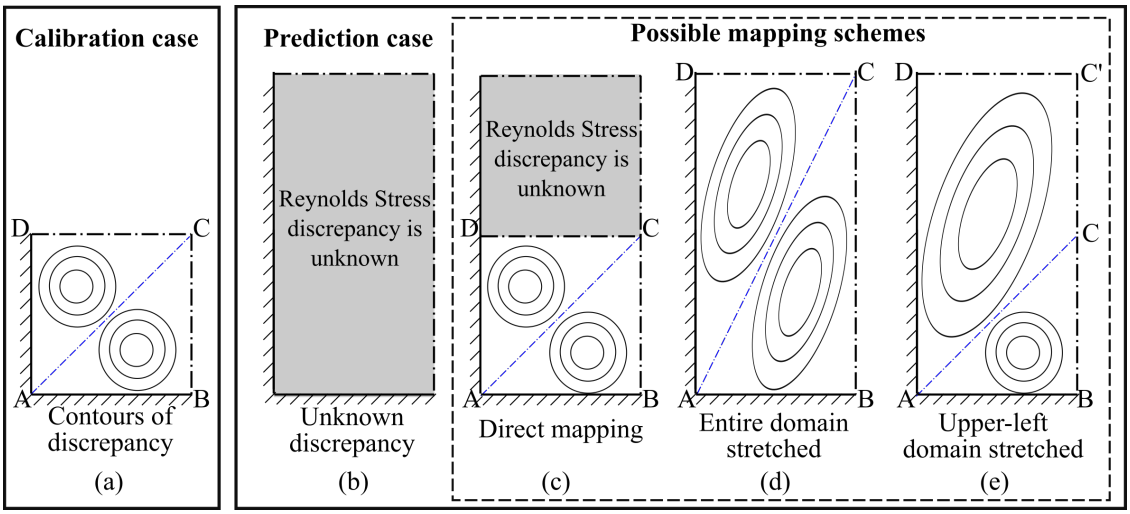

Figure 3.3: Schematic illustration of possible schemes for mapping the calibrated Reynolds stress discrepancies on a square duct to a rectangular duct, which is the flow to be predicted. Dash-dotted lines indicate lines of symmetry. Contours indicate Reynolds stress discrepancies and underlying flow structures.

a detailed discussion. There are two obstacles in the resampling of the posterior ensemble for Reynolds stress discrepancies. First, different components in the random field are correlated. Second, the distribution to be sampled is not given analytically but represented by samples. The first problem can be solved by projecting the samples to the space spanned by the eigenvectors of the covariance matrix of the random field. The covariance matrix can be estimated from the ensemble. After the change of coordinates, each component in a transformed sample field can be considered realization from an independent random variable. The coordinate transformation decorrelates the components in the random field and makes the second obstacle relatively easy to overcome. The distribution of each random variable can be estimated independently from the transformed samples. Finally, the estimated distribution can be sampled straightforwardly to obtain new samples. Sampling of a given distribution of a scalar random variable can be achieved by using standard statistical techniques (e.g., transformation of a uniform random variable with the inverse cumulative distribution function) or more advanced methods in the literature. The detailed algorithm of the resampling procedure is presented in 3.5.

The resampling procedure allows for the flexibility of using a larger number of samples for propagating the posterior uncertainties in the Reynolds stresses than that used in the inference procedure. More importantly, when simultaneously propagating uncertainties in the input along with model-form uncertainties, nested sampling or Sobol sampling [20] are needed for the uncertainty propagation. In this case it is important to be able to generate new samples for the Reynolds stress discrepancy from the obtained distribution. In the simulations presented in this work, however, the process can be simplified by using the

same posterior ensemble obtained from the calibration for the uncertainty propagation in the prediction. The resampling algorithm is presented above for the completeness of the proposed framework.

3.3 Numerical Results and Discussions

In this section we demonstrate the capability of the proposed calibration–prediction method in two scenarios as described in Section 3.1. In the first scenario, the prediction flow and the calibration flow are geometrically similar but have different Reynolds numbers. This scenario is relatively straightforward and is examined on two cases, the flow over periodic hills and the flow in a square duct. In the second scenario, the prediction case differs from the calibration case not only in Reynolds number, but also in geometry. Note that in all cases examined here, we assume that observation data are only available in the calibration case and not in the prediction case. Benchmark data in the prediction case are used only to assess the performance of the proposed method.

3.3.1 Prediction of Flow at Different Reynolds Numbers

Two canonical flows of engineering relevance, the flow over periodic hills and the flow in a square duct, are used to evaluate the performance of the proposed calibration-prediction method. Both flows are challenging for the standard RANS models.

In the calibration step, the Bayesian framework by Xiao et al. [12] is used. In this work, the prior variance field $\sigma(x)$ is chosen based on the empirical knowledge about the regions where the RANS prediction are more unreliable. For example, it is known that the RANS models have difficulty in the regions with separation, non-parallel shear flow, strong mean flow curvature etc. Therefore, larger variance σ is applied to these regions in the construction of Gaussian random field for the discrepancy of Reynolds stress. To capture the spatial pattern of this variance field, 16 modes are used for the flow over periodic hills and 8 modes are used for the flow in a square duct. It is expected that the flow over periodic hills requires more modes due to the more complicated spatial pattern of variance field, which accounts for the separation region, the non-parallel shear layer region and the region with mean flow curvature. According to our sensitivity analysis, the inference is satisfactory unless the modes are too few to account for the spatial pattern of the variance field $\sigma(x)$. Although the number of required modes differs case by case, 5 modes are usually enough for one unreliable region based on our test. However, we still recommend the user to check the modes to ensure that the desirable spatial pattern is captured, and the modes for both test cases can be found in the framework by Xiao et al. [12].

We have also tested the robustness of this Bayesian framework by using non-informative prior, which has constant variance across the whole computational domain. The result

shows that the performance of calibration is still satisfactory in the region of interest where available observation data is nearby [21]. It is consistent with our expectation that the data has more impact upon the posterior due to the iterative nature of the inverse modeling algorithm used in the framework by Xiao et al. [12].

Based on our sensitivity analysis, increasing the sample size will not significantly influence the inferred QoI if the sample size is over 50. Therefore, 60 samples are used and approximately 10 iterations are needed to achieve statistical convergence. On the other hand, the prediction procedure requires no iteration. According to the computational cost estimation of each forward RANS evaluation discussed by Xiao et al. [12], the ratio of computational cost between the proposed calibration-prediction method and the conventional eddy-viscosity-based RANS computation is around 60, and typically in the order of $O(10)$ based on our test on more complex flow problem. It should be noted that this estimated ratio will not increase with the Reynolds number or the complexity of the flow problem.

Flow over periodic hills

The flow over periodic hills is widely utilized to evaluate the performance of turbulence models due to the comprehensive experimental and numerical benchmark data at a wide range of Reynolds numbers [22]. The geometry of the computational domain is shown in Fig. 3.4. The Reynolds number Re is based on the crest height H and the bulk velocity U_b at the crest. Periodic boundary conditions are applied in the streamwise (x) direction, and non-slip boundary conditions are applied at the walls. The spanwise (z) direction is not considered since the mean flow is two-dimensional. The flow is calibrated on the flow at $Re = 2800$, and then predictions are made for the flow at $Re = 10595$. Predictions of the flow at $Re = 5600$ is also performed, and the results are qualitatively similar to those presented below for the flow at $Re = 10595$. Therefore, the results for the flow at $Re = 5600$ are omitted for brevity.

The baseline RANS result of the flow at $Re = 2800$ is calibrated with the procedure presented in Section 3.2.1. The prior and posterior ensembles of velocities are shown in Fig. 3.5. The prior ensemble of velocity profiles is scattered because of the perturbations (uncertainties) introduced to the RANS-predicted Reynolds stresses. It can be seen that the prior ensemble mean velocity is close to the baseline RANS results. Compared to the prior ensemble mean velocity, the posterior mean velocity shows a much better agreement with the benchmark, especially in the recirculation zone, where the magnitude of the reverse flow velocities are significantly underestimated in the baseline RANS results.

Figure 3.6 shows the Reynolds stresses discrepancies (i.e., the difference between the baseline RANS prediction and the benchmark data) for the calibration case ($Re = 2800$) and the prediction case ($Re = 10595$). More precisely, the discrepancies δ^k, δ^ξ, and δ^η in the physical projections are presented. As shown in Figs. 3.6a and 3.6b, δ^ξ and δ^η are similar for the flows at the two Reynolds numbers. It indicates that the discrepancies in the anisotropy of

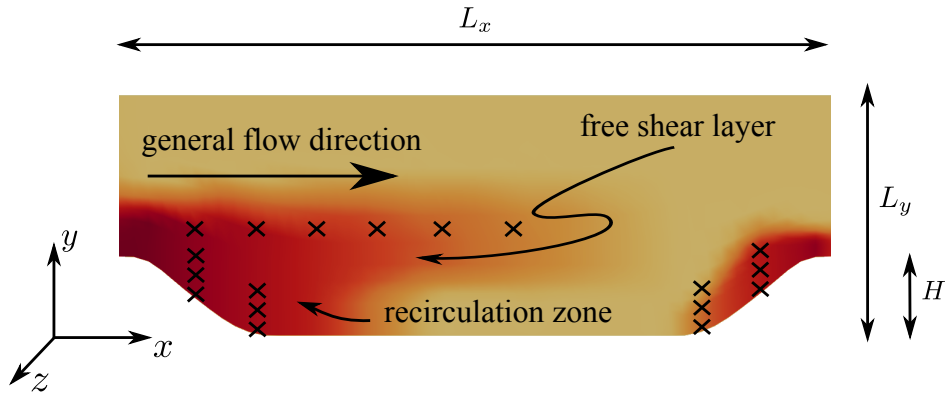

Figure 3.4: Computational domain for the flow over periodic hills. The x, y and z coordinates are aligned with streamwise, wall-normal, and spanwise, respectively. The dimensions are normalized with H with $L_x/H = 9$, $L_y/H = 3.036$, and $L_z/H = 0.1$.

the Reynolds stresses are not sensitive to a moderate change of Reynolds number from 2800 to 10595. This is because the anisotropy is mainly influenced by the geometry of the domain and the coherent structures of the flow. In contrast, the log-discrepancy δ^k in turbulent kinetic energy (TKE) is clearly different for the two flows, especially in the recirculation region. This is related to a potential deficiency of extrapolating the log-discrepancy of the turbulent kinetic energy.

It is not clear if the log-discrepancy of the TKE, its discrepancy, or a combination of both is the best choice of quantity to extrapolate from the calibration to prediction case. As the log-discrepancy is dimensionless while the discrepancy has a dimension of the TKE, the former seems to be preferred. However, the hypothetical case shown in Table 3.1 suggests otherwise. Suppose in a particular region the true turbulence intensity, defined as the ratio of the velocity fluctuations u' to the reference velocity U_b, is 10% in both the calibration and prediction cases, while the RANS simulations give 0.1% and 1%, respectively. The errors in the RANS predictions are in fact rather consistent for the two cases in that the flow has a high intensity turbulence while the predictions give low turbulence intensities. In other words, the difference between 0.1% and 1% is not as significant as that between 1% and 10%. The true log-discrepancy would be 2 and 1 for the calibration and prediction cases, respectively. Hence, extrapolating the log-discrepancy to the prediction case would lead to a corrected turbulent intensity of 100% in the prediction case, which is drastically different from the truth, and such a correction can destabilize the simulation. In contrast, the absolute discrepancies are approximately the same for both cases and is thus a more appropriate quantity to extrapolate. On the other hand, one can easily devise a scenario where extrapolating the log-discrepancy is more reasonable. A more sophisticated scheme of extrapolation is needed and is the subject of future work. In view of the considerations above, the discrepancy of the turbulent kinetic energy is not extrapolated from the calibration cases to the prediction cases in the simulations presented below. In other words, the baseline

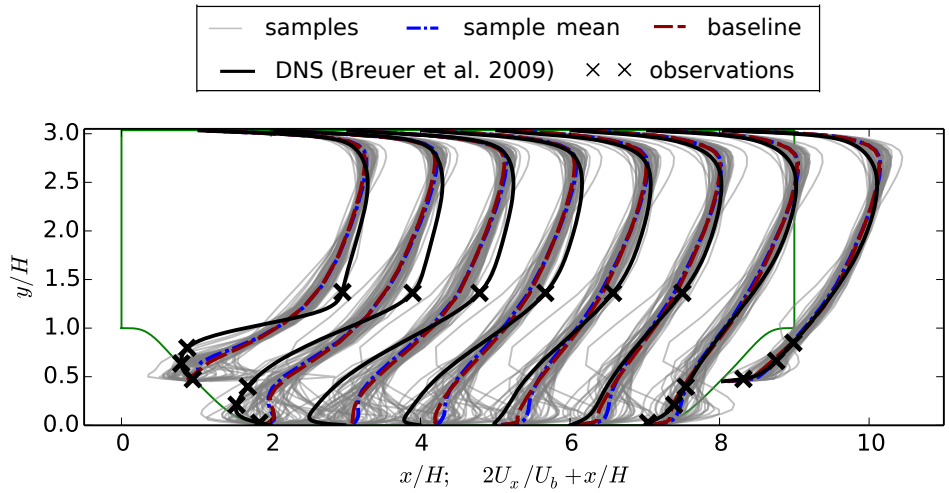

(a) Prior ensemble of velocities

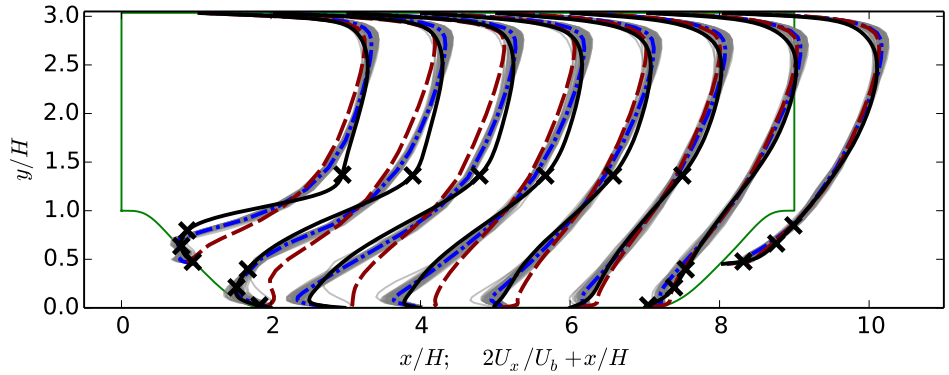

(b) Posterior ensemble velocities

Figure 3.5: Calibration of Reynolds stress discrepancies based on velocity observations in the flow over periodic hill at a low Reynolds number $Re = 2800$. This figure shows the (a) prior and (b) posterior ensembles of velocities at eight locations, $x/H = 1, 2, \cdots, 8$. Black crosses ($\times$) denote locations where velocity observations are available.

RANS-modeled turbulent kinetic energy in the latter case is not perturbed in the prediction.

	calibration case	**prediction case**
true turbulence intensity	10%	10%
baseline RANS predicted intensity	0.1%	1%
log-discrepancy of TKE	2	1
discrepancy of TKE	$\sim 10^{-2}U_b^2$	$\sim 10^{-2}U_b^2$

Table 3.1: A hypothetical case to illustrate the potential deficiency of extrapolating log-discrepancy of the turbulent kinetic energy (TKE) from the calibration case to the prediction case. Turbulent intensities u'/U_b in both the calibration case and the prediction case are shown, where u' denotes velocity fluctuation and U_b is the reference bulk velocity.

The flow over periodic hills at $Re = 10595$ is predicted based on the calibrated Reynolds stresses discrepancies, and the predictions of QoIs including the velocities, wall shear stresses, and reattachment location are compared to the benchmark data [22]. The posterior ensemble of velocities are shown in Fig. 3.7. It can be seen that the baseline RANS simulation underestimates the velocity magnitude in the recirculation zone, or equivalently the strength of the recirculation. Compared to the baseline RANS results, the posterior mean profiles of the velocities have significantly improved agreement with the benchmark data, especially in the recirculation zone. Admittedly, differences still exist between the posterior ensemble mean and the benchmark data. For example, the velocities near the flow reattachment between $x/H = 4$ and 7 are over-corrected. Such differences are expected because all samples and the mean of the posterior ensemble in the Kalman ensemble inference lie in the space spanned by the prior ensemble, but the truth may reside outside this space. More detailed discussions on this issue can be found in [12]. Figure 3.8 shows the bottom wall shear stress τ_w and the reattachment point x_{attach} of the flows in both the calibration case ($Re = 2800$) and the prediction case ($Re = 10595$). The recirculation zones are indicated by the range in which the wall shear stresses are negative. It can be seen that baseline RANS simulations underpredict the sizes of the recirculation zones in both the calibration and the prediction cases. Even without incorporating direct observation data, the predicted recirculation zone size is significantly improved. Such improvement is also confirmed by the posterior ensemble mean of reattachment point, which is much closer to the benchmark data compared to the baseline RANS result. This improvement is particularly notable considering the fact that velocity observations are not used for the inference in the prediction case ($Re = 10595$).

The main difference between the prediction and the benchmark data is near the crest of the hill, i.e., on the leeward side from $x/H = 0$ to $x/H = 1$ and on the windward side from $x/H = 8$ to $x/H = 9$. This is attributed to the lack of observation data at these locations in the calibration flow ($Re = 2800$). The wall shear stress τ_w samples are even more scattered at these locations compared to those of the calibration case. A possible explanation is that the Reynolds number in the prediction case is higher than that in the calibration case, and thus the length scale of prediction case is smaller. Consequently, spatial correlations of velocities

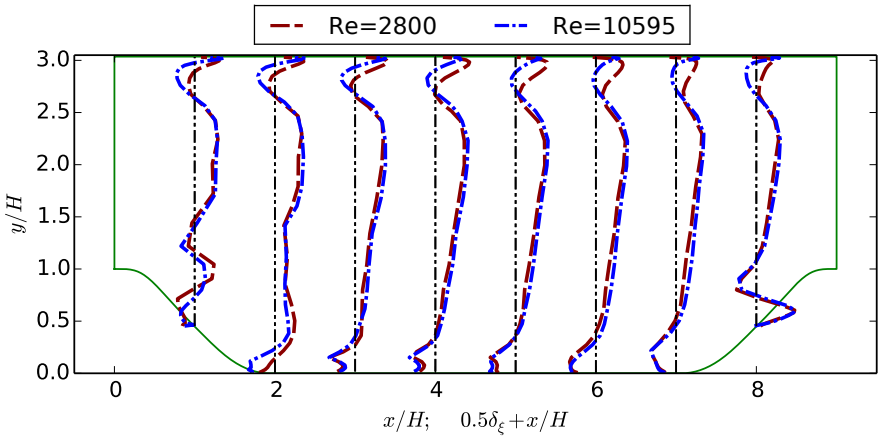

(a) Comparison of δ^{ξ}

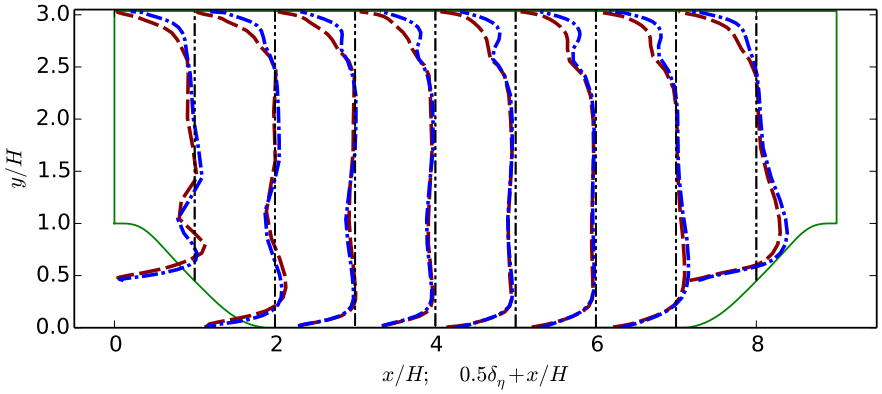

(b) Comparison of δ^{η}

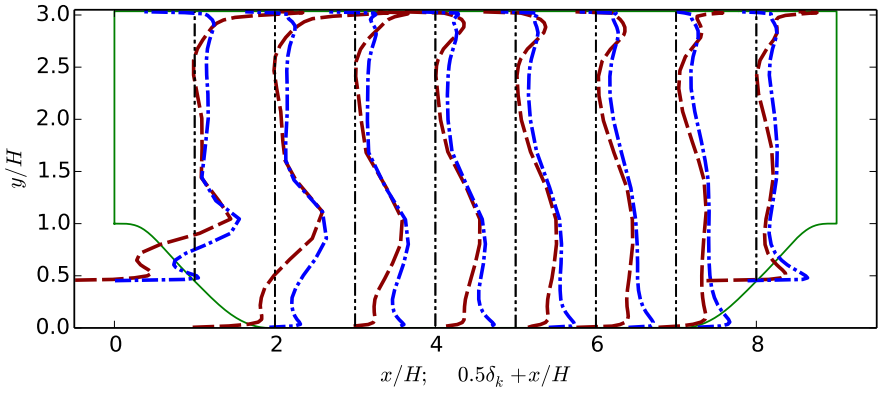

(c) Comparison of δ^{k}

Figure 3.6: The discrepancies of Reynolds stresses between baseline RANS and the benchmark data in the physically meaningful projections. This figure shows the discrepancies (a) δ^{ξ}, (b) δ^{η}, and (c) δ^{k} for the flows at $Re = 2800$ and $Re = 10595$, which are the calibration and prediction cases, respectively.

are small between the region near the crest and the locations where observation data are available (e.g., in the free shear region and the recirculation zone). The weak correlation leads to larger scattering of predicted wall shear stresses τ_w.

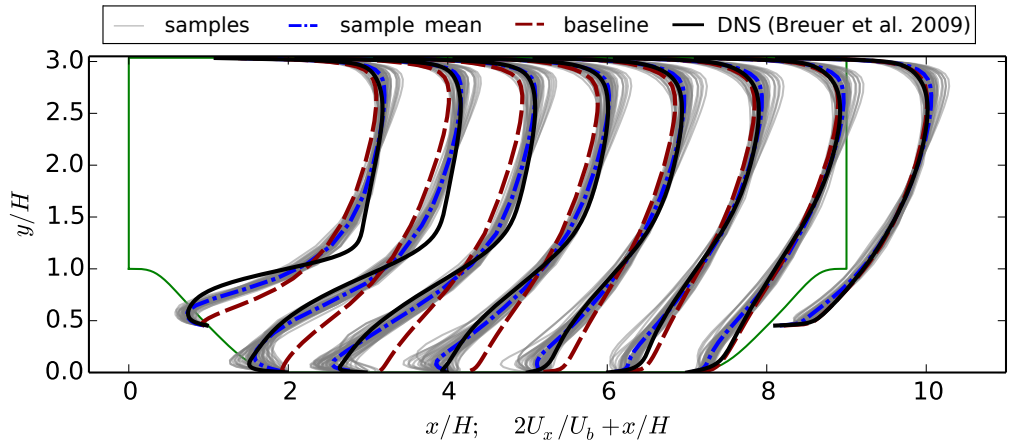

Figure 3.7: Ensemble of predicted velocity profiles of the flow over periodic hills of $Re = 10595$ at eight streamwise cross-sections $x/H = 1, 2, \cdots, 8$ compared with benchmark data and baseline results.

Flow in Square Duct

The fully developed turbulent flow in a square duct is a widely known case for which RANS models fail to predict the secondary flow induced by Reynolds stress imbalances [23]. A schematic is presented in Fig. 3.9 to show the physical domain, major features of the flow, and the dimensions of the computational domain. Since the flow is fully developed in the streamwise direction, a two-dimensional simulation is performed. The computational domain only covers a quarter of the cross-section as shown in Fig. 3.9b based on the symmetry of the computational domain along y and z directions. All lengths are normalized by the height of the computational domain $h = 0.5D$, where D is the height of the duct. The Reynolds number Re is based on duct height D and bulk velocity U_b. The Reynolds stress discrepancies are calibrated on the flow at $Re = 1 \times 10^4$, and predictions are made for flows at $Re = 8.3 \times 10^4$ and 2.5×10^5.

As in the periodic hill cases presented above, we only consider uncertainties in parameters ξ and η, which represent the anisotropy (i.e., shape) of the Reynolds stress tensor. This is because the secondary flow is primarily induced by the anisotropy of Reynolds stresses. Figure 3.10 shows the secondary velocities U_z along four lines. It can be seen from Fig. 3.10a that the prior ensemble has a large range of scattering, which is attributed to the sensitivity of the secondary flow to the turbulence anisotropy. Compared to the prior ensemble mean, the posterior ensemble mean is much closer to the benchmark data, which suggests that

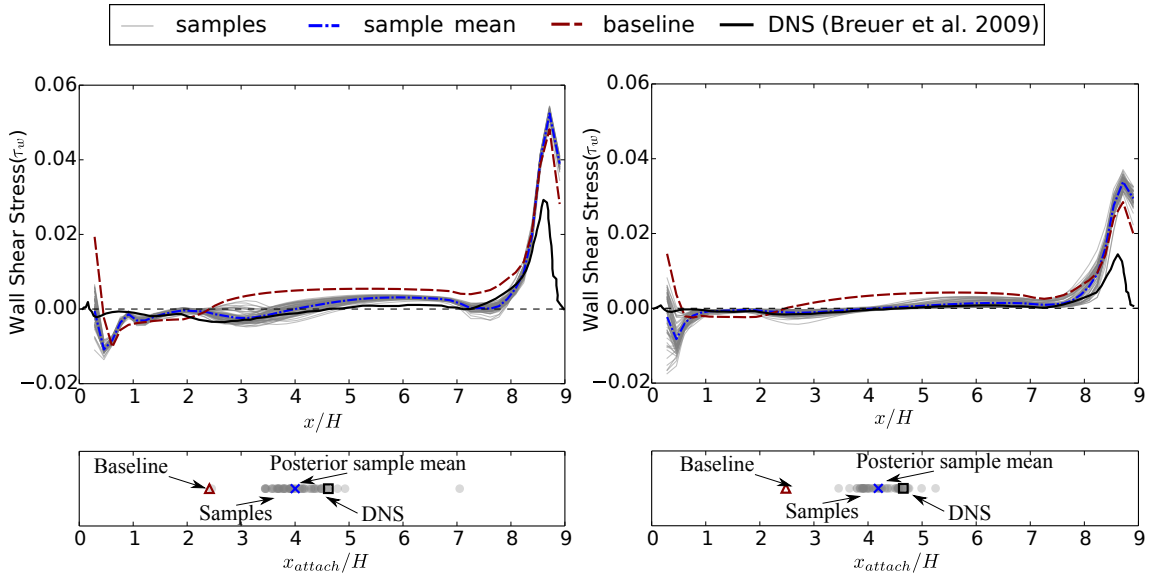

(a) Calibration case at $Re = 2800$ (b) Prediction case at $Re = 10595$

Figure 3.8: Posterior ensembles of shear stress τ_w on the bottom wall and reattachment points x_{attach} for the flow over periodic hills, showing both (a) the calibration case at $Re = 2800$ and (b) the prediction case at $Re = 10595$. The regions with negative wall shear stresses on the bottom wall are recirculation zones. The reattachment point is determined by the change of wall shear stress from negative to positive, which is the downstream end of the recirculation zone.

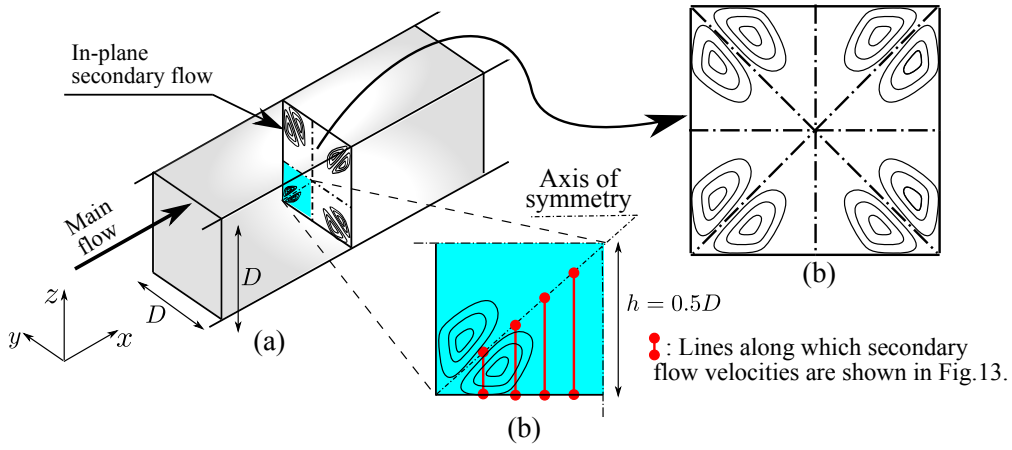

Figure 3.9: Domain shape for the flow in a square duct. The x coordinate represents the streamwise direction. Secondary flows induced by Reynolds stress imbalance exist in the y–z plane. Panel (b) shows that the computational domain covers a quarter of the cross-section of the physical domain. This is due to the symmetry of the mean flow in both y and z directions as shown in panel (c).

the discrepancies δ^{ξ} and δ^{η} are successfully calibrated. With the calibrated discrepancies, predictions are made for the two flows at higher Reynolds numbers.

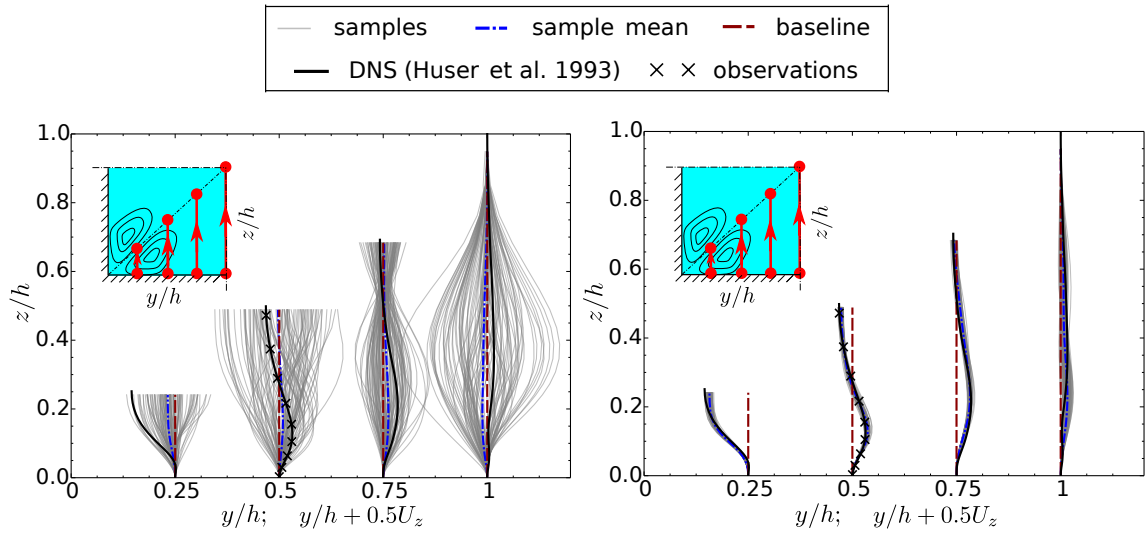

(a) Prior ensemble (b) Posterior ensemble

Figure 3.10: (a) Prior ensemble and (b) posterior ensemble of velocity U_z profiles at four locations $y/h = 0.25, 0.5, 0.75$ and 1. The sample profiles of prior are scaled by a factor of 0.3 for clarity.

Figure 3.11a shows the secondary velocity at $Re = 8.3 \times 10^4$ along the vertical axis of symmetry along $z = h$ (position shown in inset) with comparison to available experimental data of Brundrett and Bains [24]. The baseline RANS result deviates from the experimental data because RANS models with isotropic eddy viscosity are not able to capture the stress anisotropy induced secondary flows. In contrast, the present method predicts an in-plane velocity magnitude comparable to the experimental data and captures its trend of spatial variation. Similarly, the prediction for the flow at $Re = 2.5 \times 10^5$ along the same line is presented in Fig. 3.12a, which also shows a good agreement with the benchmark data, even though the Reynolds number in this case is more than an order of magnitude larger than that in the calibration case.

Figure 3.11b shows the secondary velocity at $Re = 8.3 \times 10^4$ along the diagonal of the channel with comparison to experimental data [25]. It can be seen that the prediction is significantly improved compared to the baseline RANS result. The prediction for the flow at $Re = 2.5 \times 10^5$ as presented in Fig. 3.12b also demonstrates a satisfactory agreement with the benchmark data, although the location of the velocity peak is slightly different from the benchmark results. A possible explanation for this difference is that the assumption of similar Reynolds stress discrepancies becomes less accurate with the departure of Reynolds number from that of the calibration flow. Despite this discrepancy, the prediction presented in Fig. 3.12a and 3.12b are still comparable to or better than those obtained from RANS solvers utilizing advanced turbulence models, including an explicit algebraic Reynolds stress

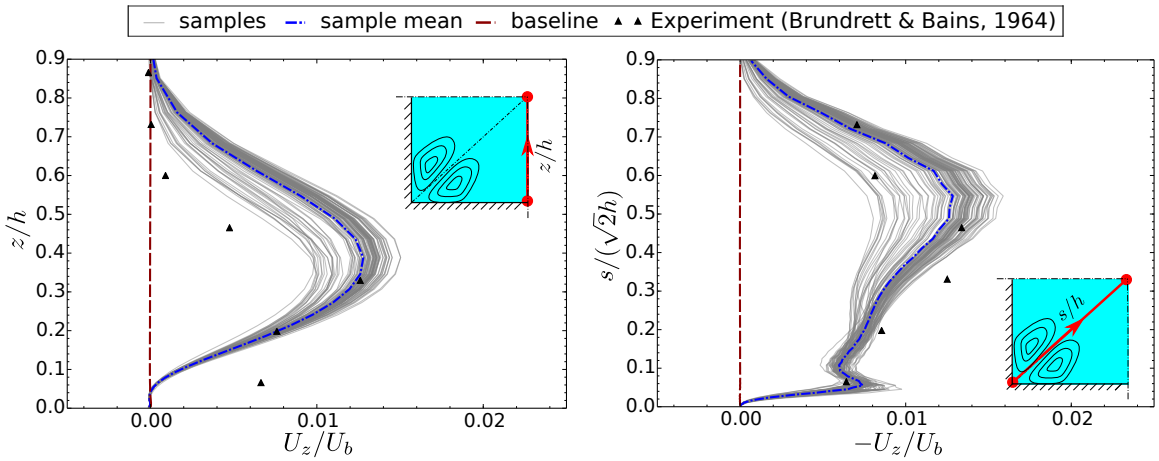

(a) Along vertical axis of symmetry (b) Along diagonal

Figure 3.11: The secondary flow velocity U_y in the prediction case (flow at $Re = 8.3 \times 10^4$, where no observation data are used). Velocity along (a) the vertical axis of symmetry and (b) the diagonal are shown. The experimental data are marked as ▲.

model (EASM) [26] and a Reynolds stress transport model (RSTM) [27]. It can be seen from Fig. 3.12a that the secondary velocity U_z of experimental data becomes negative between $z/h = 0$ and $z/h = 0.1$, a feature that is not captured by the explicit algebraic Reynolds stress model [26] or the Reynolds stress transport model [27]. Figure 3.12b shows that the velocity drop between $z/h = 0.1$ and $z/h = 0.2$ as in the experimental data is only captured by the present method, although the both Reynolds stress models capture the magnitude and general trend of the experimental data well. It is worth noting that by combining a RANS solver with a simple eddy viscosity model and indirect measurement data from a related flow (at a much lower Reynolds number), the present framework is able to achieve better predictions of in-plane velocities than advanced RANS models such as algebraic Reynolds stress model [26] and Reynolds stress transport models [27]. More assessment of advanced RANS models and comparison of their simulation results to experimental data can be found in ref. [26]. This comparison here highlights the merits of data in reducing model-form uncertainties in turbulence modeling.

Figure 3.13 shows vectors plots of the secondary flow velocity in the calibration and prediction cases. The vortex structures in both flows, which are at Reynolds numbers $Re = 8.3 \times 10^4$ and $Re = 2.5 \times 10^5$, are successfully captured as shown in Figs. 3.13a and 3.13b, respectively. In addition, two general trends can be observed from Fig. 3.13 as the Reynolds number increases. First, the secondary flow penetrates further to the corner of the duct as the Reynolds number increases. That is, the corner region where secondary flow is absent becomes smaller with increasing Reynolds number. Second, the thickness of the secondary flow boundary layers decreases as the Reynolds number increases, i.e., the velocity gradient $\partial U_y/\partial z$ near the bottom wall increases as the flow Reynolds number increases. Both trends are consistent with the findings from previous studies [24, 28]. Again, it is emphasized that these trends

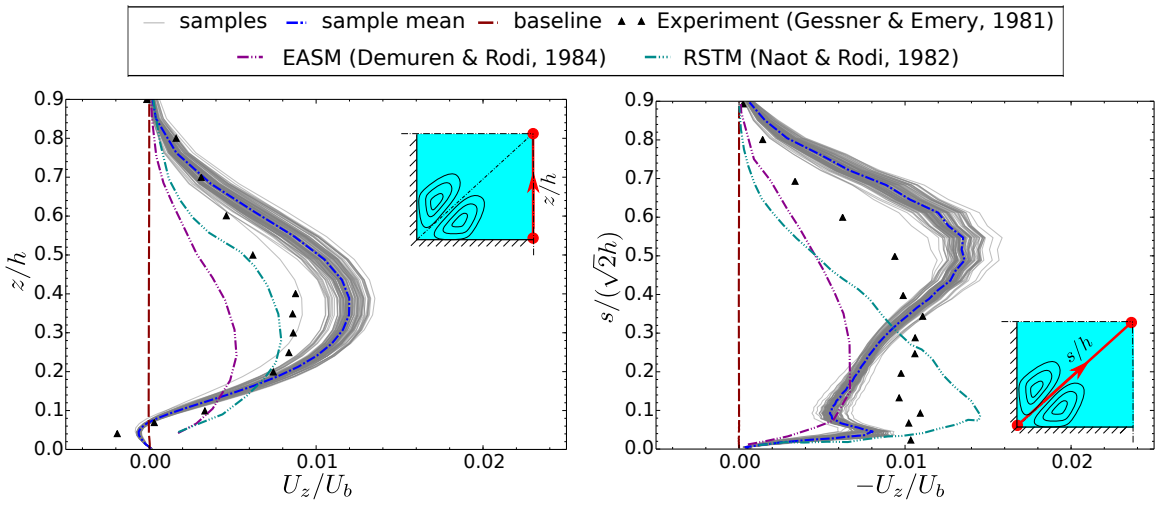

(a) Along vertical axis of symmetry (b) Along diagonal

Figure 3.12: The comparison of predicted secondary velocity U_z at Reynolds number $Re = 2.5 \times 10^5$ with experimental data (denoted as ▲) and with predictions from advanced turbulence models including an explicit algebraic Reynolds stress model (EASM) and a Reynolds stress transport model (RSTM). Comparisons are shown (a) along the vertical axis of symmetry and (b) along the diagonal. Note that the prediction does not utilize observation data from the flow at $Re = 2.5 \times 10^5$.

are predicted without utilizing observation data from the high Reynolds number cases ($Re = 8.3 \times 10^4$ or $Re = 2.5 \times 10^5$).

In addition to the favorable quantitative agreement with experimental data presented above, we also found that the qualitative features of the flows at Reynolds numbers $Re = 8.3 \times 10^4$ and 2.5×10^5 are captured well in the prediction, although full-field benchmark data are not available for a detailed comparison. Vector plots of the posterior mean of the calibrated and predicted secondary velocities are presented in the three panels of Fig. 3.13. Comparison of Figs. 3.13b and 3.13c shows that the predicted overall flow patterns of the two flows at $Re = 8.3 \times 10^4$ and 2.5×10^5 are very similar except for the minor differences near the lower left corner and in the near wall region. This is consistent with the previous findings reported in the literature [e.g., 24] that the general patterns of the secondary flows are not sensitive to the increase of Reynolds number at high Reynolds numbers. A closer examination reveals that the flow pattern does become more complex as the Reynolds number increases. For example, Figure 3.13c shows that in the flow at $Re = 2.5 \times 10^5$ the secondary flow starts to separate near the lower right part of the computational domain (the shaded region). This prediction is physical and can be confirmed by the available experimental data presented in Fig. 3.12b, in which the secondary flow velocity U_y becomes negative (leftward) at the same location [25]. Although such a phenomenon is not present in the calibration flow at a lower Reynolds number $Re = 1 \times 10^4$ (see Fig 3.13a), it is still successfully captured by the proposed method for the flow at a higher Reynolds number $Re = 2.5 \times 10^5$. Recall that

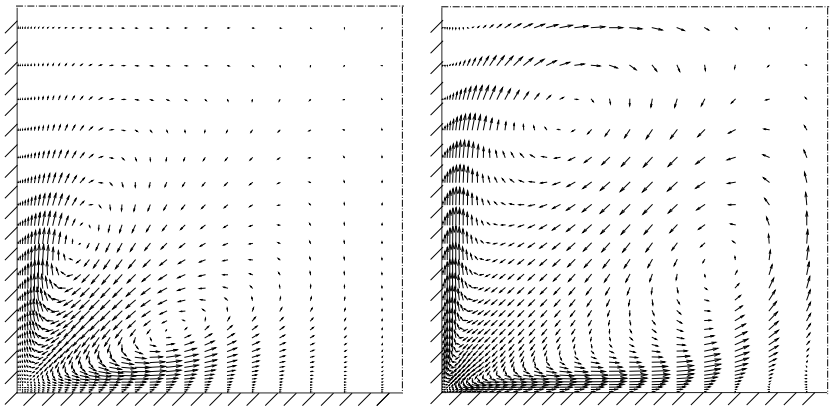

(a) Calibration ($Re = 1 \times 10^4$) (b) Prediction ($Re = 8.3 \times 10^4$)

(c) Prediction ($Re = 2.5 \times 10^5$) (d) Zoom-in view of separation

Figure 3.13: Vector plot of the posterior mean of the predicted in-plane velocities for the flows at (a) $Re = 1 \times 10^4$ (flow for calibration), (b) $Re = 8.3 \times 10^4$ (flow to be predicted), (c) $Re = 2.5 \times 10^5$ (flow to be predicted), and (d) the enlargement of shaded region in plot (c). The directions and lengths of arrows indicate the directions and magnitude, respectively, of the secondary velocities. The shaded region highlight the presence of separation of secondary flow in the lower-left region (near the bottom wall and the vertical axis of symmetry).

in the present Bayesian framework, information in the prediction can only come from the specified prior knowledge, observation data, or the physical dynamics model (i.e., the RANS solver), but the former two sources do not have information on presence of the separation. Therefore, one can only attribute the successful prediction of the separation to the RANS solver. This finding clearly demonstrates the merits of fully utilizing the physical model in the present method.

3.3.2 Prediction of Flow in a Different Geometry

In Section 3.3.1 above, it has been demonstrated that the calibrated Reynolds stress discrepancy can be utilized to predict flows on a geometrically similar domain but at higher Reynolds numbers. In this section we examine a more challenging case, where the Reynolds stress discrepancies calibrated on the square duct flow are used to predict the flow in a rectangular duct with aspect ratio of 1:2. The Reynolds number of the flow in the rectangular duct is $Re = 8.8 \times 10^4$, which is moderately higher than that of the calibration flow (1×10^4). However, we focus on the change of geometry here since the test cases above have demonstrated that the change of Reynolds number does not pose intrinsic difficulties for the extrapolation.

Three possible schemes have been proposed in Section 3.2.2 to extrapolate the calibrated Reynolds stress discrepancies on the square duct to the rectangular domain in the prediction case. The schemes have been illustrated in Fig. 3.3 and are summarized below for completeness: (1) direct mapping of the square to the lower half of the rectangle, (2) linear stretching of the square to the rectangle, and (3) direct mapping of the lower triangle and linear stretching of the upper triangle.

The three seemingly arbitrary choices are in fact based on three clear assumptions of the rectangular duct flow. Comparing the domains of the calibration case in Fig. 3.3 and the prediction case in Fig. 3.3 suggests that the major difference is that the upper boundary CD is moved further away from the bottom wall AB. The assumptions, i.e., assumed physical prior knowledge, on the change of the boundary location behind the three schemes can be described as follows:

Scheme 1: The change of the upper boundary location does not change the size and locations of the two vortices, and new flow patterns develop in the upper half of the rectangle.

Scheme 2: The flow in the rectangular duct maintains the same symmetric pattern as in the square duct case, with both vortices elongated approximately to the same aspect ratio of the rectangle.

Scheme 3: The change of the upper boundary location influences the upper vortex structure only, and the lower vortex remains unchanged.

While possibly none of the three assumptions is completely physical, the third one is the most realistic, which we will justify as follows. One of the most prominent features of the flows in both the square and the rectangular ducts is the secondary flows induced by the anisotropy of Reynolds stress tensor. This anisotropy is caused by the interactions between the boundary layers along the two perpendicular walls (AD and AB). It should be expected that moving the upper boundary further away has larger influence on the boundary layer of the vertical wall (AD) than on that of the horizontal wall (AB), since the flow in the upper half of the rectangular duct interacts only weakly with the boundary layer of the bottom wall. Based on this reasoning, the assumption associated with scheme 3 seems most reasonable, i.e., the change of boundary location influences only on the upper vortex and no the lower vortex. Consequently, scheme 3 as shown in Fig. 3.3 is the more appropriate choice.

The obtained flow patterns with the three mapping schemes above largely reflect their respective physical assumptions as detailed above. The in-plane streamlines from experiments [29] are presented in Fig. 3.14a, which shows two vortices. The two vortices in the rectangular duct have different sizes, which is in contrast to the two symmetric vortices in the square duct. The major vortex is located at the upper right, while the minor structure is located at the lower left. The relative locations of the two vortices are similar to those in the square duct flow. The predicted streamlines based on the mapping schemes 1–3 are presented in Fig. 3.14b–3.14d, respectively. Figure 3.14b shows two vortices in the lower half of the duct similar to those in the square duct flow. It is noteworthy that a third vortex develops on the upper half of the duct, which is driven by the vortex below it. This predicted flow pattern is qualitatively different from that shown in Fig. 3.14a, suggesting that the assumption associated with scheme 1 is unphysical. Figure 3.14c shows that the prediction based on scheme 2 does capture the qualitative features of the major and the minor vortices, although the predicted center locations and the vortices sizes do not completely agree with the experimental results. Finally, the predicted streamlines based on scheme 3 are presented in Figure 3.14d, which has an even better agreement with the experimental data compared to that obtained with scheme 2. In particular, the center and the size of the minor vortex are very well predicted. The general pattern of the major vortex is also captured successfully, although the prediction quality is not as good as for the minor vortex. The remaining difference can be explained by the fact that the mapping scheme is linear, which may not be true due to the different influences of the boundary layer interactions.

Comparison of the three predictions above suggest that the assumed physical knowledge has a critical impact on the obtained predictions. An unphysical assumption as that behind scheme 1 leads to a qualitatively incorrect prediction of overall flow patterns. An assumption based on sound physical reasoning as in scheme 3 leads to the more favorable predictions.

Figure 3.15 shows the comparison of secondary flow velocity magnitude contours between experimental data [29] and the prediction based on scheme 3. It can be seen that the predicted contour patterns are similar to those of the experimental data, and the predicted magnitude is also comparable to the experimental data. Admittedly, the predicted secondary flow field

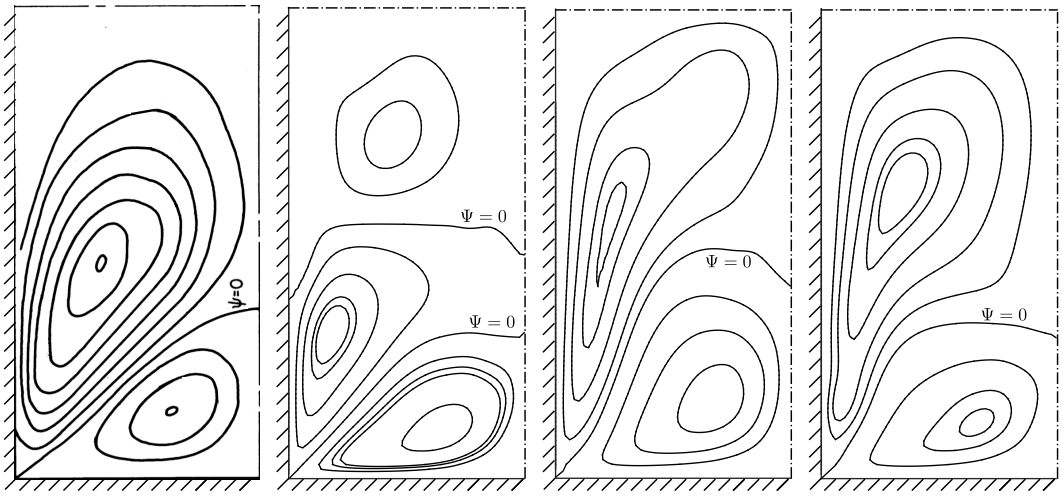

(a) Experiment [29] (b) Scheme 1 (c) Scheme 2 (d) Scheme 3

Figure 3.14: Comparison of experimentally measured and the predicted secondary flow patterns (posterior mean) based on three schemes of mapping Reynolds stress discrepancy from the calibration case to prediction case. Panel (a) shows streamlines obtained from experiments [29]. Panels (b)–(d) show predicted streamlines based on schemes 1–3, respectively. The baseline RANS prediction is omitted here as it predicts no secondary flows.

is not exactly the same as the experimental data, e.g., the velocity magnitude is greater than the experimental data at the near wall region and smaller than the experimental data away from the wall. A possible reason is that the prior physical knowledge incorporated in scheme 3 is still far from enough to accurately account for the additional physics introduced by the geometry change. However, it can be seen from Fig. 3.14 that the prediction qualitatively captures the flow pattern, which is totally absent in baseline RANS results, with much lower computational cost compared to high fidelity simulations. Therefore, we argue that the proposed method provides a practical approach to quickly and approximately search the design space with low computational costs in the preliminary design stage of engineering systems. It will help identify the promising design candidates for the further investigations with high fidelity simulations and/or model experiments.

3.4 Discussion

3.4.1 The limitation and the possible extension for the calibration step

In the calibration step, the posterior mean velocity profiles show much better agreement with the benchmark data compared to the baseline RANS results. Therefore, the reduced

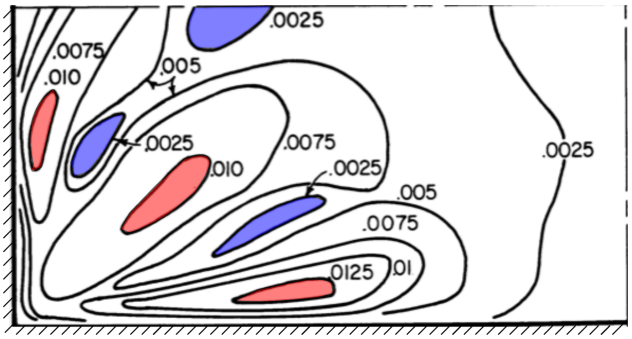

(a) Experiment (Hoagland, 1960)

(b) Prediction

Figure 3.15: Comparison of experimentally measured and the predicted contours of secondary velocity magnitude (posterior mean). Panel (a) shows contours obtained from experiment [29]. Panel (b) shows predicted contours based on scheme 3. Black crosses (+) and the numbers nearby indicate the values of the contours. Peaks and troughs are denoted as red (light shade) and blue (dark shade) to facilitate interpretation of flow field structure. The baseline RANS prediction is omitted here as it predicts no secondary flows.

scattering from prior to posterior ensembles can be interpreted as increased confidence upon the posterior mean. However, it should be noted that the reduction of the scattering is not an exact measure of "increased confidence" in the final results. This is because the iterative ensemble-based Kalman method is used in calibration step to perform the inference. This method is an approximate Bayesian inference approach, which is based on maximum likelihood estimation (MLE). Stuart et al. [30] pointed out that, using the Kalman-filtering-based data assimilation methods, the posterior mean can achieve a relatively high accuracy. However, the variance tends to be underestimated, which can also leads to the reduced scattering of posterior ensemble. We are currently trying to use fully Bayesian inference approach (e.g., MCMC) as a gauge to assess the estimated uncertainties in the posterior ensemble of current approach. This comparison and the corresponding extension of the current work are still underway, which are not explored in this paper.

Another limitation of this work is that only a single dataset can be incorporated in the calibration step for a specific flow problem. Therefore, it is required to determine the most relevant dataset if multiple datasets are available. The incorporation of multiple datasets into Bayesian inference has been demonstrated in the work by Edeling at al. [31]. In their work, the potentially informative data are incorporated as much as possible, and thus it is expected to has better robustness of the choice of dataset. Compared to the work by Edeling at al. [31], our work provides a mathematically rigorous approach to incorporate not only the information from dataset, but also the physical insights about the realizability and the anisotropy state of Reynolds stress. It is possible to extend our current work to incorporate multiple datasets of a series of closely related flow, since the coefficients used to parameterize the discrepancy of anisotropy is analogous to the closure parameters θ in the work by Edeling et al. [31] within the framework of Bayesian inference. However, it should be noted that if the extreme situation is considered, for example, that all the available datasets are not representative for the flow problem of interest, none of the approaches can give reliable prediction. This is because the Bayesian inference can only incorporate the existing information, rather than creating information which is lacking.

3.4.2 The limitation and the valid scenario for this calibration-prediction method

The closeness defined in this work is different from the conventional similarity in fluid mechanics such as dynamical similarity or geometrical similarity. In this work, we define that one flow problem is close to another if the mean flow feature is not significantly changed. Compared to the calibration case, the prediction case can have a moderate change of Reynolds number, or a moderate change of geometry, or the combination of these two changes. The key assumption here is that the anisotropy of Reynolds stress tensor is mainly determined by the mean flow feature, including the geometrical constraints. Such assumption is physically reasonable, since the extent of restrain of mean flow velocity in different

directions has direct impact upon the anisotropy state of the Reynolds stress tensor. In practice, whether the mean flow feature would be significantly changed can be estimated by comparing the two RANS baseline results of calibration case and prediction case, and we recommend the user to trust the calibration-prediction result only if there is no significant change of mean flow feature between two RANS baseline results. To ensure the performance of this proposed work, we also suggest that the whole procedure should be performed by experienced engineers and researchers, since the framework provides a mathematically rigorous approach to incorporate the information and knowledge from different sources, including the empirical knowledge from the user.

Although this calibration-prediction method is only valid if the flow in calibration step and the one in prediction step are closely related, there are still common scenarios which could be benefited from the proposed method. For instance, when mission-critical systems are developed, laboratory experiments are often performed on a down-scaled model at a lower Reynolds number. The calibration-prediction method provides a novel and physically reasonable approach to predict the full-scale scenario based on the laboratory-scale experiment, with a much lower cost than the high fidelity simulation or the experiment of the full-scale system. Another promising application of this method is to assist the detailed design stage of a product, provided that only minor geometry modification is involved. Since the wall time of the prediction step is at the same order as the RANS prediction if the samples are propagated in parallel, this proposed method can search the test matrix at the similar speed of the conventional RANS simulation, whereas provides a better prediction of the mean quantities.

3.5 Conclusion

Recently, Xiao et al. [12] proposed a framework for quantifying and reducing uncertainty in RANS simulations based on sparse observations of velocities. In the present work we extend the original framework to flows with no observation data, leading to a Bayesian calibration–prediction method. As in the original framework, the model-form uncertainty in RANS simulations are localized to the Reynolds stresses, which are modeled as a random field. The uncertainty distribution of the discrepancy is first calibrated with available data on a related flow (e.g., the flow in a geometrically similar domain or in a slightly different geometry). Subsequently, the obtained distribution is extrapolated to the prediction case and is sampled to correct the RANS-modeled Reynolds stresses. The merits of the proposed method are demonstrated with two canonical flows of engineering relevance, the flow over periodic hills and the flow in a square duct. In the case of periodic hill flows, the uncertainty distribution of the discrepancy is calibrated in the flow at a lower Reynolds number and extrapolated to a higher Reynolds number. In the duct flow cases, the discrepancy distribution is calibrated in a square duct flow and used to predict flows at higher Reynolds number flows and that in a rectangular duct. Numerical simulation results demonstrate that the predictions of

posterior mean velocities have significantly improved agreement with the benchmark data compared to the baseline RANS predictions. It is noteworthy that even the flow features that are not present in the calibration flow have been successfully captured in the prediction case by the proposed procedure, demonstrating the merits of framework in fully utilizing the RANS model. Based on the simulation results, we conclude that the proposed calibration–prediction method is a promising candidate for reducing model-form uncertainties in RANS simulations.

The proposed method is an algorithmically straightforward yet practically profound extension of the original framework. Since direct observation data are not required on the flow to be predicted, the range of applications is greatly expanded compared to the original framework. This is particularly relevant for turbulent flow simulations in support of engineering design, where the prototype system has not been build yet in the design stage.

An important assumption in the proposed method is that the flow used for calibration and the flow to be predicted are closely related. Specifically, they share the same overall characteristics despite the fact that the two flows are not dynamically similar (i.e., they have different Reynolds numbers) or not even geometrically similar (e.g., flow in a square duct versus flow in a rectangular duct). This assumption is valid in many scenarios in engineering design. On the other hand, the assumption also implies that the quality of the prediction inevitably depends on the judgment of the analyst. We argue that this is an intrinsic feature of Bayesian methods, and it is often an advantage for a framework to be able to incorporate insights and prior knowledge from the users, who are often experts of the model and the problem of concern.

Acknowledgment

The authors would like to acknowledge the comments from Dr. Alireza Doostan of University of Colorado Boulder during a conference presentation made by HX, which prompted the work presented in this manuscript. Discussions with Dr. Chris Roy and Dr. Eric Paterson of Virginia Tech are gratefully acknowledged.

Bibliography

[1] M. Scheuerer, M. Heitsch, F. Menter, Y. Egorov, I. Toth, D. Bestion, S. Pigny, H. Paillere, A. Martin, M. Boucker, et al., Evaluation of computational fluid dynamic methods for reactor safety analysis (ECORA), Nuclear Engineering and Design 235 (2-4) (2005) 359–368.

[2] U. Bieder, C. Calvin, H. Mutelle, Detailed thermal hydraulic analysis of induced break severe accidents using the massively parallel CFD code Trio-U/PRICELES, in: Supercomputing in Nuclear Applications, Paris, 2003.

[3] C. Murray, RELAP Theory Manual, U.S. Department of Energy Office of Nuclear Energy (2014).

[4] M. C. Kennedy, A. O'Hagan, Bayesian calibration of computer models, Journal of the Royal Statistical Society: Series B (Statistical Methodology) 63 (3) (2001) 425–464.

[5] E. Dow, Q. Wang, Quantification of structural uncertainties in the k–ω turbulence model, in: 52nd AIAA/ASME/ASCE/AHS/ASC Structures, Structural Dynamics and Materials Conference, AIAA, Denver, Colorado, 2011, aIAA Paper, 2011-1762.

[6] M. Emory, R. Pecnik, G. Iaccarino, Modeling structural uncertainties in Reynolds-averaged computations of shock/boundary layer interactions, AIAA paper 479 (2011) 1–16.

[7] M. Emory, J. Larsson, G. Iaccarino, Modeling of structural uncertainties in Reynolds-averaged Navier-Stokes closures, Physics of Fluids 25 (11) (2013) 110822.

[8] C. Gorlé, G. Iaccarino, A framework for epistemic uncertainty quantification of turbulent scalar flux models for Reynolds-averaged Navier-Stokes simulations, Physics of Fluids 25 (5) (2013) 055105.

[9] S. Banerjee, R. Krahl, F. Durst, C. Zenger, Presentation of anisotropy properties of turbulence, invariants versus eigenvalue approaches, Journal of Turbulence 8 (32) (2007) 1–27.

[10] H. Tennekes, J. L. Lumley, A first course in turbulence, MIT press, 1972.

[11] T. Oliver, R. Moser, Uncertainty quantification for RANS turbulence model predictions, in: APS Division of Fluid Dynamics Meeting Abstracts, Vol. 1, 2009.

[12] H. Xiao, J.-L. Wu, J.-X. Wang, R. Sun, C. J. Roy, Quantifying and reducing model-form uncertainties in Reynolds-Averaged Navier-Stokes simulations: An open-box, physics-based, bayesian approach, submitted. Available at http://arxiv.org/abs/1508.06315 (2015).

[13] M. A. Iglesias, K. J. Law, A. M. Stuart, Ensemble Kalman methods for inverse problems, Inverse Problems 29 (4) (2013) 045001.

[14] E. Torenbeek, Design of the well-tempered aircraft, Advanced Aircraft Design: Conceptual Design, Analysis and Optimization of Subsonic Civil Airplanes 1–30.

[15] J. H. McMasters, R. M. Cummings, Rethinking the airplane design processan early 21st century perspective, AIAA Paper 693 (2004) 5–8.

[16] O. P. Le Maître, O. M. Knio, Spectral methods for uncertainty quantification: with applications to computational fluid dynamics, Springer, 2010.

[17] G. Evensen, Data assimilation: the ensemble Kalman filter, Springer, 2009.

[18] OpenCFD, OpenFOAM User Guide, see also `http://www.opencfd.co.uk/openfoam` (2014).

[19] P. Glasserman, Monte Carlo Methods in Financial Engineering, Springer, 2004.

[20] S. Joe, F. Y. Kuo, Constructing Sobol sequences with better two-dimensional projections, SIAM Journal on Scientific Computing 30 (5) (2008) 2635–2654.

[21] J.-X. Wang, J.-L. Wu, H. Xiao, Incorporating prior knowledge for quantifying and reducing model-form uncertainty in rans simulations, submitted. Available at: arXiv:1512.01750 (2015).

[22] M. Breuer, N. Peller, C. Rapp, M. Manhart, Flow over periodic hills–numerical and experimental study in a wide range of reynolds numbers, Computers & Fluids 38 (2) (2009) 433–457.

[23] A. Huser, S. Biringen, Direct numerical simulation of turbulent flow in a square duct, Journal of Fluid Mechanics 257 (1993) 65–95.

[24] E. Brundrett, W. Baines, The production and diffusion of vorticity in duct flow, Journal of Fluid Mechanics 19 (03) (1964) 375–394.

[25] F. Gessner, A. Emery, The numerical prediction of developing turbulent flow in rectangular ducts, Journal of Fluids Engineering 103 (3) (1981) 445–453.

[26] A. Demuren, W. Rodi, Calculation of turbulence-driven secondary motion in non-circular ducts, Journal of Fluid Mechanics 140 (1984) 189–222.

[27] D. Naot, W. Rodi, Calculation of secondary currents in channel flow, Journal of the Hydraulics Division 108 (8) (1982) 948–968.

[28] R. K. Madabhushi, S. Vanka, Large eddy simulation of turbulence-driven secondary flow in a square duct, Physics of Fluids A: Fluid Dynamics (1989-1993) 3 (11) (1991) 2734–2745.

[29] L. C. Hoagland, Fully developed turbulent flow in straight rectangular ducts–secondary flow, its cause and effect on the primary flow (thesis). technical report no. 2, Tech. rep., Massachusetts Inst. of Tech., Cambridge (1960).

[30] M. A. Iglesias, K. J. Law, A. M. Stuart, Ensemble kalman methods for inverse problems, Inverse Problems 29 (4) (2013) 045001.

[31] W. Edeling, P. Cinnella, R. Dwight, Predictive rans simulations via bayesian model-scenario averaging, Journal of Computational Physics 275 (2014) 65–91.

Appendix

Appendix.C: Algorithm for Resampling the Posterior Distribution of Reynolds Stress Discrepancies

Given an ensemble $\{\boldsymbol{\omega}_i\}_{i=1}^N$ of size N representing the posterior distribution of Reynolds stress discrepancy, the objective is to obtain another ensemble of size N' drawn from the same distribution. Each sample $\boldsymbol{\omega}_i$ is a vector of size $3m \times 1$, consisting of the coefficients for the retained m modes of the three discrepancy fields δ^k, δ^ξ and δ^η. The following algorithms are used for the resampling:

1. Estimate the sample mean and sample co-variance of the ensemble $\{\boldsymbol{\omega}_i\}_{i=1}^N$ as follows:

$$\bar{\boldsymbol{\omega}} = \frac{1}{N}\sum_{i=1}^{N}\boldsymbol{\omega_i} \tag{3.4}$$

$$C = \frac{1}{N-1}\sum_{i=1}^{N}(\boldsymbol{\omega}_i - \bar{\boldsymbol{\omega}})^T(\boldsymbol{\omega}_i - \bar{\boldsymbol{\omega}}) \tag{3.5}$$

2. Perform eigendecomposition of covariance matrix C as below

$$C\phi_j = \lambda'_j\phi_j \tag{3.6}$$

   to obtain the orthogonal eigenvectors $\{\phi_j\}_{j=1}^{3m}$.

3. Project the samples $\{\boldsymbol{\omega}_i\}_{i=1}^N$ on the basis functions $\{\phi_j\}_{j=1}^{3m}$ to obtain $\{\boldsymbol{\alpha}_i\}_{i=1}^N$, where $\boldsymbol{\alpha}_i$ is the coordinate of the sample $\boldsymbol{\omega}_i$ on the new basis set $\{\phi_j\}_{j=1}^{3m}$. The transformed ensemble $\{\boldsymbol{\alpha}_i\}_{i=1}^N$ can be considered realizations of a random vector $\mathbf{a}$ of size $3m \times 1$ with uncorrelated components.

4. The probability distribution functions and the corresponding cumulative density functions (CDF) for each component of the random vector $\mathbf{a}$ is estimated from the samples, i.e., $\{\boldsymbol{\alpha}_i\}_{i=1}^N$, by using kernel density estimation techniques.

5. Generate N' samples for each of the component from the estimated CFD by using standard sampling techniques [19].

6. Reconstruct sample $\{\boldsymbol{\omega}'_i\}_{i=1}^{N'}$ of size N' from the resampled coefficients $\{\boldsymbol{\alpha}'_i\}_{i=1}^N$ and the basis $\{\phi_j\}_{j=1}^{3m}$.

Chapter 4

Physics-Informed Machine Learning Approach for Augmenting Turbulence Models: A Comprehensive Framework

(Published on *Physical Review Fluids*, 3 (7), 074602, 2018.)

J.-L. Wu, H. Xiao, E. Paterson
Department of Aerospace and Ocean Engineering, Virgina Tech, Blacksburg, VA, 24061, USA

Abstract

Reynolds-averaged Navier–Stokes (RANS) equations are widely used in engineering turbulent flow simulations. However, RANS predictions may have large discrepancies due to the uncertainties in modeled Reynolds stresses. Recently, Wang et al. demonstrated that machine learning can be used to improve the RANS modeled Reynolds stresses by leveraging data from high fidelity simulations (Physics informed machine learning approach for reconstructing Reynolds stress modeling discrepancies based on DNS data. Physical Review Fluids. 2, 034603, 2017). However, solving for mean flows from the improved Reynolds stresses still poses significant challenges due to potential ill-conditioning of RANS equations with Reynolds stress closures. Enabling improved predictions of mean velocities are of profound practical importance, because often the velocity and its derived quantities (QoIs, e.g., drag, lift, surface friction), and not the Reynolds stress itself, are of ultimate interest in RANS simulations. To this end, we present a comprehensive framework for augmenting turbulence models with physics-informed machine learning, illustrating a complete workflow from identification of input features to final prediction of mean velocities. This work has two innovations. First, we demonstrate a systematic procedure to generate mean flow features based on the integrity basis for mean flow tensors. Second, we propose using machine

learning to predict linear and nonlinear parts of the Reynolds stress tensor separately. Inspired by the finite polynomial representation of tensors in classical turbulence modeling, such a decomposition is instrumental in overcoming the ill-conditioning of RANS equations. Numerical tests demonstrated merits of the proposed framework.

4.1 Introduction

Numerical simulations based on Reynolds-averaged Navier–Stokes (RANS) models are still the work-horse tool in engineering design involving turbulent flows. However, predictions from RANS simulations are known to have large discrepancies in many flows of engineering relevance, including those with swirl, pressure gradients, or mean streamline curvature [2]. It is a consensus that the dominant cause for such discrepancies is the RANS-modeled Reynolds stresses [3]. In light of the long stagnation in traditional turbulence modeling, researchers [4, 5, 6, 7, 8] explored machine learning as an alternative to improve RANS modeling by leveraging data from high-fidelity simulations.

4.1.1 Data-driven methods for reducing model discrepancies in RANS simulations

Data-driven methods have been devised to calibrate the model form uncertainties in RANS simulations based on optimization [9] and Bayesian inference approaches [9, 10, 11, 12, 13]. However, these data-driven calibration approaches inferred the model discrepancies of a given flow and thus lack the generalization capabilities for predicting flows with vastly different geometries from the calibration flow. Therefore, follow-on works of these researchers build data-driven turbulence models in the mean flow features space (as opposed to physical space). Such an approach enables prediction for flows in different geometries yet with similar physics (e.g., curved pipes and wing–body juncture, both featuring secondary flows driven by Reynolds stress anisotropies). Duraisamy and co-workers [4, 14, 15] used non-dimensional flow variables as the input features and a multiplicative correction term in the Spalart–Allmaras model as the machine learning output. Their machine-learning-augmented model demonstrated good generalization capabilities within a class of flows around airfoils [15]. Ling et al. [6] pointed out the importance of embedding the tensorial invariance properties in the machine learning process and used this approach to predict the Reynolds stress with a deep neural network [7]. Wang et al. [8] build a machine-learning model to predict the discrepancies in the RANS modeled Reynolds stresses. Encouraging results have been demonstrated in prediction of Reynolds stresses in two sets of canonical flows (separated flows over periodic hills and secondary flows in a square duct). However, the machine-learning-predicted Reynolds stress leads to large error of solved mean velocities when substituted into the RANS equations. Such an ill-conditioning issue is a common challenge for data-driven

Reynolds stress models that must be addressed to unleash the power of such models.

A distinctly different approach of data-driven modeling is pursued by Weatheritt and Sandsberg [16, 17], who used symbolic regression and gene expression programming to develop algebraic Reynolds stress models. To some extent, their approach is a combination of traditional modeling and data-driven modeling methods reviewed above. Specifically, while data-driven methods are used to obtain their model, the end product is an algebraic Reynolds model in the traditional sense. As such, the ill-conditioning issue for their model would be similar to the traditional models with explicit analytical forms and not the data-driven models.

4.1.2 Conditioning of data-driven Reynolds stress models

In this work we refer to solving the RANS equations for mean velocities with a given Reynold stress field as "propagation", which is a critical component in data-driven turbulence modeling. Poroseva et al. [18] referred to such simulation as "RANS–DNS simulations". Admittedly, both terminology could cause potential confusions, which thus warrants the explicitly clarification here.

Recently, several researchers have observed that small errors in the Reynolds stresses can be amplified to large errors in the mean velocities when solving the RANS equations with specified Reynolds stresses. Thompson et al. [19] propagated Reynolds stresses in channel flows at a wide range of frictional Reynolds numbers ($Re_\tau = 180$ to 5200) to mean velocities by using several reputed DNS databases. They reported that the propagated mean velocities can deviate significantly from the mean velocities from the DNS, especially for flows at high Reynolds numbers (notably $Re_\tau = 5200$). Poroseva et al. [18] also made similar observations, and Poroseva [20] further pointed out that the discrepancies between the propagated velocities and DNS velocities were observed for flows at Reynolds numbers as low as $Re_\tau = 395$, depending on the dataset used. Considering that errors in DNS Reynolds stress are typically less than 0.5% [21, 22], these exercises of propagating DNS Reynolds stresses to mean velocities thus represent an ideal scenario for data-driven turbulence models with negligible modeling errors. Wu et al. [22] explained such observations by pointing out that RANS equations with Reynolds stress closure models can be ill-conditioned. They further proposed a condition number function defined based on the local velocities to quantify the ill-conditioning. For plane channel flows, the local condition number does increase with Reynolds number, which thus explained the increased ill-conditioning with increasing Reynolds number. In contrast, the traditional, matrix-based conditional number was not able to explain such observations. A physical explanation is that viscous stresses are negligible at high Reynolds numbers and the mean velocity is determined by the dependence of the Reynolds stresses on the mean velocity gradients. Therefore, obtaining the mean velocity would fail from an *a priori* specification of the Reynolds stresses. A unique issue associated with data-driven modeling is that it can be difficult or even impossible to treat the Reynolds

stress implicitly as in traditional models, and in such cases segregated solvers are the only option. More detailed discussion can be found in [22].

Similar ill-conditioning issue also exists in traditional Reynolds stress models (RSM), where Reynolds stresses are obtained by solving transport equations. To enhance the stabilities, Jarklic and co-workers [23, 24] blended $\boldsymbol{\tau}_{\text{RSM}}$ obtained from solving the Reynolds stress transport equation with that given by a linear eddy viscosity model (LEVM), i.e., $\boldsymbol{\tau} = \alpha\boldsymbol{\tau}_{\text{RSM}} + (1-\alpha)\boldsymbol{\tau}_{\text{LEM}}$. However, the specification of a blending factor α is largely *ad hoc* and lacks physical basis. In this work, we aim at introducing a more rigorous, physics-based implicit treatment in the context of data-driven Reynolds stress models.

4.1.3 Data-driven closure modeling beyond RANS simulations

In addition to RANS modeling as reviewed above, data and machine learning have been used to provide closures for (1) the subgrid-scale (SGS) fluxes for in LES, (2) the inter-phase momentum fluxes in multiphase flow simulations [25, 26], and (3) the unresolved boundary layer physics in potential flow simulations [27]. Among these, researchers reported ill-conditioning issues in data-driven SGS models in LES that are similar to the ill-conditioning issue in the context of RANS modeling discussed above. For example, Gamahara et al. [28] used neural network to model the subgrid-scale stress in a turbulent channel flow. Compared to the predictions of Smagorinsky models, the machine learning model predicted better SGS stresses but the less satisfactory mean velocities. This observation clearly highlights the gap between *a priori* and *a posterior* performances in assessment of turbulence models, particularly in the context of data-driven turbulence modeling. Furthermore, Durieux [29] reported that the LES with neural network predicted SGS models become unstable if velocity-derived variables are chosen as neural network inputs, suggesting possible error amplification in the propagation of SGS stresses to mean velocities.

Note that the ill-conditioning issue only emerges if the data-driven SGS model is explicitly substituted into filtered transport equations to solve for velocities or other quantities of interest (QoIs). Many other works that focus on the data-driven prediction of SGS terms (i.e., *a priori* tests) did not encounter this problem. For example, Vollant et al. [30, 31] modeled SGS scalar flux by using neural networks based on optimal estimation. King et al. [32] proposed a fully adaptive, self-optimizing SGS closure and demonstrated superior *a priori* performance than traditional dynamic SGS models. Maulik and San [33] trained a neural network to represent the deconvolution of flow quantities from filtered flow field. They also demonstrated excellent *a priori* performance in several canonical, boundary-free flows. All these promising works have the potential of becoming data-driven SGS closures for stresses or scalar fluxes in LES. However, similar ill-conditioning issue in the context of RANS modeling as outlined in Section 4.1.2 still needs to be addressed if the successes in these *a priori* tests are to be translated into *a posteriori* tests.

4.1.4 Summary and novelty of present contribution

In the present work, we demonstrate a *systematic* approach in choosing the input feature variables for machine learning in the context of turbulence modeling. Specifically, we first identify a set of vectorial or tensorial mean flow variables, e.g., strain-rate tensor, rotation-rate tensor, pressure gradient, and turbulence kinetic energy gradient. Choosing these quantities as inputs for machine learning has clear physical justifications and are supported by the practice in traditional turbulence modeling. Subsequently, we construct an invariant basis set from these variables based on the tensor representation theorem. While this approach was first proposed by Ling et al. [6] and is not new in the present work, the application in turbulence modeling is challenging and could serve as good illustration for researchers in many other fields where the physical quantities are described by a large number of vectors and tensors. This procedure is a clear improvement compared to earlier works with *ad hoc* choice of many scalar variables [34, 8].

Moreover, we propose a data-driven, machine learning based turbulence modeling framework where the Reynolds stresses are decomposed into linear and nonlinear parts and then learned separately form DNS data. This decomposition allows implicit treatment of linear term of the Reynolds stress, which enhances the model conditioning in solving the RANS equations for mean velocity field without *ad hoc* blending as used in traditional turbulence modeling [23, 24]. More importantly, such a decomposition clearly reflects the respective roles of linear and nonlinear terms in turbulent models. Specifically, the linear term is by far the dominant term in almost all turbulent flows in engineering practice, which partly explains the wide spread use of linear eddy viscosity models in engineering CFD. On the other hand, the nonlinear terms can emerge as important factors in specific flows (e.g., swirling, jet impingement, and juncture flows [2, 35]). Hence, treating them separately helps the machine learning algorithms distinguish these two terms. With numerical examples, we show that such a treatment enabled accurate prediction of mean velocities with a data-driven Reynolds stress model.

The rest of this paper is organized as follows. Section 4.2 summarizes the machine-learning-assisted turbulence modeling framework of Wang et al. [8] and presents the proposed approach. Section 4.3 first highlights the ill-conditioning issues of data-driven Reynolds stress models and further demonstrates the merits of the proposed machine learning framework in a posteriori tests of different kinds of flows. Section 4.4 discusses the potentials and limitations of the data-driven turbulence models. Finally, Section 4.5 concludes the paper.

4.2 Methodology

Taking incompressible turbulent flows as an example, the RANS momentum equations are:

$$\frac{\partial \mathbf{U}}{\partial t} + \mathbf{U} \cdot \nabla \mathbf{U} + \nabla p - \nu \nabla^2 \mathbf{U} = \nabla \cdot \boldsymbol{\tau} \tag{4.1}$$

where $\mathbf{U}$, p, ν are the mean velocity, mean pressure (normalized by density), and viscosity, respectively. The Reynolds stress $\boldsymbol{\tau}$ accounts for the momentum flux due to unresolved turbulence and needs closure modeling. A turbulence model aims to close the RANS equations by constructing a mapping from the mean velocity field $\mathbf{U}$ to the Reynolds stress field $\boldsymbol{\tau}$.

In view of the inaccuracy in RANS modeled Reynolds stresses as a critical bottleneck in the prediction accuracy of CFD simulations, Wang et al. [8] proposed a machine learning model for predicting Reynolds stress discrepancies by training on DNS data from similar flows. Specifically, a functional mapping $\mathbf{q} \mapsto \Delta\boldsymbol{\tau}$ from mean flow features $\mathbf{q}$ (obtained from RANS simulations) to Reynolds stress discrepancies $\Delta\boldsymbol{\tau}$ is built by using machine learning, with the discrepancy defined as the difference between RANS predicted and DNS Reynolds stresses, i.e., $\Delta\boldsymbol{\tau} \equiv \boldsymbol{\tau}^{\mathrm{DNS}} - \boldsymbol{\tau}^{\mathrm{RANS}}$. Although an improved prediction of Reynolds stresses was achieved, they reported that the mean flow velocity is sensitive to the errors in Reynolds stress prediction. Since it is usually the mean velocity field and the derived quantities of interest (e.g., drag and lift) required in engineering applications, it is important to understand the error amplification in solving for the mean velocity field. The main reason is that substituting the modeled Reynolds stress explicitly into RANS equations may lead to ill-conditioned RANS equations, especially in high Reynolds number flows [19, 22]. Moreover, the choice of mean flow features lacks a systematic procedure, which raises questions on the completeness and redundancy on the set of flow features included in the machine learning. The present work aims to address these challenges.

4.2.1 Overview of the machine-learning scheme

It has been recognized that all algebraic Reynolds stress and eddy viscosity models can be written in the following general form [36]:

$$\begin{aligned}\mathbf{b}(\mathbf{S},\boldsymbol{\Omega}) =& \sum_{n=1}^{10} G^{(n)}\mathcal{T}^{(n)} \\ =& G^{(1)}\mathbf{S} + G^{(2)}(\mathbf{S}\boldsymbol{\Omega} - \boldsymbol{\Omega}\mathbf{S}) + G^{(3)}(\mathbf{S}^2 - \frac{1}{3}\mathrm{tr}(\mathbf{S}^2)\mathbf{I}) \\ &+ G^{(4)}(\boldsymbol{\Omega}^2 - \frac{1}{3}\mathrm{tr}(\boldsymbol{\Omega}^2)\mathbf{I}) + \cdots (\text{high order terms})\end{aligned} \tag{4.2}$$

where $\mathrm{tr}(\cdot)$ denotes the trace, $\mathbf{I}$ denotes the identity matrix, $\mathbf{b}$ is the deviatoric part of Reynolds stress tensor, $\{\mathcal{T}^{(n)}\}_{n=1}^{10}$ is the tensorial basis formed from strain-rate tensor $\mathbf{S} = \frac{1}{2}\left(\nabla\mathbf{U} + (\nabla\mathbf{U})^T\right)$ and rotation tensor $\boldsymbol{\Omega} = \frac{1}{2}\left(\nabla\mathbf{U} - (\nabla\mathbf{U})^T\right)$. In particular, $\mathcal{T}^{(1)} = \mathbf{S}$ and thus $G^{(1)}\mathcal{T}^{(1)}$ represents the linear part (with respective to $\mathbf{S}$) of the anisotropy tensor $\mathbf{b}$.

Inspired by this general form of algebraic Reynolds stress models, we separate the anisotropy stress tensor $\boldsymbol{b}$ into linear and nonlinear parts:

$$\mathbf{b} = \nu_t^L\mathbf{S} + \mathbf{b}^{\perp} \tag{4.3}$$

where linear part $\nu_t^L \mathbf{S}$ (co-axial with $\mathbf{S}$ corresponds to the term $G^{(1)}\mathbf{S}$ in Eq. (4.2)), and $\mathbf{b}^\perp$ represents the sum of the non-linear terms. It is similar to the tensorial expansion of anisotropy stress tensor $\mathbf{b}$ in Eq. (4.2), while all the nonlinear terms are lumped into $\mathbf{b}^\perp$. The linear term can be treated implicitly to enhance the conditioning when solving the RANS equations. More details of numerical procedure for solving the RANS equations are detailed in 4.5. As discussed above in Sec. 4.1.4, this decomposition is more than just a numerical implicit treatment but has clear physical justifications.

In order to compute the two terms in Eq. (4.3) from a given Reynolds stress and strain tensor, we introduce an optimal eddy viscosity that minimizes the discrepancy between the anisotropy Reynolds stress tensor and its linear part, i.e.,

$$\nu_t^L = \arg\min_{\nu_t} \|\mathbf{b} - \nu_t \mathbf{S}\| \tag{4.4}$$

where $\|\cdot\|$ denotes the Frobenius norm of a matrix, e.g., $\|\mathbf{S}\| = \sqrt{S_{ij}S_{ij}}$. Based on this definition, the optimal eddy viscosity ν_t^L can be computed by projecting the anisotropy stress tensor on the strain rate tensor:

$$\nu_t^L = 2\frac{\mathbf{b} : \mathbf{S}}{\|\mathbf{S}\|\|\mathbf{S}\|} \tag{4.5}$$

where $\mathbf{b} : \mathbf{S} = b_{ij}S_{ij}$ denotes tensor double dot product.

The nonlinear term $\mathbf{b}^\perp$ in Eq. (4.3) could be important even for simple shear flows in the near wall region, since the linear term incorrectly predicts isotropic normal stresses. For more complex flows, e.g., swirling and impinging, neglecting this nonlinear term can cause the model to miss important flow physics completely. In this work, we use machine learning techniques and existing DNS database to build regression functions that predict the optimal eddy viscosity ν_t^L and the nonlinear part $\mathbf{b}^\perp$ of the anisotropy Reynolds stress tensor. In machine learning terminology the flows used to build regression functions are referred to as the *training flows*, and the flow to be predicted is referred to as the *test flow*. The detailed workflow of building these regression functions via machine learning is presented in 4.5.

4.2.2 Construction of mean flow features as inputs of machine learning

The construction of input features is among the most critical considerations when using machine learning for physical problems. First, the choice of input and output variables must be physically motivated and justified to ensure that the function learned from the data has physical meaning. Second, the variables must be normalized properly to ensure extrapolative capabilities of the learned function. Finally, the learned function should ideally be objective with function form invariances under transformations of the coordinate system and the reference frame. Our perspective is that almost all principles that are observed in traditional turbulence modeling [see, e.g., 37] should be equally respected in data-driven

turbulence modeling. These three considerations in the present framework are presented below.

Physical consideration in the choice of mean flow feature variables

The general form of nonlinear turbulent-viscosity model in Eq. 4.2 assumes a universal functional mapping from the strain-rate tensor $\mathbf{S}$ and the rotation-rate tensor $\mathbf{\Omega}$ to the Reynolds stress $\boldsymbol{\tau}$:

$$\boldsymbol{\tau} = \boldsymbol{\tau}(\mathbf{S}, \mathbf{\Omega}) \tag{4.6}$$

We note that there are at least two aspects of missing physics in this assumption. First, the turbulence is also influenced by pressure gradient. For example, turbulence would be suppressed under strong favorable pressure gradient [37]. On the other hand, the general form in Eq. 4.6 assumes equilibrium turbulence, i.e., the turbulence production balances dissipation everywhere in the field. With such an assumption, the Reynolds stress at location $\boldsymbol{x}$ only depends on the *local* mean velocity $\mathbf{U}(\boldsymbol{x})$, or more precisely, its gradient $\nabla\mathbf{U}(\boldsymbol{x})$. However, the convection and diffusion of turbulence exist in many real applications, indicating strong non-equilibrium effects and making this single-point-based turbulent constitutive law invalid [38]. To account for the missing physics outlined above, we also include the pressure gradient ∇p and the TKE gradient ∇k in the input, leading to a more general functional mapping from mean flow quantities to the Reynolds stress:

$$\boldsymbol{\tau} = g(\mathbf{S}, \mathbf{\Omega}, \nabla p, \nabla k) \tag{4.7}$$

where the set of varialbles $\mathcal{Q} = \{\mathbf{S}, \mathbf{\Omega}, \nabla p, \nabla k\}$ are chosen as input features, which are summarized in Table 4.1.

In addition to the tensor set $\mathcal{Q}$, three other features as presented in Table 4.2 are chosen from Ref. [8] to further supplement the mean flow features, all of which have clear physical interpretations. First, at the near wall region the viscous effect becomes more important and the local Reynolds number reduces to $O(1)$. Therefore, a low Reynolds number turbulence model is needed for the viscous sublayer in the traditional turbulence modeling. In this work, q_1 is an important indicator to inform the wall distance to the machine-learning-assisted turbulence models, leading to a data-driven low-Re model as a counterpart of the traditional low-Re models. Second, features q_2 and q_3 carry information on the length-scale and time-scale of the turbulence, serving as supplements of the mean flow tensors in the set $\mathcal{Q}$.

Normalization of input features

To ensure non-dimensionality of the raw inputs, the normalization scheme proposed by Ling and Templeton [34] is adopted. All raw features are normalized by *local* quantities, as

Table 4.1: Non-dimensional raw mean flow variables used to construct the invariant basis. The normalized feature $\widehat{\alpha}$ is obtained by normalizing the corresponding raw input α with normalization factor β according to $\widehat{\alpha} = \alpha/(|\alpha| + |\beta|)$. Notations are as follows: $\mathbf{U}$ is mean velocity vector, k is turbulence kinetic energy (TKE), ρ is fluid density, ε is the turbulence dissipation rate, $\mathbf{S}$ is the strain-rate tensor, $\mathbf{\Omega}$ is the rotation-rate tensor, $|\cdot|$ denotes vector norm, $\|\cdot\|$ indicates matrix norm.

Normalized raw input $\widehat{\alpha}$	description	raw input α	normalization factor β
$\widehat{\mathbf{S}}$	strain-rate tensor	$\mathbf{S}$	$\dfrac{\varepsilon}{k}$
$\widehat{\mathbf{\Omega}}$	rotation-rate tensor	$\mathbf{\Omega}$	$\|\mathbf{\Omega}\|$
$\widehat{\nabla p}$	pressure gradient	∇p	$\rho\|D\mathbf{U}/Dt\|$
$\widehat{\nabla k}$	TKE gradient	∇k	$\dfrac{\varepsilon}{\sqrt{k}}$

Table 4.2: Supplementary mean flow features used as inputs in the regression. The normalized feature q_β is obtained by normalizing the corresponding raw features value $\widehat{q}_\beta$ with normalization factor q^*_β according to $q_\beta = \widehat{q}_\beta/(|\widehat{q}_\beta| + |q^*_\beta|)$ except for $\beta = 1$. Notations are as follows: U_i is mean velocity, k is turbulent kinetic energy (TKE), ε is the turbulence dissipation rate, $\mathbf{S}$ is the strain rate tensor, d is the distance to the wall. $\|\cdot\|$ indicates matrix norms.

feature (q_β)	description	raw feature ($\widehat{q}_\beta$)	normalization factor (q^*_β)
q_1	wall-distance based Reynolds number	$\min\left(\dfrac{\sqrt{k}d}{50\nu}, 2\right)$	not applicable[(a)]
q_2	turbulence intensity	k	$\nu\|\mathbf{S}\|$
q_3	ratio of turbulent time-scale to mean strain time-scale	$\dfrac{k}{\varepsilon}$	$\dfrac{1}{\|\mathbf{S}\|}$

Note: (a) Normalization is not necessary as the Reynolds number is non-dimensional.

is preferred in the practice of traditional turbulence modeling [37]. In CFD simulations these would be quantities based on the same grid point as the raw feature variables. The normalization factors for all the raw input variables are listed in Table 4.1. Specifically, each element α in the raw input set $\mathcal{Q}$ is normalized by a corresponding normalization factor β based on the following scheme:

$$\widehat{\alpha} = \frac{\alpha}{|\alpha| + |\beta|}, \tag{4.8}$$

which ensures that the normalized variable $\widehat{\alpha}$ falls within the range $[-1, 1]$. Note that such a normalization scheme is slightly different from that frequently used in physics and engineering, which would take either the form $\widehat{\alpha} = \alpha/|\alpha|$ or $\widehat{\alpha} = \alpha/|\beta|$ instead. The choice in Eq. 4.8 is justified by the practice of machine learning where the inputs are usually normalized to the range $[-1, 1]$ or $[0, 1]$. This helps avoid clustering of training data along certain directions within the input feature space and improves the convergence rate in the training process.

Invariance considerations in the choice of input features

As summarized in Table 4.1, the raw variables for the mean flow consist of a finite tensorial set $\mathcal{Q} = \{\mathbf{S}, \mathbf{\Omega}, \nabla p, \nabla k\}$ with four elements, where ∇p and ∇k are transformed to anti-symmetric tensors as detailed in Eq. (4.14). As in traditional turbulence modeling, it is equally desirable in data-driven turbulence modeling that the trained functional form $g : (\mathbf{S}, \mathbf{\Omega}, \nabla p, \nabla k) \mapsto \boldsymbol{\tau}$ should be objective. That is, the function form of g should be invariant under rotational and reflectional transformations of the coordinate system or Galilean transformation (i.e., translation by a constant velocity) of reference frame. The function form invariances associated with the rotation and reflection of the coordinate system and the Galilean transformation of the reference frame are referred to as *coordinate rotational invariance*, *coordinate reflectional invariance*, and *Galilean invariance*, respectively. Our formulation has rotational invariance and Galilean invariance but not reflectional invariance. However, the lack of reflectional invariance can be remedied by data augmentation, which is a standard procedure for pre-processing training data in machine learning. The three invariance properties of the present formulation and strategies to remedy the lack of reflectional invariance are examined below.

Invariance properties If the constructed function relation $\boldsymbol{\tau} = g(\mathbf{S}, \mathbf{\Omega}, \nabla p, \nabla k)$ is to be valid under arbitrary rotations of the coordinate system, the following relation should be satisfied [39]:

$$\mathbf{Q}\boldsymbol{\tau}\mathbf{Q}^T = g(\mathbf{Q}\mathbf{S}\mathbf{Q}^T, \mathbf{Q}\mathbf{\Omega}\mathbf{Q}^T, \mathbf{Q}\nabla p, \mathbf{Q}\nabla k) \tag{4.9}$$

for any rotation matrix $\mathbf{Q}$, where $\mathbf{Q}$ is an orthogonal matrix (i.e., $\mathbf{Q}^T = \mathbf{Q}^{-1}$) with determinant equaling to 1. The rotational invariance of the learned function g as stated in Eq. (4.9) can be guaranteed by choosing invariant inputs and outputs in the learning process, specifically, by choosing the *minimal integrity bases* for the set $\{\mathbf{S}, \mathbf{\Omega}, \nabla p, \nabla k\}$ and the

invariants of $\boldsymbol{\tau}$ as inputs and outputs, respectively. A minimal integrity bases is the minimal set of invariants that can represent all the polynomial invariants associated with a tensorial set under the designated transformation (rotation here). The *Hilbert basis theorem* states that a minimal integrity basis for a finite tensorial set has finite number of invariants [40]. Specifically for the set $\mathcal{Q} = \{\mathbf{S}, \mathbf{\Omega}, \nabla p, \nabla k\}$ of second-order tensors considered here[1], the minimal integrity basis consists of all the traces of the independent matrix products that can be formed from the tensors according to Cayley-Hamilton theorem [41], which amount to 47 invariants (see Table 4.4 for details). Note that choosing the invariant tensorial bases, rather than the raw tensorial variables, as inputs and output of the machine learning only guarantees the rotational invariance of the learned function. Galilean invariance needs to be independently achieved by ensuring each raw variable and their normalization factors to be Galilean invariant, which is discussed below.

Galilean invariance states that the laws of motion are the same in all frames with constant velocities, which is an important prerequisite of any turbulence model [37] and should be equally satisfied by traditional or data-driven models. Therefore, the velocity *per se* is usually not a valid term in a model as mentioned in [37], because the velocity is not Galilean invariant. In contrast, the velocity *gradient* $\nabla \mathbf{U}$ and thus its symmetric and anti-symmetric parts ($\mathbf{S}$ and $\mathbf{\Omega}$, respectively) are all Galilean invariant and thus are valid terms to be included in a turbulence model. Similarly, the gradient of pressure ∇p and the gradient of kinetic energy ∇k are both Galilean invariant (and does not depends on the choice of reference pressure). Finally, it is straightforward to show that a term involving only Galilean invariant quantities is also Galilean invariant. Based on the general principles outlined above, the machine learning inputs and outputs in the present formulation are all Galilean invariant. Specifically, the raw inputs in Table 4.1 are all Galilean invariants since they only involves spatial gradients, e.g., $\mathbf{S}$ and $\mathbf{\Omega}$. The raw inputs in Table 4.2 are all Galilean invariant since they only involves scalar quantities that are Galilean invariant. The normalization factors in both tables are all Galilean invariant as well. In particular, it can be shown that the normalization factor $\rho|D\mathbf{U}/Dt|$ is Galilean invariant, and the details are presented in 4.5.

Finally, the invariants associated with the anti-symmetric tensors are only rotational invariants but not reflection invariants. The main motivation for using these anti-symmetric tensors is that the machine learning outputs include the quantification of 3-D rotation of eigenvectors of stress tensors that does not have reflection invariance. The details are discussed as follow:

- *Motivation of the chosen outputs:* Our framework aims to augment traditional turbulence models, instead of completely replacing them, by using machine learning to predict the discrepancies between RANS modeled and true Reynolds stresses. Such discrepancies are parameterized by the scaling of the Reynolds stress tensor along its eigenvectors and the rotation of the eigenvectors. Although the scaling factors are all

[1]Vectors such as ∇p and ∇k can be first transformed to the corresponding anti-symmetric tensors based on Eq. (4.14) in 4.5

scalars and invariants under coordinates system transformation, the rotation of the eigenvectors does not have reflection invariance. For instance, the sign of the angle between any two vectors depends on the defined direction of the rotation axis.

- *Reasons of including inputs without reflection invariance:* If we only introduce machine learning inputs with both rotational and reflection invariance, the similar inputs would correspond to totally different outputs of tensor rotations (potentially with flipped signs) in the training dataset. Therefore, the functional form $\mathcal{F} : \boldsymbol{q} \mapsto \Delta\boldsymbol{\tau}$ would be a noisy function with spikes due to the sign flipping learned from the training data. Such a machine learning model would be nonphysical with diminishing predictive capabilities.

- *Consistency between outputs and inputs:* We adopted the invariants of pseudo-tensors constructed from the TKE gradient and the pressure gradient as a part of machine learning inputs. Similar to the invariants corresponds to a 3-D rotation, the invariants of these pseudo-tensors are also rotational invariants but not reflection invariants. Therefore, the sign flipping of the machine learning outputs can be distinguished by different corresponding inputs and the unphysical noisy behavior of the functional form $\mathcal{F}$ would not exist. The main purpose here is to ensure a consistent framework to predict tensor rotations, which is critical in augmenting the traditional tensor models.

Indeed, it would be more elegant to include only objective inputs and output in the machine learning, as the coordinate transformation invariance is a basic requirement in turbulence modeling. Further work is needed in identifying such formulations.It should be noted that the different conventions of coordinate system handedness would lead to different machine learning inputs even with identical training and test flows. An alternative albeit rather inefficient approach is to use training flows under both right-handed and left-handed coordinates system to augment the training data, and it has been demonstrated in [6] that the invariance can be learned by such data augmentation.

Data augmentation for achieving invariance in machine learning In machine learning the lack of invariance property in the model to be learned from data can be remedied by data augmentation [6]. Specifically, the training dataset is augmented by duplicating them in various transformed coordinate systems before performing the training. That way, the training process would be able to "see" the same data in almost all transformed coordinates. Consequently, only the functional forms that are valid (i.e., invariant) in all coordinate systems are learned, and any coordinate- or frame-dependent functional forms would be rejected in the training. However, depending on the invariance to be achieved through data augmentation (as detailed below), this procedure could significantly increase the amount of data and the computational costs for the training and prediction.

- In order to achieve reflectional invariance through data augmentation, one only needs

to duplicate the data in the reflected coordinate system, which is a moderate two-fold increase in the amount of data.

- On the other hand, achieving three-dimensional rotational invariance required duplicating the training data in 1000 coordinate systems, as is shown by Ling et al. [6]. Therefore, using data augmentation to learn rotational invariance would significantly increase the computational cost and memory consumption, both of which are important considerations in machine learning.
- Finally, it is not straightforward to remedy the lack of Galilean invariance with data augmentation, since the translation velocity of the reference frame is unbounded (i.e., it can be any value from $-\infty$ to ∞).

In summary, a total of 50 normalized, invariant mean flow field variables (collectively denoted as $\mathbf{q}$) are constructed and used as input features for the machine learning. While such a high-dimensional feature space may appear daunting even for the most experienced experts in turbulence modeling, it is not particularly challenging in the context of modern data science, as many machine learning techniques routinely handle feature spaces of thousands of dimensions or even higher [42].

4.2.3 Representation of Reynolds stress discrepancy as outputs of machine learning

Similar to choosing the inputs of machine learning, we represent the Reynolds stress discrepancies with rotationally invariant variables as the outputs of the machine learning. Following [43, 8], we formulate the Reynolds stress discrepancies as six physically interpretable components (i.e., magnitude, shape, and orientation) based on eigen-decomposition of anisotropic Reynolds stress tensor.

$$\boldsymbol{\tau} = 2k\left(\frac{1}{3}\mathbf{I} + \mathbf{b}\right) = 2k\left(\frac{1}{3}\mathbf{I} + \mathbf{V}\Lambda\mathbf{V}^T\right) \tag{4.10}$$

where k is the turbulent kinetic energy, which indicates the magnitude of $\boldsymbol{\tau}$; $\mathbf{I}$ is the second order identity tensor; $\mathbf{b}$ is the deviatoric part of $\boldsymbol{\tau}$; $\mathbf{V} = [\mathbf{v}_1, \mathbf{v}_2, \mathbf{v}_3]$ and $\Lambda = \mathrm{diag}[\lambda_1, \lambda_2, \lambda_3]$ with $\lambda_1 + \lambda_2 + \lambda_3 = 0$ are the orthonormal eigenvectors and eigenvalues of $\mathbf{b}$, respectively, indicating its shape and orientation.

The eigenvalues λ_1, λ_2, and λ_3 are transformed to Barycentric coordinates C_1, C_2, and C_3 and then to Cartesian coordinates ξ and η as in Refs. [8] and [44].

To ensure that the predicted TKE is non-negative, Wang et al. [8] introduce the TKE discrepancy $\Delta \log k$ as the logarithm of the ratio of the target TKE (k^*) to the RANS-simulated TKE (k^{RANS}), i.e.,

$$\Delta \log k \equiv \log \frac{k^*}{k^{\mathrm{RANS}}}. \tag{4.11}$$

This is what we adopted in the current work. Finally, the unit quaternions are used to represent the transformation from the RANS eigenvectors $\mathbf{V}^{\mathrm{RANS}}$ to the target eigenvectors $\mathbf{V}^*$ [45]:

$$\mathbf{h} = \left[\cos\frac{\theta}{2}, n_1 \sin\frac{\theta}{2}, n_2 \sin\frac{\theta}{2}, n_3 \sin\frac{\theta}{2}\right]^T \tag{4.12}$$

where $\mathbf{n} \equiv [n_1, n_2, n_3]$ denotes a unique axis of unit vector, and θ represents the rotation angle such that $\mathbf{V}^*$ can be obtained via rotating $\mathbf{V}$ by θ about the axis $\mathbf{n}$. This unit quaternions representation is rotational invariant and thus is preferred than the Euler angles representation using by Wang et al. [8]. Note that the current representation of the rotation of Reynolds stress eigenvectors is not reflectional invariant, i.e., the magnitude of each component of the unit quaternion $\mathbf{h}$ remains the same under the reflection of frame while the sign of each component is not. As mentioned in Section 4.2.2, the reflection invariance of the trained machine learning model can be achieved by augmenting the training database with reflected coordinates system.

In summary, the discrepancies ($\Delta \log k$, $\Delta\xi$, $\Delta\eta$, h_1, h_2, h_3), collectively denoted as $\Delta\boldsymbol{\tau}$, are used as the machine learning outputs to represent the discrepancies between the target Reynolds stress and the RANS modeled Reynolds stress. Here h_1, h_2 and h_3 denote the first three components of the unit quaternion $\mathbf{h}$. All six variables are invariant under rotations of the coordinate system. In this work, random forest regression is adopted to represent the dependence of these Reynolds stress discrepancies on a large number of scalar inputs as identified in Section 4.2.2. Therefore, the mean velocity and other quantities (e.g., k and ε) from RANS simulations are used to calculate the machine learning inputs, since it can be expected that the Reynolds stress discrepancies are related to the specific choice of the RANS model. Because of the dependence of the trained machine learning function on the RANS model, we recommend the usage of the same RANS model for both the training flows and the flow to be predicted.

4.2.4 Choice of machine learning algorithm and parameters

In this work, random forest regression [46] as implemented in R [47] is used to build functional mappings from the inputs (mean flow features $\mathbf{q}$) to the responses as identified in Sec. 4.2.1. Random forest regression is a tree-based ensemble learning method, i.e., the regression outputs are the mean prediction of individual decision trees. In this work, the regression outputs are directly used as explicit values and the detailed formulation of the random forest has no influence upon the convergence of solving mean velocity via RANS equations. An advantage of the random forest regression is that it can provide importance scores for inputs after training, which can be further used to assist the modelers to improve the existing RANS models [8]. Random forest has robust performances with only a small set of tuning parameters, which is in contrast to the commonly used neural networks [48]. The number of max features is set as 7, i.e., $(1 + \log_2 n)$, where $n = 50$ is the number of input

features in this work, based on the recommendation in Ref. [46]. The number of trees is set as 300. This number is chosen by observing the out-of-bag (OOB) error to avoid possible overfitting on the training sets. We have observed the OOB error with different numbers of trees and this error is not sensitive based on our current setting of the number of trees. An example of using random forest regression to assist RANS modeling is publicly available at https://github.com/xiaoh/turbulence-modeling-PIML.

The computational costs of machine learning consist of the training cost and the prediction cost. The training cost depends on the amount of the training data, and it should be noted that the training procedure can be done offline and the trained machine learning model can be applied to the prediction of other flows as well. In this work, only one training flow is used at one time and the computational cost of the training procedure is less than the corresponding standard RANS simulation. The computational cost of the prediction procedure is usually negligible compared with the cost of a typical RANS simulation. Therefore, with the trained machine-learning-assisted model, the computational cost for the baseline RANS simulation in combination with the prediction of a given flow is still much lower than large-eddy simulations (LES) of the same flow.

4.3 Numerical results

Two canonical flows, the flow in a square duct and the flow over periodic hills, are investigated to evaluate the performance of the proposed method. The flow in a square duct is featured by stress-induced secondary flow, and the flow over periodic hills is featured by the massive separation. These two features are challenging for traditional RANS modeling [49, 50]. In this work, we first perform a *propagation* test by using DNS Reynolds stress. The purpose of the *propagation* of DNS Reynolds stress to the mean velocity is to demonstrate the merit of physics-based implicit treatment. In the *a posteriori* test, the Reynolds stress field is modeled by machine learning techniques and propagated to mean velocities to evaluate the predicative capability of the proposed machine-learning-assisted turbulence modeling framework with physics-based implicit treatment.

4.3.1 Case setup

A schematic of the flow in a square duct is presented in Fig. 4.1 to show the physical domain and the computational domain. A two-dimensional simulation is performed, since the flow is fully developed along the stream-wise direction. In addition, the computational domain only covers a quarter of the cross-section as shown in Fig. 4.1b due to the symmetry of the flow along y and z directions. All lengths are normalized by the height of the computational domain $h = 0.5D$, where D is the height of the duct. The Reynolds number Re is based on the height of the computational domain h and bulk velocity U_b. Launder-Gibson Reynolds

stress transport model [51] is used for the RANS simulations of both the training flow and the test flow. DNS data at $Re = 2200$ and 3500 are obtained from Pinelli et al. [52]. Experimental data at $Re = 125000$ is obtained from Gessner and Emery [53].

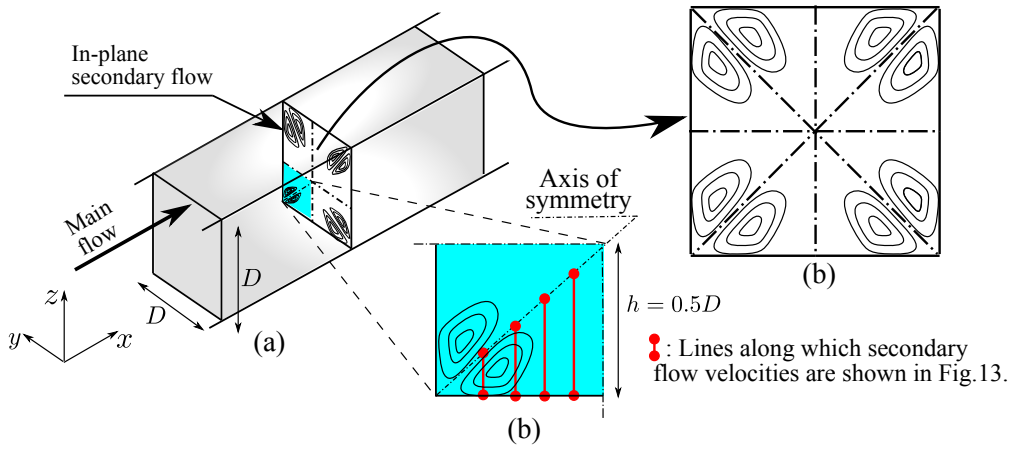

Figure 4.1: Computational domain for the flow in a square duct. The x coordinate represents the streamwise direction. Secondary flows induced by Reynolds stress imbalance exist in the y–z plane. Panel (b) shows that the computational domain covers a quarter of the cross-section of the physical domain. This is due to the symmetry of the mean flow in both y and z directions as shown in panel (c).

Another training-prediction case with the flows over periodic hills is shown in Fig. 4.2. The test flow is the flow over periodic hills at $Re = 5600$ [50]. The geometry of the computational domain of the test flow is shown in Fig. 4.2. The training flow has a steeper hill profile indicated by the dashed line in Fig. 4.2 . The Reynolds number Re is based on the crest height H and the bulk velocity U_b at the crest. Periodic boundary conditions are applied in the streamwise (x) direction, and non-slip boundary conditions are applied at the walls. The baseline RANS simulations used Launder-Sharma k-ε model [54].

All the RANS simulations are performed in an open-source CFD platform OpenFOAM, using a built-in steady-state incompressible flow solver `simpleFoam` [55], in which the SIMPLE algorithm [56] is used. In the RANS simulations, the y^+ of the first cell center is kept less than 1 and thus no wall model is applied.

The training-prediction cases in the *a posteriori* test are summarized in Table. 4.3. The case 1 is investigated to show the Reynolds number extrapolation for which DNS data is available to examine the prediction performance in details. The case 2 is chosen to demonstrate the capability of the proposed framework at higher Reynolds number where only experimental data is available. The case 3 is studied to demonstrate the prediction performance for which the training flow and the test flow have different geometry configurations.

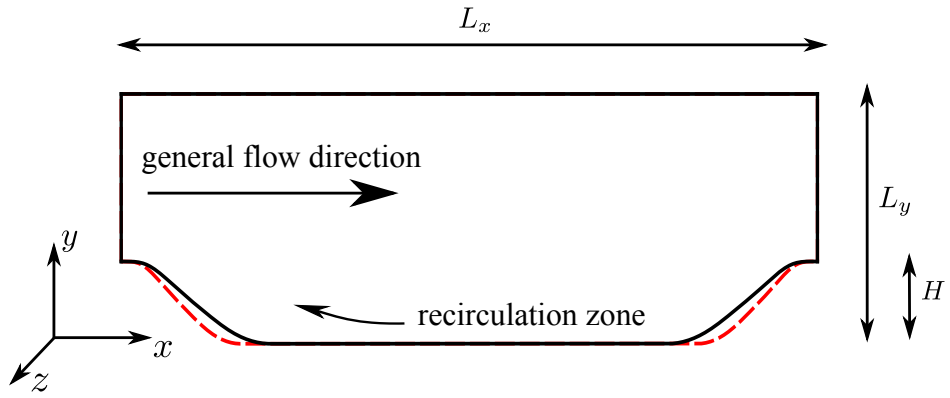

Figure 4.2: Computational domain for the flow over periodic hills. The solid line indicates the configuration of the test flow, and the dashed line indicates the configuration of the training flow. The hill width of the training flow is 0.8 of the hill width of the test flow. The x, y and z coordinates are aligned with streamwise, wall-normal, and spanwise, respectively.

Table 4.3: The training-prediction scenarios in *a posteriori* test.

Cases	Training set	Test set
1	Flow in a square duct at $Re = 2200$ [52]	Flow in a square duct at $Re = 3500$ [52]
2	Flow in a square duct at $Re = 2200$ [52]	Flow in a square duct at $Re = 125000$ [53]
3	Flow over periodic hills at $Re = 5600$ (steeper hill profile)	Flow over periodic hills at $Re = 5600$ [50]

4.3.2 Propagation of DNS Reynolds stresses

In this test, the DNS Reynolds stresses are used to illustrate the merit of physics-based implicit treatment. Three types of turbulence models are compared: Reynolds stress models (RSM) with explicit treatment, linear eddy viscosity models and RSM with implicit treatment. The *explicit treatment* means that the modeled Reynolds stress is directly substituted into the RANS equations to solve for mean velocity as an explicit term. The dependence of Reynolds stress upon the strain rate can still be taken into account by updating the modeling of Reynolds stress during the time stepping (or iterations for steady problems). However, merely updating the Reynolds stress explicitly based on the solved mean velocity would not improve the conditioning of the RANS equations, which has been further discussed in [22]. The *implicit treatment* means that the modeled Reynolds stress implicitly depends on the strain rate through an optimized eddy viscosity. Such an implicit treatment would improve the conditioning of RANS equations since the optimized eddy viscosity has impact upon the coefficient matrix of the discretized RANS equations and thus influences the condition number.

In the test of Reynolds stress models, the unclosed term in momentum equation is substituted with DNS Reynolds stress. In the test of linear eddy viscosity models, the eddy viscosity term is substituted with the optimal eddy viscosity ν_t^L obtained from DNS data. Specifically, the optimal eddy viscosity ν_t^L is computed by minimizing the discrepancy between the linear eddy viscosity model and the DNS Reynolds stress data, i.e., $\nu_t^L = \arg\min_{\nu_t} ||\mathbf{b}^{DNS} - \nu_t \mathbf{S}^{DNS}||$. Compared with the eddy viscosity models, the RSM with implicit treatment further takes into account the non-linear part of Reynolds stress, i.e., $\boldsymbol{\tau} = \nu_t^L \mathbf{S} + (\boldsymbol{\tau}^{DNS} - \nu_t^L \mathbf{S}^{DNS})$. Two canonical flows, the flow in a square duct and the flow over periodic hills, are studied to compare the performance of these three types of models. This propagation test demonstrates that the linear eddy viscosity model is unreliable within the region where the misalignment between Reynolds stress tensor and strain-rate tensor is not negligible. In the test with explicit treatment of Reynolds stress, the DNS data is employed to demonstrate the problem of the machine learning modeling approach under an ideal scenario. Specifically, this ideal scenario means that the initial mean velocity field is already the same as DNS mean velocity and the modeled Reynolds stress is also the same as DNS Reynolds stress. Such an ideal scenario represents an absolute performance ceiling of any machine-learning-assisted modeling approach with the explicit treatment. Under this ideal scenario, we demonstrate that a small error in DNS Reynolds stress (e.g., sampling error) can lead to a relatively large error in the solved mean velocity field. If the modeling of Reynolds stress is further updated by evaluating the data-driven model with the solved mean velocity, the errors in the modeled Reynolds stress and the solved mean velocity would be further amplified as has been demonstrated for the plane channel flow in [22]. Therefore, an implicit treatment is needed to improve the conditioning of the machine-learning-assisted RANS modeling.

Flow in a square duct

The secondary velocity U_z based on DNS Reynolds stress is shown in Fig. 4.3 by using Reynolds stress models with explicit and implicit treatments. It can be seen in Fig. 4.3a that the solved secondary velocity U_z agrees well with DNS data within most regions, except along the symmetry plane $y/h = 1$. Such good agreement of solved secondary velocity indicates that the Reynolds stress models lead to well-conditioned discretized momentum equations for the flow in a square duct. Similar quality of secondary velocity can be obtained by using RSM with implicit treatment. On the other hand, the linear eddy viscosity models cannot predict the secondary flow due to the limitation in representing the normal stress imbalance, the results of which are omitted here for simplicity.

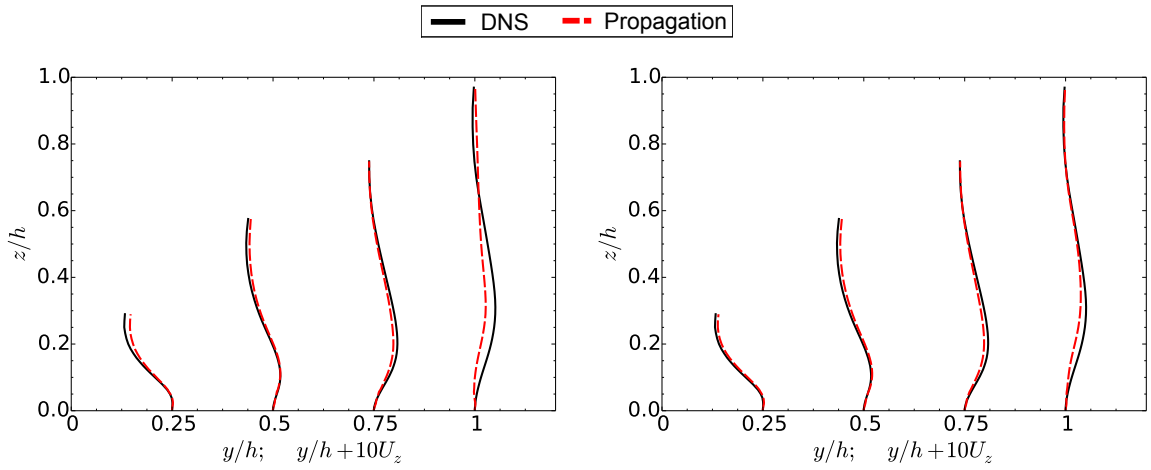

(a) RSM with explicit treatment

(b) RSM with implicit treatment

Figure 4.3: The comparison of secondary flow velocity U_z by using (a) Reynolds stress model with explicit treatment and (b) Reynolds stress model with implicit treatment. The results by using linear eddy viscosity model capture no secondary flow and are thus omitted here.

Flow over periodic hills

Although the Reynolds stress models with explicit treatment perform well for the flow in a square duct, they are potentially unreliable since it can lead to pronounced errors in mean velocity even for the turbulent channel flows [19, 22]. In this work, we demonstrate the issue of Reynolds stress models with explicit treatment for the flow with massive separation. Figure 4.4a shows that the solved mean velocity field does not agree with the DNS data by using Reynolds stress model with explicit treatment for the flow over periodic hills. It should be noted that the velocity shown in Fig. 4.4a is obtained by using DNS Reynolds stress, and not the modeled Reynolds stress. Therefore, the unsatisfactory results in Fig. 4.4a indicates

the best possible performance of machine-learning-assisted turbulence modeling via directly substituting the modeled Reynolds stress into RANS equations.

Better results of mean velocity can be achieved as shown in Fig. 4.4b by using linear eddy viscosity models than Reynolds stress models with explicit treatment. However, noticeable differences can still be observed between the solved mean velocity and the DNS data. The main reason is that the misalignment between the Reynolds stress tensor and the strain rate tensor is neglected by using linear eddy viscosity models. Such misalignment can be quantified by the rotation matrix $\mathbf{R}$ from the eigenvectors of Reynolds stress tensor to the ones of strain rate tensor. Figure 4.5 presents an indicator of misalignment calculated based on the deviation of the rotation matrix $\mathbf{R}$ from the identity matrix $\mathbf{R_I}$.

Unlike the eddy viscosity models, the RSM with implicit treatment take into account the difference between the linear part of Reynolds stress $\boldsymbol{\tau}^L$ and the true Reynolds stress $\boldsymbol{\tau}$. The purpose is to address the misalignment of eigenvectors between Reynolds stress tensor and strain rate tensor. It can be seen in Fig. 4.4c that the solved mean velocity field has a much better agreement with DNS data, compared with the results by using the Reynolds stress models with explicit treatment in Fig. 4.4a and the eddy viscosity models in Fig. 4.4b. By using DNS Reynolds stress data as the ideal machine-learning-modeled stress, the propagation test results in Fig. 4.4 demonstrate the superiority of RSM with implicit treatment in achieving predicative capability of mean velocity field.

4.3.3 A posteriori test

Flow in a square duct

In the first case, the random forest is trained by using the flow in a square duct at Reynolds number $Re = 2200$. The flow at Reynolds number $Re = 3500$ is used as the test flow. It should be noted that the DNS data at $Re = 3500$ is only used to evaluate the machine learning prediction, and not being used for training the machine learning model. The baseline RANS indicates the results obtained from standard RANS simulations. The machine learning results are denoted by ML in the legends of figures for simplicity. It can be seen in Fig. 4.6 that the baseline RANS simulated normal components of Reynolds stress qualitatively captures the imbalance between $\boldsymbol{\tau}_{yy}$ and $\boldsymbol{\tau}_{zz}$. However, the simulated normal stress imbalance is noticeably greater than the DNS data, especially around the near wall region. Such greater normal stress imbalance between $\boldsymbol{\tau}_{yy}$ and $\boldsymbol{\tau}_{zz}$ explains the stronger secondary flow of baseline RANS simulation. Compared with the baseline RANS simulated stress components, the machine-learning-predicted normal stress components $\boldsymbol{\tau}_{yy}$ and $\boldsymbol{\tau}_{zz}$ demonstrate a much better agreement with the DNS data in Fig. 4.6.

The linear part of Reynolds stress $\boldsymbol{\tau}^L$ is predicted and presented in Fig. 4.7. It can be seen that the normal components $\boldsymbol{\tau}^L_{yy}$ and $\boldsymbol{\tau}^L_{zz}$ of linear part of Reynolds stress are similar to each other. The main reason is that the linear part of Reynolds stress is obtained by projecting

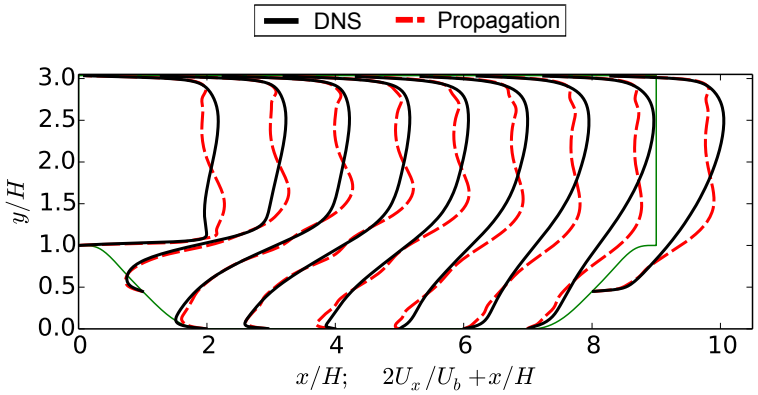

(a) RSM with explicit treatment

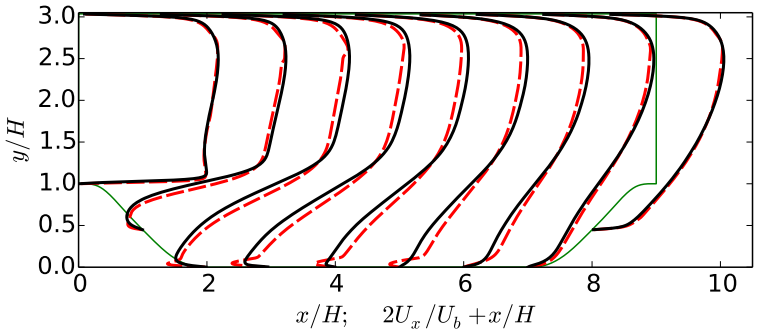

(b) Eddy viscosity model

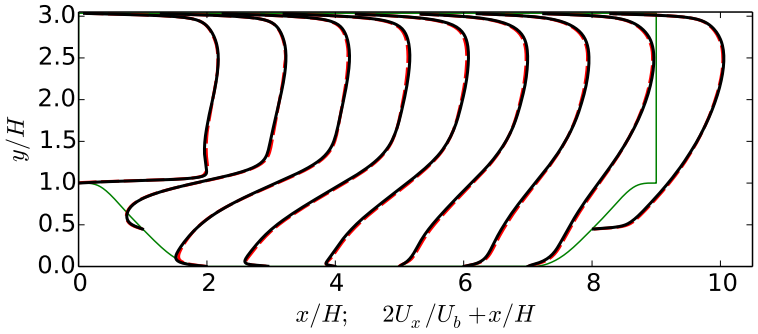

(c) RSM with implicit treatment

Figure 4.4: The solved mean velocity field for the flow over periodic hills at $Re = 5600$ by using (a) Reynolds stress model with explicit treatment, (b) eddy viscosity model and (c) Reynolds stress model with implicit treatment. The DNS data is utilized as the modeled term to represent the best possible performance among the respective class of models.

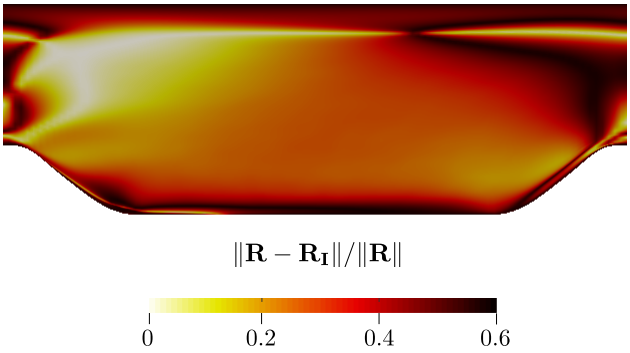

Figure 4.5: An indicator of the deficiency of linear eddy viscosity model due to the misalignment of eigenvectors between Reynolds stress tensor and strain rate tensor.

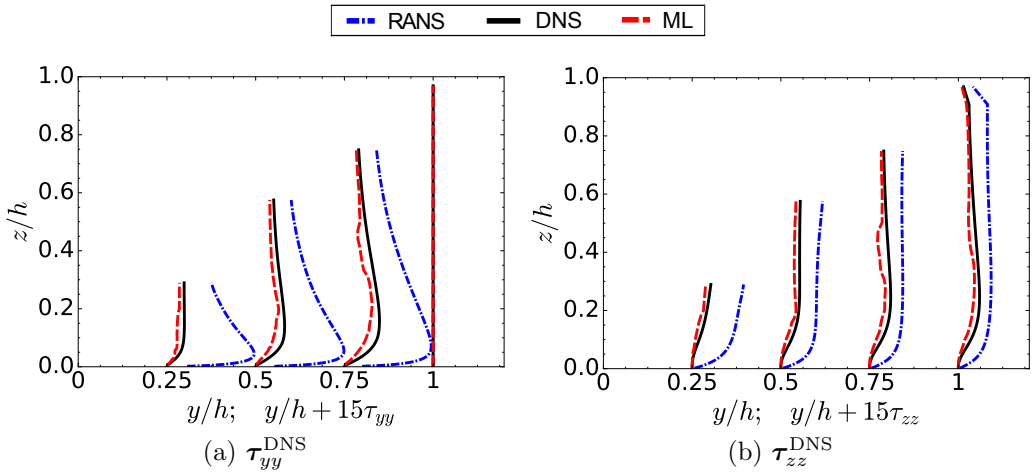

(a) $\boldsymbol{\tau}_{yy}^{\mathrm{DNS}}$ (b) $\boldsymbol{\tau}_{zz}^{\mathrm{DNS}}$

Figure 4.6: The prediction of **DNS Reynolds stress components** of the flow in a square duct at Reynolds number $Re = 3500$, including (a) $\boldsymbol{\tau}_{yy}^{\mathrm{DNS}}$ and (b) $\boldsymbol{\tau}_{zz}^{\mathrm{DNS}}$ at $y/h = 0.25, 0.5, 0.75$ and 1. The training flow is at Reynolds number $Re = 2200$.

the DNS Reynolds stress onto the strain rate tensor and neglecting the nonlinear parts of the DNS Reynolds stress. Therefore, the linear part of Reynolds stress follows the eddy viscosity assumption and thus would have no normal stress imbalance. It can be seen in Fig. 4.7 that the machine-learning-predicted linear part of Reynolds stress shows a good agreement with the linear part of Reynolds stress obtained from DNS data.

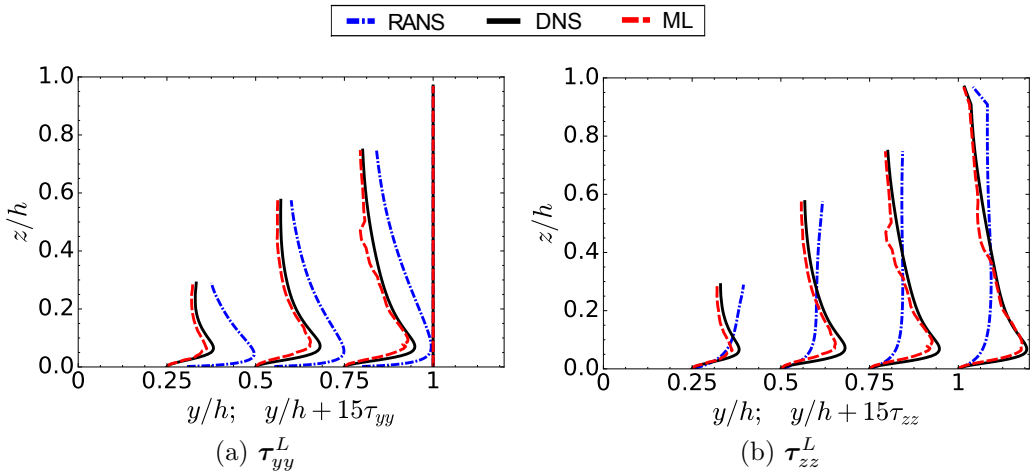

(a) $\boldsymbol{\tau}^L_{yy}$ (b) $\boldsymbol{\tau}^L_{zz}$

Figure 4.7: The prediction of **linear part of Reynolds stress components** of the flow in a square duct at Reynolds number $Re = 3500$, including (a) $\boldsymbol{\tau}^L_{yy}$ and (b) $\boldsymbol{\tau}^L_{zz}$ at $y/h = 0.25, 0.5, 0.75$ and 1. The training flow is at Reynolds number $Re = 2200$.

With both the satisfactory machine learning prediction of Reynolds stress in Fig. 4.6 and its linear part in Fig. 4.7, it can be expected that the nonlinear term $\boldsymbol{\tau}^\perp = \boldsymbol{\tau} - \boldsymbol{\tau}^L$ would have a good agreement with the nonlinear part of the DNS Reynolds stress. The comparison of the non-linear Reynolds stress term is presented in Fig. 4.8. It can be seen that the noticeable negative stress $\boldsymbol{\tau}^\perp_{yy}$ can be seen near both the side wall and the bottom wall of the duct based on the DNS data. However, the negative non-linear stress is over-predicted near the side wall and under-predicted near the bottom wall for the RANS simulation. Compared with the RANS results, the machine learning prediction in Fig. 4.8 demonstrates a much better agreement with the pattern of DNS data.

In addition to the nonlinear part of Reynolds stress, the optimal eddy viscosity ν_t^L is also needed in solving for the mean velocity. It can be seen in Fig. 4.9 that the eddy viscosity is close to zero in the near-wall region and increases towards to the diagonal of the duct. The machine-learning-predicted eddy viscosity agrees well with the DNS eddy viscosity at most regions in Fig. 4.9. It should be noted that a few noticeable differences can be observed between the machine-learning-predicted eddy viscosity and the DNS data, e.g., along $y/h = 0.75$ and $y/h = 1$. However, the velocity gradient is relatively small within these regions and thus such difference has little influence in solving for mean velocity field as demonstrated in Fig. 4.11.

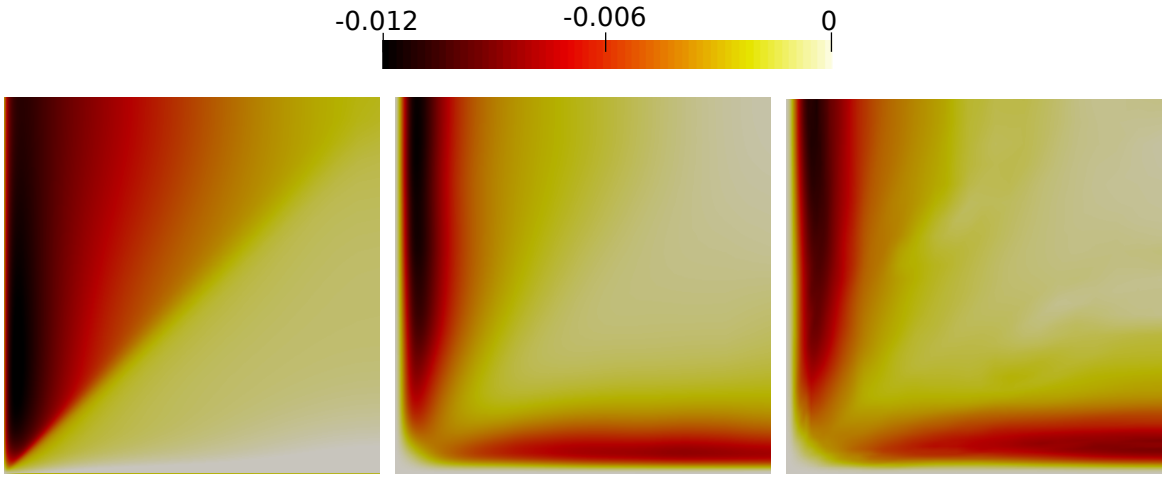

(a) RANS (b) DNS (c) Machine Learning

Figure 4.8: The non-linear part of Reynolds stress $\boldsymbol{\tau}_{yy}^{\perp}$ in a square duct at Reynolds number $Re = 3500$, including (a) RANS simulated results, (b) DNS data and (c) prediction of RSM with implicit treatment. The training flow is at Reynolds number $Re = 2200$. The color of the contour denotes the value of the stress component, and the light color here indicates small magnitude.

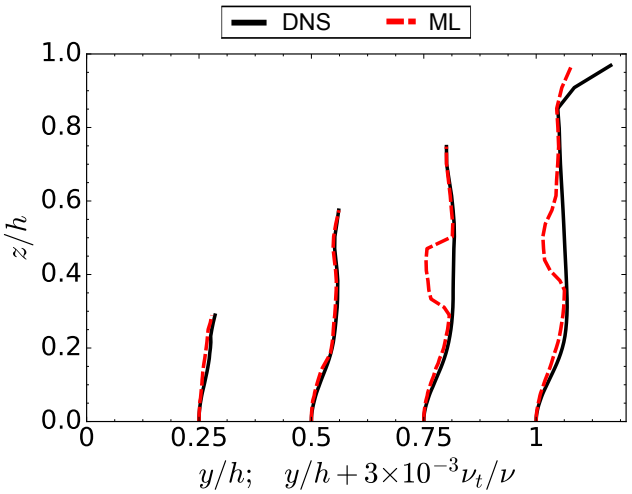

Figure 4.9: The optimal eddy viscosity ν_t^L of the flow in a square duct at Reynolds number $Re = 3500$ at $y/h = 0.25, 0.5, 0.75$ and 1. The training flow is at Reynolds number $Re = 2200$.

By substituting the machine-learning-predicted eddy viscosity and nonlinear part of Reynolds stress into RANS equations, the mean velocity field is solved and presented in Fig. 4.10. It can be seen in Fig. 4.10a that the RANS simulated secondary flow penetrates too much toward the left bottom region (corner region between the perpendicular walls). The machine learning predicted secondary flow in Fig. 4.10c demonstrates a better agreement with DNS data in this corner region. In addition, the shape and location of the secondary vortex are better predicted by our machine learning framework as shown in Fig. 4.10c.

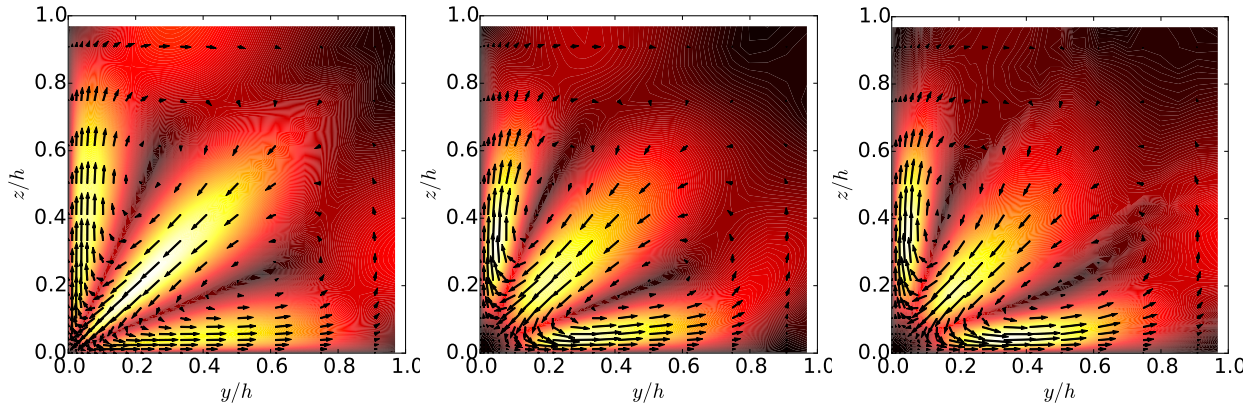

(a) RANS (b) DNS (c) Machine Learning

Figure 4.10: The secondary flow fields in a square duct at Reynolds number $Re = 3500$, including (a) RANS simulated results, (b) DNS data and (c) prediction of RSM with implicit treatment. The training flow is at Reynolds number $Re = 2200$. The color of the contour denotes the magnitude of the secondary flow. The light color here indicates large magnitude.

Four profiles of secondary flow are presented in Fig. 4.11 for a more quantitative comparison of the secondary flow prediction. It can be seen that the baseline RANS simulated mean velocity field overestimates the magnitude of the secondary flow, especially around the corner region. On the other hand, the mean velocity based on the RSM with implicit treatment shows a much better agreement with the DNS data. However, it should be noted that the test flow is at Reynolds number $Re = 3500$, close to that of the training flow ($Re = 2200$). Therefore, the satisfactory predictive capability as demonstrated in Fig. 4.11 does not necessarily guarantee similar performance at a higher Reynolds number.

To further demonstrate the general applicability of the proposed framework, we employ the same training flow and investigate another test flow, i.e., the flow in a square duct at a much higher Reynolds number $Re = 1.25 \times 10^5$. We evaluate the prediction performance of the proposed framework by using the experimental data of this test flow along the vertical axis of symmetry and along the diagonal of the square duct [53]. The inverse flow near the bottom of the axis of symmetry is not captured by the baseline RANS simulation in Fig. 4.12a. This inverse flow in experimental data indicates that there is a small vortex with an opposite rotation direction around this region, in addition to the main vortex of the secondary flow.

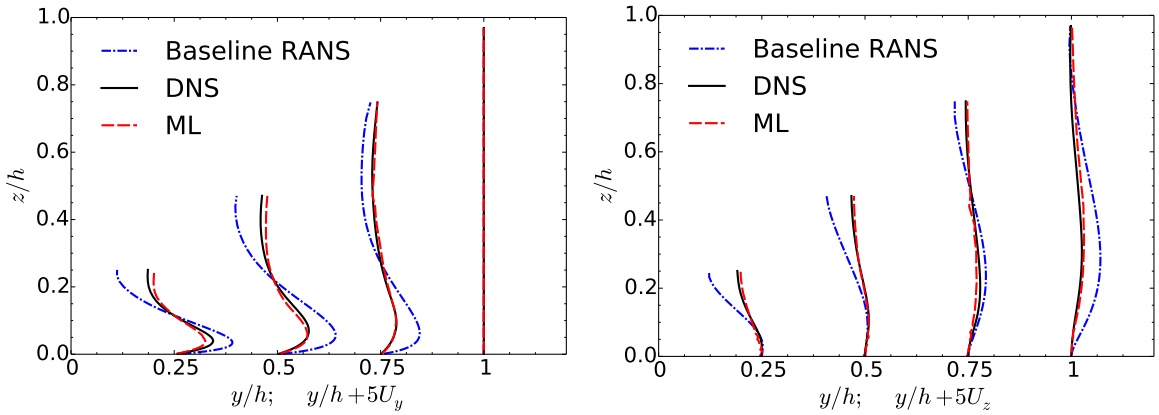

(a) U_y (b) U_z

Figure 4.11: The secondary flow in a square duct at Reynolds number $Re = 3500$ predicted by RSM with implicit treatment at $y/h = 0.25, 0.5, 0.75$ and 1. The training flow is at Reynolds number $Re = 2200$.

The failure of predicting the inverse flow in Fig. 4.12a means that this small vortex is completely missing in the baseline RANS simulation results. In contrast, this missing flow characteristic is successfully captured by the machine-learning prediction. It should be noted that this flow characteristic is not observed in the training flow at a much lower Reynolds number $Re = 2200$. One reason for the successful prediction of the small inverse flow is the formulation of our data-driven augmentation framework, i.e., it is the Reynolds stress discrepancies but not the whole Reynolds stress that is predicted by the machine learning framework. Specifically, Wu et al. [13] calibrated the Reynolds stress discrepancies at a lower Reynold number $Re \approx 5000$ and applied the calibrated discrepancies to correct the RANS simulation at a higher Reynolds number $Re = 125000$. They reported that the trend of inverse flows could be re-produced even though the Reynolds stress discrepancies are calibrated at a much lower Reynolds number. Therefore, the trend of small inverse flows can be predicted even if the machine learning model is overfitted for the training database at a lower Reynolds number. However, it should be noted that the inverse flow was noticeably underestimated in the work by Wu et al. [13], and the machine learning prediction in this work achieves better agreement with the experimental data. Therefore, the successful prediction of the inverse flow in Fig. 4.12a is a strong evidence that the machine-learning-assisted turbulence modeling indeed has the potential of revealing the physics within the data, rather than simply interpolating with the available data.

As shown in Fig. 4.12b, the secondary flow U_z is over-predicted by baseline RANS simulation along the diagonal of the duct. On the contrary, the mean velocity U_z obtained by the proposed framework underestimates the magnitude of the secondary flow in Fig. 4.12b. Although there is no significant improvement of results along the diagonal, it should be noted that the machine learning prediction in Fig. 4.12b indeed corrects the baseline RANS

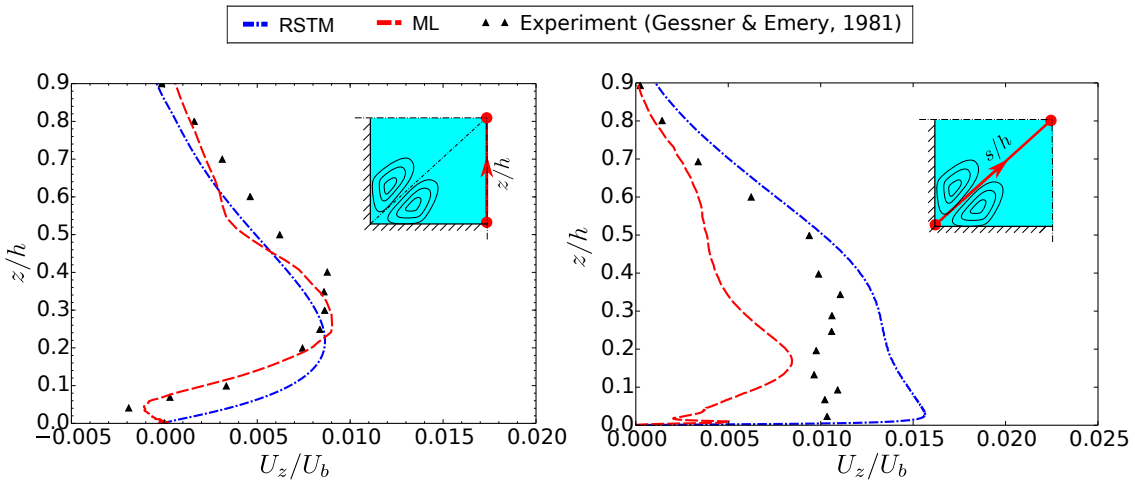

(a) Along vertical axis of symmetry (b) Along diagonal

Figure 4.12: The comparison of predicted secondary velocity U_z at Reynolds number $Re = 1.25 \times 10^5$ with experimental data [53] (denoted as ▲). Comparisons are shown (a) along the vertical axis of symmetry and (b) along the diagonal of the duct. The training flow is at Reynolds number $Re = 2200$.

simulated results towards the right direction.

Flow over periodic hills

In the cases investigated above, the training flow and the test flow share the same geometry configuration and only differ in Reynolds numbers. In order to demonstrate the capability of the proposed framework for the flows with different geometries, we further study the flows over periodic hills with different shape of hill profiles. The training flow is the flow over periodic hill at $Re = 5600$ [50], and the test flow is also at $Re = 5600$ but has a steeper hill profile as described in Sec. 4.3.1. It can be seen in Fig. 4.13a that the RANS simulation under-predicts the shear stress τ_{xy} at downstream of the hill crest. Such under-prediction of shear stress is mainly due to the under-prediction of TKE of RANS simulation as shown in Fig. 4.13b. Compared with the results of RANS simulation, the machine learning prediction shows a better agreement with DNS data for both the shear stress and the TKE. Although such improvement is limited at $x/H = 1$, it still better predicts the magnitude of Reynolds stress than RANS simulation as shown in Fig. 4.13. The improvement of the machine learning prediction at further downstream becomes more prominent.

The linear part of Reynolds stress $\boldsymbol{\tau}^L$ is also predicted. It can be seen in Fig. 4.14 that the linear part of Reynolds stress is similar to the DNS Reynolds stress in Fig. 4.13 except for several regions, e.g., the region around the bottom wall and the region within upper channel around $y/H = 2.5$. Therefore, the nonlinear part of the DNS Reynolds stress is expected

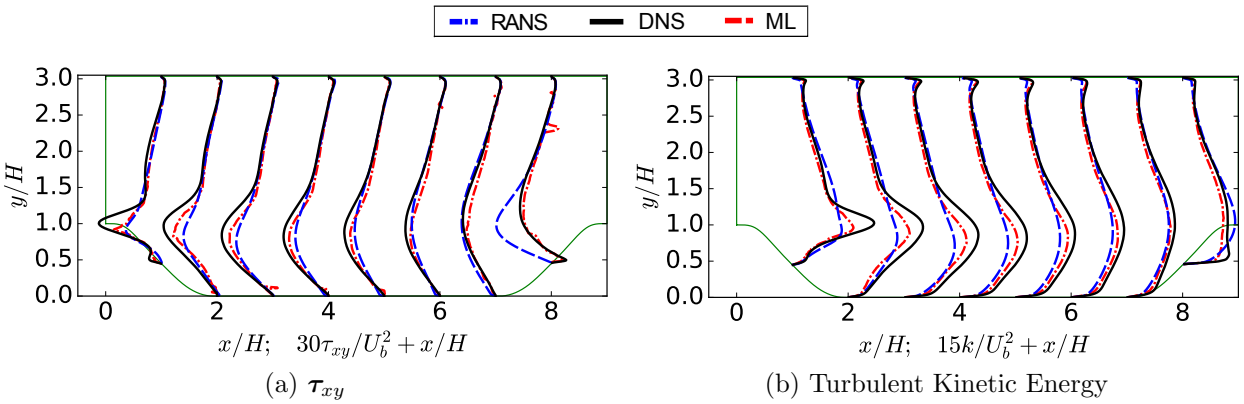

(a) $\boldsymbol{\tau}_{xy}$ (b) Turbulent Kinetic Energy

Figure 4.13: The prediction of (a) shear stress component $\boldsymbol{\tau}_{xy}$ of the **Reynolds stress** tensor and (b) the turbulent kinetic energy (TKE) at $x/H = 1, 2, \ldots, 8$. The test flow is the flow over periodic hill at $Re = 5600$. The training flow is at the same Reynolds number but has a steeper hill profile as shown in Fig. 4.2.

to be less dominant in most regions for the flow over periodic hills. The prediction of the proposed framework shows a good agreement with the linear part of Reynolds stress obtained from DNS data. Similar to the prediction of Reynolds stress, the machine learning prediction of the linear part of Reynolds stress shows less noticeable improvement at $x/H = 1$.

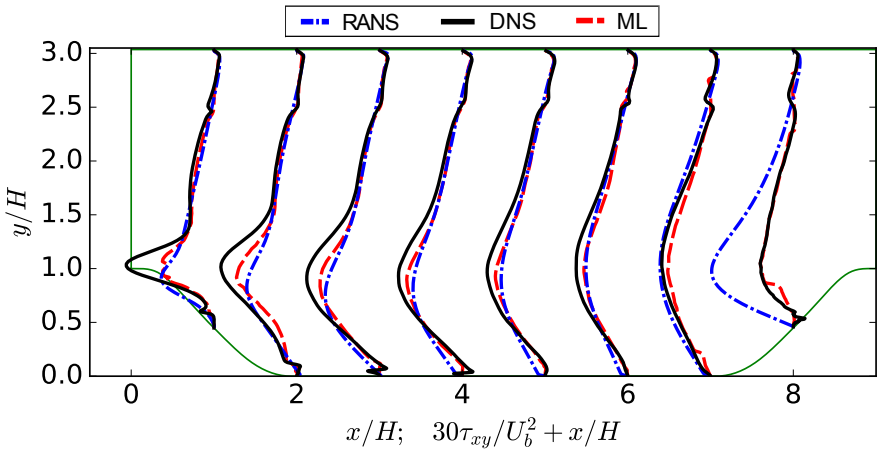

Figure 4.14: The prediction of shear stress component $\boldsymbol{\tau}_{xy}$ of **linear part of Reynolds stress** at $x/H = 1, 2, ..., 8$. The test flow is the flow over periodic hill at $Re = 5600$. The training flow is at the same Reynolds number but has a steeper hill profile as shown in Fig. 4.2.

In addition to the improvement shown in the prediction of DNS Reynolds stress and its linear part, the prediction of optimal eddy viscosity also demonstrates improvement as shown in Fig. 4.15. It can be seen in Fig. 4.15 that the machine-learning-predicted eddy viscosity has a good agreement with the DNS eddy viscosity, except for a few regions where the

DNS eddy viscosity changes rapidly. Such deterioration in the performance of machine learning prediction is expected, since the functions with such behavior pose more difficulties in machine learning. However, the peak value of eddy viscosity at these regions is usually not important for solving for mean velocity. It is because the strain rate tensor is close to zero in these regions, corresponding to the peak value of eddy viscosity.

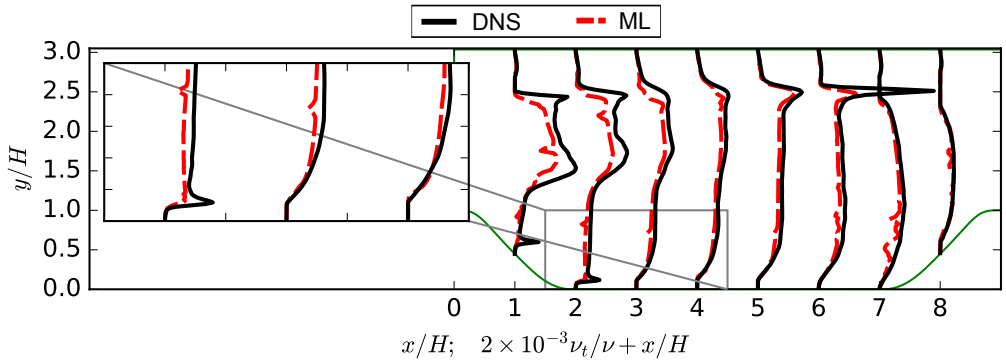

Figure 4.15: The machine-learning-predicted optimal eddy viscosity at $x/H = 1, 2, ..., 8$. The test flow is the flow over periodic hill at $Re = 5600$. The training flow is at the same Reynolds number but has a steeper hill profile as shown in Fig. 4.2.

The comparison of mean velocity field in Fig. 4.16 shows that the mean velocity obtained by the proposed framework has a better agreement with the DNS data. Specifically, the reverse flow extends to $x/H = 4$ in DNS data, denoting the size of the separation bubble downstream of the hill crest. The RANS simulation results indicate that the reverse flow ends approximately around $x/H = 3$, which significantly underestimate the size of the separation bubble. The magnitude of velocity at upper channel region is also under-predicted by the RANS simulation results from $x/H = 1$ to $x/H = 5$. Compared with the RANS simulation results, the machine learning prediction provides more accurate reverse flow, especially from $x/H = 1$ to $x/H = 3$. Although over-prediction of reverse flow can be observed in the prediction of the proposed framework from $x/H = 3$ to $x/H = 4$, the separation region is still better predicted than RANS simulation results. In addition, the proposed framework achieves a much better prediction of mean velocity than the RANS simulation results at the upper channel region.

4.4 Discussion: Potentials and Limitations of Data-Driven Turbulence Models

The present work addresses the ill-conditioning issue in a class of data-driven turbulence models that aim to model the Reynolds stresses with machine learning. Therefore, it is helpful to provide a broad yet brief view of data-driven turbulence modeling, which has

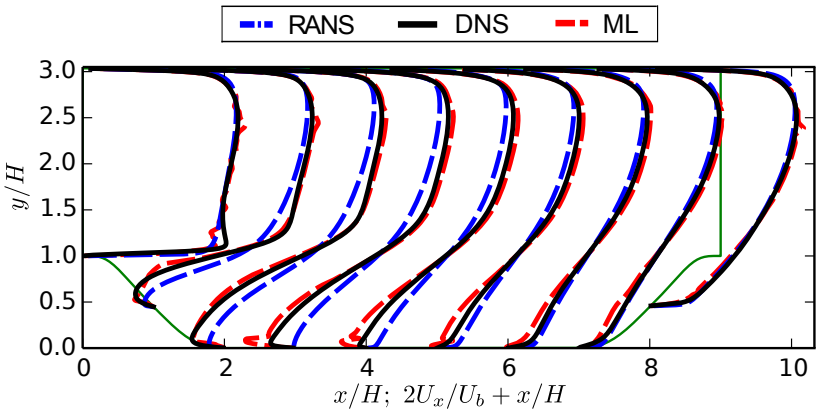

Figure 4.16: The stream-wise velocity by RSM with implicit treatment at $x/H = 1, 2, ..., 8$. The test flow is the flow over periodic hill at $Re = 5600$. The training flow is at the same Reynolds number but has a steeper hill profile as shown in Fig. 4.2.

emerged as a promising yet controversial subject in the past few years. A more comprehensive state-of-the-art overview will be presented in a forthcoming review article [57]. Summarized briefly, three distinctly different approaches to data-driven turbulence modeling have been pursued by different groups:

(i) Weatheritt and Sandsberg [16, 17] used Gene Expression Programming to develop algebraic Reynolds stress models based on symbolic regression.

(ii) Duraisamy and co-workers [15, 58] used machine learning to predict discrepancies in the source terms in the turbulence transport equations for existing models (e.g., S–A model, k–ω model, or Reynolds stress models).

(iii) Wang et al. [8] and Ling et al. [7] used machine learning to directly predict the Reynolds stresses or their discrepancies compared to the truth.

A widely accepted yardstick used in the turbulence modeling community to assess turbulence models is that an ideal model should

- demonstrate robust predictive capabilities in a wide range of flows without flow-specific tuning
- be interpretable, ideally in explicit analytical forms

which are referred to as *universality* and *interpretability* requirements, respectively, hereafter. The three approaches above are discussed in light of each of these requirements.

4.4.1 Universality of turbulence models

In terms of the universality requirement, existing traditional turbulence models are still far from satisfactory. To our knowledge, most existing data-driven turbulence models, including the one presented in our work, are still in their infancy and have shown only limited predictive capabilities, typically in flows that are close to the training flows. That is, the training and predictions flows belong to the same class of flows (e.g., massively separated flows) but with variations of flow configurations such as geometry or Reynolds number. However, their predictive capabilities may improve as more experiences are accumulated and the methodologies are refined later on. The machine learning inputs and outputs in this work are all rotational invariants and the Galilean invariants. Therefore, the trained model is objective under any rotation transformation and Galilean transformation. Although several inputs and outputs are not reflection invariants, the associated extrapolation capability can be achieved by reflecting the coordinates system to augment the training data. However, the extrapolation capability still depends on the diversity of the training data. By using the training database of flows with a specific characteristic, e.g., recirculation or stress-induced secondary flow, we have demonstrated that an unknown flow with similar characteristics can be predicted. We envision that the extrapolation capability can be extended to more complex flows with more diversified and systematically generated high fidelity simulation database. In addition, the extrapolation capability for more complex flows can also be achieved by automatically classifying the flow field into different regions and making prediction for each region accordingly. On the other hand, if we take a less ambitious perspective and consider the data-driven models (particularly the second and third approaches) as augmentation of traditional models through a data-driven, flow-specific correction, then their universality become less critical. For example, in a practical applications, a data-driven model could turn itself off when the part of the flow is not present in the training dataset and is too "far" from the flows in the data. That is, the data-driven model can revert back to the traditional, baseline turbulence model that is used. To this end, Wu et al. [59] has demonstrated a fully automatic, statistically rigorous way of measuring the "distance" between two flows (or any parts thereof) based on the mean flow fields obtained from RANS simulations. With such a distance metric, it is possible to ensure that a machine-learning-augmented model is at least better than or the same as the corresponding baseline model it utilizes.

4.4.2 Interpretability of turbulence models

Regarding the interpretability requirement, it may appear that the symbolic regression approach specifically aims to find Reynolds stress models that are in analytical forms, while the second and third approaches based on machine learning (neural networks and random forests) do not produce models in analytical forms and are not amenable for interpretation. However, the delineation between these approaches may not be as clear as it first appears. First, although the analytical Reynolds stress model learned from one class of flows [16] may

rather simple and indeed has similar complexity to existing advanced turbulence models, this may not necessarily be true for other flows. For example, a model learned from a diverse datasets from different flows may be an analytical expression with the number of terms too large for human comprehension, which may still be difficult to interpret despite its analytical nature. Second, if one is willing to compromise the predictive performance, a neural network based model (used in the second and third approaches) may be regularized (e.g., by using Ridge and LASSO [60]) to yield simple architecture and thus becomes more interpretable. Finally, both neural networks and random forest can provide the importance of input mean flow features (see, e.g. the discussions in [8]), which may help traditional model developers incorporate additional variables to existing models. Efforts along such a direction are underway [61]. Therefore, the fundamental differences among the three approaches above lie in the classical trade-off between predicative capability and interpretability in models [60], and not in the specific forms of the chosen model (e.g., symbolic regression v.s. neural networks or random forests).

Ultimately, both universality and interpretability requirements are intimately related to the fundamental question in turbulence modeling: does there exist a universal turbulent constitutive relation? Generations of researchers have labored for many decades on dozens of turbulence models, yet none of them achieved predictive generality, which seems to indicate that the answer is "no". If so, then flow-specific tuning and fudge factors would be inevitable if good predictive performances are desirable. The machine learning based turbulence models can be considered automatic, flow-specific tuning schemes based on the flow regime to be predicted and the flow regimes that present in the training database.

4.5 Conclusion

While earlier works demonstrated the capabilities of machine learning in predicting improved Reynolds stresses, obtaining improved mean velocity field remains a challenge of machine-learning-assisted turbulence modeling. The main reason is the sensitivity of mean velocity with regard to the errors in the prediction of Reynolds stress. In this work we propose a physics-based implicit treatment to model Reynolds stress by using machine learning techniques. Specifically, the optimal eddy viscosity and the nonlinear part of Reynolds stress are both predicted. In the propagation test, the DNS Reynolds stress is used in solving for mean velocity to illustrate the ideal scenario of machine-learning-assisted turbulence modeling approaches. The propagation test with DNS Reynolds stress shows that satisfactory mean velocity can be achieved by the Reynold stress models with implicit treatment. In the *a posteriori* test, three training-prediction cases are investigated to demonstrate the predictive capability of the proposed framework. In the first and second cases, a machine learning model is trained on the flow in a square duct at Reynolds number $Re = 2200$, and the flows in a square duct at Reynolds numbers $Re = 3500$ and $Re = 1.25 \times 10^5$ are predicted. In the third case, machine learning model is trained on the flow over periodic hills at Reynolds

number $Re = 5600$, and the flow with a steeper hill profile is predicted. The satisfactory prediction performance of mean velocity field demonstrates the predictive capability of the proposed machine-learning-assisted framework. Specifically, machine-learning-trained model successfully predicts the mean flow pattern in the second case that is not even shown in the training flow. It provides a strong evidence that machine-learning-assisted turbulence modeling can reveal flow physics from the existing data, instead of merely fitting on the existing data. With the capability in predicting the mean velocity field, the proposed physics-based implicit treatment leads to a practical machine-learning-assisted turbulence modeling framework in real applications where mean velocity field and other quantities of interests need to be predicted.

Acknowledgment

The authors would like to thank the two reviewers for their constructive and valuable comments, which helped improving the quality and clarity of this manuscript. In particular, one of the reviewers pointed out the lack of Galilean invariance in two of the normalization constants in our manuscript, which we fixed during the revision. We gratefully acknowledge the reviewer's constructive comments.

Bibliography

[1] J.-X. Wang, J.-L. Wu, J. Ling, G. Iaccarino, H. Xiao, Towards a complete framework of physics-informed machine learning for predictive turbulence modeling, Tech. rep., Proceedings of Summer Research Program, Center of Turbulence Research, Stanford University, Stanford, CA, USA (2016).

[2] T. Craft, B. Launder, K. Suga, Development and application of a cubic eddy-viscosity model of turbulence, International Journal of Heat and Fluid Flow 17 (1996) 108–115.

[3] T. Oliver, R. Moser, Uncertainty quantification for RANS turbulence model predictions, in: APS Division of Fluid Dynamics Meeting Abstracts, Vol. 1, 2009.

[4] B. Tracey, K. Duraisamy, J. Alonso, Application of supervised learning to quantify uncertainties in turbulence and combustion modeling, in: 51st AIAA Aerospace Sciences Meeting, 2013, Dallas, TX, paper 2013-0259.

[5] B. Tracey, K. Duraisamy, J. J. Alonso, A machine learning strategy to assist turbulence

model development, in: 53rd AIAA Aerospace Sciences Meeting, 2015, Kissimmee, FL, paper 2015-1287.

[6] J. Ling, R. Jones, J. Templeton, Machine learning strategies for systems with invariance properties, Journal of Computational Physics 318 (2016) 22–35.

[7] J. Ling, A. Kurzawski, J. Templeton, Reynolds averaged turbulence modelling using deep neural networks with embedded invariance, Journal of Fluid Mechanics 807 (2016) 155–166.

[8] J.-X. Wang, J.-L. Wu, H. Xiao, Physics-informed machine learning approach for reconstructing Reynolds stress modeling discrepancies based on DNS data, Physical Review Fluids 2 (3) (2017) 034603.

[9] E. Dow, Q. Wang, Quantification of structural uncertainties in the k–ω turbulence model, in: 52nd AIAA/ASME/ASCE/AHS/ASC Structures, Structural Dynamics and Materials Conference, 2011, Denver, CO, paper 2011-1762.

[10] E. J. Parish, K. Duraisamy, A paradigm for data-driven predictive modeling using field inversion and machine learning, Journal of Computational Physics 305 (2016) 758–774.

[11] A. P. Singh, K. Duraisamy, Using field inversion to quantify functional errors in turbulence closures, Physics of Fluids 28 (2016) 045110.

[12] H. Xiao, J.-L. Wu, J.-X. Wang, R. Sun, C. J. Roy, Quantifying and reducing model-form uncertainties in Reynolds-averaged Navier-Stokes equations: A data-driven, physics-based, Bayesian approach, Journal of Computational Physics 324 (2015) 115–136.

[13] J.-L. Wu, J.-X. Wang, H. Xiao, A Bayesian calibration–prediction method for reducing model-form uncertainties with application in RANS simulations, Flow, Turbulence and Combustion 97 (2016) 761–786.

[14] K. Duraisamy, Z. J. Zhang, A. P. Singh, New approaches in turbulence and transition modeling using data-driven techniques, in: 53rd AIAA Aerospace Sciences Meeting, 2015, Kissimmee, FL, paper 2015-1284.

[15] A. P. Singh, S. Medida, K. Duraisamy, Machine-learning-augmented predictive modeling of turbulent separated flows over airfoils, AIAA Journal 55 (7) (2017) 2215–2227.

[16] J. Weatheritt, R. Sandberg, A novel evolutionary algorithm applied to algebraic modifications of the RANS stress–strain relationship, Journal of Computational Physics 325 (2016) 22–37.

[17] J. Weatheritt, R. Sandberg, The development of algebraic stress models using a novel evolutionary algorithm, International Journal of Heat and Fluid Flow.

[18] S. V. Poroseva, J. D. Colmenares F, S. M. Murman, On the accuracy of RANS simulations with DNS data, Physics of Fluids 28 (11) (2016) 115102.

[19] R. L. Thompson, L. E. B. Sampaio, F. A. de Bragança Alves, L. Thais, G. Mompean, A methodology to evaluate statistical errors in DNS data of plane channel flows, Computers & Fluids 130 (2016) 1–7.

[20] S. Poroseva, Personal communication (2018).

[21] M. Lee, R. D. Moser, Direct numerical simulation of turbulent channel flow up to $Re_\tau \approx 5200$, Journal of Fluid Mechanics 774 (2015) 395–415.

[22] J.-L. Wu, R. Sun, H. Xiao, Q. Wang, RANS equations with Reynolds stress closure can be ill-conditioned, submitted, arXiv preprint arXiv:1803.05581. (2018).

[23] B. Basara, S. Jakirlic, A new hybrid turbulence modelling strategy for industrial CFD, International Journal for Numerical Methods in Fluids 42 (1) (2003) 89–116.

[24] R. Maduta, S. Jakirlic, Improved RANS computations of flow over the 25°-slant-angle Ahmed body, SAE International Journal of Passenger Cars-Mechanical Systems 10 (2017-01-1523) (2017) 649–661.

[25] M. Ma, J. Lu, G. Tryggvason, Using statistical learning to close two-fluid multiphase flow equations for a simple bubbly system, Physics of Fluids 27 (9) (2015) 092101.

[26] M. Ma, J. Lu, G. Tryggvason, Using statistical learning to close two-fluid multiphase flow equations for bubbly flows in vertical channels, International Journal of Multiphase Flow 85 (2016) 336–347.

[27] A. N. Marques, Q. Wang, Y. Marzouk, Data-driven integral boundary-layer modeling for airfoil performance prediction in laminar regime, AIAA Journal (2017) 1–15.

[28] M. Gamahara, Y. Hattori, Searching for turbulence models by artificial neural network, Physical Review Fluids 2 (5) (2017) 054604.

[29] T. Durieux, Exploring the use of artificial neural network based subgrid scale models in a variational multiscale formulation, Master's thesis, Delft University of Technology (2015).

[30] A. Vollant, G. Balarac, G. Geraci, C. Corre, Optimal estimator and artificial neural network as efficient tools for the subgrid-scale scalar flux modeling, Tech. rep., Proceedings of Summer Research Program, Center of Turbulence Research, Stanford University, Stanford, CA, USA (2014).

[31] A. Vollant, G. Balarac, C. Corre, Subgrid-scale scalar flux modelling based on optimal estimation theory and machine-learning procedures, Journal of Turbulence (2017) 1–25.

[32] R. N. King, P. E. Hamlington, W. J. Dahm, Autonomic closure for turbulence simulations, Physical Review E 93 (3) (2016) 031301.

[33] R. Maulik, O. San, A neural network approach for the blind deconvolution of turbulent flows, Journal of Fluid Mechanics 831 (2017) 151–181.

[34] J. Ling, J. Templeton, Evaluation of machine learning algorithms for prediction of regions of high Reynolds-averaged Navier–Stokes uncertainty, Physics of Fluids (1994-present) 27 (8) (2015) 085103.

[35] D. Apsley, M. Leschziner, Investigation of advanced turbulence models for the flow in a generic wing-body junction, Flow, Turbulence and Combustion 67 (1) (2001) 25–55.

[36] S. Pope, A more general effective-viscosity hypothesis, Journal of Fluid Mechanics 72 (2) (1975) 331–340.

[37] P. R. Spalart, Philosophies and fallacies in turbulence modeling, Progress in Aerospace Sciences 74 (2015) 1–15.

[38] J. Lumley, Toward a turbulent constitutive relation, Journal of Fluid Mechanics 41 (02) (1970) 413–434.

[39] C. G. Speziale, S. Sarkar, T. B. Gatski, Modelling the pressure–strain correlation of turbulence: an invariant dynamical systems approach, Journal of Fluid Mechanics 227 (1991) 245–272.

[40] A. Spencer, R. Rivlin, Isotropic integrity bases for vectors and second-order tensors, Archive for Rational Mechanics and Analysis 9 (1) (1962) 45–63.

[41] R. W. Johnson, Handbook of Fluid Dynamics, CRC Press, 2016.

[42] C. M. Bishop, Pattern recognition and machine learning, springer, 2006.

[43] M. Emory, J. Larsson, G. Iaccarino, Modeling of structural uncertainties in Reynolds-averaged Navier-Stokes closures, Physics of Fluids 25 (11) (2013) 110822.

[44] S. Banerjee, R. Krahl, F. Durst, C. Zenger, Presentation of anisotropy properties of turbulence, invariants versus eigenvalue approaches, Journal of Turbulence 8 (32).

[45] J.-L. Wu, R. Sun, S. Laizet, H. Xiao, Representation of Reynolds stress perturbations with application in machine-learning-assisted turbulence modeling, submitted, arXiv preprint arXiv:1709.05683 (2017).

[46] L. Breiman, Random forests, Machine learning 45 (1) (2001) 5–32.

[47] R. Ihaka, R. Gentleman, R: a language for data analysis and graphics, Journal of Computational and Graphical Statistics 5 (3) (1996) 299–314.

[48] A. Liaw, M. Wiener, et al., Classification and regression by randomforest, R news 2 (3) (2002) 18–22.

[49] A. Huser, S. Biringen, Direct numerical simulation of turbulent flow in a square duct, Journal of Fluid Mechanics 257 (1993) 65–95.

[50] M. Breuer, N. Peller, C. Rapp, M. Manhart, Flow over periodic hills: Numerical and experimental study in a wide range of Reynolds numbers, Computers & Fluids 38 (2) (2009) 433–457.

[51] M. Gibson, B. Launder, Ground effects on pressure fluctuations in the atmospheric boundary layer, Journal of Fluid Mechanics 86 (03) (1978) 491–511.

[52] A. Pinelli, M. Uhlmann, A. Sekimoto, G. Kawahara, Reynolds number dependence of mean flow structure in square duct turbulence, Journal of Fluid Mechanics 644 (2010) 107–122.

[53] F. Gessner, A. Emery, The numerical prediction of developing turbulent flow in rectangular ducts, Journal of Fluids Engineering 103 (3) (1981) 445–453.

[54] B. Launder, B. Sharma, Application of the energy-dissipation model of turbulence to the calculation of flow near a spinning disc, Letters in Heat and Mass Transfer 1 (2) (1974) 131–137.

[55] H. G. Weller, G. Tabor, H. Jasak, C. Fureby, A tensorial approach to computational continuum mechanics using object-oriented techniques, Computers in physics 12 (6) (1998) 620–631.

[56] S. Patankar, Numerical heat transfer and fluid flow, CRC press, 1980.

[57] K. Duraisamy, G. Iaccarino, H. Xiao, Turbulence modeling in the age of data, under review for Annual Review in Fluid Mechanics, arXiv preprint arXiv:1804.00183 (2018).

[58] A. P. Singh, R. Matai, K. Duraisamy, P. Durbin, Data-driven augmentation of turbulence models for adverse pressure gradient flows, in: 23rd AIAA Computational Fluid Dynamics Conference, 2017, Denver, CO, paper 2017-3626.

[59] J.-L. Wu, J.-X. Wang, H. Xiao, J. Ling, A priori assessment of prediction confidence for data-driven turbulence modeling, Flow, Turbulence and Combustion 99 (2017) 25–46.

[60] G. James, D. Witten, T. Hastie, R. Tibshirani, An introduction to statistical learning, Vol. 112, Springer, 2013.

[61] P. Durbin, personal communication (2017).

Appendix

Appendix.D: Data-Driven Reynolds Stress Model: Detailed Algorithms

The detailed work flow of constructing a data-driven Reynolds stress model with implicit treatment and use it for solving the RANS equations are presented as follows. First, we write Eq. 4.3 in terms of the Reynolds stress tensor rather than anisotropy tensor:

$$\mathbf{b} = \nu_t^L \mathbf{S} + (\mathbf{b} - \nu_t^L \mathbf{S}) = \nu_t^L \mathbf{S} + (\boldsymbol{\tau} - (\nu_t^L \mathbf{S} + \mathrm{tr}(\boldsymbol{\tau}))) = \nu_t^L \mathbf{S} + (\boldsymbol{\tau} - \boldsymbol{\tau}^L) \tag{4.13}$$

where $\mathrm{tr}(\boldsymbol{\tau})$ represents the trace of the Reynolds stress tensor, and $\boldsymbol{\tau}^L$ denotes the linear part of Reynolds stress tensor.

The procedure of the proposed framework are as follows:

(i) Perform baseline RANS simulations on both the training flows and the test flow to obtain mean flow features $\mathbf{q}$ and Reynolds stress tensor $\boldsymbol{\tau}^{\mathrm{RANS}}$.

(ii) Train regression functions for Reynolds stress discrepancies $\Delta\boldsymbol{\tau}$ and $\Delta\boldsymbol{\tau}^L$, and use the trained regression functions to predict the test flow.

  (a) Compute the discrepancies fields $\Delta\boldsymbol{\tau} = \boldsymbol{\tau}^{\mathrm{DNS}} - \boldsymbol{\tau}^{\mathrm{RANS}}$ and $\Delta\boldsymbol{\tau}^L = \boldsymbol{\tau}^L - \boldsymbol{\tau}^{\mathrm{RANS}}$ for the training flows based on the DNS data, and construct regression functions $f_1 : \mathbf{q} \mapsto \Delta\boldsymbol{\tau}$ and $f_2 : \mathbf{q} \mapsto \Delta\boldsymbol{\tau}^L$ by using PIML framework [8].

  (b) Use trained regression functions f_1 and f_2 to predict the discrepancies fields $\Delta\boldsymbol{\tau}$ and $\Delta\boldsymbol{\tau}^L$ for the test flow, and compute the corresponding Reynolds stress fields $\boldsymbol{\tau}$ and $\boldsymbol{\tau}^L$ by adding the predicted discrepancies fields to the RANS simulated Reynolds stress $\boldsymbol{\tau}^{\mathrm{RANS}}$.

(iii) Train regression functions for eddy viscosity ν_t^L, and use the trained regression functions to predict for the test flow.

  (a) Compute the least squares eddy viscosity ν_t^L for the training flows based on the DNS data, and construct regression function $f_3 : \mathbf{q} \mapsto \nu_t^L$ by using machine learning.

  (b) Use trained regression functions f_3 to predict the least squares eddy viscosity ν_t^L for the test flow.

(iv) Substitute the predicted ν_t^L, $\boldsymbol{\tau}$ and $\boldsymbol{\tau}^L$ into RANS equations for the anisotropy stress tensor as shown in Eq. 4.13, and solve for the corresponding mean velocity field.

In this workflow, the linear part and nonlinear part of Reynolds stress are predicted separately. For the linear part, we only predict the optimal eddy viscosity ν_t^L and thus treat the linear part implicitly. To obtain the nonlinear part, we predict both the Reynolds stress

itself and the linear part of Reynolds stress, and we calculate the nonlinear part of Reynolds stress by subtracting the linear part of Reynolds stress from the Reynolds stress itself.

The solving for mean velocity are performed in a finite-volume CFD platform OpenFOAM, using a modified flow solver that allows the implicit treatments of Reynolds stress predicted by the machine learning model. Specifically, the modified flow solver is based on a built-in steady-state incompressible flow solver `simpleFoam` [55], in which the SIMPLE algorithm [56] is used. Unlike the standard `simpleFoam` solver, the modified flow solver uses the machine learning predicted ν_t^L, $\boldsymbol{\tau}$ and $\boldsymbol{\tau}^L$ to represent the modeled Reynolds stress $\boldsymbol{\tau}^m$, i.e. $\boldsymbol{\tau}^m = \nu_t^L \mathbf{S} + (\boldsymbol{\tau} - \boldsymbol{\tau}^L) + \mathrm{tr}(\boldsymbol{\tau})$. The strain rate tensor $\mathbf{S}$ is treated implicitly in the modified flow solver. For numerical discretizations of the RANS equations, the second-order central difference scheme is chosen for all terms except for the convection term, which is discretized with a second-order upwind scheme.

For the boundary conditions of the machine learning predicted ν_t^L, $\boldsymbol{\tau}$ and $\boldsymbol{\tau}^L$ in this work, the fixed zero values are applied at the walls and periodic boundary conditions are applied in the streamwise (x) direction. The boundary conditions of the mean velocity and the pressure are treated the same as the standard RANS simulations, i.e., periodic boundary conditions are applied in the streamwise (x) direction, and non-slip boundary conditions are applied at the walls.

Appendix.E: Integrity Basis of Mean Flow Features

The minimal integrity bases for rotational invariance with given input set

$$\widehat{\mathcal{Q}} = \{\widehat{\mathbf{S}}, \widehat{\mathbf{\Omega}}, \widehat{\nabla p}, \widehat{\nabla k}\}$$

of tensors is shown in Table 4.4. Spencer [40, 41] provided a systematic procedure of generating minimal invariant bases from a set of symmetric and anti-symmetric tensors. In order to utilize this procedure, we need to first transform the vectors $\widehat{\nabla p}$ and $\widehat{\nabla k}$ to the corresponding antisymmetric tensors by using the following mapping [41]:

$$\widehat{\mathbf{A}}_p = -\mathbf{I} \times \widehat{\nabla p} \tag{4.14a}$$

$$\widehat{\mathbf{A}}_k = -\mathbf{I} \times \widehat{\nabla k} \tag{4.14b}$$

where $\mathbf{I}$ is the second order identity tensor, and the symbol $\times$ denotes tensor cross product.

Appendix.F: Galilean Invariance

In Section 4.2.2, we stated that the all feature variables in Table 4.1 and 4.2 and their corresponding normalization factors are Galilean invariant. This is evidence from the fact

Table 4.4: Minimal integrity basis for symmetric tensor $\widehat{\mathbf{S}}$ and antisymmetric tensors $\widehat{\mathbf{\Omega}}$, $\widehat{\mathbf{A}}_p$, and $\widehat{\mathbf{A}}_k$. In the implementation, $\widehat{\mathbf{S}}$ is the strain-rate tensor, $\widehat{\mathbf{\Omega}}$ is the rotation-rate tensor; $\widehat{\mathbf{A}}_p$ and $\widehat{\mathbf{A}}_k$ are the antisymmetric tensors associated with pressure gradient $\widehat{\nabla p}$ and the gradient of turbulence kinetic energy $\widehat{\nabla k}$; n_S and n_A denote the numbers of symmetric and antisymmetric raw tensors for the integrity basis.

(n_S, n_A)	feature index	invariant bases[(a)]
(1, 0)	1–2	$\widehat{\mathbf{S}}^2$, $\widehat{\mathbf{S}}^3$
(0, 1)	3–5	$\widehat{\mathbf{\Omega}}^2$, $\widehat{\mathbf{A}}_p^2$, $\widehat{\mathbf{A}}_k^2$
(1, 1)	6–14	$\widehat{\mathbf{\Omega}}^2\widehat{\mathbf{S}}$, $\widehat{\mathbf{\Omega}}^2\widehat{\mathbf{S}}^2$, $\widehat{\mathbf{\Omega}}^2\widehat{\mathbf{S}}\widehat{\mathbf{\Omega}}\widehat{\mathbf{S}}^2$; $\widehat{\mathbf{A}}_p^2\widehat{\mathbf{S}}$, $\widehat{\mathbf{A}}_p^2\widehat{\mathbf{S}}^2$, $\widehat{\mathbf{A}}_p^2\widehat{\mathbf{S}}\widehat{\mathbf{A}}_p\widehat{\mathbf{S}}^2$; $\widehat{\mathbf{A}}_k^2\widehat{\mathbf{S}}$, $\widehat{\mathbf{A}}_k^2\widehat{\mathbf{S}}^2$, $\widehat{\mathbf{A}}_k^2\widehat{\mathbf{S}}\widehat{\mathbf{A}}_k\widehat{\mathbf{S}}^2$;
(0, 2)	15–17	$\widehat{\mathbf{\Omega}}\widehat{\mathbf{A}}_p$, $\widehat{\mathbf{A}}_p\widehat{\mathbf{A}}_k$, $\widehat{\mathbf{\Omega}}\widehat{\mathbf{A}}_k$
(1, 2)	18–41	$\widehat{\mathbf{\Omega}}\widehat{\mathbf{A}}_p\widehat{\mathbf{S}}$, $\widehat{\mathbf{\Omega}}\widehat{\mathbf{A}}_p\widehat{\mathbf{S}}^2$, $\widehat{\mathbf{\Omega}}^2\widehat{\mathbf{A}}_p\widehat{\mathbf{S}}*$, $\widehat{\mathbf{\Omega}}^2\widehat{\mathbf{A}}_p\widehat{\mathbf{S}}^2*$, $\widehat{\mathbf{\Omega}}^2\widehat{\mathbf{S}}\widehat{\mathbf{A}}_p\widehat{\mathbf{S}}^2*$; $\widehat{\mathbf{\Omega}}\widehat{\mathbf{A}}_k\widehat{\mathbf{S}}$, $\widehat{\mathbf{\Omega}}\widehat{\mathbf{A}}_k\widehat{\mathbf{S}}^2$, $\widehat{\mathbf{\Omega}}^2\widehat{\mathbf{A}}_k\widehat{\mathbf{S}}*$, $\widehat{\mathbf{\Omega}}^2\widehat{\mathbf{A}}_k\widehat{\mathbf{S}}^2*$, $\widehat{\mathbf{\Omega}}^2\widehat{\mathbf{S}}\widehat{\mathbf{A}}_k\widehat{\mathbf{S}}^2*$; $\widehat{\mathbf{A}}_p\widehat{\mathbf{A}}_k\widehat{\mathbf{S}}$, $\widehat{\mathbf{A}}_p\widehat{\mathbf{A}}_k\widehat{\mathbf{S}}^2$, $\widehat{\mathbf{A}}_p^2\widehat{\mathbf{A}}_k\widehat{\mathbf{S}}*$, $\widehat{\mathbf{A}}_p^2\widehat{\mathbf{A}}_k\widehat{\mathbf{S}}^2*$, $\widehat{\mathbf{A}}_p^2\widehat{\mathbf{S}}\widehat{\mathbf{A}}_k\widehat{\mathbf{S}}^2*$;
(0, 3)	42	$\widehat{\mathbf{\Omega}}\widehat{\mathbf{A}}_p\widehat{\mathbf{A}}_k$
(1, 3)	43–47	$\widehat{\mathbf{\Omega}}\widehat{\mathbf{A}}_p\widehat{\mathbf{A}}_k\widehat{\mathbf{S}}$, $\widehat{\mathbf{\Omega}}\widehat{\mathbf{A}}_k\widehat{\mathbf{A}}_p\widehat{\mathbf{S}}$, $\widehat{\mathbf{\Omega}}\widehat{\mathbf{A}}_p\widehat{\mathbf{A}}_k\widehat{\mathbf{S}}^2$, $\widehat{\mathbf{\Omega}}\widehat{\mathbf{A}}_k\widehat{\mathbf{A}}_p\widehat{\mathbf{S}}^2$, $\widehat{\mathbf{\Omega}}\widehat{\mathbf{A}}_p\widehat{\mathbf{S}}A_3\mathbf{S}^2$

Note: (a) The invariance basis is the trace of each tensor listed below.
(b) The asterisk ($*$) on a term indicates that all terms formed by cyclic permutation of anti-symmetric tensor labels (e.g., $\widehat{\mathbf{\Omega}}^2\widehat{\mathbf{A}}_p\widehat{\mathbf{S}}*$ is short for $\widehat{\mathbf{\Omega}}^2\widehat{\mathbf{A}}_p\widehat{\mathbf{S}}$ and $\widehat{\mathbf{A}}_p^2\widehat{\mathbf{\Omega}}\widehat{\mathbf{S}}$) are also included.

that most of the variables and normalization factors contains only terms associated with the velocity gradient $\nabla \mathbf{U}$ (e.g., $\mathbf{S}$ and $\mathbf{\Omega}$), pressure gradient ∇p, and TKE gradient ∇k. However, the Galilean invariance of the normalization facor $\rho|Du/Dt|$ is not evident. In this appendix we show that the material derivative of velocity is Galilean invariant.

The mean velocity at location $\boldsymbol{x}$ and time t observed in a stationary reference frame is denoted as $\mathbf{U}(\boldsymbol{x}, t)$. The mean velocity observed in reference frame moving with constant velocity $\mathbf{C}$ can be written as $\mathbf{U}^*(\boldsymbol{x}^*, t) = \mathbf{U}(\boldsymbol{x} - \mathbf{C}t, t) + \mathbf{C}$, where $\boldsymbol{x}^* = \boldsymbol{x} - \mathbf{C}t$ represents the spatial location observed in the moving reference frame. The material derivative of the velocity U_j^* in the moving reference frame is derived as follows:

$$\frac{\partial U_i^*}{\partial t} = \frac{\partial U_i}{\partial t} - C_j \frac{\partial U_i^*}{\partial x_j^*} \quad \text{and} \quad U_j^* \frac{\partial U_i^*}{\partial x_j^*} = (U_j + C_j) \frac{\partial U_i^*}{\partial x_j^*} \tag{4.15}$$

Combining the two terms in Eq. 4.15 and utilizing the fact that $\partial U_i^*/\partial x_j^* = \partial U_i/\partial x_j$ (because the reference frame velocity is constant) yields:

$$\frac{\partial U_i^*}{\partial t} + U_j^* \frac{\partial U_i^*}{\partial x_j^*} = \frac{\partial U_i}{\partial t} + U_j \frac{\partial U_i}{\partial x_j}, \tag{4.16}$$

That is,

$$\frac{DU_i^*}{Dt} = \frac{DU_i}{Dt} \tag{4.17}$$

which demonstrates that the material derivative of velocity $\mathbf{U}$ is invariant under Galilean transformation. The merit of ensuring Galilean invariance is that the trained machine learning model $g(\mathbf{U})$ is valid in all inertial frames, i.e., $g(\mathbf{U}) = g(\mathbf{U}+\mathbf{C})$, enhancing the generality of the trained model.

It is noted that several input features in the works of Wang et al. [8] and Ling and Templeton [34] are not Galilean invariant. For example, the raw features of pressure gradient along streamline $U_i \partial P/\partial x_i$ and the ratio of convection to production of turbulent kinetic energy $U_i dk/dx_i$, and the normalization factor $U_i U_i$ for turbulence intensity and the normalization factor $\rho \partial U_i^2/\partial x_i$ for the ratio of pressure normal stresses to shear stresses. Therefore, the machine learning framework in this work is expected to achieve better extrapolation capability with the Galilean invariance for all input and output quantities.

Chapter 5

Representation of Stress Tensor Perturbations with Application in Machine-Learning-Assisted Turbulence Modeling

(Accepted, *Computer Methods in Applied Mechanics and Engineering*, 2018.)

J.-L. Wu, R. Sun, S. Laizet, H. Xiao
Department of Aerospace and Ocean Engineering, Virgina Tech, Blacksburg, VA, 24061, USA

Abstract

Numerical simulations based on Reynolds-Averaged Navier–Stokes (RANS) equations are widely used in engineering design and analysis involving turbulent flows. However, RANS simulations are known to be unreliable in many flows of engineering relevance, which is largely caused by model-form uncertainties associated with the Reynolds stresses. Recently, a machine-learning approach has been proposed to quantify the discrepancies between RANS modeled Reynolds stress and the true Reynolds stress. However, it remains a challenge to represent discrepancies in the Reynolds stress eigenvectors in machine learning due to the requirements of spatial smoothness, frame-independence, and realizability. This challenge also exists in the data-driven computational mechanics in general where quantifying the perturbation of stress tensors is needed. In this work, we propose three schemes for representing perturbations to the eigenvectors of RANS modeled Reynolds stresses: (1) discrepancy-based Euler angles, (2) direct-rotation-based Euler angles, and (3) unit quaternions. We compare these metrics by performing *a priori* and *a posteriori* tests on two canonical flows: fully developed turbulent flows in a square duct and massively separated flows over peri-

odic hills. The results demonstrate that the direct-rotation-based Euler angles representation lacks spatial smoothness while the discrepancy-based Euler angles representation lacks frame-independence, making them unsuitable for being used in machine-learning-assisted turbulence modeling. In contrast, the representation based on unit quaternion satisfies all the requirements stated above, and thus it is an ideal choice in representing the perturbations associated with the eigenvectors of Reynolds stress tensors. This finding has clear importance for uncertainty quantification and machine learning in turbulence modeling and for data-driven computational mechanics in general.

Notation

We summarize the notations to illustrate the convention of the nomenclature used in this paper. Upper case letters (e.g., $\mathbf{Q}$) indicate matrices or tensors; lower case letters with bold font (e.g., $\mathbf{n}$) indicate vectors; undecorated letters in lower cases indicate scalars. Tensors (matrices) and vectors are also indicated with index notations, e.g., R_{ij} and u_i with $i, j = 1, 2, 3$. In this paper, i and j are used with tensor indices while α is used as general indexes. The ensemble average is indicated by $\overline{\square}$. The superscript $\square^o$ denotes original quantities given by the Reynolds-Averaged Navier–Stokes simulations (baseline for the perturbations), and the superscript $\square^*$ represents the truth or the target of perturbations.

5.1 Introduction

5.1.1 Challenges and new developments in turbulence modeling

Numerical simulations based on Reynolds-Averaged Navier–Stokes (RANS) equations are still the dominant tool for industry applications involving turbulent flows, even though the rapid growth of computational resource has greatly expanded the reach of the high-fidelity simulation methods such as Direct Numerical Simulation (DNS) and Large Eddy Simulation (LES) in the past few decades. However, commonly used RANS models (e.g., k-ε models, k-ω models and S-A models) are known to be unreliable in many flows such as those with three-dimensional separations, strong pressure gradients or mean streamline curvature [1]. This lack of accuracy mainly originates from a large discrepancy between the modeled and the true Reynolds stresses, leading to the unreliable predictions of other quantities of interests (QoIs) such as mean velocity, mean pressure, surface friction, and drag and lift forces.

In light of the decades-long stagnation in traditional RANS modeling, several researchers developed machine-learning-assisted turbulence models [2, 3, 4]. These efforts aimed at leveraging machine learning algorithms and large amounts of data made available by advances in experimental techniques and computational sciences. Duraisamy and co-workers [5, 4]

identified the target of machine-learning-assisted models as the multiplicative discrepancy in the production term of the transport equations of turbulent quantities (e.g., $\tilde{\nu}_t$ in the S–A model). Although recent studies showed the potential of extrapolation capabilities of this approach among different flows [6, 4], such capabilities are potentially limited by the lack of physical anchoring and uniqueness of the multiplicative discrepancy term. On the other hand, Ling et al. [3] incorporated physical knowledge in designing the architecture of a machine-learning-assisted model by adopting an invariant-set-based representation of Reynolds stress anisotropy tensor [7]. Their approach has clear physical justification, but note that their aim was to replace the traditional turbulence models with a data-driven, machine-learning-based counterpart. Xiao and co-workers [8, 2] argued that data-driven models should be used to assist and complement, rather than replace, the traditional turbulence models. They justified their philosophical argument with the fact that currently used turbulence models condensed a lot of physical and theoretical insights, which in turn were distilled from large amounts of data and empirical knowledge in decades of engineering practice. In addition, these models have achieved great successes in engineering turbulent flow simulations despite the above-mentioned limitations. As such, Wang et al. [2] proposed a machine-learning-assisted turbulence modeling framework, where they identified the perturbations that can correct RANS-modeled Reynolds stresses to the true Reynolds stress as the target of learning. While this work focuses on RANS modeling, we note that several data-driven approaches have also been proposed in the context of LES to improve sub-grid scale stress models [9] and scalar fluxes models [9, 10].

5.1.2 Stress perturbations in machine-learning-assisted RANS modeling

Wang et al. [2] represented the perturbations to RANS modeled Reynolds stress by following the decomposition method of Iaccarino and co-workers in their model-form uncertainty quantification work [11, 12, 13]. Emory et al. [11] decomposed the Reynolds stress anisotropic tensor into eigenvalues and eigenvectors, and then they used Barycentric triangle to provide a realizability map for the eigenvalues. The Barycentric triangle is equivalent to the well-known Lumley triangle [14, 15]. These two equivalent maps provide a convenient way to ensure the realizability of the perturbed Reynolds stresses by bounding the mapped eigenvalues within the respective triangles. The theoretical foundation is that, after the corresponding transformations [14], a Reynolds stress tensor must reside within or on the edge of the Lumley or Barycentric triangle. However, much less work has been devoted to representing the perturbations to the eigenvectors of the RANS modeled Reynolds stress tensor.

Perturbations to eigenvectors are much more difficult to impose compared with that to the eigenvalues, which is due to several reasons. First, there is no straightforward bound on eigenvector perturbations – Reynolds stress realizability as represented by the Barycentric

triangle only provides a bound for the eigenvalues and not for the eigenvectors. In the context of uncertainty estimation, researchers investigated several representations of eigenvector perturbations. Thompson et al. [16] used the Reynolds stress transport equations to constrain the eigenvector perturbations based on the bounds on the eigenvalue perturbations. Their work can potentially address the challenge of bounding eigenvector perturbations. However, it should be noted that the Reynolds stress transport equations have several unclosed source terms (e.g., pressure-strain tensor, triple correlation) that must be estimated, which makes the transport-equation-based constraint a soft rather than a strict one. On the other hand, Iaccarino et al. [17] proposed an approach to augment their eigenvalue perturbations by using the maximum and minimum of turbulence production as bounds for perturbing the eigenvectors. Such bounds are physically sound, albeit not necessarily as mathematically rigorous as that in [16]. In addition to the lack of straightforward bounds, another challenge is that any perturbations introduced to the eigenvectors must retain their orthonormality. This is to ensure the symmetry and realizability of the perturbed Reynolds stress tensor. Such a requirement immediately rules out the option of introducing componentwise discrepancy tensor to eigenvectors or to the Reynolds stress tensor itself. Instead, a straightforward method to retain such orthonormality is to represent the eigenvector perturbations as a three-dimensional rigid-body rotation. In this spirit, Wang et al. [18] introduced such perturbations to the eigenvectors by using Euler angles for quantifying RANS model-form uncertainties [18].

The work reviewed above on introducing perturbations to modeled Reynolds stresses are all concerned with RANS model-form uncertainty estimations. A closely related topic is machine-learning-assisted turbulence modeling as in the framework of [2], where the objective is to predict the perturbations $\Delta\mathbf{R}$ needed to correct the modeled Reynold stresses $\mathbf{R}^{rans}$ to the true $\mathbf{R}^{*}$. They used machine learning to train a function $f : \mathbf{q} \mapsto \Delta\mathbf{R}$ between mean flow features $\mathbf{q}$ and Reynolds stress perturbations $\Delta\mathbf{R}$. It should be noted that a general functional form $f : \mathbf{q} \mapsto \Delta R$ is trained to map the mean flow features $\mathbf{q}$ at any given location of the training flows to the corresponding Reynolds stress discrepancy ΔR. By doing so, the machine learning trained function f carries no information of the geometry of the training flows, which enables the prediction of the flow with different geometry configuration. By correcting the RANS-predicted Reynolds stresses towards the DNS counterparts, such perturbations are expected to improve the predictions of the velocity field and other quantities of interest. Wang et al. [2] used the random forest to learn such perturbations from a database of training flows with DNS data. In that work, the fully developed turbulent flow in a square duct and the flow over periodic hills were first studied to demonstrate the merit of modeling Reynolds stress by using machine learning. In a following report of Wang et al. [19], they further demonstrated the improvement of mean velocity prediction. The more general philosophy of machine-learning-assisted turbulence modeling was discussed in [8, 20]. Recently, Wu et al. [21] proposed a stabilized machine learning scheme for RANS modeling and demonstrate better predictive capability of mean velocity. Wu et al. [22] further demonstrated that the performance of the machine-learning-assisted model depends on the choice of training flows by studying a group of flows with massive separation. In addition,

Wu et al. [22] proposed two statistical metrics to assess the prediction performance *a priori* by evaluating the difference between the training flow and the test flow. In the context of machine-learning-assisted RANS modeling, the bounds for the eigenvectors perturbations are not required explicitly; instead, the main concern is to ensure the orthonormality of the machine-learning-corrected Reynolds stress eigenvectors. To this end, they used Euler angles to represent the eigenvectors perturbations as rigid-body rotations following the work by Wang et al. [18]. In fact, the representation of rigid-body rotation has attracted much more attention in robotics and computer vision [23], where different approaches including those based on Euler angles [24], unit quaternion [25] and rotation matrices of direction-cosines [26] have been evaluated and compared.

However, the usages of the above approaches to represent the eigenvectors perturbations to Reynolds stress tensors pose unique requirements in the context of machine-learning-assisted modeling. In particular, the functional form $f : \mathbf{q} \mapsto \Delta\mathbf{R}$ between mean flow features and desired Reynolds stress perturbations should be smooth to ensure that f can be learned from data [27]. Otherwise, the machine learning algorithms tend to fit the noise rather than the true functional relation. Another requirement is the frame-independence of the representation of Reynolds stress perturbations. In this work, we first address the smoothness requirement by comparing three representations of eigenvectors perturbations via *a priori* tests in Sec. 5.4.2. We then evaluate the performances of Euler angles and unit quaternion in the context of the machine-learning-assisted turbulence modeling in Sec. 5.4.3.

5.1.3 Novelty and potential impact of present work

The novelty of the present contribution is twofold. First, we explored several alternatives in representing the perturbations on Reynolds stress eigenvectors as rigid-body rotations, which ensure the orthonormality of the perturbed eigenvectors by construction and thus the symmetry and positive definiteness (realizability) of the perturbed Reynolds stresses. Second, we performed a comprehensive comparison of two types of representation of rigid-body rotations, Euler angles and unit quaternions, in light of the two requirements posed by machine-learning-assisted turbulence modeling, i.e., smoothness and frame-independence. The assessment demonstrates that the unit-quaternion-based representation satisfies both requirements, making it a superior to Euler-angle-based representations of eigenvectors perturbation for machine-learning-assisted turbulence modeling. As the machine learning techniques have gained increasing interests in turbulence modeling, the present manuscript deals with one of the most important aspects, i.e., to incorporate the physical constraints into machine-learning-based computational physics. Specifically, the objectivity requirement of the model is ensured by properly choosing the inputs and outputs of machine learning. The authors hope that the attempt of this work can inspire more turbulence modeling researchers to incorporate their domain knowledge of flow physics into machine-learning-assisted modeling.

Although this work mainly focus on the representation of Reynolds stress perturbations for machine-learning-assisted turbulence modeling, it is also applicable to the modeling of stress tensor field in general and thus has following potential broader impact in other research areas:

1. The objectivity (frame-independence) requirement is also important for machine-learning-assisted physics modeling in general and this work illustrated one possibility to satisfy such a requirement by properly choosing the outputs of machine learning in our framework.

2. We highlighted the smoothness requirements for machine-learning-assisted physics modeling where a spatial field needs to be predicted. Such highlighted requirement is also of importance in the model-form uncertainty quantification of the stress tensor field, particularly for the uncertainty quantification for the orientation of the modeled stress tensor.

3. The representation of perturbations on Reynolds stress tensors is directly applicable in other fields of computational mechanics, e.g., plasticity, where sequential increments of stress tensors are used to find a path from the current stress state to the new state.

The rest of the paper is organized as follows. Section 5.2 summarizes the machine-learning-assisted turbulence modeling framework of Wang et al. [2]. Section 5.3 introduces three representations of the eigenvectors perturbations to the Reynolds stress tensor, including direct-rotation-based Euler angles, discrepancy-based Euler angles, and the unit quaternion. Section 5.4 presents the results in evaluating these three representations of eigenvectors perturbations. Finally, Section 5.5 presents the conclusions.

5.2 Summary of machine-learning-assisted turbulence modeling framework

5.2.1 Origin of RANS model-form uncertainty

The Navier–Stokes (NS) equations for incompressible flows with a constant density ρ can be written as follows:

$$\frac{\partial u_i}{\partial t} + \frac{\partial \left(u_i u_j \right)}{\partial x_j} = -\frac{1}{\rho}\frac{\partial p}{\partial x_i} + \nu \frac{\partial^2 u_i}{\partial x_j \partial x_j} \tag{5.1a}$$

$$\text{and} \quad \frac{\partial u_i}{\partial x_i} = 0 \tag{5.1b}$$

where u_i and p are instantaneous velocity and pressure, respectively; t and x_i are time and space coordinates, respectively; ν is the kinematic viscosity. Solving the Navier–Stokes equations directly would necessitate resolving a wide range of spatial and temporal scales, which would incur prohibitive computational costs. Therefore, when simulating turbulent flows in engineering, the instantaneous fields u_i and p in the NS equations are usually decomposed into their means ($\overline{u}_i$ and $\overline{p}$, respectively) and the fluctuations (u_i' and p') around the means, i.e.,

$$u_i = \overline{u}_i + u_i' \tag{5.2}$$

$$p = \overline{p} + p' \tag{5.3}$$

Substituting the Reynolds decomposition above into the NS equation yields the RANS equations, which describe the mean velocities and pressure:

$$\frac{\partial \overline{u}_i}{\partial t} + \frac{\partial \left(\overline{u}_i \overline{u}_j\right)}{\partial x_j} = -\frac{1}{\rho}\frac{\partial \overline{p}}{\partial x_i} + \nu \frac{\partial^2 \overline{u}_i}{\partial x_j \partial x_j} - \frac{\partial \langle u_i' u_j' \rangle}{\partial x_j} \tag{5.4a}$$

$$\text{and} \quad \frac{\partial \overline{u}_i}{\partial x_i} = 0 \tag{5.4b}$$

where negative of the velocity fluctuation covariance $\langle u_i' u_j' \rangle$ is referred to as Reynolds stress and is denoted as R_{ij} or $\mathbf{R}$ for simplicity. It is a consensus that in incompressible, fully turbulent flows (i.e., flows without transition, heat transfer, or compressible effects), the modeled Reynolds stress term is the main source of model-form uncertainties in RANS simulations [28, 7]. At any point in the flow field, the true Reynolds stress $\mathbf{R}^*$ can be written as the sum of the RANS-modeled value and a discrepancy term, i.e., $\mathbf{R}^* = \mathbf{R}^{rans} + \Delta\mathbf{R}$. Aiming at estimating the Reynolds stress discrepancy $\Delta\mathbf{R}$, Wang et al. [2] proposed a machine-learning-assisted turbulence modeling framework, which is detailed below.

5.2.2 Machine-learning-assisted turbulence modeling framework

The essence of the machine-learning-assisted turbulence modeling framework of Wang et al. [2] is to predict the discrepancy term $\Delta\mathbf{R}$ by learning a model from high-fidelity simulation (e.g, DNS) data. This is achieved by learning a functional mapping $f : \mathbf{q} \mapsto \Delta\mathbf{R}$, where $\mathbf{q}$ indicates mean flow features obtained from RANS simulations, e.g., mean pressure gradient, mean flow curvature, all normalized with local quantities. In machine learning terminology the discrepancy $\Delta\mathbf{R}$ is referred to as *responses*, the feature vector $\mathbf{q}$ as the *inputs*, and the mappings f as *regression functions*. The flows used to train the *regression functions* is referred to as *training flows*, and the flow to be predicted as *test flow*. Random forest regression is used to build the regression functions. An advantage of the random forest regressor is that importance scores are also provided for each input flow feature, which can be used to further assist the modelers to improve the existing RANS models [2].

Wang et al. [2] used a group of hand-crafted ten features q_i based on the RANS simulated mean flow fields (velocity $\overline{u}_i$ and pressure $\overline{p}$) as inputs $\mathbf{q}$ to the regression function. In a more

recent work [29], an additional 47 mean flow features were constructed as the invariant set $\{\mathbf{S}, \mathbf{\Omega}, \nabla p, \nabla k\}$, where $\mathbf{S}$ denotes the strain-rate tensor, $\mathbf{\Omega}$ the rotation-rate tensor, ∇p the pressure gradient and ∇k the gradient of turbulent kinetic energy, all of which are obtained from RANS-simulated mean flow fields.

Wang et al. [2] used a physics-based perturbation via the following decomposition to represent the Reynolds stress perturbations $\Delta\mathbf{R}$ [11, 14]:

$$\mathbf{R} = 2k\left(\frac{\mathbf{I}}{3} + \mathbf{A}\right) = 2k\left(\frac{\mathbf{I}}{3} + \mathbf{V}\mathbf{\Lambda}\mathbf{V}^T\right) \tag{5.5}$$

where k is the turbulent kinetic energy, which indicates the magnitude of $\mathbf{R}$; $\mathbf{I}$ is the second order identity tensor; $\mathbf{A}$ is the anisotropy tensor; $\mathbf{\Lambda} = \text{diag}[\lambda_1, \lambda_2, \lambda_3]$ and $\mathbf{V} = [\mathbf{v}_1, \mathbf{v}_2, \mathbf{v}_3]$ are the eigenvalues and orthonormal eigenvectors of $\mathbf{A}$, representing its shape (i.e., aspect ratio) and orientation, respectively. The eigenvectors $\mathbf{V}$ consist of three orthonormal vectors (nine elements in total) but has only three degrees of freedom.

Therefore, if we visualize the Reynolds stress as an ellipsoid [30], the discrepancy between the modeled Reynolds stress $\mathbf{R}$ and the corresponding true $\mathbf{R}^*$ can be formulated as three consecutive transformations (i.e., perturbations):

1. The size of the ellipsoid (magnitude of the tensor) is scaled by a positive factor of $\gamma_k = k^*/k^{rans}$ while keeping the shape the same, as illustrated in Fig. 5.1a.

2. The aspect ratio of ellipsoid is perturbed while keeping the size (sum of the three axes) and orientation unchanged. This is achieved by perturbing the eigenvalues, i.e., $\mathbf{\Lambda}^* = \mathbf{\Lambda} + \Delta\mathbf{\Lambda}$, as illustrated in Fig. 5.1b.

3. Finally, the ellipsoid experiences a rigid-body rotation, which is represented as $\mathbf{V}^* = \mathbf{Q}\mathbf{V}$, where $\mathbf{Q}$ is a rotation matrix. This perturbation is illustrated in Fig. 5.1c.

The objective of the machine learning is to predict the mapping $f : \mathbf{q} \mapsto (\gamma, \Delta\mathbf{\Lambda}, \mathbf{Q})$, with which the corrected Reynolds stress $\mathbf{R}^*$ can be recovered as follows:

$$\mathbf{R}^* = 2k^*\left(\frac{\mathbf{I}}{3} + \mathbf{V}^*\mathbf{\Lambda}^*\mathbf{V}^{*T}\right) = 2\gamma_k k\left(\frac{\mathbf{I}}{3} + \mathbf{Q}\mathbf{V}(\mathbf{\Lambda} + \Delta\mathbf{\Lambda})\mathbf{V}^T\mathbf{Q}^T\right) \tag{5.6}$$

With perturbations of the magnitude, the shape and the orientation as introduced above, the perturbations to the Reynolds stress tensor are parameterized by six independent variables, which account for the six degrees of freedom of a symmetric second-order tensor. Noted that the perturbations can be alternatively introduced through the coefficients in the general form of eddy viscosity model [31], which has ten coefficients and introduces redundancy. This approach has been explored by Ling et al. [32]. In contrast, the scheme we adopt here is free from such redundancy in the parameterization. That is, different perturbations are

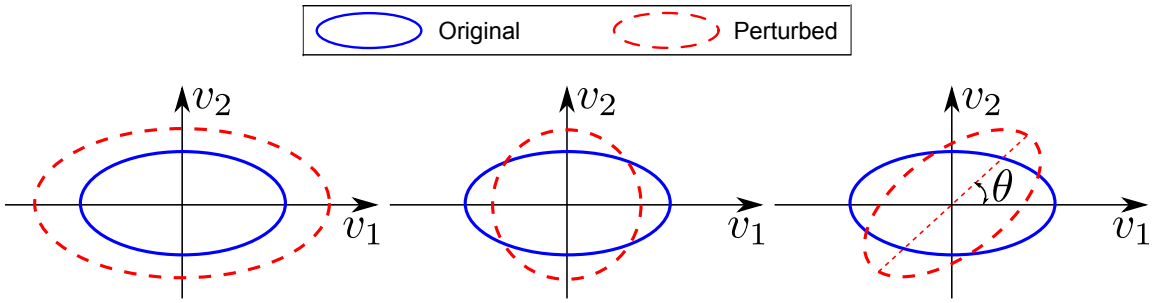

(a) TKE k (b) Eigenvalues $\mathbf{\Lambda}$ (c) Eigenvectors $\mathbf{V}$

Figure 5.1: The perturbations on (a) the magnitude (turbulent kinetic energy k), (b) eigenvalues $\mathbf{\Lambda}$, and (c) eigenvectors $\mathbf{V}$ of a Reynolds stress tensor $\mathbf{R}$. For clarity, the tensor is represented in the two-dimensional space as an ellipsis instead of a three-dimensional ellipsoid. In addition, perturbations on k, $\mathbf{\Lambda}$, and $\mathbf{V}$ are shown individually on each panel and not as three consecutive perturbations.

guaranteed to result in different perturbed Reynolds stress. The perturbation on the magnitude is parameterized by the logarithmic discrepancy $\log_2(k^*/k^{rans})$ [2]. The perturbations on the eigenvalues are parameterized by the Barycentric coordinates [14, 11], which ensure the realizability of the perturbed Reynolds stresses. See ref. [2] for more details. While representing the perturbations on the magnitude and the shape is straightforward, the rotation can be difficult to represent. Several schemes are introduced and examined below.

5.3 Representing rigid-body rotation of eigenvectors in machine learning

It has been established above that representing eigenvector perturbations as rigid-body rotations ensures orthonormality of the obtained eigenvectors and realizability of the perturbed Reynolds stresses. An apparently straightforward representation of such a rotation is to use the matrix $\mathbf{Q}$. However, it has nine elements (i.e., direction cosines) but only three intrinsic degrees of freedom due to the orthonormality constraint $\mathbf{Q}^T\mathbf{Q} = \mathbf{I}$. Existing machine learning algorithms are not suitable for learning quantities with hard constraints, since they were developed mostly for commercial applications (e.g., product preferences of customers), where hard constraints are uncommon. Building constraints into the learning problem is not trivial. Hence, it is more desirable to use a formulation with the same number of *independent* variables as the number of intrinsic degrees of freedom. Two candidate representations, Euler angles and unit quaternion, are introduced and compared in the context of machine learning.

Before presenting the two representations, we shall first put forward two desirable properties of the regression function $f : \mathbf{q} \mapsto \Delta\mathbf{R}$ to be learned from training data. First, the function

must be smooth for it to have good generalization performance, i.e., the predictive performance of the trained function on data unseen during the training. The word "smooth" shall be interpreted in liberal sense (i.e., the output $\Delta\mathbf{R}$ varies mildly in the feature $\mathbf{q}$ space) rather than in a mathematical sense (i.e., the existence of arbitrarily high order derivatives). The reason for such a requirement is that non-smooth functions are more susceptible to overfitting caused by the noises in the training data, which would in turn diminish the predictive capabilities of the trained functions [27]. Second, the regression function itself must be frame-independent. This is a requirement unique for constitutive modeling in computational mechanics (including turbulence modeling) [see e.g., 31, 7], which is equally applicable to theory-based modeling and data-driven modeling.

For flows considered in this work (incompressible flows free from any geometric discontinuities), the mean flow features $\mathbf{q}$ are smooth spatially. Moreover, all chosen features are frame-independent. Consequently, the two requirements outlined above on f translates to those on the output $\Delta\mathbf{R}$, i.e., it should be spatially smooth and frame-independent. Note that it is possible that both the input and the output (e.g., $\mathbf{q}$ and $\Delta\mathbf{R}$) are frame-dependent but the mapping f is frame-independent, which is common in many analytical constitutive relations. We use the linear eddy viscosity model $\mathrm{dev}(\mathbf{R}) = 2\nu_t\mathbf{S}$ to illustrate this subtle point, where ν_t is a scalar eddy viscosity field. Here, both $\mathbf{R}$ and $\mathbf{S}$ are frame-dependent, but the mapping itself is frame-independent. However, if this function is to be learned from data, the training data need to be duplicated in a large number of rotated frames so that the machine learning algorithm can discover the uniqueness of that function in all these frames, which dramatically increases computational costs. Therefore, it is preferable to use the invariants of the tensors of concern ($\mathbf{S}$ and $\mathbf{R}$) as inputs and outputs instead [33]. This is a unique complication in machine-learning-based modeling that is not present in traditional, theory-based modeling.

5.3.1 Euler angles

The Euler angles used in this work follows the z–x'–z'' convention in rigid body dynamics [34]. That is, if a local coordinate system x–y–z spanned by the three eigenvectors was initially aligned with the global coordinate system (X–Y–Z), the current configuration could be obtained by the following three consecutive intrinsic rotations about the axes of the local coordinate system: (1) a rotation about the z axis by angle ϕ_1, (2) a rotation about the x axis by ϕ_2, and (3) another rotation about its z axis by ϕ_3. In general the local coordinate axes change orientations after each rotation. Such a convention provides a set of Euler angles (ϕ_1, ϕ_2, ϕ_3) to describe the current orientation of a rigid body (or eigenvectors $\mathbf{V}$ in this case) within a global coordinate system. We refer to this description as "absolute Euler angles". With this description, the discrepancy between two sets of eigenvectors, $\mathbf{V}$ and $\mathbf{V}^*$, can be described by the *discrepancies $\Delta\phi_\alpha$ in their absolute Euler angles*, ϕ_α and ϕ_α^*, respectively, with $\Delta\phi_\alpha = \phi_\alpha^* - \phi_\alpha$ and $\alpha = 1, 2, 3$. In the machine-learning-assisted turbulence modeling framework of Wang et al. [2], regression functions for $\Delta\phi_\alpha$ were trained

by using high-fidelity data. However, it can be seen that this representation relies on a global coordinate system, which makes it frame-dependent. In particular, it is inadequate for more complex scenarios and can lead to deteriorated predictive performances. The importance of frame-independence in machine-learning-assisted physical modeling has been discussed in [33]. A possible remedy of the frame dependence in the formulation above is to directly describe the rotation from $\mathbf{V}$ to $\mathbf{V}^*$ in Euler angles $\phi_\alpha^{o\to *}$, where o and $*$ in the superscript indicate original and corrected, respectively. However, as will be shown by the *a priori* test in Section 5.4.2, the direct-rotation-based Euler angles $\phi_\alpha^{o\to *}$ are non-smooth spatially and thus undesirable in light of the smoothness requirement explained above.

In summary, the two variants of Euler-angle-based representations of the perturbation from $\mathbf{V}$ to $\mathbf{V}^*$, i.e., discrepancy-based representation $\Delta\phi_\alpha$ and direct-rotation-based representation $\phi_\alpha^{o\to *}$, are plagued by their own weaknesses, namely the frame-independence and non-smoothness, respectively. These difficulties prompted us to explore the unit quaternion as an alternative representation.

5.3.2 Unit quaternion

Given two sets of orthonormal eigenvectors $\mathbf{V}$ and $\mathbf{V}^*$ sharing the same origin O, the Euler's rotation theorem states there exists a unique axis of unit vector $\mathbf{n} \equiv [n_1, n_2, n_3]$ and an angle θ such that $\mathbf{V}^*$ can be obtained via rotating $\mathbf{V}$ by θ about an axis $\mathbf{n}$ that runs through the origin O. The rotation can thus be represented compactly with a unit quaternion:

$$\mathbf{h} = \left[\cos\frac{\theta}{2},\ n_1\sin\frac{\theta}{2},\ n_2\sin\frac{\theta}{2},\ n_3\sin\frac{\theta}{2}\right]^T \tag{5.7}$$

which clearly verifies $\|\mathbf{h}\| = 1$, with $\|\cdot\|$ indicating Euclidean-norm. The axis $\mathbf{n}$ and the angle θ are both determined by $\mathbf{V}$ and $\mathbf{V}^*$ and do not depend on a global coordinate system. Therefore, the unit-quaternion-based representation of the rotation is frame-independent.

To conclude this section, we point out that any rotation that transforms $\mathbf{V}$ to $\mathbf{V}^*$ can be uniquely represented by any of the following:

(i) a rotation matrix $\mathbf{Q}$;

(ii) a unique set of Euler angles $(\Delta\phi_1, \Delta\phi_2, \Delta\phi_3)$ or $(\phi_1^{o\to *}, \phi_2^{o\to *}, \phi_3^{o\to *})$ based on discrepancy or direct rotation, respectively; and

(iii) a unit quaternion $\mathbf{h}$.

A rare exception is the scenarios involving gimbal lock for the Euler angles [35].

5.4 Numerical results

Numerical examples are used to evaluate the performances of three representations of perturbations to Reynolds stress eigenvectors, i.e., (1) direct-rotation-based Euler angles, (2) discrepancy-based Euler angles, and (3) unit quaternion. In the *a priori* tests, we compute the "true" perturbations that are needed to correct the RANS modeled Reynolds stress to the DNS results by using these three representations. The smoothness of such true perturbation fields is indicative of the difficulties when using data to learn the regression functions for the perturbations. The tests show that latter two representations (discrepancy-based Euler angles and unit quaternion) satisfy the smoothness requirement. Therefore, in *a posteriori* tests we focus on these two representations. Predictive performances of the machine-learning models with the later two representations are assessed by investigating several training-prediction scenarios. The results suggest that the unit quaternion representation leads to better results due to its frame-independence. This advantage is particularly clear when the training and test flows involve different coordinate systems or geometries. In *a posteriori* tests, random forest regression [36] is used to build mappings from the 50 inputs (mean flow features $\mathbf{q}$) in [21] to the Reynolds stress discrepancies. The number features at each split is set to 7 ($\approx \sqrt{50}$) based on the recommendation in the literature [36]. The number of trees is 300, chosen by observing the out-of-bag (OOB) errors to avoid overfitting. More details about using random forest regression to assist RANS modeling can be found in refs. [2, 21] with example codes available on the senior author's GitHub site [37].

5.4.1 Simulation setup

In this work, two test cases are employed to compare the performances of three representations of eigenvectors perturbations on Reynolds stress eigenvectors. The first test case is fully developed turbulent flow in a square duct. It is well known that RANS models have difficulty in predicting the secondary flow induced by Reynolds stress imbalances [38]. A schematic is presented in Fig. 5.2 to show the physical domain and the computational domain. A two-dimensional simulation is performed, since the flow is fully developed along the stream-wise direction. In addition, the computational domain only covers a quarter of the cross-section as shown in Fig. 5.2b due to the symmetry of the flow along y and z directions. All lengths are normalized by the height of the computational domain $h = 0.5D$, where D is the height of the duct. The Reynolds number Re is based on the height of the computational domain h and bulk velocity U_b.

The RANS simulations are performed in an open-source CFD platform OpenFOAM, using a built-in steady-state incompressible flow solver `simpleFoam` [39], in which the SIMPLE algorithm [40] is used. Launder-Gibson Reynolds stress transport model [41] is used for the RANS simulations of both the training flow and the test flow. In the RANS simulations, the y^+ of the first cell center is kept less than 1 and thus no wall model is applied. DNS data of

the training flows are obtained from Pinelli et al. [42].

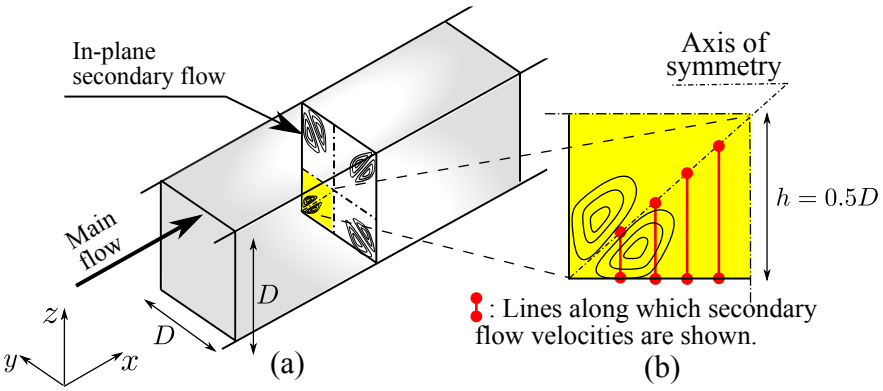

Figure 5.2: Computational domain for the flow in a square duct. The x coordinate represents the streamwise direction. Secondary flows induced by Reynolds stress imbalance exist in the y–z plane as shown in panel (a). Panel (b) shows that the computational domain covers a quarter of the cross-section of the physical domain.

Another training–prediction scenario consists of the flows over periodic hills as shown in Fig. 5.3. The test flow is the flow over periodic hills at $Re = 5600$. The geometry of the computational domain of the test flow is shown in Fig. 5.3. Compared to the test flow, the training flow is at the same Reynolds number but with a steeper hill profile as shown in Fig. 5.3 indicated by the dashed line. The Reynolds number Re is based on the crest height H and the bulk velocity U_b at the crest. Periodic boundary conditions are applied in the streamwise (x) direction, and non-slip boundary conditions are applied at the walls. Both the DNS simulations of the training flow and the test flow are performed by using Incompact3d [43]. In Incompact3d, the incompressible Navier–Stokes equations are solved on a Cartesian mesh using sixth-order finite-difference compact schemes for the spatial discretisation and a third-order Adams–Bashforth scheme for the time advancement. More details about the numerical methods used in Incompact3d can be found in [44]. A validation of our DNS results of velocity field and Reynolds stress components of the test flow show a good agreement with the results in literature [45]. All the baseline RANS simulations used Launder-Sharma k-ε model [46]. The y^+ of the first cell center is kept below 1, and thus no wall model is applied.

The *a priori* results are first studied to compare different metrics in this work without introducing machine learning. In the *a posteriori* results, the prediction error due to machine learning would be negligible if the same training and test data sets are used, and thus the results of this ideal situation are omitted. All the training-prediction scenarios in the *a posteriori* tests are summarized in Table 5.1. Scenario 1 is used to show the ideal scenario where the prediction performances based on discrepancy-based Euler angles and unit quaternion are comparable. Scenarios 2 and 3 are chosen to demonstrate the potential insufficiency of using discrepancy-based Euler angles in complex flow problems. It should be noted that the predictive capability of the machine-learning-based turbulence model is not the main focus

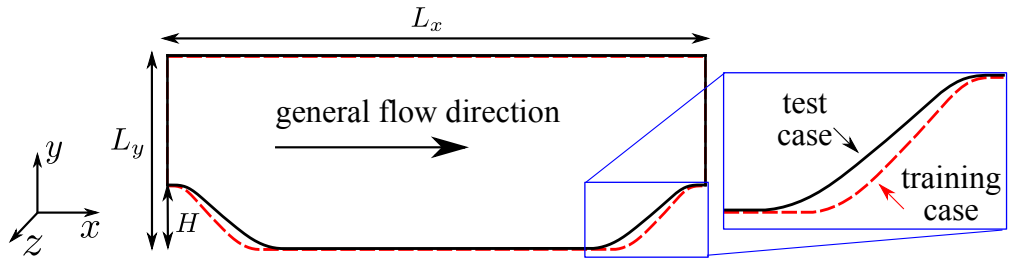

Figure 5.3: Computational domain for the flow over periodic hills. The solid line indicates the configuration of the test flow. A zoom-in view shows the comparison between the hill profiles of the training flow (dashed line) and the test flow (solid line). The hill width of the training flow is 0.8 of the hill width of the test flow. The x, y and z coordinates are aligned with streamwise, wall-normal, and spanwise, respectively.

of this work. Rather, the purpose of this paper is to illustrate the importance of embedding objectivity (frame-independence) in machine-learning-based physical modeling. Therefore, the similar training flow and test flow are intentionally chosen to make sure that the prediction error due to the difference between the training and test flows is small compared with the prediction error due to the inadequacy of discrepancy-based Euler angles with regard to frame-independence. On the other hand, the predictive capability of the machine-learning-assisted model was comprehensively investigated in [22], where different flows with massive separation were used as training flow and the prediction performance was evaluated. Two statistical metrics were also proposed in [22] to assess the prediction performance *a priori* by quantifying the difference of the training flow and the flow to be predicted.

Table 5.1: The training-prediction scenarios in *a posteriori* test.

Cases	Training set	Test set
1	Flow in a square duct at $Re = 2900$ [42]	Flow in a square duct at $Re = 3500$ [42]
2	Flow in a square duct at $Re = 2900$ (coordinate system rotated anti-clockwise by 60°)	Flow in a square duct at $Re = 3500$ [42]
3	Flow over periodic hills at $Re = 5600$ (steeper hill profile)	Flow over periodic hills at $Re = 5600$ [47]

5.4.2 Euler angles

In this *a priori* test, we first demonstrate that the discrepancy-based Euler angles are spatially smooth, while the direct-rotation-based Euler angles are not. It can be seen in

Figs. 5.4a–5.4c that the direct-rotation-based Euler angles lack the smoothness, particularly for the angles $\phi_1^{o\to *}$ and $\phi_3^{o\to *}$. Such lack of smoothness of Euler angles $\phi_1^{o\to *}$ and $\phi_3^{o\to *}$ can be explained by the rotation matrix $\mathbf{Q}$. Specifically, the angles $\phi_1^{o\to *}$ and $\phi_3^{o\to *}$ are determined by the ratio between off-diagonal terms of the rotation matrix $\mathbf{Q}$. In the scenario that the two eigenvectors systems are close to each other, it is expected that the rotation matrix $\mathbf{Q}$ would be diagonal dominant, and the off-diagonal terms should be small. However, the ratio between the off-diagonal terms are not necessarily small, and such ratio would be more sensitive to the change of off-diagonal Reynolds stress components. It explains the lack of smoothness for values of $\phi_1^{o\to *}$ and $\phi_3^{o\to *}$. On the other hand, it can be seen from Figs. 5.4d–5.4f that the discrepancy-based Euler angles are smoother than the original Euler angles. The main reason is that the discrepancy-based Euler angles are obtained based on the difference between two sets of direct-rotation-based Euler angles , i.e., one set from RANS modeled Reynolds stress and the other from DNS data, with respect to the same global reference frame. Thus, the effect of sensitivity issue due to the small off-diagonal components of Reynolds stress tends to be canceled out, and better spatial smoothness is achieved.

The spatial smoothness can also be achieved in most regions as shown in Fig. 5.5 by using unit quaternion to represent the eigenvectors perturbations. The volume-averaged magnitude of gradient $J(f)$ is defined in Eq. 5.8 to quantitatively compare the spatial smoothness for different representations of the eigenvectors perturbations:

$$J(f) = \frac{1}{V}\int_{\mathcal{V}} \|\nabla f\| dv \tag{5.8}$$

where V denotes the volume of the computational domain $\mathcal{V}$. As shown in Table 5.2, the direct-rotation-based Euler angles are much rougher across the whole domain than the other two schemes. Among the three, the unit quaternion achieved the best spatial smoothness based on the integral measure J. Noted that the spatial smoothness is not achieved in Fig. 5.5b near the diagonal of square duct, as indicated by dashed line. However, there are mean flow features within the invariant set of $\{\mathbf{S}, \mathbf{\Omega}, \nabla p, \nabla k\}$ with the similar antisymmetric pattern. Therefore, the smoothness of the functional form $f : \mathbf{q} \mapsto \Delta\mathbf{R}$ can still be guaranteed. In addition, all the four components of unit quaternion show either symmetric or anti-symmetric pattern along the diagonal of the square duct denoted by the dashed line, indicating that these four components are invariants under the rotation of reference frame. It demonstrates the main advantage of unit quaternion compared to the discrepancy-based Euler angles shown in the bottom row of Fig. 5.4. More detailed comparisons between these two representations are presented in the *a posteriori* tests below.

5.4.3 A posteriori results

In the posteriori tests, we investigate three training-prediction scenarios to demonstrate the merit of unit quaternion by comparing the machine learning performances of discrepancy-

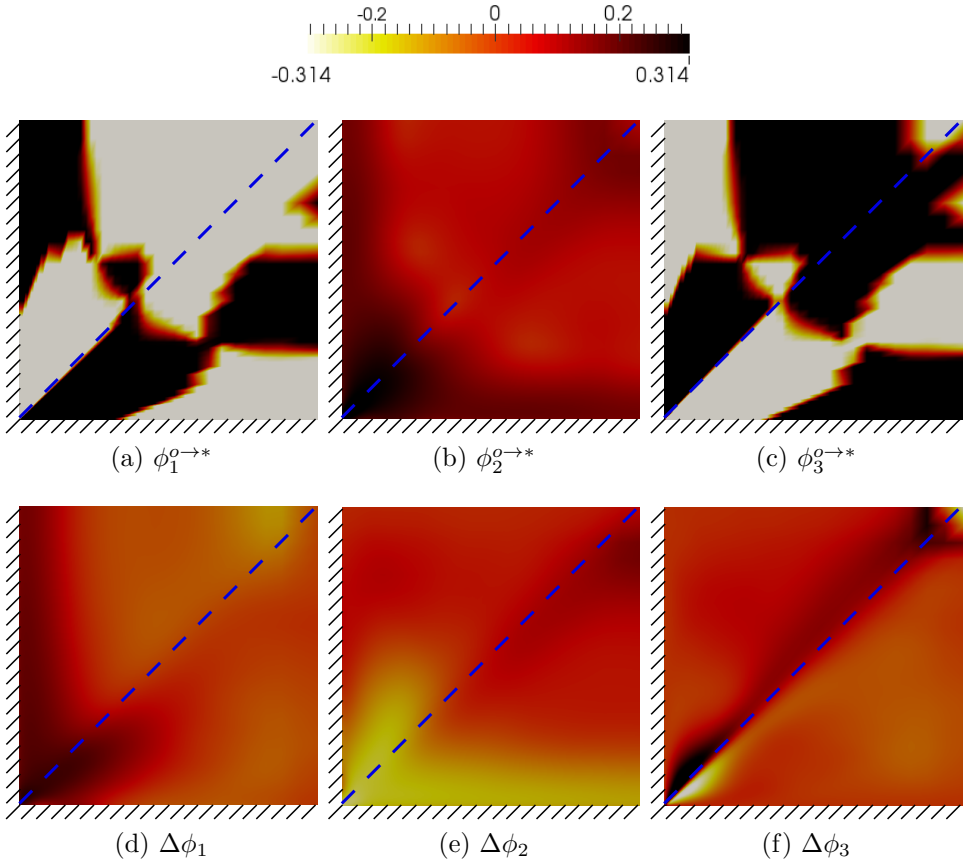

(a) $\phi_1^{o\to *}$ (b) $\phi_2^{o\to *}$ (c) $\phi_3^{o\to *}$

(d) $\Delta\phi_1$ (e) $\Delta\phi_2$ (f) $\Delta\phi_3$

Figure 5.4: Desired perturbations between the eigenvectors of the RANS modeled Reynolds stress and that of the DNS data, represented by direct-rotation-based Euler angles $\phi_\alpha^{o\to *}$ (top row) and discrepancy-based Euler angles $\Delta\phi_\alpha$ (bottom row). The dashed line denotes the diagonal of the square duct.

Table 5.2: Volume-averaged magnitude of gradient J as defined in Eq. 5.8, showing the comparison of the smoothness obtained by using three representations of the eigenvectors perturbations to the Reynolds stress tensor: direct-rotation-based Euler angle, discrepancy-based Euler angle, and unit quaternion. Symbol i denotes the index of each component.

scheme	$i = 1$	$i = 2$	$i = 3$
direct-rotation-based Euler angle, $J(\phi_i^{o\to *})$	8.63	0.45	8.40
discrepancy-based Euler angle, $J(\Delta\phi_i)$	0.46	0.47	0.93
unit quaternion, $J(h_i)$	0.01	0.24	0.26

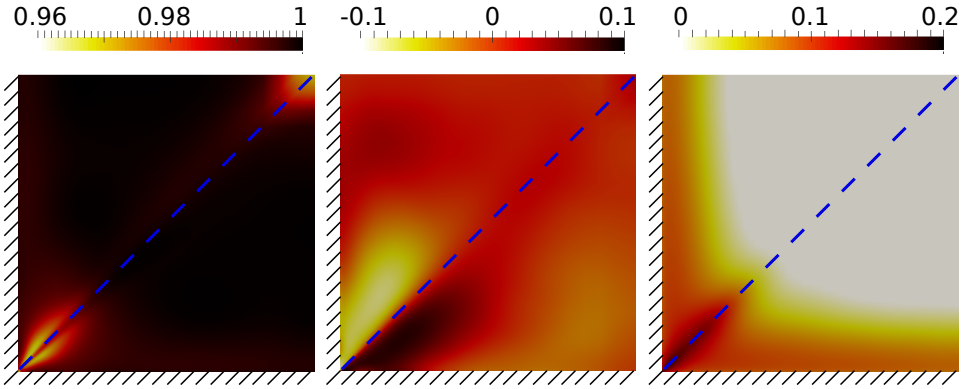

(a) h_1 (b) h_2 (c) h_3

Figure 5.5: The desired perturbation between the eigenvectors of the RANS modeled Reynolds stress and that of the DNS data, represented by unit quaternion $\mathbf{h}$. The component h_4 is omitted here since it can be expressed in terms of h_1, h_2, and h_3. The dashed line denotes the diagonal of the square duct.

based Euler angles and the unit quaternion.

Discrepancy-based Euler angles

In the first scenario, the flow in a square duct at $Re = 3500$ is predicted by using the flow at a lower Reynolds number $Re = 2900$ as the training case. We first present the prediction of discrepancy-based Euler angles in Fig. 5.6. It can be seen that the machine-learning-predicted discrepancy-based Euler angles demonstrate good agreements with the desired discrepancy-based Euler angles that perturb the eigenvectors of RANS modeled Reynolds stress to that of DNS data. The predictions of the desired perturbations of the eigenvalues and the turbulent kinetic energy (TKE) achieve the similar quality and thus are omitted here, considering that this work focuses on the perturbations of the eigenvectors.

The reconstructed Reynolds stress components R_{xy} and R_{xz} based on the machine learning prediction of discrepancy-based Euler angles are shown in Fig. 5.7. It should be noted that the machine-learning-predicted perturbations of the eigenvalues and the TKE are also employed in reconstructing the Reynolds stress components in all the following *a posteriori* tests. As shown in Fig. 5.7a, the Reynolds stress component R_{xy} is significantly overestimated by the baseline RANS simulation, especially at the near corner region. The baseline RANS modeled Reynolds stress component R_{xz} is not satisfactory either, particularly near the corner. Compared to the baseline RANS results, both the reconstructed components R_{xy} and R_{xz} show much better agreements with the DNS data. This satisfactory prediction performance demonstrates the capability of using discrepancy-based Euler angles in this specific training-prediction scenario, where the training case and the prediction case share

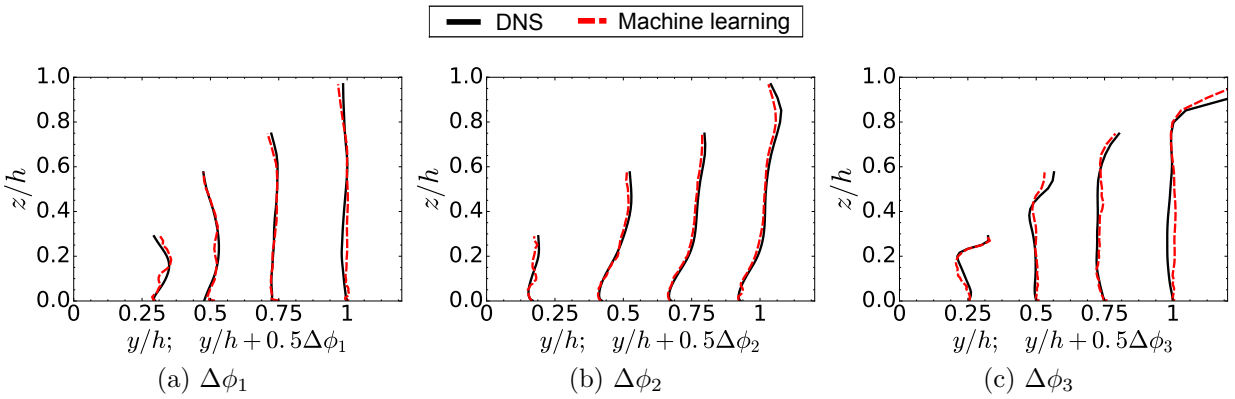

(a) $\Delta\phi_1$ (b) $\Delta\phi_2$ (c) $\Delta\phi_3$

Figure 5.6: The prediction of **discrepancy-based of Euler angles** for the flow in a square duct at $Re = 3500$, showing three components: (a) $\Delta\phi_1$, (b) $\Delta\phi_2$ and (c) $\Delta\phi_3$. The training flow is the flow in a square duct at $Re = 2900$.

the same geometry configuration and coordinate system.

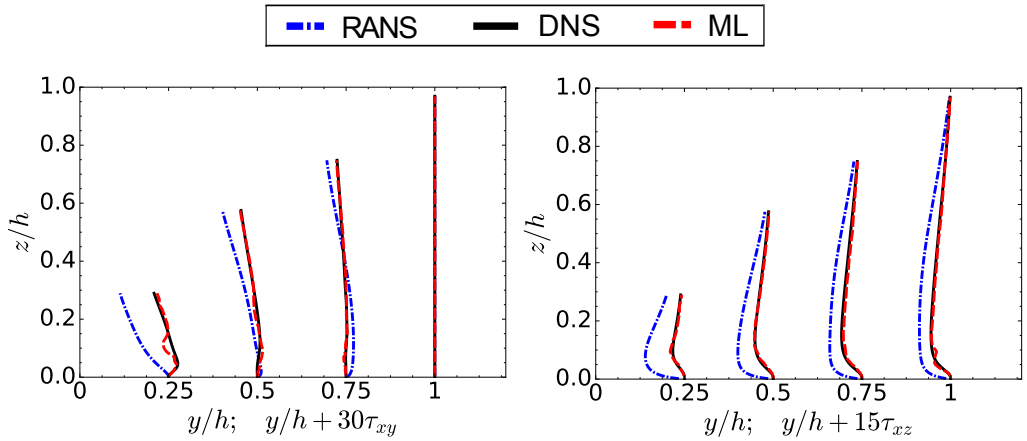

(a) R_{xy} (b) R_{xz}

Figure 5.7: The prediction of Reynolds stress components (a) R_{xy} and (b) R_{xz} based on **discrepancy-based Euler angles** for the flow in a square duct at $Re = 3500$. The training flow is the flow in a square duct at $Re = 2900$.

The second training-prediction scenario is chosen to demonstrate the shortcoming of the discrepancy-based Euler angles. The training flow and the test flow are the same as the first training-prediction scenario, while the coordinate system is rotated anti-clockwise by 60° for the training flow. The coordinate system of the test flow remains unchanged. The objective of this training-prediction scenario is to mimic the possible situation in complex flows in industrial applications, where the training flow and the test flow locally share the similar flow physics but different flow direction or orientations. In this situation, it is unlikely that a choice of global coordinate system is able to take into account the difference between

local flow directions, and thus the coordinate system relative to the flow direction would be different for the training flow and the test flow. The prediction of discrepancy-based Euler angles for the flow in a square duct at $Re = 3500$ is shown in Fig. 5.8. Compared to the prediction performance as shown in Fig. 5.6, the predicted discrepancy-based Euler angles in Fig. 5.8 is less satisfactory when different coordinate systems are applied to the training flow and the test flow. Specifically, the deterioration of Euler angles is more pronounced for $\Delta\phi_1$ and $\Delta\phi_2$. This is because the discrepancy-based Euler angles are not invariants under the rotation of the reference frame.

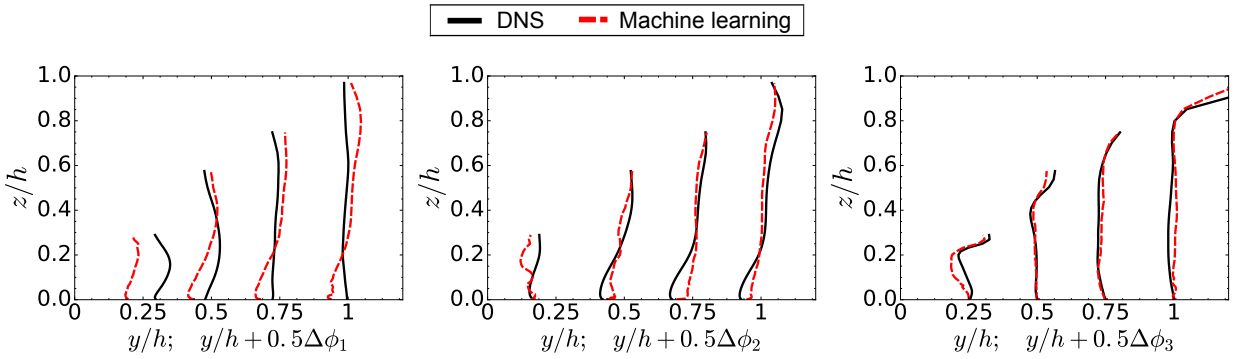

(a) $\Delta\phi_1$ (b) $\Delta\phi_2$ (c) $\Delta\phi_3$

Figure 5.8: The prediction of discrepancy-based Euler angles $\Delta\phi_\alpha$ for the flow in a square duct at $Re = 3500$. The training flow is the flow in a square duct at $Re = 2900$ with the coordinate system rotated by 60°.

The frame-dependence of discrepancy-based Euler angles is further demonstrated in Fig. 5.9 by comparing the contours of discrepancy-based Euler angles based on the original reference frame and the rotated reference frame. Since the machine learning prediction error is negligible by testing on the training data, the results in Fig. 5.9 can also be seen as *a posteriori* results on the training data. It can be seen that discrepancy-based Euler angle $\Delta\phi_1$ changes with the rotation of the reference frame. Another component of the discrepancy-based Euler angles $\Delta\phi_2$ also changes with the rotation of the reference frame and is omitted here for brevity. The change of discrepancy-based Euler angles of training flow would lead to a different trained regression function, since the inputs mean flow features are all invariants under the rotation of reference frame [48]. The frame-dependent nature of the discrepancy-based Euler angles explains the less satisfactory prediction performance as shown in Fig. 5.8. It demonstrates that the discrepancy-based Euler angles can potentially lead to poor prediction performance in the machine-learning-assisted turbulence modeling.

The reconstructed Reynolds stress components R_{xy} and R_{xz} based on the prediction of discrepancy-based Euler angles are shown in Fig. 5.10 for the second training–prediction scenario. Compared to the reconstructed Reynolds stress as shown in Fig. 5.7, the Reynolds stress components R_{xy} and R_{xz} show less satisfactory prediction performance. In the near-wall region, the prediction of the shear component R_{xy} is even worse than the baseline RANS

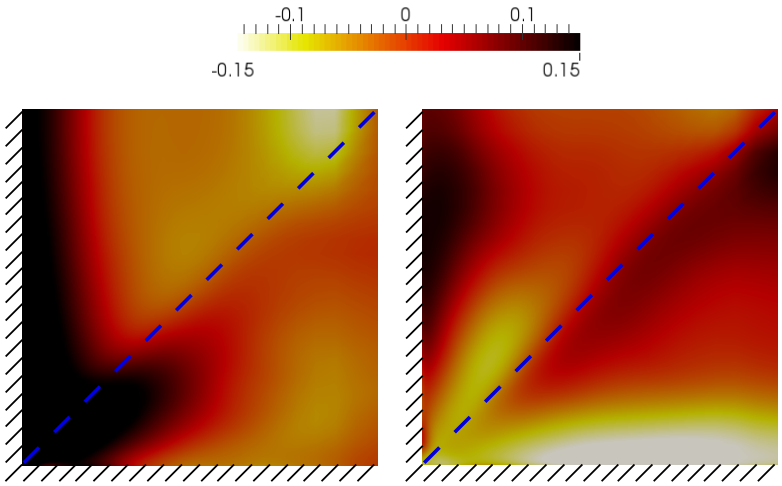

(a) Unrotated (b) Rotated

Figure 5.9: The discrepancy-based Euler angles $\Delta\phi_1$ between the RANS simulated Reynolds stress and the DNS data of the training flow in a square duct at $Re = 2900$. Panels (a) corresponds to the $\Delta\phi_1$ based on the original reference frame, for which the y and z axis align with the sidewall. Panels (b) corresponds to the $\Delta\phi_1$ based on the reference frame rotated by 60° anti-clockwise. The dashed line denotes the diagonal of the square duct.

simulated results. It demonstrates that the reconstructed Reynolds stress via machine-learning-predicted discrepancy-based Euler angles is potentially unreliable, even for the scenario where training flow and test flow share similar flow physics and only differ by Reynolds number (a relatively easy case for machine learning).

Unit quaternion

In the first training-prediction scenario, we also tested the use of the unit quaternion representation. The results of unit quaternion are shown in Fig. 5.11. It can be seen that the prediction performance of unit quaternion is similar to the prediction performance of discrepancy-based Euler angles as shown in Fig. 5.6. It is because the same geometry configuration and coordinate system are applied to both the training flow and the test flow. Thus, the frame-dependence of discrepancy-based Euler angles would not introduce additional errors into the machine learning prediction in this training-prediction scenario, explaining the similar prediction performance based on discrepancy-based Euler angles and unit quaternion.

The reconstructed Reynolds stress components R_{xy} and R_{xz} based on the prediction of unit quaternion also show satisfactory performance in Fig. 5.12. Such satisfactory prediction performance is comparable to the reconstructed Reynolds stress based on the prediction of discrepancy-based Euler angles shown in Fig. 5.7. It confirms that the similar prediction

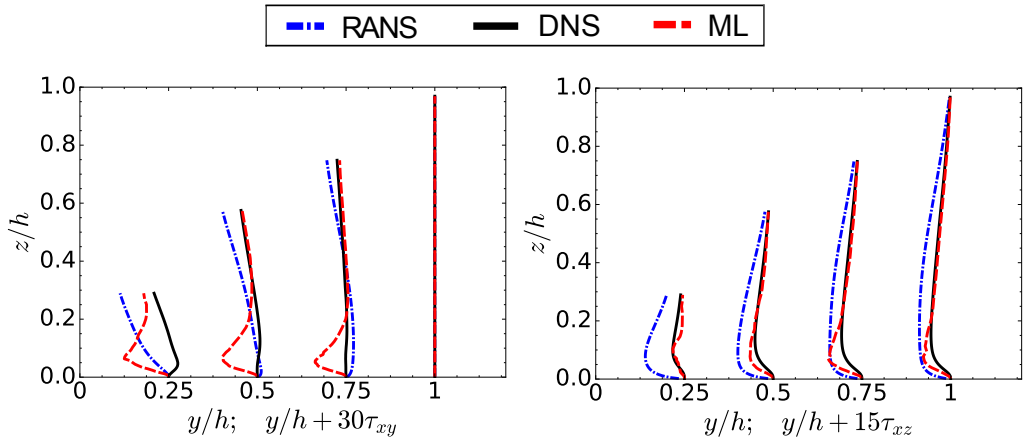

(a) R_{xy} (b) R_{xz}

Figure 5.10: The prediction of Reynolds stress components based on **discrepancy-based Euler angles** for the flow in a square duct at $Re = 3500$. The training flow is the flow in a square duct at $Re = 2900$ with the reference frame rotated by 60° anti-clockwise.

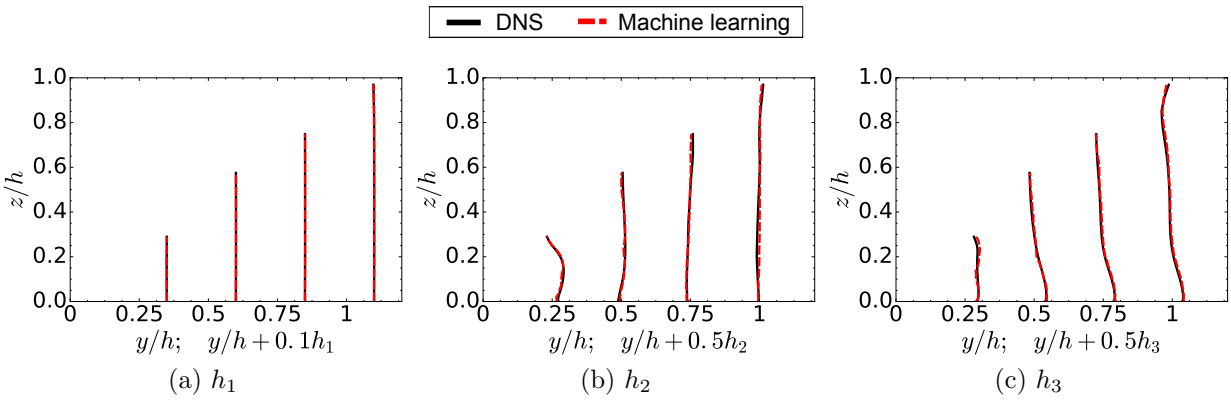

(a) h_1 (b) h_2 (c) h_3

Figure 5.11: The prediction of the components of unit quaternion for the flow in a square duct at $Re = 3500$. The training flow is the flow in a square duct at $Re = 2900$. The component h_4 is omitted here since unit quaternion only has three degrees of freedom.

performance can be achieved for Reynolds stress components based on either discrepancy-based Euler angles or unit quaternion in this ideal training-prediction scenario. It should be noted that the unit quaternion is invariant under the change of reference frame, and thus the results based on unit quaternion for the second training-prediction scenario as listed in Table 5.1 would be the same as the results shown in Figs. 5.11 and 5.12.

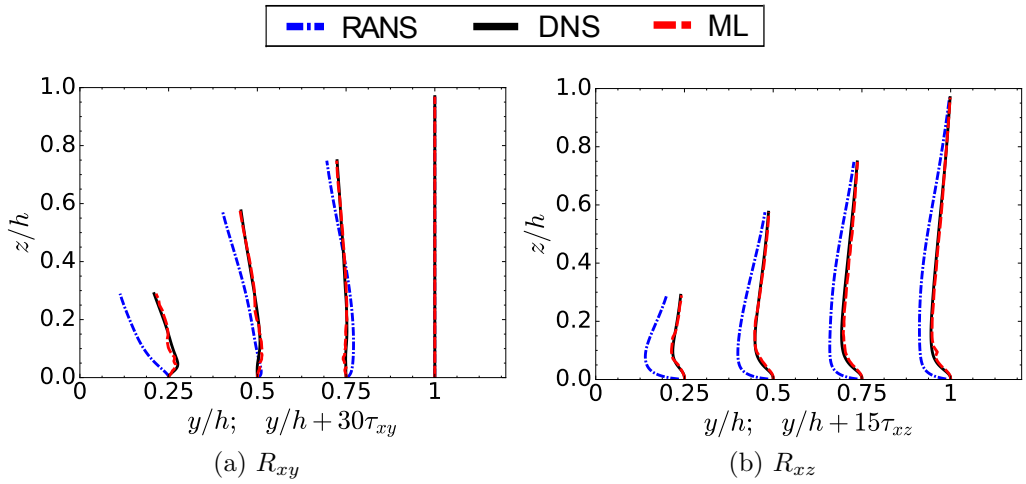

(a) R_{xy} (b) R_{xz}

Figure 5.12: The reconstructed Reynolds stress components based on the prediction of **unit quaternion** for the flow in a square duct at $Re = 3500$, including (a) shear component R_{xy} and (b) shear component R_{xz}. The training flow is the flow in a square duct at $Re = 2900$.

By investigating the third training-prediction scenario, we demonstrate the merit of unit quaternion representation in a more realistic application where training flow and test flow have different geometry configurations. Before comparing the results of Euler angles and unit quaternion, we first show the prediction performance of Reynolds stress anisotropy in Fig. 5.13. It can be seen that the RANS results of Reynolds stress anisotropy are significantly different from the DNS data. Specifically, the RANS predicted Reynolds stress is located along the line of plane strain due to the two dimensional assumption of RANS simulation. Unlike the RANS results, the DNS data show that the Reynolds stress anisotropy is close to the two-components axisymmetric state near the bottom wall. With the increase distance from the wall, the Reynolds stress anisotropy tends to approach the three components isotropic state, and gradually return toward the two components state while approaching the top wall. Figure 5.13 shows that the machine learning predicted Reynolds stress anisotropy successfully captures the trend of DNS data at several different locations. At $x/H = 3$ and $x/H = 4$, the machine learning predicted Reynolds stress anisotropy shows much better agreement with the DNS data. The reason of less satisfactory prediction at $x/H = 1$ and $x/H = 2$ is mainly due to the difference between the training flow and the test flow with regard to the steepness of the hill profile. However, it should be noted that the machine learning prediction at $x/H = 1$ and $x/H = 2$ still captures the trend of DNS data and also demonstrate quantitatively improvement than the RANS simulation results.

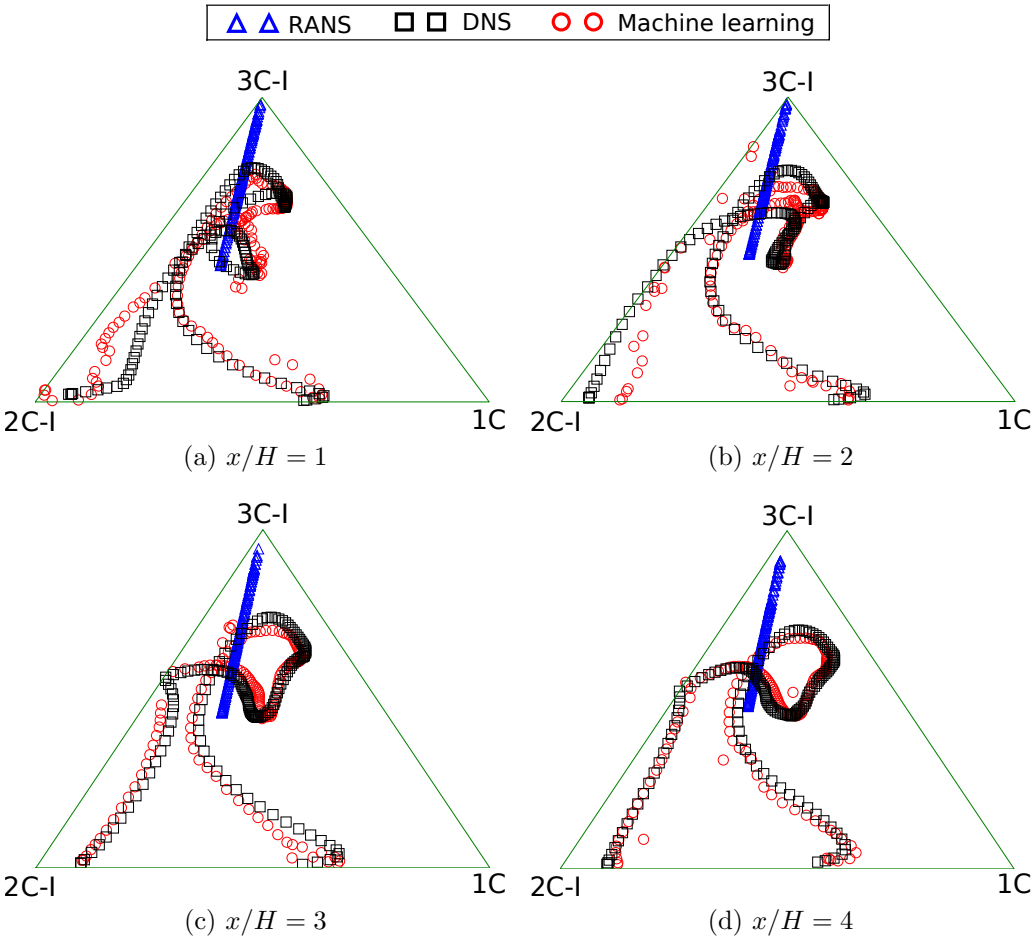

(a) $x/H = 1$ (b) $x/H = 2$

(c) $x/H = 3$ (d) $x/H = 4$

Figure 5.13: The Reynolds stress anisotropy in Barycentric triangle at $x/H = 1, 2, 3$ and 4. The three vertex of Barycentric triangle are indicated by 3C-I, 2C-I and 1C, representing the three components isotropic state, the two components axisymmetric state and the one component state, respectively. The bottom line of the Barycentric triangle denotes the two components state that corresponds to near wall turbulence due to the suppression of turbulence along the wall-normal direction.

The desired eigenvectors perturbations for the test flow are presented in Figs. 5.14 and 5.15. It can be seen in Fig. 5.14 that the desired perturbations via discrepancy-based Euler angles change with the rotation of the reference frame. The comparison shown in Fig. 5.14 confirms this drawback resulted from the frame-dependent nature of the discrepancy-based Euler angles. The Euler axis aligns along the spanwise direction for this 2-D flow. Without rotating the original reference frame, the perturbations via discrepancy-based Euler angles only involves a single rotation and thus the discrepancy-based Euler angle $\Delta\phi_1$ should be the same as the angle θ in the unit quaternion representation. However, more complex patterns can be seen in Figs. 5.14 in several regions. This is because the discrepancy-based Euler angles $\Delta\phi_2$ and $\Delta\phi_3$ are not exact zeros, which can be attributed to numerical noises.

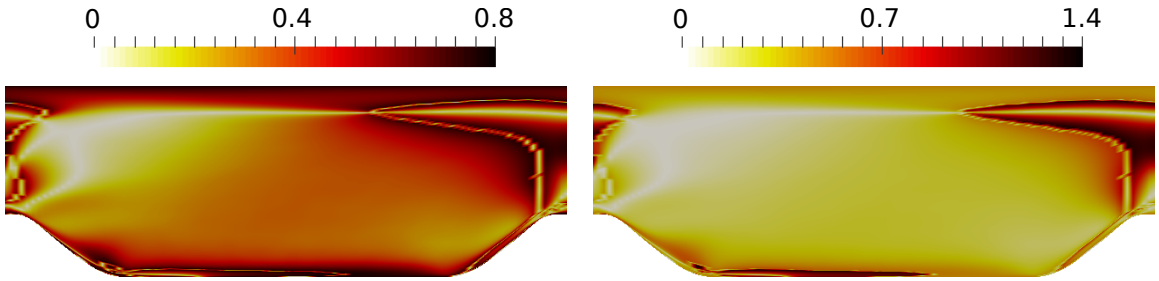

(a) Unrotated (b) Rotated

Figure 5.14: The magnitude of discrepancy-based Euler angles $\Delta\phi_1$ between the RANS simulated Reynolds stress and the DNS data of the flow over periodic hills at $Re = 5600$. The results of $\Delta\phi_2$ and $\Delta\phi_3$ are omitted here since they are all close to zeros based on the unrotated reference frame. Panels (a) corresponds to the $\Delta\phi_1$ based on the original reference frame, for which the x and z axis align with the streamwise direction and the spanwise direction. Panels (b) corresponds to the $\Delta\phi_1$ based on the reference frame rotated by 60° anti-clockwise with regard to the streamwise direction.

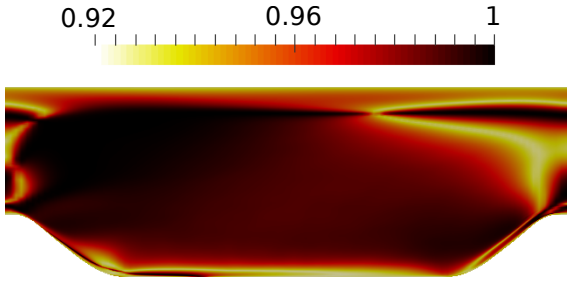

Figure 5.15: The desired perturbation h_1 between the eigenvectors of the RANS modeled Reynolds stress and that of the DNS data. The components h_2, h_3 and h_4 are omitted here since the Euler axis is known to be aligned along spanwise direction for this flow.

The reconstructed Reynolds stress shear component R_{xy} based on the prediction of discrepancy-based Euler angles is shown in Fig. 5.16a. It can be seen that the reconstructed shear stress

component R_{xy} is less satisfactory at the windward side of the hill, where the reconstructed R_{xy} is even worse than the RANS results within the near wall region. The main reason is that the different steepness of hill profiles lead to different local flow directions for the training flow and the test flow at this region. Due to the frame-dependent nature of discrepancy-based Euler angles, the trained machine-learning function from the training flow is not applicable to the test flow. Therefore, the reconstructed Reynolds stress component based on the predicted discrepancy-based Euler angles of the test flow is potentially worse than the baseline RANS results. It should be noted that the deterioration of the reconstructed shear stress component R_{xy} is less notable at the leeward of the hill, where the steepness of the hill profiles are also different for the training flow and the test flow. The main reason is that the turbulent kinetic energy is lower within the near wall region at leeward side of the hill, and thus the shifting of energy between the Reynolds stress components due to an inaccurate estimation of eigenvectors perturbation is less notable. Compared to the reconstructed Reynolds stress component in Fig. 5.16a, the reconstructed R_{xy} based on the prediction of unit quaternion shows a much better agreement with the DNS data at the windward of the hill, as highlighted by a zoom-in view in Fig. 5.16. For the leeward side of the hill, the reconstructed R_{xy} in Fig. 5.16b is also slightly better than the one shown in Fig. 5.16a. Therefore, unit quaternion provides a better representation of the eigenvectors perturbations to the Reynolds stress tensor in the context of machine-learning-assisted turbulence modeling. It can be seen that the prediction performance is less satisfactory at the leeward side in Figs. 5.16a and 5.16b, indicating that such less satisfactory prediction is mainly due to the geometry difference between the training flow and the test flow. The main reason is that the discrepancy between DNS and RANS shear stresses of the training flow is noticeably smaller than the discrepancy of the test flow at the leeward side of the hill as shown in Fig. 5.17. Therefore, the machine learning model tends to underestimate the shear stress τ_{xy} around this region in Fig. 5.16. The prediction of shear stress at the upper boundary is also less satisfactory by using discrepancy-based Euler angles. A possible explanation of the different prediction performances near the flat boundary layer regions is that the lower boundary and upper boundary have different complex patterns of Euler angles in Fig. 5.14a, and thus the machine learning model tends to have less satisfactory prediction near the flat boundary region. In contrast, the component h_1 in Fig. 5.15 has a simpler pattern near the lower wall, and thus the prediction of shear stress has a better performance near the flat boundary region as shown in Fig. 5.16b.

5.5 Conclusion

Introducing perturbations to stress tensors has important implications to model-form uncertainty estimation in RANS models and to machine-learning-assisted RANS modeling. Representing perturbations to Reynolds stress eigenvectors in the context of machine-learning-assisted modeling is challenging due to the requirements of mapping smoothness and frame-independence. In this work we formulated the eigenvector perturbations as rigid-body ro-

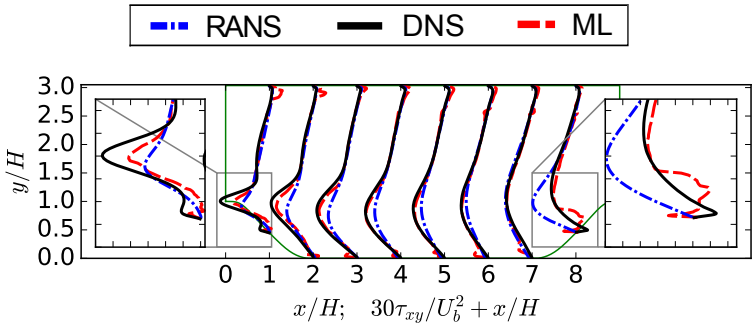

(a) Euler angles representation

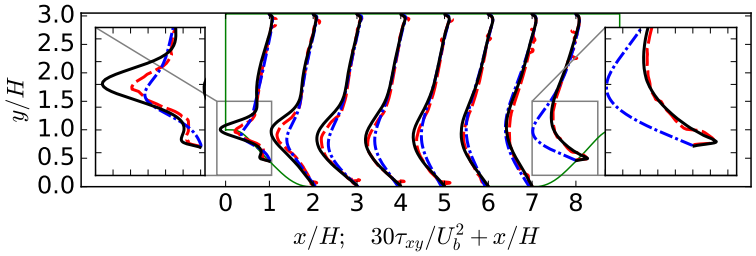

(b) Unit quaternion representation

Figure 5.16: The prediction of shear stress R_{xy} based on (a) discrepancy-based Euler angles and (b) unit quaternion for the flow over periodic hills at $Re = 5600$. The training flow is the flow over periodic hills at $Re = 5600$ with a steeper hill profile. A zoom-in view is added at both the windward side and the leeward side of the hill for clear comparison.

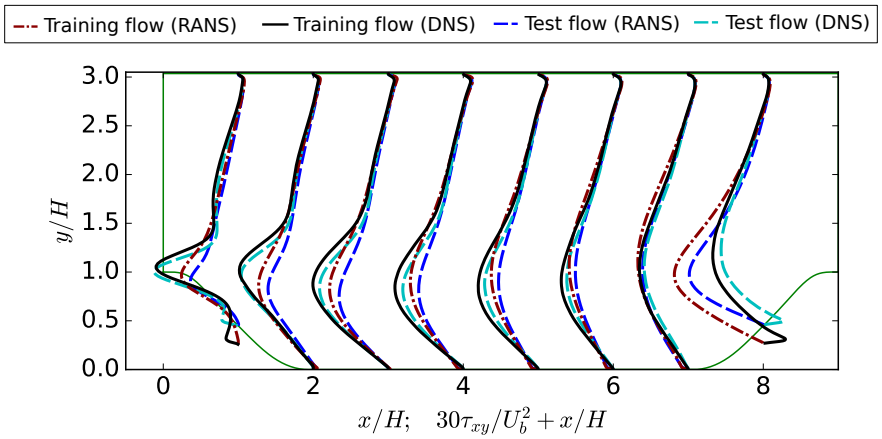

Figure 5.17: The comparison of DNS and RANS data of τ_{xy}. The hill width of the training flow is 0.8 of the hill width compared with the test flow as shown in Fig. 5.3.

tations and examined three representations: (1) the direct-rotation-based Euler angles, (2) the discrepancy-based Euler angles, and (3) the unit quaternion. A priori assessment of fully turbulent square duct flow shows that the direct-rotation-based Euler angles representation does not satisfy the smoothness requirement. On the other hand, the discrepancy-based Euler angle representation does not satisfy the frame-independence requirement, which has been shown theoretically and numerically with *a posteriori* tests on both the square duct flow and the flow over periodic hills. The numerical examples showed that the unit quaternion representation satisfies both requirements and is an ideal representation of Reynolds stress eigenvector perturbations. This finding has clear importance for uncertainty quantification and machine learning in turbulence modeling and for data-driven computational mechanics in general. For instance, it also has implications in other fields such as plasticity, where sequential increments of stress tensors are used to find the new stress state from the current one.

Acknowledgment

The authors would like to thank the two reviewers for their constructive and valuable comments, which helped improving the quality and clarity of this manuscript. The authors acknowledge Dr. Roney L. Thompson of Federal University of Rio de Janeiro and Dr. Jianxun Wang of University of Notre Dame for their helpful discussions during this work.

Bibliography

[1] D. C. Wilcox, Turbulence modeling for CFD, 3rd Edition, DCW Industries, 2006.

[2] J.-X. Wang, J.-L. Wu, H. Xiao, Physics-informed machine learning approach for reconstructing reynolds stress modeling discrepancies based on DNS data, Physical Review Fluids 2 (3) (2017) 034603.

[3] J. Ling, A. Kurzawski, J. Templeton, Reynolds averaged turbulence modelling using deep neural networks with embedded invariance, Journal of Fluid Mechanics 807 (2016) 155–166.

[4] A. P. Singh, S. Medida, K. Duraisamy, Machine learning-augmented predictive modeling of turbulent separated flows over airfoils, arXiv preprint arXiv:1608.03990.

[5] B. Tracey, K. Duraisamy, J. J. Alonso, A machine learning strategy to assist turbulence model development, AIAA Paper 1287 (2015) 2015.

[6] A. P. Singh, K. Duraisamy, Using field inversion to quantify functional errors in turbulence closures, Physics of Fluids 28 (2016) 045110.

[7] S. B. Pope, Turbulent Flows, Cambridge University Press, Cambridge, 2000.

[8] H. Xiao, J.-L. Wu, J.-X. Wang, Physics-informed machine learning for predictive turbulence modeling: Progress and perspectives, in: 2017 AIAA SciTech Forum and Exposition, 2017, Grapevine, TX, 2017 (AIAA, Reston, VA, 2017), paper 2017-1712.

[9] R. N. King, P. E. Hamlington, W. J. Dahm, Autonomic closure for turbulence simulations, Physical Review E 93 (3) (2016) 031301.

[10] A. Vollant, G. Balarac, C. Corre, Subgrid-scale scalar flux modelling based on optimal estimation theory and machine-learning procedures, Journal of Turbulence (2017) 1–25.

[11] M. Emory, J. Larsson, G. Iaccarino, Modeling of structural uncertainties in Reynolds-averaged Navier-Stokes closures, Physics of Fluids 25 (11) (2013) 110822.

[12] M. Emory, R. Pecnik, G. Iaccarino, Modeling structural uncertainties in Reynolds-averaged computations of shock/boundary layer interactions, AIAA paper 479 (2011) 1–16.

[13] M. A. Emory, Estimating model-form uncertainty in Reynolds-averaged Navier–Stokes closures, Ph.D. thesis, Stanford University (2014).

[14] S. Banerjee, R. Krahl, F. Durst, C. Zenger, Presentation of anisotropy properties of turbulence, invariants versus eigenvalue approaches, Journal of Turbulence 8 (32) (2007) 1–27.

[15] J. L. Lumley, G. R. Newman, The return to isotropy of homogeneous turbulence, Journal of Fluid Mechanics 82 (01) (1977) 161–178.

[16] R. Thompson, L. Sampaio, W. Edeling, A. A. Mishra, G. Iaccarino, A strategy for the eigenvector perturbations of the Reynolds stress tensor in the context of uncertainty quantification, in: Proceedings of the Summer Program, Center for Turbulence Research, 2016, p. 10.

[17] G. Iaccarino, A. A. Mishra, S. Ghili, Eigenspace perturbations for uncertainty estimation of single-point turbulence closures, Physical Review Fluids 2 (2) (2017) 024605.

[18] J.-X. Wang, R. Sun, H. Xiao, Quantification of uncertainties in turbulence modeling: A comparison of physics-based and random matrix theoretic approaches, International Journal of Heat and Fluid Flows 62 (2016) 577–592.

[19] J.-X. Wang, J.-L. Wu, J. Ling, G. Iaccarino, H. Xiao, Towards a complete framework of physics-informed machine learning for predictive turbulence modeling, Tech. rep., Proceedings of Summer Research Program, Center of Turbulence Research, Stanford University, Stanford, CA, USA (2016).

[20] K. Duraisamy, G. Iaccarino, H. Xiao, Turbulence modeling in the age of data, Annual Review of Fluid Mechanics, in press, vol 51, 2018.

[21] J.-L. Wu, H. Xiao, E. Paterson, Physics-informed machine learning approach for augmenting turbulence models: A comprehensive framework, Physical Review Fluids 3 (7) (2018) 074602.

[22] J.-L. Wu, J.-X. Wang, H. Xiao, J. Ling, A priori assessment of prediction confidence for data-driven turbulence modeling, Flow, Turbulence and Combustion 99 (2017) 25–46.

[23] D. Q. Huynh, Metrics for 3d rotations: Comparison and analysis, Journal of Mathematical Imaging and Vision 35 (2) (2009) 155–164.

[24] J. J. Kuffner, Effective sampling and distance metrics for 3d rigid body path planning, in: Robotics and Automation, 2004. Proceedings. ICRA'04. 2004 IEEE International Conference on, Vol. 4, IEEE, 2004, pp. 3993–3998.

[25] B. K. Horn, Closed-form solution of absolute orientation using unit quaternions, JOSA A 4 (4) (1987) 629–642.

[26] D. J. Heeger, A. Jepson, Simple method for computing 3d motion and depth, in: Computer Vision, 1990. Proceedings, Third International Conference on, IEEE, 1990, pp. 96–100.

[27] P. Domingos, A few useful things to know about machine learning, Communications of the ACM 55 (10) (2012) 78–87.

[28] T. A. Oliver, R. D. Moser, Bayesian uncertainty quantification applied to RANS turbulence models, in: Journal of Physics: Conference Series, Vol. 318, IOP Publishing, 2011, p. 042032.

[29] J.-X. Wang, J.-L. Wu, J. Ling, G. Iaccarino, H. Xiao, Physics-informed machine learning for predictive turbulence modeling: Towards a complete framework, Tech. rep., Center of Turbulence Research, Proceedings of the Summer Program, Stanford University (2016).

[30] A. Simonsen, P.-Å. Krogstad, Turbulent stress invariant analysis: Clarification of existing terminology, Physics of Fluids 17 (8) (2005) 088103.

[31] S. Pope, A more general effective-viscosity hypothesis, Journal of Fluid Mechanics 72 (02) (1975) 331–340.

[32] J. Ling, R. Jones, J. Templeton, Machine learning strategies for systems with invariance properties, Journal of Computational Physics 318 (2016) 22–35.

[33] J. Ling, R. Jones, J. Templeton, Machine learning strategies for systems with invariance properties, Journal of Computational Physics 318 (2016) 22–35.

[34] H. Goldstein, The Euler angles, Classical Mechanics, (1980) 143–148.

[35] J. B. Kuipers, et al., Quaternions and rotation sequences, Vol. 66, Princeton University press Princeton, 1999.

[36] L. Breiman, Random forests, Machine learning 45 (1) (2001) 5–32.

[37] Data-driven turbulence modeling with physics-informed machine learning, `https://github.com/xiaoh/turbulence-modeling-PIML` (2018).

[38] A. Huser, S. Biringen, Direct numerical simulation of turbulent flow in a square duct, Journal of Fluid Mechanics 257 (1993) 65–95.

[39] H. G. Weller, G. Tabor, H. Jasak, C. Fureby, A tensorial approach to computational continuum mechanics usi ng ject-oriented techniques, Computers in physics 12 (6) (1998) 620–631.

[40] S. Patankar, Numerical heat transfer and fluid flow, CRC press, 1980.

[41] M. Gibson, B. Launder, Ground effects on pressure fluctuations in the atmospheric boundary layer, Journal of Fluid Mechanics 86 (03) (1978) 491–511.

[42] A. Pinelli, M. Uhlmann, A. Sekimoto, G. Kawahara, Reynolds number dependence of mean flow structure in square duct turbulence, Journal of Fluid Mechanics 644 (2010) 107–122.

[43] S. Laizet, N. Li, Incompact3d: A powerful tool to tackle turbulence problems with up to o (105) computational cores, International Journal for Numerical Methods in Fluids 67 (11) (2011) 1735–1757.

[44] S. Laizet, E. Lamballais, High-order compact schemes for incompressible flows: A simple and efficient method with quasi-spectral accuracy, Journal of Computational Physics 228 (16) (2009) 5989–6015.

[45] M. Breuer, N. Peller, C. Rapp, M. Manhart, Flow over periodic hills: Numerical and experimental study in a wide range of reynolds numbers, Computers & Fluids 38 (2) (2009) 433–457.

[46] B. Launder, B. Sharma, Application of the energy-dissipation model of turbulence to the calculation of flow near a spinning disc, Letters in Heat and Mass Transfer 1 (2) (1974) 131–137.

[47] M. Breuer, N. Peller, C. Rapp, M. Manhart, Flow over periodic hills–numerical and experimental study in a wide range of reynolds numbers, Computers & Fluids 38 (2) (2009) 433–457.

[48] J. Ling, J. Templeton, Evaluation of machine learning algorithms for prediction of regions of high Reynolds averaged Navier Stokes uncertainty, Physics of Fluids (1994-present) 27 (8) (2015) 085103.

Chapter 6

A Priori Assessment of Prediction Confidence for Data-Driven Turbulence Modeling

(Published on *Flow, Turbulence and Combustion*, 99 (1), 25-46, 2017.)

J.-L. Wu, J.-X. Wang, H. Xiao
Department of Aerospace and Ocean Engineering, Virgina Tech, Blacksburg, VA, 24061, USA

Abstract

Although Reynolds-Averaged Navier–Stokes (RANS) equations are still the dominant tool for engineering design and analysis applications involving turbulent flows, standard RANS models are known to be unreliable in many flows of engineering relevance, including flows with separation, strong pressure gradients or mean flow curvature. With increasing amounts of 3-dimensional experimental data and high fidelity simulation data from Large Eddy Simulation (LES) and Direct Numerical Simulation (DNS), data-driven turbulence modeling has become a promising approach to increase the predictive capability of RANS simulations. However, the prediction performance of data-driven models inevitably depends on the choices of training flows. This work aims to identify a quantitative measure for *a priori* estimation of prediction confidence in data-driven turbulence modeling. This measure represents the distance in feature space between the training flows and the flow to be predicted. Specifically, the Mahalanobis distance and the kernel density estimation (KDE) technique are used as metrics to quantify the distance between flow data sets in feature space. To examine the relationship between these two extrapolation metrics and the machine learning model prediction performance, the flow over periodic hills at $Re = 10595$ is used as test set and seven flows with different configurations are individually used as training sets. The results

show that the prediction error of the Reynolds stress anisotropy is positively correlated with Mahalanobis distance and KDE distance, demonstrating that both extrapolation metrics can be used to estimate the prediction confidence *a priori*. A quantitative comparison using correlation coefficients shows that the Mahalanobis distance is less accurate in estimating the prediction confidence than KDE distance. The extrapolation metrics introduced in this work and the corresponding analysis provide an approach to aid in the choice of data source and to assess the prediction performance for data-driven turbulence modeling.

6.1 Introduction

Even with the rapid growth of available computational resources, numerical models based on Reynolds-Averaged Navier–Stokes (RANS) equations are still the dominant tool for engineering design and analysis applications involving turbulent flows. However, the development of turbulence models has stagnated–the most widely used general-purpose turbulence models (e.g., k-ε models, k-ω models, and the S–A model) were all developed decades ago. These models are known to be unreliable in many flows of engineering relevance, including flows with three-dimensional structures, swirl, pressure gradients, or curvature [1]. This lack of accuracy in complex flows has diminished the utility of RANS as a predictive simulation tool for use in engineering design, analysis, optimization, and reliability assessments.

Recently, data-driven turbulence modeling has emerged as a promising alternative to traditional modeling approaches. While data-driven methods come in many formulations and with different assumptions, the basic idea is that a model or correction term is determined based on data. In the context of turbulence, this data can come from either experiments or high fidelity simulations such as Direct Numerical Simulations (DNS) or well-resolved Large Eddy Simulations (LES). Koumoutsakos [2] trained neural networks on channel flow DNS data and applied them to the modeling of near-wall turbulence structures. Tracey et al. [3] used neural networks to predict the Reynolds stress anisotropy and source terms for transport equations of turbulence quantities (e.g., $\tilde{\nu}_t$ for the S–A model and ω for k-ω models). Duraisamy et al. [3, 4] have used Gaussian processes to predict the turbulence intermittency and correction terms for the turbulence transport equations. Ling and Templeton [5] trained random forest classifiers to predict when RANS assumptions would fail. Ling et al. [6, 7] further used random forest regressors and neural networks to predict the Reynolds stress anisotropy. Wang et al. [8] have recently investigated the use of random forests to predict the discrepancies of RANS modeled Reynolds stresses in separated flows. These studies show the significant and growing interest in applying data-driven machine learning techniques to turbulence modeling.

However, Tracey et al. [3], Ling and Templeton [5], and Wang et al. [8] all reported that their data-driven closures had diminished performance on flows that were significantly different from the ones on which they were trained. Such findings underline the importance of properly choosing the training flows. For instance, if a machine learning model for the eddy viscosity

is trained on a database of attached boundary layer flows, then it would not be surprising if the model had poor performance when making predictions on a flow with separation. In the general context of data-driven modeling, the *training set* is the set of data to which the model is fit or calibrated. The *test set* is the set of data on which the model makes predictions. It is expected that the prediction performance will not be satisfactory if the test set is significantly different from the training sets.

A key question, then, is how to determine whether the test flow is "different" from the training flows. Test flow that might appear very different could, in fact, be well-supported in the training set. For example, a model trained on flow around an airfoil might perform well on a channel flow because it will have encountered developing boundary layers in its training set. Conversely, a model trained on attached flow around an airfoil might perform very poorly on stalled flow around an airfoil, even though the flow configurations appear quite similar. Because many of these data-driven models are formulated such that their inputs are the local flow variables, it is the local flow regimes that must be well-supported in the training set, not any specific global geometry. The degree to which the test flow is well-supported by training data will in large part determine the reliability of the model closure. In deploying these data-driven models, then, it will be crucial to have efficient metrics of determining if a test flow is an extrapolation from the training set.

Ling and Templeton [5] presented one promising option for quantifying model extrapolation. They used a statistical metric called the Mahalanobis distance to calculate the probability that a test point was drawn from the training distribution, and showed that their machine learning model error was significantly higher on test points with high Mahalanobis distances. However, they did not carry out a thorough investigation of the correlation between the Mahalanobis distance and machine learning model accuracy for different test sets and training sets. Because the Mahalanobis distance assumes that the training data have a multivariate Gaussian distribution, it is not clear how generally applicable this metric will be for different flow cases. Therefore, this paper will investigate two different statistical metrics of extrapolation, the Mahalanobis distance and the distance based on Kernel Density Estimation (KDE), for a variety of training sets. These extrapolation metrics will be analyzed and compared in the context of a machine learning framework for the prediction of Reynolds stresses developed by Wang et al. [8]. The ultimate goal of this work is to provide quantitative metrics to assess the prediction confidence *a priori*, in order to guide the choice of training set when applying data-driven turbulence modeling.

The rest of the paper is organized as follows. Section 6.2 will describe the machine learning methodology of Wang et al. [8] and the database of flows used for training and testing. Section 6.3 will describe different extrapolation metrics and their relative advantages and disadvantages. Section 6.4 will analyze the performance of these extrapolation metrics in predicting the regions of high uncertainty in the machine learning models, and Section 6.5 will present conclusions and ideas for next steps.

6.2 Machine Learning Methodology

In this section we summarize the Physics-Informed Machine Learning (PIML) framework proposed by Wang et al. [8], which will be used to evaluate the efficacy of the proposed extrapolation metrics. However, note that extrapolation metrics proposed in this work are not specific to the PIML framework. Particular emphasis is placed on applications where the feature space input has high dimensions (10 to 100 features), which is typical in computational mechanics problems and in other complex physical systems (see e.g., [9]).

The overarching goal of the work of Wang et al. [8] is a physics-informed machine learning framework for turbulence modeling. The problem can be formulated as follows: given high-fidelity data for the Reynolds stresses from DNS or well-resolved LES on a database of flows, predict the Reynolds stresses on a new flow for which only RANS data are available. The flows used to fit the machine learning model are referred to as *training flows*, while the flow for which the model is evaluated is referred to as the *test flow*. It is assumed that the training flows and the test flow have similar flow physics.

Wang et al. [8] trained machine learning models to predict a corrector for the Reynolds stress tensor. The procedure is summarized as follows:

1. Perform baseline RANS simulations on both the training flows and the test flow.
2. Compute the feature vector $\mathbf{q}(\mathbf{x})$ based on the RANS state variables.
3. Compute the discrepancies field $\Delta\tau_\alpha(\mathbf{x})$ of the RANS modeled Reynolds stresses for the training flows based on the high-fidelity data, where $\Delta\tau_\alpha = \tau_\alpha^{RANS} - \tau_\alpha^{truth}$.
4. Construct regression functions $f_\alpha : \mathbf{q} \mapsto \Delta\tau_\alpha$ for the discrepancies based on the training data prepared in Step 3. These regression functions were constructed using random forest regressors [10].
5. Compute the Reynolds stresses discrepancies for the test set by evaluating the regression functions. The Reynolds stresses can subsequently be obtained by correcting the baseline RANS predictions with the evaluated discrepancies.

In machine learning terminology the discrepancies $\Delta\tau_i$ here are referred to as *responses*, the feature vector $\mathbf{q}$ as the *input*, and the mappings $f_\alpha : \mathbf{q} \mapsto \Delta\tau_\alpha$ as *regression functions*.

There are three essential components in the physics-based machine learning framework outlined above: (1) identification of mean flow features as input, (2) representation of Reynolds stresses as responses, and (3) construction of regression functions from training data. The three components of the framework are presented below. The reader is referred to [8] for further details.

6.2.1 Identification of Mean Flow Features as Regression Input

Ten features based on the RANS computed mean flow fields (velocity U_i and pressure P) are identified as inputs to the regression function, which is consistent with the mean flow features listed in the work by Wang et al. [8]. Most of these features are adopted from the work by Ling and Templeton [5], with an additional feature of mean streamline curvature. It is because that RANS models tend to be less reliable at the regions with large streamline curvature, thus including it as a mean flow feature helps in detecting those regions. Turbulence intensity is another mean flow feature in the work by Wang et al. [8], since it is an important feature in describing turbulence. Similarly, the turbulence time scale is also chosen as a feature to better describe the turbulence. Wang et al. [8] also chose the wall-distance based Reynolds number as a mean flow feature, since the presence of wall dampens the wall normal fluctuation and thus has a important impact upon the Reynolds stress anisotropy. The pressure gradient along streamline is also used as a mean flow feature, even though a uniform acceleration of an incompressible flow does not alter the turbulence. The main reason is that Reynolds stress discrepancy between the RANS simulation and DNS/LES simulation is to be predicted, and this discrepancy is influenced by dp/dx_i. For example, the RANS simulation is usually more reliable for the equilibrium boundary layer, but is less reliable for the boundary layer with strong acceleration. Therefore, larger Reynolds stress discrepancy can be expected for the boundary layer with strong acceleration, and the inclusion of dp/dx_i helps in distinguishing such scenario. Most of the mean flow features are normalized within the range between -1 to 1, except for the wall-distance based on Reynolds number that lies within the range between 0 to 2. With the same length of range, the Euclidean distance along different features is comparable to each other. The normalization also facilitate machine learning and is a common practice there.

These mean flow features are adopted from the data-driven turbulence modeling framework [8] to ensure consistency. A detailed list of the ten mean flow features used in this work can be found in the work by Wang et al. [8]. However, it should be noted that the current work focuses on the investigation of a priori assessing the closeness of flow features between the training flows and the test flow, and the *a priori* confidence assessment metrics in this work is directly applicable to other choice of mean flow features. All these features are independent under rotation, translation or reflection of the coordinate system. However, some of them are not Galilean invariant, e.g., the normalization factor U_iU_i and the streamline curvature $D\mathbf{\Gamma}/Ds$ that are dependent on the velocity of a moving reference frame. Therefore, the authors recommend the use of fixed coordinate systems for both the training and prediction flows.

6.2.2 Representation of Reynolds Stress Discrepancy as Regression Response

The discrepancies of RANS predicted Reynolds stresses, or more precisely the magnitude, shape and orientation thereof, are identified as responses of the regression functions. It has been shown that these discrepancies are likely to be universal among flows of the same characteristics, and thus the regression function constructed based on them can be extrapolated to new flows [8]. To obtain the components, the Reynolds stress tensor is decomposed as follows [12, 13]:

$$\boldsymbol{\tau} = 2k\left(\frac{1}{3}\mathbf{I} + \mathbf{A}\right) = 2k\left(\frac{1}{3}\mathbf{I} + \mathbf{V}\Lambda\mathbf{V}^T\right) \tag{6.1}$$

where k is the turbulent kinetic energy, which indicates the magnitude of $\boldsymbol{\tau}$; $\mathbf{I}$ is the second order identity tensor; $\mathbf{A}$ is the anisotropy tensor; $\mathbf{V} = [\mathbf{v}_1, \mathbf{v}_2, \mathbf{v}_3]$ and $\Lambda = \mathrm{diag}[\lambda_1, \lambda_2, \lambda_3]$ with $\lambda_1 + \lambda_2 + \lambda_3 = 0$ are the orthonormal eigenvectors and eigenvalues of $\mathbf{A}$, respectively, indicating its shape and orientation.

In the Barycentric triangle shown schematically in Fig. 6.1, the eigenvalues λ_1, λ_2, and λ_3 are mapped to the Barycentric coordinates as follows [14]:

$$C_1 = \lambda_1 - \lambda_2 \tag{6.2a}$$
$$C_2 = 2(\lambda_2 - \lambda_3) \tag{6.2b}$$
$$C_3 = 3\lambda_3 + 1\ , \tag{6.2c}$$

where $C_1 + C_2 + C_3 = 1$. Placing the triangle in a Cartesian coordinate $\boldsymbol{\xi} \equiv (\xi, \eta)$, the location of any point within the triangle is a convex combination of those of the three vertices, i.e.,

$$\boldsymbol{\xi} = \boldsymbol{\xi}_{1c}C_1 + \boldsymbol{\xi}_{2c}C_2 + \boldsymbol{\xi}_{3c}C_3 \tag{6.3}$$

where $\boldsymbol{\xi}_{1c}$, $\boldsymbol{\xi}_{2c}$, and $\boldsymbol{\xi}_{3c}$ denote coordinates of the three vertices of the triangle. Consequently, the coordinate $\boldsymbol{\xi} \equiv (\xi, \eta)$ uniquely identifies the shape of the anisotropy tensor.

In this work, the discrepancies of the coordinate $\Delta\boldsymbol{\xi} \equiv (\Delta\xi, \Delta\eta)$ are chosen as the regression responses, where $\Delta\xi = \xi_{DNS} - \xi_{RANS}$ and $\Delta\eta = \eta_{DNS} - \eta_{RANS}$ represent the discrepancy between the RANS predicted Reynolds stress anisotropy and the DNS data.

6.2.3 Random Forest for Building Regression Functions

With the input (mean flow features $\mathbf{q}$) and responses (Reynolds stress discrepancies $\Delta\tau_i$) identified above, an algorithm is needed to map from the input to the responses. In this work, random forest regression is employed [15]. Random forest regression is an ensemble learning technique that aggregates predictions from a number of decision trees. In decision tree learning, a tree-like model is built to predict the response variable by learning simple

decision rules from the training data. While decision trees have the advantages of being computationally efficient and amenable to interpretation, they tend to overfit the data, i.e., yield models that reproduce the training data very well but predict poorly for unseen data. In random forest regression, an ensemble of trees is built with bootstrap aggregation samples (i.e., sampling with replacement) drawn from the training data [16]. Moreover, only a subset of randomly chosen features is used when constructing each split in each tree, which reduces the correlation among the trees in the ensemble. By aggregating a large number of trees obtained in this manner, random forests can achieve significantly improved predictive performance and largely avoid overfitting. In addition, random forests can provide an relative importance score for each input feature by counting the times of splitting within the decision trees based on the given flow feature. These importance scores reflect the influence of the choice of flow features on the training-prediction performance. More detailed discussion of the feature importance can be found in the work by Wang et al. [8]. Random forest regression is a widely used regression method in machine learning community. Compared to the neural network, the random forest is less prone to overfitting and is thus more robust as pointed out by Breiman [15].

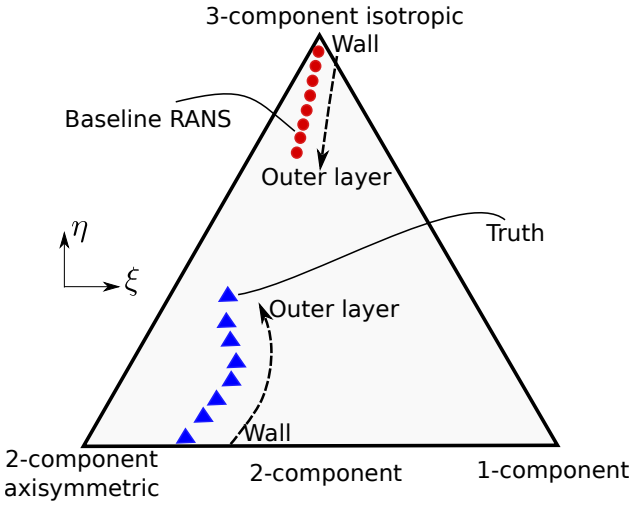

Figure 6.1: The Barycentric triangle that encloses all physically realizable states of the Reynolds stresses [14, 17]. The position within the Barycentric triangle represents the anisotropy state of the Reynolds stress. The three corners represent the limiting states.

6.3 Extrapolation Metrics

6.3.1 Motivation with Machine Learning Based Predictive Turbulence Modeling

The machine learning framework as summarized in Section 6.2 was used by Wang et al. [8] to predict Reynolds stresses in conjunction with standard RANS models. The objective was to predict the Reynolds stress in the flow over period hills at $Re = 10595$. Training flows were chosen from the NASA benchmark database [18] including (1) the flow over periodic hills at $Re = 1400$ (PH1400), 2800 (PH2800) and 5600 (PH5600) [19], (2) the flow past a curved backward facing step (CBFS13200) at $Re = 13200$ [20], (3) the flow in a converging-diverging channel (CDC11300) at Re=11300 [21], (4) the flow past a backward facing step (BFS4900) at $Re = 4900$ [22], and (5) the flow in a channel with wavy bottom wall (WC360) at $Re = 360$ [23]. The geometries and the flow characteristics of these flows are illustrated in Fig. 6.2. The Reynolds numbers are defined based on the bulk velocity U_b at the narrowest cross-section in the flow and the height H of the crest or step.

In this study we conducted an extensive evaluation of the machine learning based prediction of Reynolds stresses, in the context of extrapolation detection. In order to isolate the contribution of the data from each flow to the predictive capability and to simplify the performance assessment, each flow above is individually used for training as opposed to combining several flows. In general, our experiences suggest that better predictive performance is obtained when the training flow and the prediction flow are more similar. For example, since the test case is the flow over periodic hills at $Re = 10595$, the predictive performance is the best when the training case is the flow in the same geometry but at a different Reynolds number $Re = 5600$. In contrast, the performance is the least favorable when the backward step flow $Re = 4900$ or the wavy channel flow $Re = 360$ is used as training flow. Physical intuition suggests that the backward step and wavy channel cases are the furthest from the prediction flow in feature space. This is because the backward step has a sudden expansion (as opposed to the gradual expansion in the periodic hill geometry) and the wavy channel flow has a Reynolds number ($Re = 360$) that is drastically different from that in the test case ($Re = 10595$). The other two flows (curved step and converging–diverging channel) fall between the two extremes above because their geometries are qualitatively similar to that of the test case, and their Reynolds numbers (13200 and 11700) are comparable to 10595 as well. Hence, the predictive performances of different training cases agree well with our physical understanding of degrees of similarity between the training and test flows. However, when data-driven models are used in practical flows, the similarity between the prediction flow and various candidate sets of training flows is usually not clear. The performances of data-driven models depend on the similarity between the training flows and the test flow. Predicting the test flow with significantly different flow physics from the training flows is potentially catastrophic. To prevent these consequences that may stem from bad judgment from users of data-driven models, in this work we propose the extrapolation metrics that

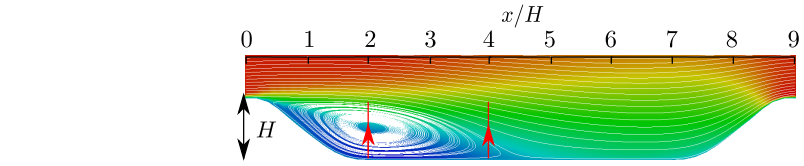

(a) Periodic hills, $Re = 10595$

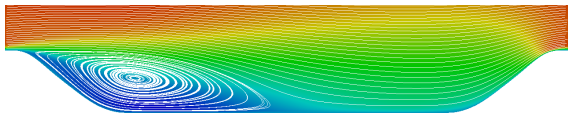

(b) Periodic hills, $Re = 5600$

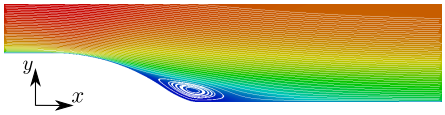

(c) Curved backward step, $Re = 13200$

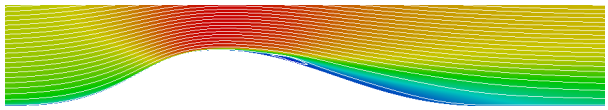

(d) Converging–diverging channel, $Re = 11700$

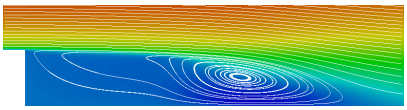

(e) Backward facing step $Re = 4700$

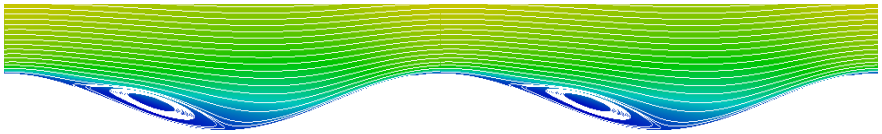

(f) Wavy channel, $Re = 360$

Figure 6.2: The mean velocity field and separation bubble of the test set and different training sets. The test set is (a) the flow over periodic hills at $Re = 10595$. The training sets include (b) the flow over periodic hills at $Re = 5600$, $Re = 2800$ and $Re = 1400$ (only the flow at $Re = 5600$ is shown here for simplicity), (c) the flow over curved backward facing step at $Re = 13200$, (d) the flow in a converging-diverging channel at $Re = 11300$, (e) the flow over a backward facing step at $Re = 4900$, and (f) the flow in a channel with wavy bottom wall at $Re = 360$. The test set is the flow over periodic hills at $Re = 10595$. All the flow fields illustrated in this figure are obtained based on RANS simulations, in which Launder-Sharma k-ϵ model [28] is used. The lines with arrows in panel (a) indicate the profile locations for the anisotropy presented in Figs. 6.4 and 6.5.

objectively quantifies the similarity between the training flows and the test flow. These extrapolation metrics can assess the prediction performance of the data-driven model *a priori*, and they also have the potential to provide guidelines for selecting more suitable training flows to improve the prediction.

6.3.2 Extrapolation Metrics

Before presenting the details of the two metrics investigated in this work, we examine a few apparently attractive candidates of extrapolation metrics based on nearest neighbor distances and marginal distributions. We discuss and illustrate why they are not suitable.

The idea behind extrapolation metrics is to determine the extrapolation distance between a given test point or test set and the training data. There are several different approaches for quantifying this distance. One metric would be the *nearest neighbor distance*. The nearest neighbor distance is the Euclidean distance in feature space between the test point and the nearest point in the training set. Because this nearest neighbor distance is susceptible to noise, a common variation is the K^{th} nearest neighbor distance [24], which is the Euclidean distance to the K^{th} nearest point in the training set, where K is some pre-determined integer. Unfortunately, these methods are unwieldy–they require retaining the entire training database to compare against. In turbulence simulations, even the mean flow data from a single simulation can consume many gigabytes of memory, so transferring the training database to each user of the machine learning model based on these training data sets is impractical.

Another seemingly appealing yet equally unsuitable indicator of distance between two sets of points is the *marginal probability density functions*. This is illustrated in Fig. 6.3 for the simple example of a two-dimensional feature space. This figure shows two data sets S_1 and S_2 have identical marginal densities (indicated by the bell-shaped curves on the two axes) but cover distinctly different regions in the feature space. If S_1 is used for training to predict the response of points in S_2, most of the evaluations would involve aggressive extrapolations, and thus poor predictive performance would be expected. The situation will be even more pronounced in higher-dimensional feature spaces.

After evaluating a number of alternatives, we identified the Mahalanobis distance and Kernel Density Estimation (KDE) as two promising metrics for evaluating the predictive performance of training–prediction methods. In both metrics, only the inputs of the training and test data are used and information of the response is not needed. More importantly, only the statistical quantities (e.g., mean, covariance, estimated probability density function of the training set) are used, and the complete raw training data set is not needed. This characteristic leads to much lower memory consumption, which is in contrast to the nearest neighbor distance methods.

The Mahalanobis distance [25] is an efficient method of representing the extrapolation dis-

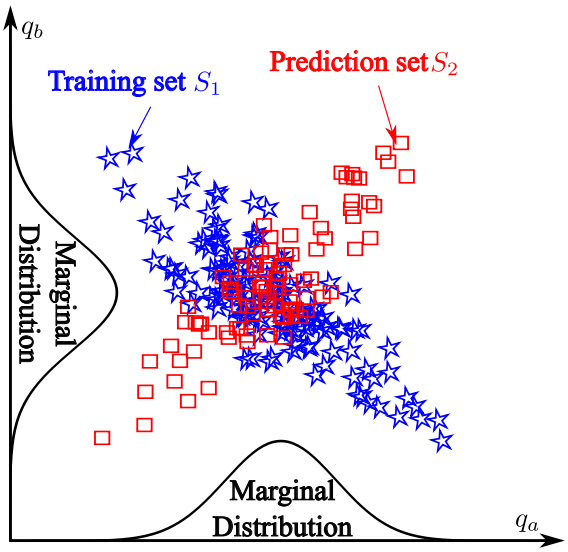

Figure 6.3: Illustration of two data sets that have identical marginal distributions but cover different regions in feature space.

tance that does not rely on marginal distributions. The Mahalanobis distance is defined as the distance between a point $\tilde{\mathbf{q}}$ and the mean of the training points $\boldsymbol{\mu}$, scaled by the covariance matrix Σ of the training points,

$$D = \sqrt{(\tilde{\mathbf{q}} - \boldsymbol{\mu})^T \Sigma^{-1} (\tilde{\mathbf{q}} - \boldsymbol{\mu})} \tag{6.4}$$

The basic idea of the Mahalanobis distance is that it measures the distance between a point and a distribution–in this case, the distribution of training points. The larger the Mahalanobis distance, the greater the degree of extrapolation. To determine the Mahalanobis distance of a test point, it is not necessary to compare against all of the training data–only the mean and covariance matrix of the training data must be saved, which is highly memory efficient.

In this paper, the Mahalanobis distance has been normalized based on percentiles from the training set. The normalized Mahalanobis distance of a test point is given by $1 - \gamma_{dm}$, where γ_{dm} is the fraction of training points with a larger raw Mahalanobis distance than the test point. This normalization ensures that the distance lies in the range between 0 and 1, with a normalized distance of 0 indicating no extrapolation and a distance of 1 indicating very high extrapolation. With this normalization convention, larger raw Mahalanobis distance leads to larger normalized distance. This is because the raw Mahalanobis distance takes into account the scattering of the training flow points by incorporating the covariance matrix Σ. Therefore, larger raw distance means the distance from the test flow point to the mean of the training flow points is greater relative to the scattering of the training flow points. In other words, fewer training points have a greater raw distance than the raw distance of the test flow point, and thus a larger normalized Mahalanobis distance can be expected.

An underlying assumption for the Mahalanobis distance is that the training set distribution is a multivariate Gaussian. However, this may be a poor assumption in many turbulent flows, where multi-modal distributions may be common. Therefore, the performance of the Mahalanobis distance as an extrapolation metric will be compared against Kernel Density Estimation (KDE) [26]. KDE is a method of approximating the distribution of the training data. The KDE at a point $\tilde{\mathbf{q}}$ from a distribution of training data $\mathbf{q}_i$ for $i = 1, \cdots, n$ is:

$$\hat{f} = \frac{1}{n\sigma} \sum_{i=1}^{n} K \left(\frac{\tilde{\mathbf{q}} - \mathbf{q}_i}{\sigma} \right) \tag{6.5}$$

Often, a Gaussian kernel is used, and the bandwidth σ is the standard deviation of the Gaussian kernel. In this work, the bandwidth is determined based on Scott's rule [27].

Unlike the Mahalanobis distance, the Gaussian KDE distance does not assume that the training set has a multivariate Gaussian distribution. Instead, it has a much less stringent assumption–that the training data distribution can be approximated as a sum of multivariate Gaussians. KDE can be used as an extrapolation metric by determining the probability that a given test point was drawn from the training data. The KDE distance has been normalized by comparing the KDE probability estimation to a uniform distribution, as shown in Eq. 6.6.

$$D_{KDE} = 1 - \frac{P_{KDE}}{P_{KDE} + 1/A} \tag{6.6}$$

In Eq. 6.6, D_{KDE} is the normalized KDE distance and P_{KDE} is the KDE probability estimate. A is the area in state space covered by the training set: $A = \prod_i (q_{i,max} - q_{i,min})$. This normalization therefore compares how likely a point is given the KDE probability distribution estimate versus a uniform distribution. As with the normalized Mahalanobis distance, this normalized KDE distance varies from 0 (no extrapolation) to 1 (high extrapolation).

The trade-off between the Mahalanobis distance and the KDE distance is between memory efficiency and flexibility. While the Mahalanobis distance is more memory efficient–it only requires retaining the mean and covariance matrix of the training data–it also makes strong assumptions about the Gaussian nature of the training data. The KDE distance requires much more memory usage, since it stores the convolution of the Gaussian kernel with the entire training set. However, it is able to account for strongly non-Gaussian training data distributions. Therefore, a key question addressed by this paper is whether the Mahalanobis distance is an effective extrapolation metric, or whether the Gaussian assumption undermines its efficiency. The KDE method , which does not make this assumption, is less memory efficient and more computationally costly.

In this paper we will investigate the effectiveness of these two extrapolation metrics in detecting regions of extrapolation for data-driven turbulence closures. It should be noted that the calculations of these two extrapolation metrics only involve the RANS simulated mean flow field. This is because the high fidelity data are usually unavailable for the flow to

be predicted. For the RANS simulations, the same RANS model is used for both the training flows and the test flow, and the extrapolation metrics are calculated based on these RANS simulations. Compared to DNS/LES, RANS simulations may fail to detect a flow feature and miss the correct flow topology. For instance, the separation would be falsely suppressed with a much shallower hill for the flow over periodic hills. Assuming shallower hill in both the training flow and the test flow, a similar suppression effect would exist for both flows if k-ε model is used, and the closeness between these two flows can still be detected. However, if such suppression only occurs in the training flows and is absent in the test flow, the extrapolation metrics would not suggest a close relationship between the training flows and the test flow, which can be seen as a conservative choice of estimating closeness between flow physics. As we used RANS simulations, the calculated extrapolation metrics would depend on the choice of RANS model. This impact of RANS model selection is especially desirable for the data-driven turbulence modeling, since the mean flow features used as inputs in the existing data-driven turbulence modeling [8, 7] are obtained based on RANS simulations. The extrapolation metrics are thus calculated based on the RANS simulations to assess the closeness of these inputs between the training flows and the test flow. In this work we explore the correlation of these extrapolation metrics with the machine learning prediction error for the test case where the high-fidelity data is available. By demonstrating such positive correlation, these two metrics can be used as indicators of the machine learning performance for the flows where the high-fidelity data are absent.

6.4 Numerical Results

In this work, the extrapolation metrics based on Mahalanobis distance and kernel density estimation are assessed for a given test set and several different training sets. The relationship between machine learning prediction performance and these extrapolation metrics is also studied. The flow over periodic hills [19] at $Re = 10595$ is chosen as the test set. As shown in Section 6.3, seven different training sets are employed in this work. The flow configurations of training sets are illustrated in Fig. 6.2. It should be noted that only the lower part ($y/H < 1.2$) of the training set is used for the random forest regression due to the available high fidelity data from training sets. For all the baseline RANS simulations, Launder-Sharma k-ϵ model [28] is used. It should be noted that the method proposed in this work is also directly applicable to other RANS models. However, the same RANS model needs to be employed for both the calculation of extrapolation metrics and the data-driven turbulence modeling procedure to ensure consistency. The y^+ of the first cell center is kept less than 1 and thus no wall model is applied. The RANS simulations are performed in an open-source CFD platform OpenFOAM, using a built-in steady-state incompressible flow solver `simpleFoam` [29], in which the SIMPLE algorithm is used. We choose the steady-state solver because the flow problems investigated in this work are all steady-state problems. For the numerical schemes, second-order central difference scheme is chosen for all terms except for the convection term, which is discretized with second-order upwind scheme.

The random forest regression is performed based on each of the training sets. The number of max features is set as 6, considering that there are 10 input features in this work. The number of trees is set as 100. This number is chosen by observing the out-of-bag (OOB) error to avoid possible overfitting on the training sets. We have observed the OOB error with different numbers of trees (50, 100, 150) and this error is not sensitive based on our current setting of the number of trees. Representative results for the Reynolds stress anisotropy from four of the training sets are shown in Figs. 6.4 and 6.5. The Reynolds stress anisotropy profiles were taken along two lines at $x/H = 2$ and $x/H = 4$, both of which are within the recirculation region. It can be seen in Figs. 6.4(a) and 6.5(a) that the predicted Reynolds stress anisotropies are in good agreement with the benchmark data if the flow over periodic hills at $Re = 5600$ is used as the training set. The prediction is less accurate but still captures the general pattern of benchmark data if the flow at $Re = 1400$ is used as training set. If the training set is the flow over curved step, the predicted Reynolds stress anisotropy is still significantly improved versus the default RANS predictions and the pattern of the benchmark data is generally predicted as shown in Figs. 6.4(c) and 6.5(c). The predicted Reynolds stress anisotropy state is significantly less accurate if the training set is the flow in a channel with a wavy bottom wall as shown in Figs. 6.4(d) and 6.5(d). In this work, these quantities that directly predicted by the trained discrepancy functions are compared with the extrapolation metrics. The reconstructed Reynolds stress components can be found in a separate work by Wang et al. [8]. It should be noted that the specification of DNS Reynolds stress into RANS equations would reduce the robustness of the numerical simulation [30, 31]. For the data-driven turbulence modeling, some attempts to propagate the predicted Reynolds stress to the mean velocity via RANS equations can be found in the work by Wang et al. [32]. The comparison in Figs. 6.4 and 6.5 indicates that the prediction performance depends on the choice of the training set. If the training set is closely related to the test set, e.g., the geometry is the same and the Reynolds number is slightly different, the predicted Reynolds stress anisotropy is more reliable. To assess the confidence of the prediction in the practical scenario where benchmark data are not available, the closeness between different flows needs to be defined.

We use the Mahalanobis distance and the KDE distance as extrapolation metrics to gauge the closeness between different flows in feature space. The distribution of normalized Mahalanobis distance between the flow over periodic hills at $Re = 10595$ and each training set is shown in Fig. 6.6. For the training set with same geometry but different Reynolds numbers, it can be seen in Fig. 6.6 that the mean Mahalanobis distance increases as the difference between the Reynolds numbers becomes larger. This is consistent with the empirical knowledge that flows with same geometric configuration are often closely related if the Reynolds number difference is small.

For the training sets with a different geometry, it can be seen in Fig. 6.6(b) that the Mahalanobis distances are generally greater than that shown in Fig. 6.6(a). In addition, the Mahalanobis distances based on the flow in a wavy channel are generally larger than the Mahalanobis distances based on the flow over curved step. Compared with the prediction

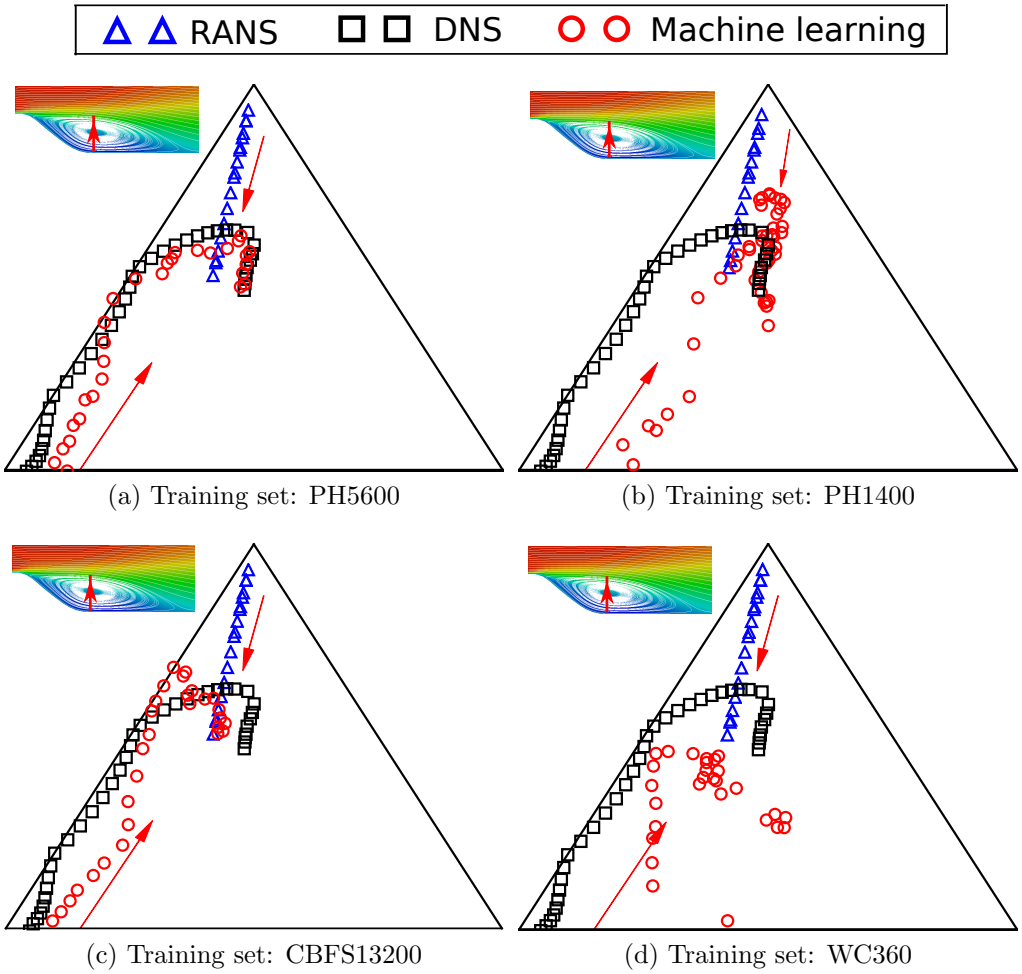

(a) Training set: PH5600

(b) Training set: PH1400

(c) Training set: CBFS13200

(d) Training set: WC360

Figure 6.4: Prediction of Reynolds stress anisotropy for the flow over periodic hills at $Re = 10595$ along the line at $x/H = 2$. The panels show the Reynolds stress anisotropy (a) with the flow over periodic hills at $Re = 5600$ (PH5600) as training set, (b) with the flow over periodic hills at $Re = 1400$ (PH1400) as training set, (c) with the flow over curved backward facing step (CBFS13200) as training set and (d) with the flow in wavy channel (WC360) as training set.

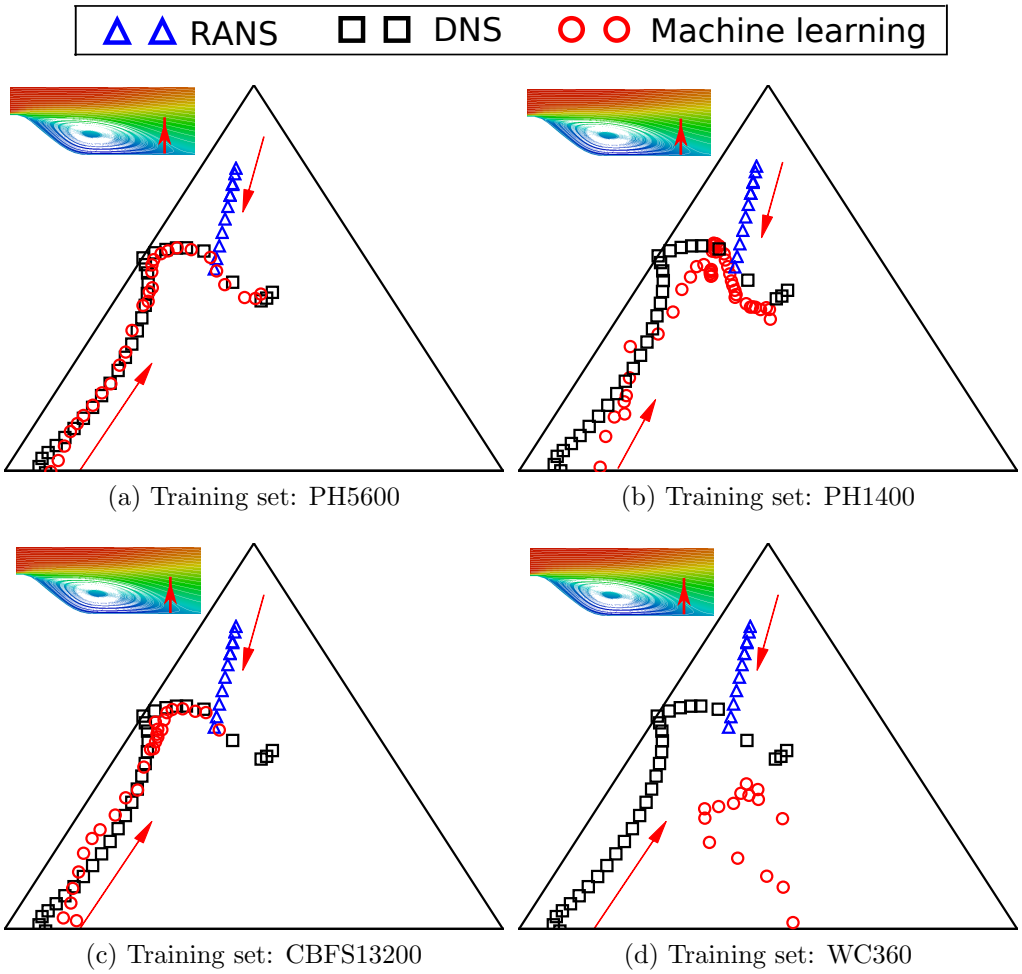

(a) Training set: PH5600

(b) Training set: PH1400

(c) Training set: CBFS13200

(d) Training set: WC360

Figure 6.5: Prediction of Reynolds stress anisotropy for the flow over periodic hills at $Re = 10595$ along the line at $x/H = 4$. The panels show the Reynolds stress anisotropy (a) with the flow over periodic hills at $Re = 5600$ (PH5600) as training set, (b) with the flow over periodic hills at $Re = 1400$ (PH1400) as training set, (c) with the flow over curved backward facing step (CBFS13200) as training set and (d) with the flow in wavy channel (WC360) as training set.

performance as shown in Figs. 6.4 and 6.5, this suggests that the Mahalanobis distance can be an indicator to estimate the prediction performance when the benchmark data are not available. In practice, the normalized Mahalanobis distances can be obtained *a priori* based on the mean flow features from training set and test set. Generally speaking, smaller mean Mahalanobis distance indicates that the RANS simulation of the training set is more similar to the RANS simulation of the test set. Assuming that similar RANS simulation results indicate similar flow physics, better prediction performance can be expected.

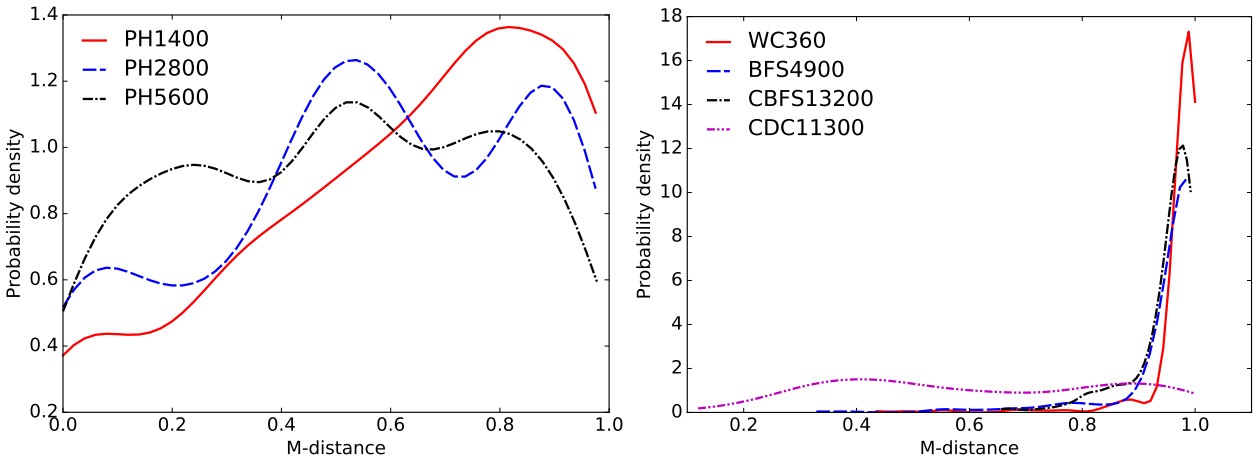

(a) Reynolds number extrapolation (b) Geometry extrapolation

Figure 6.6: Probability density function of Mahalanobis distance based on different training sets. (a) The distribution of Mahalanobis distance based on Reynolds number extrapolation. (b) The distribution of Mahalanobis distance based on geometry extrapolation. All the Mahalanobis distances have been normalized into the range from zero to one, as detailed in Section 6.3.

Similar to the Mahalanobis distance, the KDE distances are generally smaller for Reynolds number extrapolation as shown in Fig. 6.7(a), compared with the KDE distances based on geometry extrapolation as shown in Fig. 6.7(b). This is consistent with the Mahalanobis distance results as shown in Fig. 6.6, indicating that Mahalanobis distance can provide an overall reliable extrapolation estimation in spite of its Gaussian distribution assumption.

By analyzing the mean prediction error of Reynolds stress anisotropy based on different training sets, we can see that there is a positive correlation between mean prediction error of Reynolds stress anisotropy and the extrapolation metrics as shown in Fig. 6.8. Figure 6.8 also shows that the Mahalanobis distance based on geometry extrapolation is close to one and the standard deviation is much smaller than that based on Reynolds number extrapolation. A possible explanation is that the normalization procedure may lead to a dense clustering near the value of one. Compared to the KDE distance as shown in Fig. 6.8(b), it can be seen in Fig. 6.8(a) that the trend of Mahalanobis distance is similar to that of KDE distance for different training sets. This result suggests that the Mahalanobis distance, while simpler,

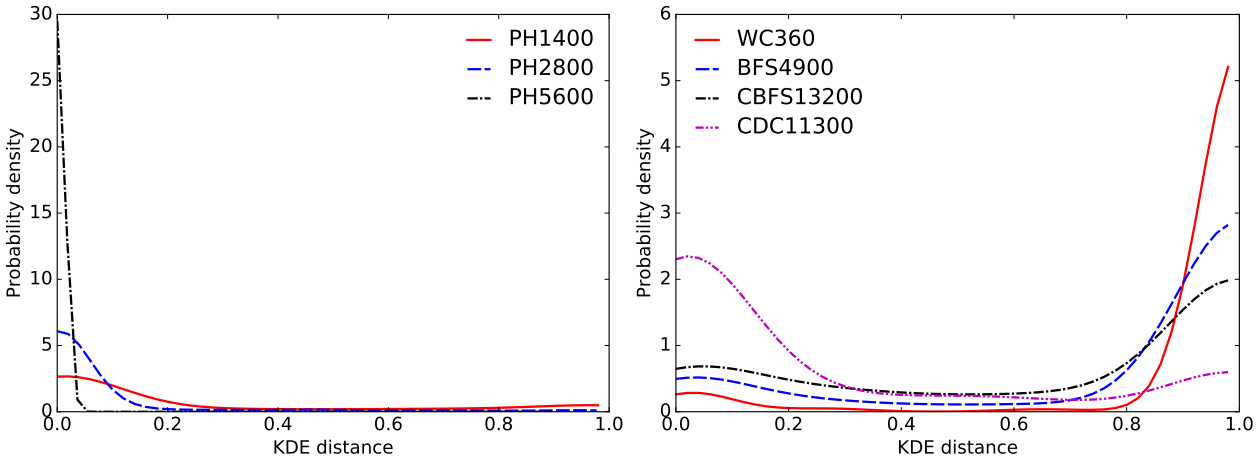

(a) Reynolds number extrapolation (b) Geometry extrapolation

Figure 6.7: Probability density function of KDE distance based on different training sets. (a) The distribution of KDE distance based on Reynolds number extrapolation. (b) The distribution of KDE distance based on geometry extrapolation. All the KDE distances have been normalized by the estimated area occupied by training set in feature space.

may still be effective as an extrapolation metric on turbulence data sets.

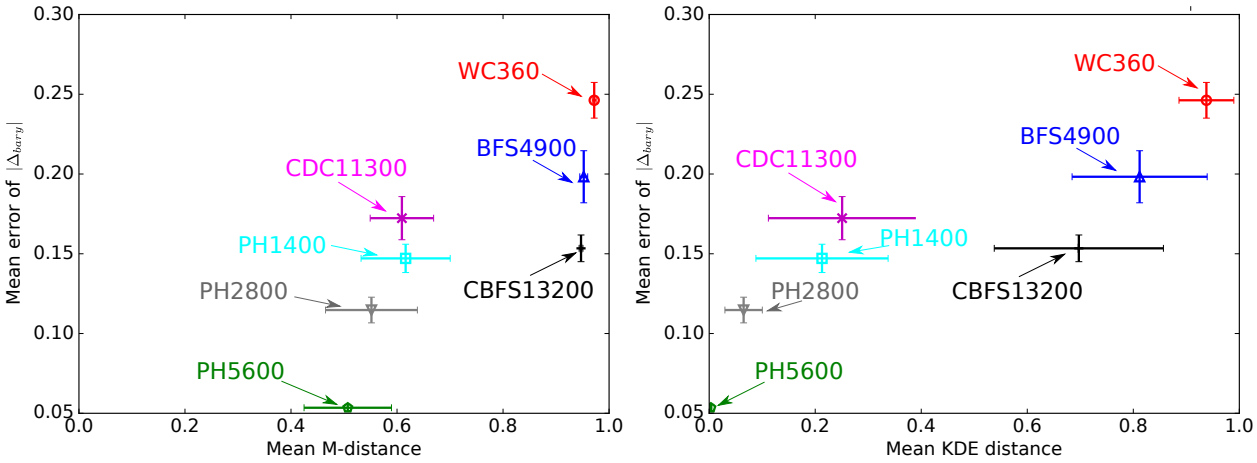

(a) Mahalanobis distance (b) KDE distance

Figure 6.8: The relationship between the mean error of the prediction of Reynolds stress anisotropy and the mean value of extrapolation metrics, i.e., (a) Mahalanobis distance and (b) KDE distance. The standard deviations of both extrapolation metrics are shown as the horizontal bars. The standard deviations of the prediction error of anisotropy are also shown as the vertical bars.

After demonstrating the positive correlation between prediction error and extrapolation metrics through an integral view as shown in Fig. 6.8, the next step is to investigate the relationship between local prediction performance and extrapolation metrics as shown in Figs. 6.9 to 6.11.

The predictions of Reynolds stress anisotropy as shown in Figs. 6.9(a) and 6.9(b) have a good agreement with the benchmark data, which demonstrates that the prediction performance is satisfactory. The training set is the flow over periodic hills at $Re = 5600$. It should be noted that such satisfactory prediction performance is not necessarily guaranteed for Reynolds number extrapolation. In this work, there is no significant change of flow physics for the flows over periodic hills from $Re = 5600$ to $Re = 10595$, which explains the successful Reynolds number extrapolation as shown in Fig. 6.9. For other flows such as boundary layer transition, it is unlikely to achieve the similar quality of prediction by training on the boundary layer without transition and predicting one with a transition. Therefore, the satisfactory Reynolds number extrapolation results shown here should be interpreted with caution. The KDE distance is close to zero in most areas as shown in Fig. 6.9(d), indicating that the extrapolation extent from training set to test set is small. It is consistent with the prediction performance of Reynolds stress anisotropy as shown in Figs. 6.9(a) and 6.9(b). In addition, it can be seen in Fig. 6.9(d) that the KDE distance is large near the bottom wall at the regions from $x/H = 1$ to $x/H = 2$ and from $x/H = 2$ to $x/H = 3$. The reason is that the training set only has data along $x/H = 1$, 2 and 3, and the extrapolation extent is expected to be high between these lines due to the flow separation, which leads to a rapid change of flow features. Compared to KDE distance, the Mahalanobis distance is generally high near the bottom wall at the region from $x/H = 1$ to $x/H = 3$, which indicates that Mahalanobis distance is a more rough estimation of extrapolation compared with KDE distance.

The prediction of Reynolds stress anisotropy as shown in Fig. 6.10 is less satisfactory than the prediction as shown in Fig. 6.9, when the flow over curved backward facing step at $Re = 13200$ is used as the training set. Specifically, the prediction of anisotropy shown in Figs. 6.10(a) and 6.10(b) still have a good agreement with the benchmark data at the regions from $x/H = 2$ to $x/H = 4$ (the mean squared error of ξ and η are 0.0046 and 0.0095, respectively). The prediction of anisotropy is less satisfactory at the downstream region from $x/H = 5$ to $x/H = 7$ (the mean squared error of ξ and η are 0.0124 and 0.0097, respectively), and the prediction is even less satisfactory near the hill crest at inlet and within the contraction region from $x/H = 7$ to $x/H = 9$ (the mean squared error of ξ and η are 0.036 and 0.037, respectively). A possible reason is that the mean flow feature of contraction and the favorable pressure gradient is not covered in the training set, which means that the extrapolation extent at the contraction region is greater. Due to the periodic inlet boundary condition, it is expected that the extrapolation extent near the inlet would also be high. From the contour of KDE distance as shown in Fig. 6.10(d), it can be seen that such a pattern of extrapolation extent is faithfully represented. Compared to the KDE distance, the Mahalanobis distance as shown in Fig. 6.10(c) is less informative. It demonstrates that the normalized Mahalanobis distance is less able to estimate the extrapolation extent based

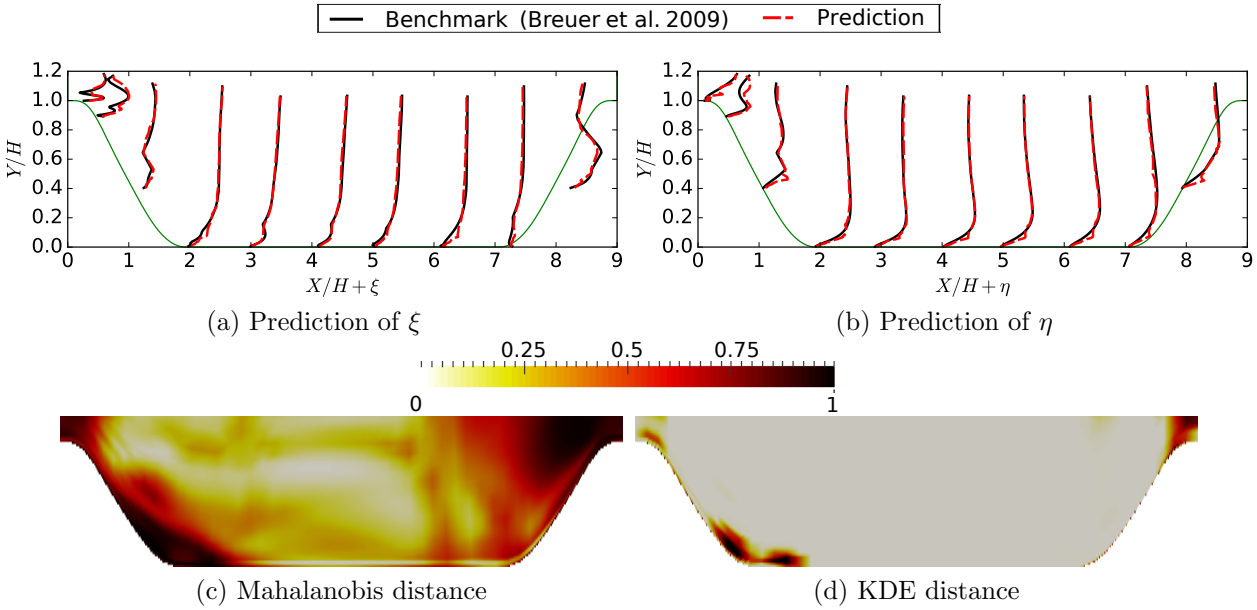

(a) Prediction of ξ (b) Prediction of η

(c) Mahalanobis distance (d) KDE distance

Figure 6.9: Prediction of Reynolds stress anisotropy for the flow over periodic hills at $Re = 10595$ along (a) horizontal direction ξ and (b) vertical direction η of Barycentric triangle. **The training set is the flow over periodic hills at $Re = 5600$**. The profiles are shown at 10 locations, $x/H = 0$, 0.5, 1, 2, ..., 8. The benchmark discrepancy is obtained based on the Reynolds stress from LES simulation [19]. The contours of (c) Mahalanobis distance and (d) KDE distance are presented for comparison.

on geometry extrapolation.

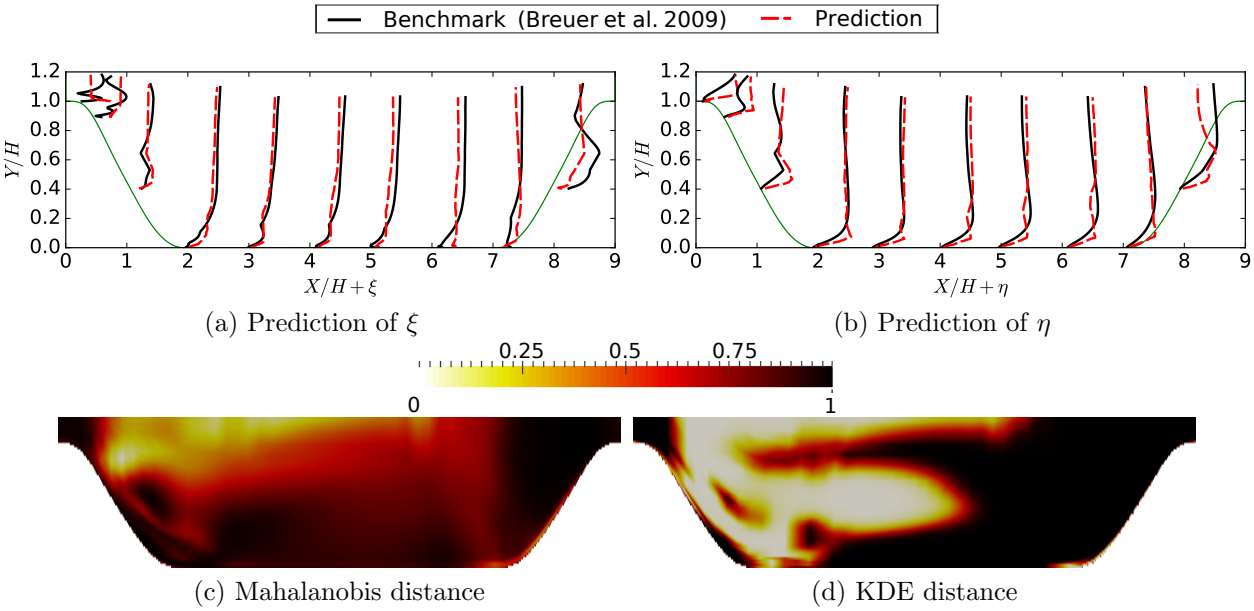

(a) Prediction of ξ (b) Prediction of η

(c) Mahalanobis distance (d) KDE distance

Figure 6.10: Prediction of Reynolds stress anisotropy for the flow over periodic hills at $Re = 10595$ along (a) horizontal direction ξ and (b) vertical direction η of Barycentric triangle. **The training set is the flow over curved backward facing step at $Re = 13200$**. The profiles are shown at 10 locations, $x/H = 0$, 0.5, 1, 2, ..., 8. The benchmark discrepancy is obtained based on the Reynolds stress from LES simulation [19]. The contours of (c) Mahalanobis distance and (d) KDE distance are presented for comparison.

Compared to the prediction of anisotropy as shown in Figs. 6.9 and 6.10, the prediction performance is much less satisfactory as shown in Fig. 6.11, where the training case is the flow in a wavy channel at $Re = 360$. The main reason is that the Reynolds number of the training set is much smaller than that of the prediction set, and extrapolation extent is expected to be high across the whole domain. From the contours of Mahalanobis distance and KDE distance as shown in Figs. 6.11(c) and 6.11(d), it can be seen that such a pattern of extrapolation extent is represented by both the Mahalanobis distance and KDE distance. Both metrics are near one for almost the entire extent of the domain.

The scatter plot of local prediction error of Reynolds stress anisotropy and extrapolation metrics are presented in Figs. 6.12 and 6.13. The correlation coefficients are also presented in Table. 6.1 for a more quantitative comparison.

The scatter pattern is more random as shown in Fig. 6.12(a) when the Mahalanobis distance is employed as extrapolation metric and the training set is the flow over periodic hills at $Re = 5600$. A possible explanation is that when Mahalanobis distance becomes small, it is expected that the extrapolation error is also small. Therefore, other error sources, such as non-local effect that is not correlated with Mahalanobis distance, will dominate and

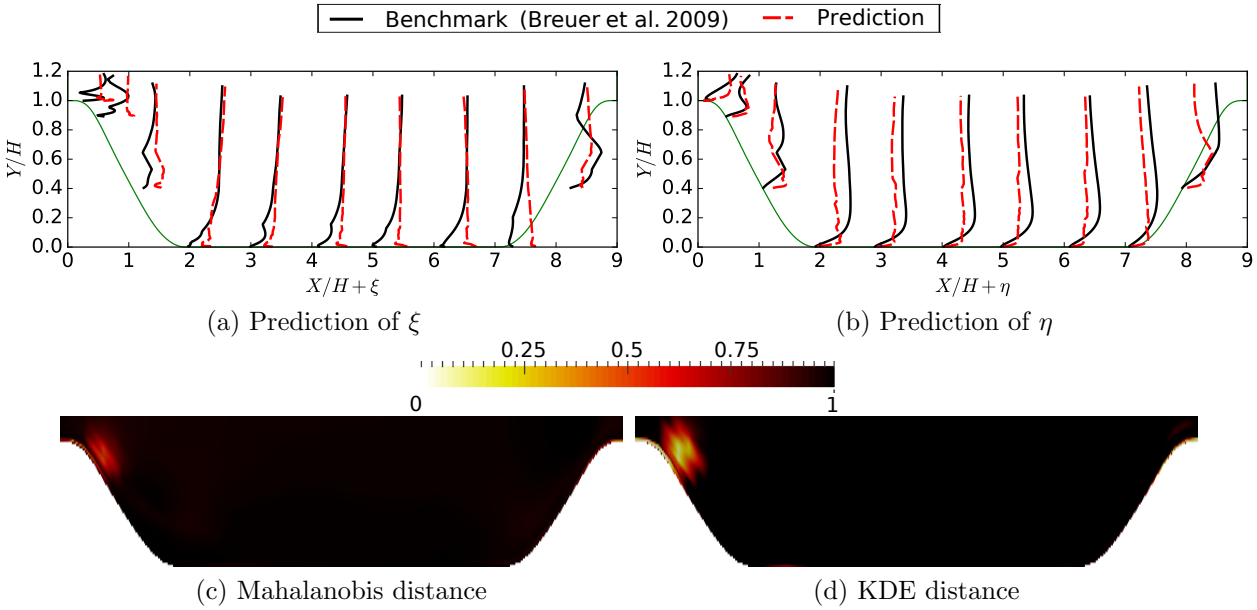

(a) Prediction of ξ (b) Prediction of η

(c) Mahalanobis distance (d) KDE distance

Figure 6.11: Prediction of Reynolds stress anisotropy for the flow over periodic hills at $Re = 10595$ along (a) horizontal direction ξ and (b) vertical direction η of Barycentric triangle. **The training set is the flow in a wavy channel at $Re = 360$**. The profiles are shown at 10 locations, $x/H = 0$, 0.5, 1, 2, ..., 8. The benchmark discrepancy is obtained based on the Reynolds stress from LES simulation [19]. The contours of (c) Mahalanobis distance and (d) KDE distance are presented for comparison.

the relationship between prediction error and Mahalanobis distance tends to become more random.

Table 6.1: Correlation coefficients between extrapolation metrics and the prediction error of anisotropy

Training Set	Mahalanobis Distance	KDE Distance
Periodic Hills ($Re = 5600$)	0.31	0.40
Periodic Hills ($Re = 2800$)	0.38	0.66
Periodic Hills ($Re = 1400$)	0.40	0.70
Curved Step ($Re = 13200$)	0.28	0.53
C-D Channel ($Re = 11300$)	0.42	0.54
Backward Step ($Re = 4900$)	0.41	0.57
Wavy Channel ($Re = 360$)	-0.06	0.08

Compared to the correlation shown in Fig. 6.12(a), it can be seen in Figs. 6.12(b) and 6.12(c) that the correlation is stronger when the training set is the flow over periodic hills at $Re = 1400$ or the flow over curved backward facing step, which is also confirmed by the quantitative comparison of correlation coefficients as shown in Table 6.1. In these cases, therefore, it can be seen that the extrapolation error is a dominant source of error in the regression models. If the extrapolation extent further increases, it is shown in Fig. 6.12(d) that the correlation between Mahalanobis distance and prediction error becomes weak again. This is due to the clustering of Mahalanobis distance near one, which significantly reduces the resolution of Mahalanobis distance. In such a scenario, the correlation between prediction error of Reynolds stress anisotropy and Mahalanobis distance is weaker, which leads to a more random relationship between Mahalanobis distance and prediction error.

The pattern of correlation between the prediction error of Reynolds stress anisotropy and KDE distance as shown in Fig. 6.13 is similar to that based on Mahalanobis distance. Specifically, there exists a positive correlation if the training set is the flow over periodic hills at $Re = 1400$ or the flow over curved backward step at $Re = 13200$. The correlation is weaker if the training set is the flow over periodic hills at $Re = 5600$ or the flow in a wavy channel at $Re = 360$. Although the correlation pattern is similar based on Mahalanobis distance and KDE distance, the clustering pattern is different. The Mahalanobis distance based on Reynolds number extrapolation is more evenly distributed from zero to one, while the KDE distance based on Reynolds number extrapolation tends to cluster near zero. On the other hand, the Mahalanobis distance based on geometry extrapolation is more likely to cluster near one as shown in Fig. 6.12(d), while such clustering is less noticeable for KDE distance as shown in Fig. 6.13(d).

The correlation coefficient is smaller based on Mahalanobis distance as shown in Table 6.1, indicating that the prediction error of Reynolds stress anisotropy is less correlated with

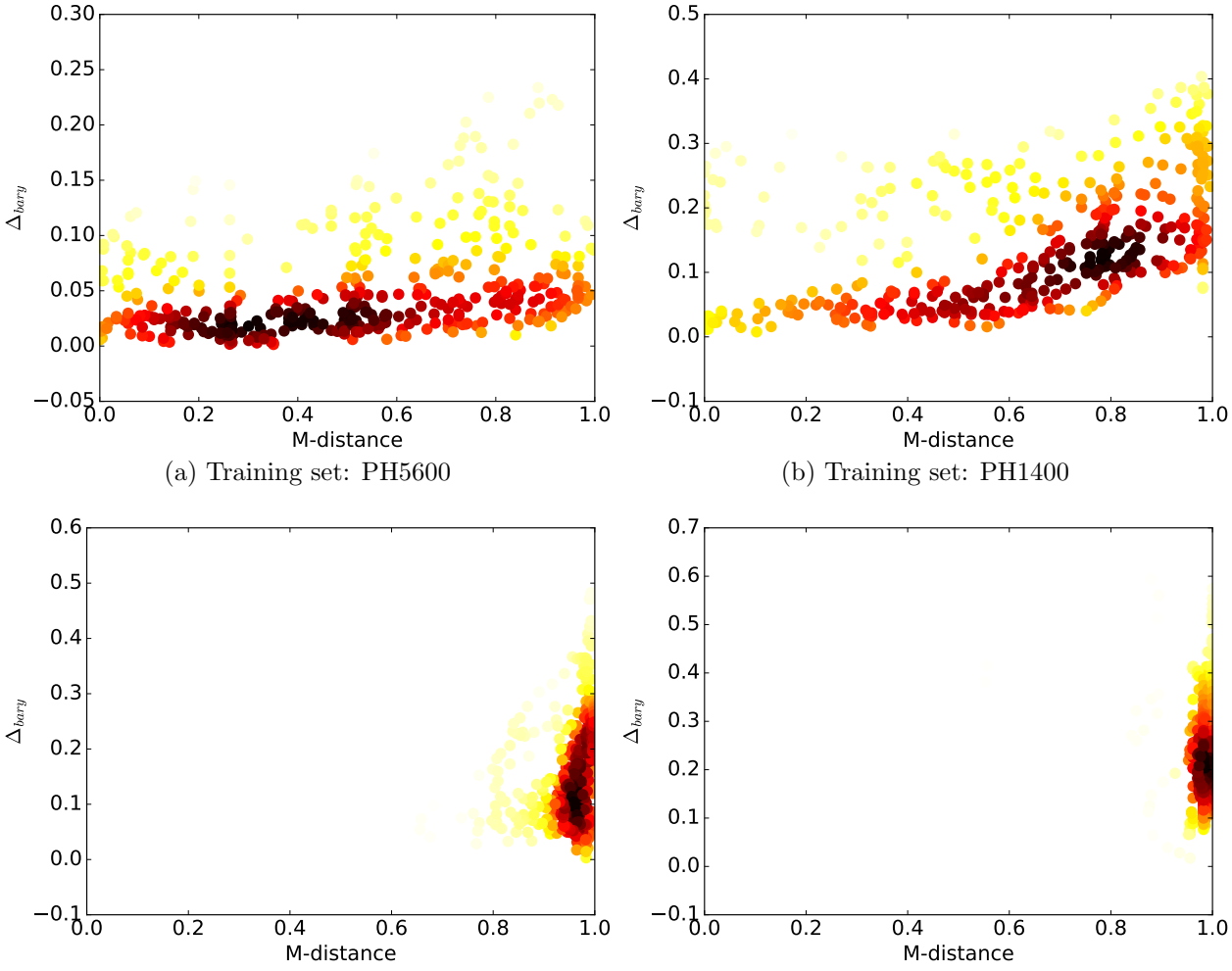

(a) Training set: PH5600

(b) Training set: PH1400

(c) Training set: CBFS13200

(d) Training set: WC360

Figure 6.12: The correlation between the Mahalanobis distance and the prediction error of Reynolds stress anisotropy. The results based on four training sets are presented, including (a) the flow over periodic hills at $Re = 5600$ (PH5600), (b) the flow over periodic hills at $Re = 1400$ (PH1400), (c) the flow over curved backward facing step at $Re = 13200$ (CBFS13200) and (d) the flow in a wavy channel at $Re = 360$ (WC360). Points are colored by the local density of the scatter plot, and the brighter color indicates the higher density.

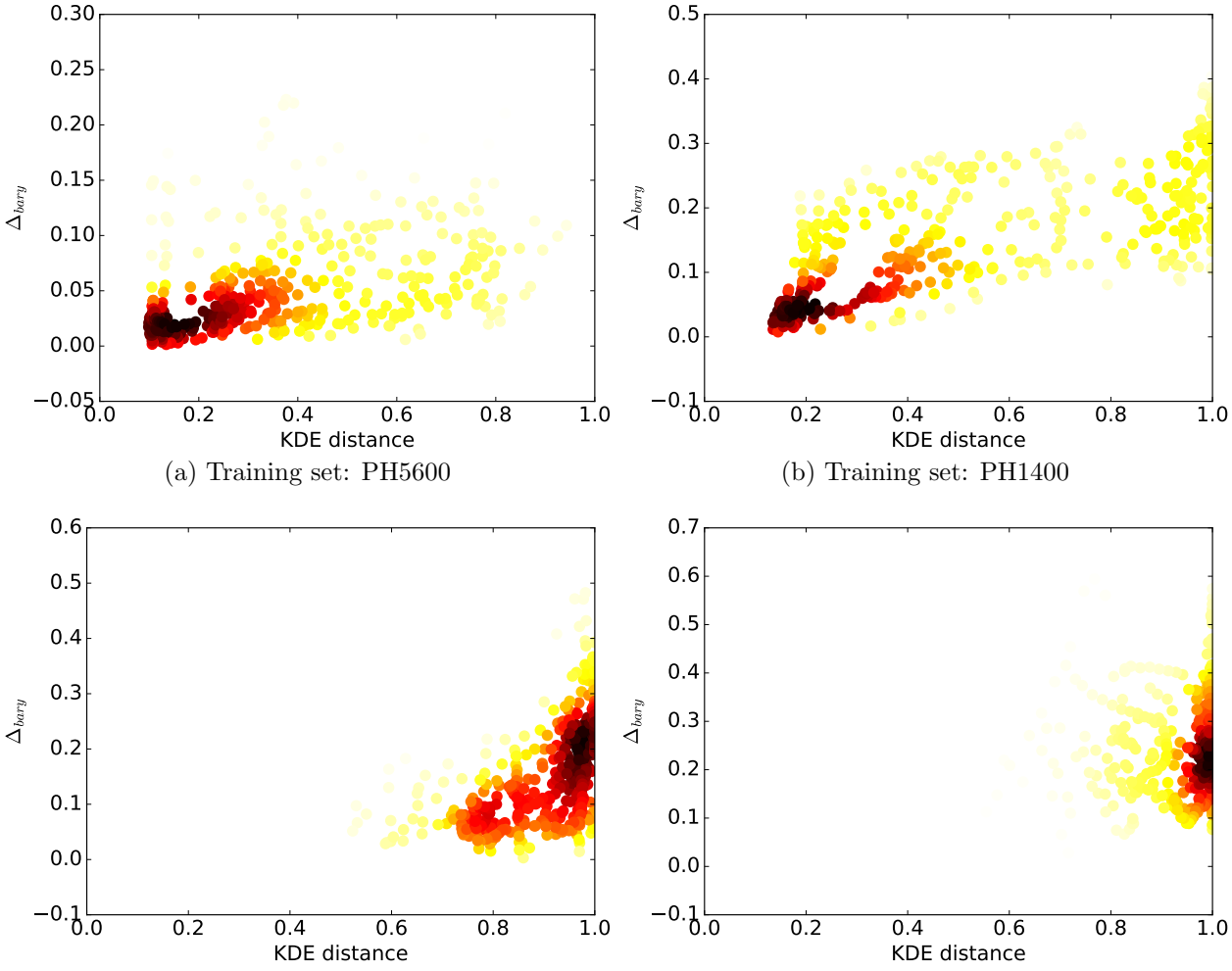

(a) Training set: PH5600

(b) Training set: PH1400

(c) Training set: CBFS13200

(d) Training set: WC360

Figure 6.13: The correlation between the KDE distance and the prediction error of Reynolds stress anisotropy. The results based on four training sets are presented, including (a) the flow over periodic hills at $Re = 5600$ (PH5600), (b) the flow over periodic hills at $Re = 1400$ (PH1400), (c) the flow over curved backward facing step at $Re = 13200$ (CBFS13200) and (d) the flow in a wavy channel at $Re = 360$ (WC360). Points are colored by the local density of the scatter plot, and the brighter color indicates the higher density.

Mahalanobis distance. In addition, the correlation coefficient based on Mahalanobis distance can become negative if the extrapolation extent is high, e.g., the flow in a wavy channel at $Re = 360$ is used as training set. Therefore, Mahalanobis distance is less accurate in estimating the extrapolation extent and prediction performance compared with the KDE distance. This is consistent with our expectation since the Gaussian distribution assumption in calculating Mahalanobis distance may not be appropriate. However, it should be noted that the Gaussian distribution assumption reduces the memory usage and the computational cost of extrapolation metrics, which is the advantage of the Mahalanobis distance.

6.5 Conclusion

Recently, the increasing interest in data-driven turbulence modeling has created a demand for simple metrics for evaluating extrapolation. Such *a priori* evaluation can provide an estimate of the predictive performance in real applications where high fidelity data are not available for the flow to be predicted. In addition, it can guide the choice of training flows to achieve better prediction performance. In the present work we discuss the evaluation of extrapolation between different flows in feature space. The Mahalanobis distance and KDE distance are used as two extrapolation metrics in feature space to measure the closeness between different flows. Specifically, the flow over periodic hills at $Re = 10595$ is used as the test set in this work. Three training sets at different Reynolds numbers and four training sets with different geometries are individually used to investigate the relationship between the prediction error and the extrapolation metrics. In particular, two training sets at different Reynolds numbers and two training sets with different geometries are chosen for detailed analysis. The results demonstrate that the relationship between extrapolation metrics and the prediction error is less correlated in two extreme scenarios, i.e., when the training set is very similar to the test set or very different from the test set. In the former case, other sources of error besides extrapolation error dominate the prediction uncertainty. In the later case, the degree of extrapolation is so high that the machine learning algorithm is just "guessing", leading to a plateau in the error rate. Except for these two extreme scenarios, both the Mahalanobis distance and the KDE distance are positively correlated with the prediction error, demonstrating that both extrapolation metrics can be used in estimating the extrapolation extent and prediction performance. However, the quantitative comparison of correlation coefficient shows that the prediction error is less correlated with the Mahalanobis distance, indicating that the estimation of extrapolation extent based on Mahalanobis distance is less accurate. On the other hand, the Gaussian distribution assumption of Mahalanobis distance reduces the memory usage and the computational cost, which is the advantage of using Mahalanobis distance. In conclusion, the KDE distance is preferable if the accuracy of extrapolation estimation is more important, while the Mahalanobis distance is still acceptable in some applications in which the memory usage or the computational cost of high dimensional kernel density estimation is not affordable.

Acknowledgment

HX would like to thank Dr. Eric G. Paterson for numerous helpful discussions during this work.

Sandia National Laboratories is a multi-program laboratory managed and operated by Sandia Corporation, a wholly owned subsidiary of Lockheed Martin Corporation, for the U.S. Department of Energy's National Nuclear Security Administration under contract DE-AC04-94AL85000. SAND2016-6700J

Bibliography

[1] T. Craft, B. Launder, K. Suga, Development and application of a cubic eddy-viscosity model of turbulence, International Journal of Heat and Fluid Flow 17 (1996) 108–115.

[2] M. Milano, P. Koumoutsakos, Neural network modeling for near wall turbulent flow, Journal of Computational Physics 182 (2002) 1–26.

[3] B. Tracey, K. Duraisamy, J. Alonso, Application of supervised learning to quantify uncertainties in turbulence and combustion modeling, AIAA Aerospace Sciences Meeting, AIAA 2013-0259, 2013.

[4] K. Duraisamy, Z. Shang, A. Singh, New approaches in turbulence and transition modeling using data-driven techniques, AIAA 2015–1284, 2015.

[5] J. Ling, J. Templeton, Evaluation of machine learning algorithms for prediction of regions of high reynolds averaged navier stokes uncertainty, Physics of Fluids (1994-present) 27 (8) (2015) 085103.

[6] J. Ling, A. Ruiz, G. Lacaze, J. Oefelein, Uncertainty analysis and data-driven model advances for a jet-in-crossflow, ASME Turbo Expo 2016.

[7] J. Ling, A. Kurzawski, J. Templeton, Reynolds averaged turbulence modelling using deep neural networks with embedded invariance, Journal of Fluid Mechanics 807 (2016) 155–166.

[8] J.-X. Wang, J.-L. Wu, H. Xaio, A physics informed machine learning approach for reconstructing Reynolds stress modeling discrepancies based on DNS data, accepted, Physics Review Fluids (2017).

[9] J. Ling, R. Jones, J. Templeton, Machine learning strategies for systems with invariance properties, Journal of Computational Physics 318 (2016) 22–35.

[10] A. Liaw, M. Wiener, Classification and regression by randomforest, R news 2 (3) (2002) 18–22.

[11] C. Gorle, M. Emory, G. Iaccarino, RANS modeling of turbulent mixing for a jet in supersonic cross flow: model evaluation and uncertainty quantification, in: ICHMT DIGITAL LIBRARY ONLINE, Begel House Inc., 2012.

[12] M. Emory, R. Pecnik, G. Iaccarino, Modeling structural uncertainties in reynolds-averaged computations of shock/boundary layer interactions, AIAA paper 479 (2011) 2011.

[13] H. Xiao, J.-L. Wu, J.-X. Wang, R. Sun, C. J. Roy, Quantifying and reducing model-form uncertainties in Reynolds-Averaged Navier-Stokes simulations: A data-driven, physics-based Bayesian approach, Journal of Computational Physics 324 (2016) 115–136.

[14] S. Banerjee, R. Krahl, F. Durst, C. Zenger, Presentation of anisotropy properties of turbulence, invariants versus eigenvalue approaches, Journal of Turbulence 8 (32) (2007) 1–27.

[15] L. Breiman, Random forests, Machine learning 45 (1) (2001) 5–32.

[16] J. Friedman, T. Hastie, R. Tibshirani, The elements of statistical learning, Springer, Berlin, 2001.

[17] M. Emory, J. Larsson, G. Iaccarino, Modeling of structural uncertainties in Reynolds-averaged Navier-Stokes closures, Physics of Fluids 25 (11) (2013) 110822.

[18] G. H. Chris Rumsey, Brian Smith, Turbulence modeling resource (2016). `http://turbmodels.larc.nasa.gov`

[19] M. Breuer, N. Peller, C. Rapp, M. Manhart, Flow over periodic hills–numerical and experimental study in a wide range of reynolds numbers, Computers & Fluids 38 (2) (2009) 433–457.

[20] Y. Bentaleb, S. Lardeau, M. A. Leschziner, Large-eddy simulation of turbulent boundary layer separation from a rounded step, Journal of Turbulence (13) (2012) N4.

[21] J.-P. Laval, M. Marquillie, Direct numerical simulations of converging–diverging channel flow, in: Progress in Wall Turbulence: Understanding and Modeling, Springer, 2011, pp. 203–209.

[22] H. Le, P. Moin, J. Kim, Direct numerical simulation of turbulent flow over a backward-facing step, Journal of fluid mechanics 330 (1997) 349–374.

[23] C. Maaß, U. Schumann, Direct numerical simulation of separated turbulent flow over a wavy boundary, in: Flow Simulation with High-Performance Computers II, Springer, 1996, pp. 227–241.

[24] T. Cover, P. Hart, Nearest neighbor pattern classification, IEEE Transactions 13 (1967) 21–27.

[25] P. C. Mahalanobis, On the generalized distance in statistics, Proceedings of the National Institute of Sciences (Calcutta) 2 (1936) 49–55.

[26] B. Silverman, Density estimation for statistics and data analysis, CRC Press, 1986.

[27] D. W. Scott, Multivariate density estimation: theory, practice, and visualization, John Wiley & Sons, 2015.

[28] B. Launder, B. Sharma, Application of the energy-dissipation model of turbulence to the calculation of flow near a spinning disc, Letters in heat and mass transfer 1 (2) (1974) 131–137.

[29] H. G. Weller, G. Tabor, H. Jasak, C. Fureby, A tensorial approach to computational continuum mechanics usi ng ject-oriented techniques, Computers in physics 12 (6) (1998) 620–631.

[30] R. L. Thompson, L. E. B. Sampaio, F. A. de Bragança Alves, L. Thais, G. Mompean, A methodology to evaluate statistical errors in DNS data of plane channel flows, Computers & Fluids 130 (2016) 1–7.

[31] S. V. Poroseva, J. D. Colmenares F, S. M. Murman, On the accuracy of RANS simulations with DNS data, Physics of Fluids 28 (11) (2016) 115102.

[32] J.-X. Wang, J. Wu, J. Ling, G. Iaccarino, H. Xiao, A comprehensive physics-informed machine learning framework for predictive turbulence modeling, submitted. Available at arXiv:1701.07102 (2017).

Chapter 7

Conclusion and Future Work

Reynold-Averaged Navier–Stokes (RANS) simulations are still a workhorse tool of simulating turbulent flows in engineering applications. Due to the large model-form uncertainties in RANS simulations for complex flows, it is of critical importance to quantify such model-form uncertainties. In this work, two data-driven approaches are presented to quantify the RANS model-form uncertainties by utilizing either sparse online measurement data or offline high-fidelity simulation databases. The first data-driven approach is based on Bayesian inverse modeling, where an ensemble Kalman method is utilized to leverage the sparse online measurement data with empirical prior knowledge about the RANS model-form uncertainties. Specifically, the Reynolds stress tensor is decomposed into six physical components to facilitate the imposing of physical constraints, e.g., realizability of Reynolds stress. The model-form uncertainties with regard to each physical components are modeled by Gaussian processes, and compact parameterizations are further obtained by using truncated Karhunen–Loève expansion. The coefficients of the Karhunen–Loève expansion are then calibrated by using an ensemble Kalman method with sparse online measurement data. A calibration-prediction procedure is also presented to apply the calibrated RANS model-form uncertainties to some closely-related flows where measurement data are not available. It is further showed that the proper geometry transformation is difficult to determine when the calibration flow and the prediction flow have different geometry configurations. Therefore, another data-driven approach is proposed to build the functional form between the Reynolds stress discrepancies and some mean flow features, instead of physical coordinates. Such a functional form is trained by machine learning techniques with existing offline high-fidelity simulation databases. Specifically, a systematic way is presented to extract invariants to represent Reynolds stress discrepancies and mean flow features. With the extracted invariants as inputs and outputs in machine learning, the important invariances (e.g., Galilean invariance) can be preserved in the trained functional form. Considering that RANS equations can be ill-conditioned for some flows, a stabilized machine learning scheme is also proposed to improve the conditioning for data-driven RANS modeling. In order to assess the prediction confidence for real applications, two *a priori* metrics are proposed to evaluate how well the

flow to be predicted is supported by the training data within the mean flow features space.

The quantification of RANS model-form uncertainties by using data-driven methods is still a recently emerging research area. In the following, a few potential research directions are listed for future investigation:

1. In the data-driven Bayesian inverse modeling framework for quantifying model-form uncertainties in RANS simulations (presented in Chapter 2), there are three limitations. One limitation is the non-unique mapping from mean velocity to Reynolds stress. Therefore, it is only possible to use mean velocity measurement data to infer the correct divergence of Reynolds stress, instead of the Reynolds stress itself. To overcome this limitation, proper regularization techniques are needed to further constrain the inversely modeled Reynolds stress. The second limitation is the specification of covariance kernel for Gaussian processes to represent the prior model-form uncertainties. Square exponential kernel with homogeneous length scales is likely to be insufficient for more complex flows. Considering that the spatial correlation information is encoded in the differential operators of the governing PDEs, it is possible to develop a systematic way for constructing a PDEs-informed covariance kernel. Another limitation of this framework is the quantified uncertainties from the iterative ensemble Kalman methods. The computed uncertainties from the iterative ensemble Kalman methods are not accurate and tend to underestimate the true uncertainties. This is because ensemble Kalman methods are an approximate Bayesian approach. Therefore, the computed uncertainties from ensemble Kalman methods can be compared to the exact Bayesian approach based on Markov Chain Monte-Carlo (MCMC) sampling, in order to understand the impact of approximate Bayesian methods upon the quantified uncertainties.

2. In the physics-informed machine learning framework, there are three potential future directions. First, the extrapolation capability is still relatively limited in the current framework, and thus the machine learning prediction is much less reliable if the flow to be predicted is significantly different from the training flows. The extrapolation capability may be further enhanced by utilizing some domain adaptation techniques, i.e., finding a latent space where the difference between the flow to be predicted and the training flows is minimized in terms of some distance metrics (e.g., Kullback–Leibler divergence or more generally f-divergence). Second, the current physics-informed machine learning framework only provides deterministic prediction of Reynolds stress discrepancies, and the prediction confidence is evaluated separately as presented in Chapter 6. It is possible to combine the prediction of Reynolds stress discrepancies and the evaluation of prediction confidence by using Bayesian neural networks. Finally, the current physics-informed machine learning framework only utilizes offline high-fidelity simulation databases but not online sparse measurement data. It is possible to develop a new machine learning architecture to combine the use of offline high-fidelity simulation databases and online sparse measurement data.